Geochemical Mechanisms of Biomineralization from Analysis of Deep-Sea and Laboratory Cultured Corals

Thesis by

Alexander C. Gagnon

In Partial Fulfillment of the Requirements

for the Degree of

Doctor of Philosophy

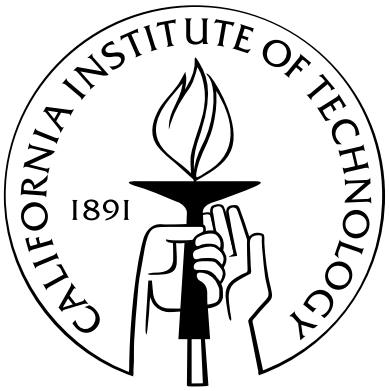

California Institute of Technology

Pasadena, California

2010

(Defended October 8, 2009)

Acknowledgements

This thesis is a direct result of the enthusiasm and guidance of my two advisors, Jess Adkins and Doug Rees. Jess introduced me to geochemistry and mass spectrometry, made me an uncompromising data analyst, taught me the importance of distilling scientific results into accessible mathematical models, took me to the bottom of the ocean and around the world. Most of all Jess was always excited to do science—a source of constant encouragement and inspiration. Doug was steadfast in his support: even as my project drifted from his area of direct expertise he was always available to share his experience, advice and encouragement.

Jonathan Erez acted as a generous mentor during my two visits to Israel and during the sabbatical he took to work at Caltech while I finished my thesis. The hours spent together beside a microscope or an aquarium were invaluable. Jonathan shared two great gifts with me. He shared the Art of science, which is the ability to look at a complex organism like coral and see important patterns, and he shared his industrious creativity. I am also deeply indebted to the incredibly warm welcome offered by all my hosts in Jerusalem, especially Michal Schwartz and Sharon Reuveni.

A special thanks to Dr. Stephen Cairns and The Smithsonian Institution National Museum of Natural History for allowing the analysis of the deep-sea coral specimens in this study, for the time he spent with me during my short visit to the Smithsonian.

My scientific journey through Caltech was graced by many amazing individuals. Diego Fernandez is a modest genius with the soul and intellect of a renaissance virtuoso. Laura Robinson is sharp, spreads infectious smiles, is tirelessly supportive, ridiculously patient and plays a mean game of fish. Yunbin Guan taught me to operate the nanoSIMS, hardly a trivial education, and was accessible day, night and weekends to guide me through the inevitable technical problems. Lindsey M. Hedges

has to be the most selfless person at Caltech and was always up for a conversation. The Adkins lab is filled with superb people and great friends: Jeff, Anna, Nithya, Seth, Adam, Rinat, Selene and others—hopefully they think the same of me after weeks at sea and years sharing offices, labs and equipment. Weifu and I spent many long nights in N. Mudd dreaming up new scientific projects between experiments and writing. Thanks also to Akif, Jens, Chad and all the Rees group members: who knew postdocs could fly. John Eiler's questions, whether directed to me or a visiting speaker, were a constant reminder of the need to link the small part of science we do everyday into a more broadly relevant context. I would like to thank George Rossman for always making time to talk science, for providing access to the Caltech Mineral Collection, and for enthusiastically allowing me to analyze Amy's science diamond on every available lab instrument before I mounted it in a ring and asked her to marry me.

This project benefited from the help and advice of many individuals, some of whom are mentioned here. Will Berelson of USC made his lab available for DIC measurements. Several assistants at Hebrew University, Jerusalem helped with alkalinity measurements when I was overwhelmed by samples. Christie Canaria and Chris Waters assisted with confocal microscopy. I am sure I have missed countless contributions and apologize for these omissions.

The friends I met at Caltech outshine even the consuming god(ess) of science: Daven, Jesse, Ryan, Kenji, Dan Fisher, ML, Dan Feldman, Eric and many others. To meet such incredible and lifelong friends is the greatest gift bequeathed by Caltech. May the C-boys ride again even if it means we will have to jump out of a Pavehawk with Fisher. Eric Ostby is the only person I know to have been broadsided by a whale. Ricketts Hovse loudly embraced my tenure under their roof—rare be the group with souls as raucous, warm and aligned with my own.

Even though it often feels as if the world begins and ends between Del Mar and California Blvd., I owe thanks to many people and places outside of Caltech. The list is too long to cover completely, Pat Bixler of Crane School and Susan Park of SBHS made me fall in love with science while putting up with what must have been awfully nerdy questions. Gary Carroll of Santa Barbara City College believed a little high school junior could do well in organic chemistry and taught the best chemistry

class I have ever taken. Friends from Santa Barbara, Berkeley and beyond kept me sane when necessary and crazy when crucial: Sean, John Burke, Will, Dave, Colin, and Billy—somehow we still have all our limbs. Annual runs for pancreatic cancer research with Tyler were a highlight of the last few years at Caltech.

The members of Sierra Madre Search and Rescue are volunteers dedicated to responding anywhere in the wilderness where someone needs help. They are selfless, incredibly inspirational, and committed to a level of excellence which surpasses even the most single minded scientist. I am intensely proud of the team's work and of the short time I was able to count myself a member.

Had you been blind perhaps I could convey the importance of the sun, the awe as it rises out of nothing and the way it shines for all of us to see, by comparing the sun to parents. My parents have shined on my whole life. They teach me so much, encouraging excellence and independence, nurturing my creativity, analytical ability, and heart. It was little things like cartesian coordinate connect the dots or playing inventor and big things too. I have been blessed by four amazing parents and I love you all.

Somehow the most important people always end up at the bottom the acknowledgements. Perhaps it is because they are the foundation of our lives filling us with the love, hope, strength and smiles upon which all else is based. Dr. Amy Eastwood is the most generous, supportive, tolerant, adventurous, intelligent, and loving woman. It still amazes me that we met in the midst of Caltech and I am so thankful for it. (I should have believed Harry Gray during my graduate school visit when promised to marry me off).

Abstract

The ocean is a major component of global heat transport and represents a large exchangeable reservoir of CO_2. The importance of these effects on climate can be quantified with records of ocean temperature, chemistry and dynamics spanning past climate change. One approach to reconstruct past ocean conditions relies on the chemical composition of $CaCO_3$ skeletons from coral. Despite the utility of these geochemical proxies, several lines of evidence suggest that biomineralization, the process corals use to build their skeletons, also influences composition, complicating the interpretation of past records. Coral grown under constant environmental conditions, either collected from the deep-sea or cultured in the laboratory, are used to quantify and spatially map the effects of biomineralization on skeletal composition.

In modern deep-sea coral, Mg/Ca increases with decreasing Sr/Ca in most the skeleton, consistent with closed-system (Rayleigh) precipitation. Results also show composition strongly follows skeletal architecture. Centers of calcification (COCs) are small regions of disorganized crystals thought to be the initial stage of skeletal extension. Unlike the rest of the skeleton, Mg/Ca ratios vary more than two fold within the COCs while Sr/Ca is near constant. Our data provide new constraints on a number of possible mechanisms for this effect.

In a complementary set of experiments the nanoSIMS, a new instrument capable of accurate sub-micron compositional analysis, is applied to adult cultured surface coral (1) mapping the pattern of metal ion incorporation in new growth and showing that the calcifying fluid is likely in direct exchange with seawater; and (2) testing the sensitivity of Me/Ca ratios to aragonite saturation (Ω). Despite a large range of Ω and calcification rates, the average Sr/Ca of nanoSIMS spot measurements in cultured coral are within 1.2% (2 std. dev. of the 5 means). These data suggest that

temperature is a more significant control on Sr/Ca than aragonite saturation between $\Omega = 2.5$–5. Within the framework of a closed-system (Rayleigh) model for biomineralization the results constrain explanations for the sensitivity of coral calcification rates to ocean acidification, improving our understanding of how anthropogenic CO_2 will impact coral reefs.

Contents

List of Figures

List of Tables

Chapter 1

Introduction

The ocean accounts for a significant portion of global poleward heat transport and represents a large reservoir of exchangeable CO_2 (Trenberth & Caron, 2001; Ganachaud & Wunsch, 2000; Takahashi et al., 2002). The role of these processes in the climate system over time can be tested with records of ocean temperature, chemistry and dynamics spanning past climate change. One approach to reconstruct past ocean conditions relies on metal/calcium (Me/Ca) ratios in the $CaCO_3$ skeletons of marine organisms. For example, Sr/Ca in skeletons of surface coral is used as a proxy for temperature (Smith et al., 1979; Beck et al., 1992). Applied to well dated records of past Me/Ca in coral these calibrations are used to reconstruct sea-surface temperatures (Beck et al., 1992).

Understanding millennial scale changes in deep-ocean circulation, temperature and chemistry is a major target of paleoceanography (Broecker, 2002). Deep-sea coral have several characteristics that make them a promising subject for proxy development: they can be accurately dated and there is a large and growing global fossil collection including climatically relevant regions of the ocean. One aspect of this thesis is to test if Sr/Ca is a useful paleothermometer in the relatively new archive of deep-sea coral. The typically small magnitude of deep-ocean temperature variability through time and space and an expected small relative temperature sensitivity requires precise Sr/Ca measurements. In Chapter 2 an improved analytical method for measuring Sr/Ca with high precision and throughput is developed and then applied to modern deep-sea coral from a range of growth conditions to test for temperature sensitivity.

Despite the utility of certain Me/Ca ratios as proxies of a single environmental parameter, several

lines of evidence suggest that Me/Ca ratios are each sensitive to a number of environmental and biological factors, complicating the interpretation of past records. One way to address this problem is to identify proxies that are influenced by secondary environmental or biological factors in a constant manner and then calibrate this offset using modern samples. For many proxies this is conducted with "core-top" calibrations. Regression-analysis of modern samples collected from parts of the ocean that collectively span a range of environmental conditions is used to determine the sensitivity of a proxy to different parameters. This core-top approach, however, is limited to resolving the influence of environmental parameters that do not co-vary. Combining geochemical analysis with coral culture has the potential to isolate separate environmental conditions on skeletal composition and growth. For example, proxy calibrations of organisms cultured under controlled conditions can be used to (1) ensure accurate reconstructions of past climate; (2) separate environmental signals from biological variability; and (3) resolve the influence of environmental parameters which co-vary in much of the modern ocean, (i.e., T and $[CO_3^{2-}]$), but likely diverged in the past.

In Chapter 4 a new technique is developed to determine the skeletal composition of adult surface coral in response to different experimentally controlled conditions during short periods of culture (6 day). Using a sequence of progressively more spatially resolved techniques, from bulk isotope analysis to nanoSIMS spot measurements, this newly grown material is mapped and compositionally characterized. As an initial application of the short culture method, Me/Ca ratios are measured in coral cultured under a range of $[CO_3^{2-}]$, a largely untested environmental factor in coral with the potential to bias past temperature records.

While more specific calibrations will certainly improve proxy interpretation, a mechanistic understanding of biomineralization that can separate biological and environmental signals in a systematic way would greatly advance the field. The aragonite ($CaCO_3$) skeleton of coral is typically different in minor element and isotope composition than inorganic $CaCO_3$ precipitated from seawater at a similar temperature (Gaetani & Cohen, 2006; Dietzel et al., 2004; Kinsman & Holland, 1969; Correge, 2006). These differences as well as the patterns of other elements and isotopes within biogenic carbonates can be explained by a set of chemical, biochemical, and physical processes—the biomineral-

alizing mechanism. Many fundamental questions about biomineralization are unanswered: including how open the calcifying region is to external seawater—a major factor controlling environmental vs. biological control. This question is addressed in Chapter 3 using Me/Ca ratios in deep-sea coral.

Unlike the variable surface ocean, much of the deep-sea acts as a"culture medium" of constant composition for the lifetime of a coral. Variability in proxies like Me/Ca ratios are therefore entirely attributable to the process of skeletal formation. These "vital effects" are a chemical fingerprint of the biomineralizing mechanism. Closed system precipitation predicts a quantitative relationship between different Me/Ca ratios. Correlated Mg/Ca and Sr/Ca data from micromilled samples are used to test the role of closed-system behavior in Me/Ca vital effects across skeletal structural features. By examining a key component of many biomineralization models, this work aims to improve the understanding of vital-effect mechanisms during calcification and help better interpret Me/Ca temperature proxies.

Understanding the magnitude and impact of anthropogenic changes to the earth-climate system continues to be an important cross-diciplinary goal. One indisputable effect of fossil-fuel burning is the titration of the marine carbonate system by dissolved CO_2. This "ocean acidifcation" is predicted to increasingly impact marine calcifiers and coral reefs (Kleypas et al., 1999; Orr et al., 2005). Experiments on many scales generally show that coral reduce calcification rate as a response to CO_2 enrichment (Gattuso et al., 1998; Schneider & Erez, 2006; Langdon et al., 2000; Marubini et al., 2003; Silverman et al., 2007). However, the mechanism of this response is still unclear and somewhat puzzling as most models of biomineralization invoke a calcifying region controlled more by the organism than the surrounding seawater. In this thesis, data on Me/Ca sensitivity to $[CO_3^{2-}]$ collected in Chapter 4 are interpreted within the framework of a closed-system model of biomineralization to better understand how coral modulate growth in response to ocean acidification, linking nano-scale measurements to global processes.

Chapter 2

Precise and Accurate Me/Ca ratios in Carbonates by Isotope Dilution using a MC-ICP-MS: Test of a Sr/Ca Paleothermometer in Deep-Sea Coral

2.1 Introduction

Deep-sea corals are a relatively new archive in paleoceanography with several promising characteristics. Their unbioturbated skeletons provide century long records of deep ocean change with the potential for sub-decadal resolution. High concentrations of uranium allow for accurate independent calendar ages with ±1%, or better, precision (Cheng et al., 2000). Together these features of deep-sea corals promise to produce paleoclimate records with the potential for ice core-like resolution in the deep ocean. In an attempt to utilize this new archive, both Sr/Ca and Mg/Ca temperature proxies, long applied to surface corals (Smith et al., 1979; Beck et al., 2005; Mitsuguchi et al., 1996), have been recently investigated in deep-sea corals (Shirai et al., 2005; Cohen et al., 2006). This study is designed to systematically test if bulk skeletal Sr/Ca acts as a useful paleothermometer in scleractinian deep-sea coral by analyzing five different genera collected from growth temperatures between 0.5–15 °C. The primary focus is *Desmophyllum dianthus*, a cosmopolitan species with an extensive fossil collection (Robinson et al., 2007).

Calibrations of the Sr/Ca to temperature relationship in both inorganically precipitated aragonite and surface coral are linear with sensitivities of $\sim$ 4 permil and $\sim$ 7 permil, respectively (Gaetani & Cohen, 2006; Dietzel et al., 2004; Kinsman & Holland, 1969; Correge, 2006). Assuming similar sensitivities apply to deep-sea coral, a high precision Sr/Ca method is necessary since the entire change in deep-ocean temperature since the last glacial maximum (LGM) is estimated to be a few degrees (Adkins et al., 2002). Several analytical methods with varying levels of precision are commonly used to measure Sr/Ca ratios in carbonate materials, summarized in Table 2.1.

Table 2.1: Comparison of commonly used analytical methods to measure Sr/Ca in carbonates

Technique	Precision (2σ, permil)		Reference
ICP-AES	4–2	[Ca] of samples and standards must be carefully matched. High throughput	Schrag (1999)
ICP-MS External Standard	4–10	High throughput	Lea & Martin (1996) LeCornec & Correge (1997) Shen et al. (2007)
TIMS Isotope Dilution	0.3–1	Slow and labor intensive	Beck et al. (1992) DeVilliers et al. (1995)

All the commonly used analytical techniques require some sort of standardization and typically produce both more accurate and precise results when the standards and samples are as similar as possible. Isotope dilution is one way to produce a robust internal standard. In this technique, a sample is mixed with known amounts of naturally rare isotopes from the element of interest. As detailed below (Section 2.2) isotope ratio measurements of this now spiked sample are used to determine elemental concentration. By using a mixed spike, with enriched isotopes of calcium and any number of other elements, it is possible to measure metal/calcium ratios without accurately measuring the amount spike—greatly increasing throughput and improving precision (Fernandez et al., in press; Alibert & McCulloch, 1997). Previous work in our lab using isotope-diluton on a single-collector inductively coupled plasma-mass spectrometer (ICP-MS) resulted in accurate Me/Ca ratios at 8 permil or better precision, as described in Fernandez et al. (in press). High resolution multi-collector

ICP-MS is an increasingly important instrumental technique in geochemistry, allowing high throughput and high precision isotope ratio analysis. In this study, multi-collector ICP-MS is combined with the demonstrated precision and accuracy of isotope dilution to measure Sr/Ca ratios in carbonates to 1 permil or better. A combined method is developed to simultaneously measure Mg/Ca ratios and this technique is then used to measure Sr/Ca in deep-sea coral and test for a paleothermometer.

2.2 Isotope-Dilution

A previously calibrated mixed-spike enriched in 25Mg, 43Ca, and 87Sr is added to each sample (Fernandez et al., in press). By measuring the spiked-to-unspiked isotope ratios 25Mg/24Mg, 43Ca/48Ca and 87Sr/88Sr, the isotope-dilution equation (a form of the 2-component isotope mixing relationship) can be solved for the Mg/Ca and Sr/Ca of each carbonate material. The mathematical foundation for the isotope-dilution approach is demonstrated here for Sr/Ca.

When a mixed spike is added to a natural abundance sample, the strontium isotope ratio is simply the ratio of the number of moles (n) of each isotope from both sources,

$$\left(\frac{87}{88}\right)_{measured} = \frac{{}^{87}n_o + {}^{87}n_x}{{}^{88}n_o + {}^{88}n_x}. \tag{2.1}$$

With some algebra we can put (2.1) in terms of natural and spike isotope ratios:

$$\begin{aligned}
\left(\frac{87}{88}\right)_m {}^{88}n_o + \left(\frac{87}{88}\right)_m {}^{88}n_x &= {}^{87}n_o + {}^{87}n_x \\
\left(\frac{87}{88}\right)_m {}^{88}n_x - {}^{87}n_x &= {}^{87}n_o - \left(\frac{87}{88}\right)_m {}^{88}n_o \\
{}^{88}n_x \left[\left(\frac{87}{88}\right)_m - \left(\frac{87}{88}\right)_x\right] &= {}^{88}n_o \left[\left(\frac{87}{88}\right)_o - \left(\frac{87}{88}\right)_m\right] \\
\frac{{}^{88}n_x}{{}^{88}n_o} &= \left[\frac{\left(\frac{87}{88}\right)_o - \left(\frac{87}{88}\right)_m}{\left(\frac{87}{88}\right)_m - \left(\frac{87}{88}\right)_x}\right].
\end{aligned} \tag{2.2}$$

Similarly, for the calcium isotopes ^{43}Ca and ^{48}Ca,

$$\frac{^{48}n_x}{^{48}n_o} = \left[\frac{\left(\frac{43}{48}\right)_o - \left(\frac{43}{48}\right)_m}{\left(\frac{43}{48}\right)_m - \left(\frac{43}{48}\right)_x}\right]. \tag{2.3}$$

Dividing Equations (2.2) and (2.3) above, we obtain an expression for the composition of the sample:

$$\left(\frac{88}{48}\right)_o = \left(\frac{88}{48}\right)_x \frac{\left[\frac{\left(\frac{43}{48}\right)_o - \left(\frac{43}{48}\right)_m}{\left(\frac{43}{48}\right)_m - \left(\frac{43}{48}\right)_x}\right]}{\left[\frac{\left(\frac{87}{88}\right)_o - \left(\frac{87}{88}\right)_m}{\left(\frac{87}{88}\right)_m - \left(\frac{87}{88}\right)_x}\right]}. \tag{2.4}$$

Isotope ratios in the spike are independently calibrated and ratios in the sample are assumed to follow natural terrestrial and marine abundances (Tables 2.2–2.3), since fractionation between seawater and coral is small, < 1 permil, with < 0.04 permil T sensitivity (Fietzke & Eisenhauer, 2006; Böhm et al., 2006).

Table 2.2: Modern marine strontium isotope abundances. Calculated using $87/86 = 0.7092$ DePaolo & Ingram (1985); $84/88 = 0.006743$ DePaolo (1986); and assuming $86/88 = 0.1194$. For example, $^{88}A = (84/88 + 86/88 + 87/88 + 1)^{-1}$.

Isotope	% Abundance
^{84}Sr	0.5569
^{86}Sr	9.861
^{87}Sr	6.993
^{88}Sr	82.59

Table 2.3: Natural terrestrial calcium isotope abundances from Russell et al. (1978)

Isotope	% Abundance
^{40}Ca	96.98
^{42}Ca	0.6421
^{43}Ca	0.1334
^{44}Ca	2.057
^{46}Ca	0.00313
^{48}Ca	0.18246

2.3 Instrumental Method

Carbonate samples (as small as 10 μg) are dissolved in 5% trace-metal clean nitric acid (Seastar) to a concentration of 0.2 mM [Ca^{2+}]. Isotope ratios are measured on a Neptune multi-collector ICP-MS (ThermoFinniagn) with a PC3 peltier cooled spray chamber (Elemental Scientific, Inc.). All ion beams are collected in Faraday cups that are gain calibrated once at the beginning of each analytical session. To measure over a wide mass range spanning 24Mg to 88Sr with both high internal precision and high throughput, we use a combination of multi-collection and magnet field changes, or hops, in a single instrumental method. For example, the ions 43Ca+, 87Sr2+, 44Ca+, and 48Ca+ are measured simultaneously in four different cups for 10 cycles of 2 seconds each before the center mass of the magnet moves to measure 86Sr+, 87Sr+, and 88Sr+, with a 5 second setting time between mass moves. Table 2.4 describes all cup sub-configurations, the series of magnet hops and the ions collected for each center mass and dispersion. Typically 10 cycles are collected for each sub-cup configuration between magnet hops, and the pattern of subconfigurations is repeated for the desired number of total cycles. Samples and standards are typically measured from between 30 and 150 total cycles while blanks are only measured half as long. The hot plasma (1200W RF power) is tuned by maximizing 88Sr+ intensity. Zoom optic focus is then adjusted for best peak shape and mass resolving power. Sample uptake is via a microflow Teflon nebulizer into a PC3 peltier cooled spray chamber (both from Elemental Scientific, Inc.). Typical ion intensities for a typical deep-sea coral sample with Mg/Ca $\sim$ 3 mmol/mol and Sr/Ca $\sim$ 10 mmol/mol are 20–250 mV for Mg isotopes, 40–2000 mV for calcium isotopes, and $>$ 500 mV for the efficiently ionized strontium isotopes. Each sample was preceded by a pre-wash, wash, and blank of 5% trace-metal clean nitric acid (Seastar). Average blank intensity is subtracted from each isotope off-line during data processing. Instrumental mass fractionation is corrected using sample-standard bracketing with a previously described isotopically enriched coral matrix standard, SGSk (Fernandez et al., in press).

Isobaric Interferences: Several interferences complicate the measurement of accurate and precise magnesium and calcium isotope ratios on the ICP-MS. Since poly-atomic interferences are typically slightly heavier (by 10s of mAMU) than atomic ions of similar mass, atomic ions are optically

L4	L3	L2	L1	Center	H1	H2	H3	H4
$^{43}Ca^{+2}$				(22.780)			$^{24}Mg^{+}$	
			$^{24}Mg^{+}$	(24.275)		$^{25}Mg^{+}$		$^{26}Mg^{+}$
$^{43}Ca^{+}$	$^{87}Sr^{2+}$	$^{44}Ca^{+}$		(45.500)			$^{48}Ca^{+}$	
			$^{86}Sr^{+}$	$^{87}Sr^{+}$	$^{88}Sr^{+}$			

Table 2.4: Cup configuration. Different ions are focused into the detectors for each center mass magnet position during the multi-dynamic method. Calcium configuration adapted from Wieser et al. (2004) and strontium configuration adapted from Ramos et al. (2004).

resolved by positioning the appropriate Faraday cup to only catch the low mass edge of a mixed ion peak (Wieser & Schwieters, 2005). This is demonstrated in a mass scan of the peak mass 44 (Figure 2.1). As magnet field strength is adjusted from low mass to high mass across the cups, $^{44}Ca^{+}$ falls into the cup first; then, since the entrance of the Faraday cup is large compared to the distance between peaks, both $^{44}Ca^{+}$ and $^{12}C^{16}O_2^{+}$ are collected; finally at higher magnet field strength, $^{44}Ca^{+}$ is focused outside the cup and only $^{12}C^{16}O_2^{+}$ is collected. During analysis, the magnet field is positioned on the low mass shoulder so that only $^{44}Ca^{+}$ is collected. In addition to the interferences described by Wieser et al. (2004) two additional interferences on $^{48}Ca^{+}$, $^{36}Ar^{12}C^{+}$, and $^{16}O_3^{+}$, were identified in this study. These interferences require that the Faraday cups and magnet field are set up to only collect on the $\sim$ 15 mAMU low mass shoulder of mass 48 (Figure 2.2). This narrow plateau necessitates minimal mass drift during a typical 40 hour run. Automatic peak centering is conducted before each sample using a clean mass from each cup sub-configuration. As a diagnostic for mass drift, the position of the 48Ca+ and 44Ca+ peak edges were monitored in a single multi-dynamic analytical session, with a drift of less than 5 mAMU. Samples are typically analyzed using a medium resolution entrance slit with a measured mass resolving power of $>$ 6000 M/deltaM (5 to 95% peak edge definition). Although data rarely show evidence of mass drift off the $^{48}Ca^{+}$ and $^{44}Ca^{+}$ plateaus, I now typically use the high resolution entrance slit to ensure optical resolution of interferences. Other calcium, strontium, and magnesium peaks were free of *optically resolvable* interferences. The large and non-optically resolvable interferences from double charge formation, 48Ca2+ on 24Mg+, 86Sr2+ on 43Ca, and 88Sr2+ on 44Ca+ are corrected using double charge formation ratios derived from 43Ca2+ and 87Sr2+ intensities as described in Fernandez et al. (in

press).

2.4 Internal Error

Internal error in isotope mass spectroscopy is the raw precision with which an instrument measures each beam current to yield isotope ratios. If blank contributions, instrumental mass fractionation, and other sources of error are perfectly accounted for, internal error sets the analytical uncertainty of a method. During ion collection with Faraday cups in a multi-collector mass spectrometer, internal error is primarily controlled by two sources of uncertainty: thermal or "johnson nose" in the amplifiers and the theoretical limit of Poisson distribution counting statistics.

The Poisson distribution controls theoretical counting error for experiments like plasma source mass spectrometry where the chance of measuring a particular ion or event is small (Bevington, 1969). The theoretical minimal variance of a Faraday cup current measurement assuming a Poisson distributed sample is the mean number of counting event for that sample:

$$\sigma_x^2 = x \ .$$

Putting this in terms of relative error yields the iconic counting statistics error equation:

$$\sigma_x^{rel} = \frac{\sqrt{x}}{x} \ . \tag{2.5}$$

A log plot of relative internal error vs. the number of counts (x) yields a line of slope -1/2. Thus precision of a current measurement improves with more counts. Detector design is unimportant with regards to this fundamental limit, so it makes no difference that ion current is typically measured as the voltage drop across a resistor.

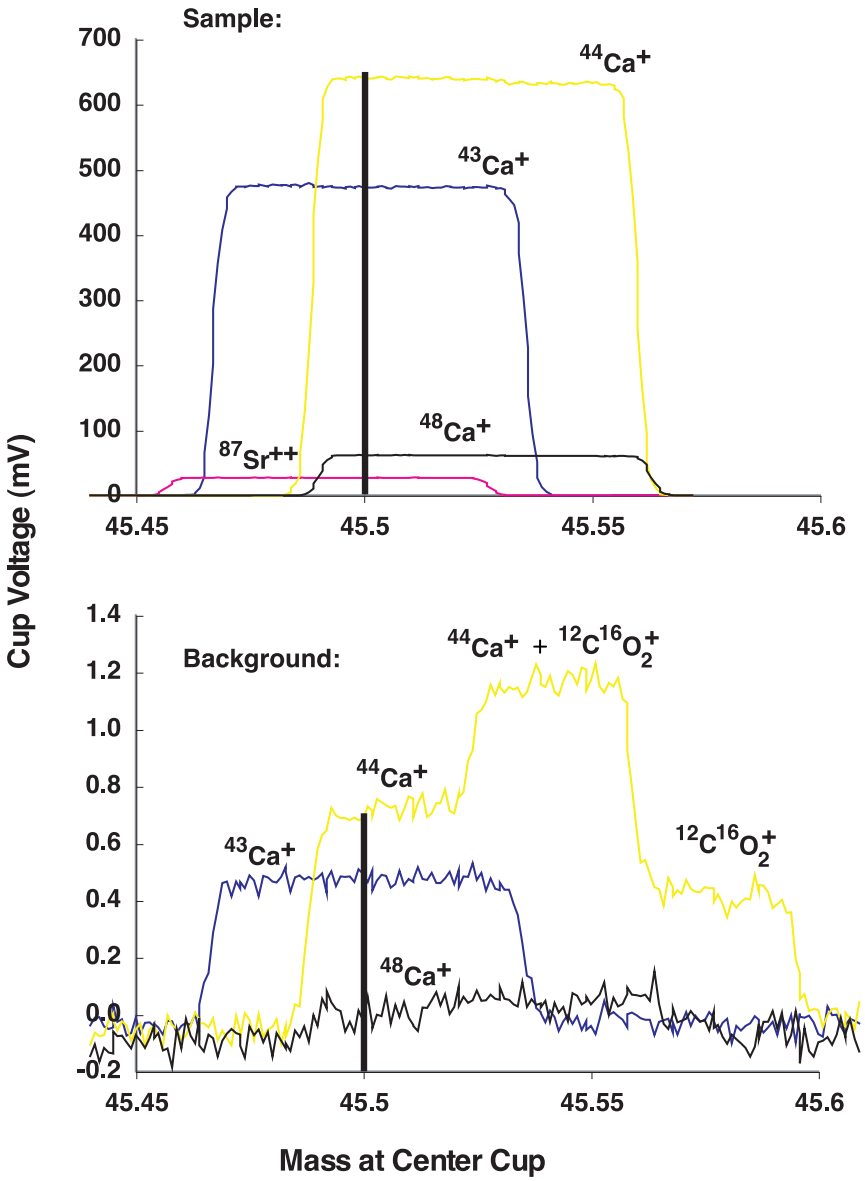

Figure 2.1: Calcium isotope peak shapes of a typical sample and background showing magnet position to optically resolve isobaric interferences. The CO_2 interference on 44Ca is avoided by measuring on the low mass shoulder corresponding to the pure atomic ion as described in Wieser et al. (2004).

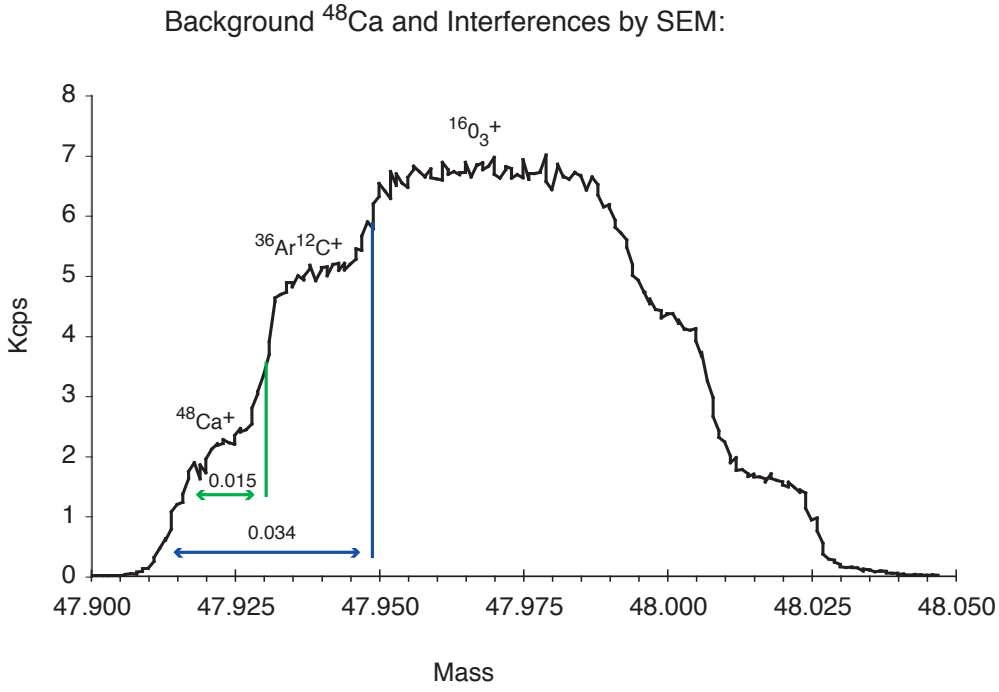

Figure 2.2: $^{48}Ca^{+}$ background peak shape and identification of isobaric interferences in medium resolution. Cup configuration designed such that the $^{48}Ca^{+}$ is collected on the 15 mAMU low mass pure ion shoulder.

For a ratio, error in both the numerator and denominator contribute to uncertainty:

$$R = \frac{x}{y}$$
$$\sigma_R^{rel} = \sqrt{(\sigma_x^{rel})^2 + (\sigma_y^{rel})^2}\ .$$

Substituting the relative counting statistics error of both x and y into the above equation,

$$\sigma_R^{rel} = \sqrt{\frac{x}{x^2} + \frac{y}{y^2}}$$
$$\sigma_R^{rel} = \sqrt{\frac{x+y}{xy}}$$
$$\sigma_R^{rel} = \left(\frac{1}{x} + \frac{1}{y}\right)^{-1/2}\ .$$

Like the number of counts in Equation 2.5, a log plot of relative internal ratio error vs. the term $(1/x + 1/y)$ also results in a line of slope -1/2. The term $(1/x + 1/y)$ therefore acts like an effective

number of counts, N_{eff}, for a ratio measurement and determines the lower limit of internal error.

The role of amplifier Johnson noise in isotope ratio mass spectrometry is described in Wieser & Schwieters (2005). J-noise is simply the RMS background amplifier noise, so measuring large signals to boost S:N and longer integration times both reduce the relative contribution of J-noise. J-noise is also reduced by using high-Ω resistors in each amplifier. The ICP-MS used in this study has a mix of 10^{11} and 10^{12} Ω resistors. Calcium isotopes are all collected on 10^{11} resistors, while other isotope ratios may mix resistors. John & Adkins (submitted) conveniently derives an equation for J-noise in terms of N_{eff} with a steeper slope than counting statistics. At low beam currents J-noise dominates, while counting statics dominates at high currents.

Measured internal error from isotope-dilution samples in this study is compared to predicted counting statistics and J-noise error in Figure 2.3. Internal error is estimated as the relative standard error of the mean across all cycle ratios of a particular sample. Internal error of isotope ratios where both ions are measured on 10^{11} Ω resistors ranges from 0.01–1 permil and follows the theoretical error curve. Uncertainty in these isotope ratios is only limited by N_{eff} up to at least 0.01 permil precision. For ions collected using mixed Ω resistors, the internal error does does not improve beyond 0.1 permil. This is likely due to the fact that amplifiers with different resistors respond to plasma flicker with different relaxation time-scales. Finally, double charge formation ratios, where each ion of the ratio is collected at a different magnet position yield 1 permil precision at best. Although this final set of ratios do not affect Me/Ca measurements (double charge intensities are used to correct isotopes multi-collected during the same sub-configuration), the ratios are helpful for understanding the different controls on internal precision. Together these results suggest at least 0.1 permil internal error is achievable for all relevant ratios depending on beam current and collection time, both of which are controlled by sample size. Provided other sources of error do not dominate, sub-permil precision should be achievable.

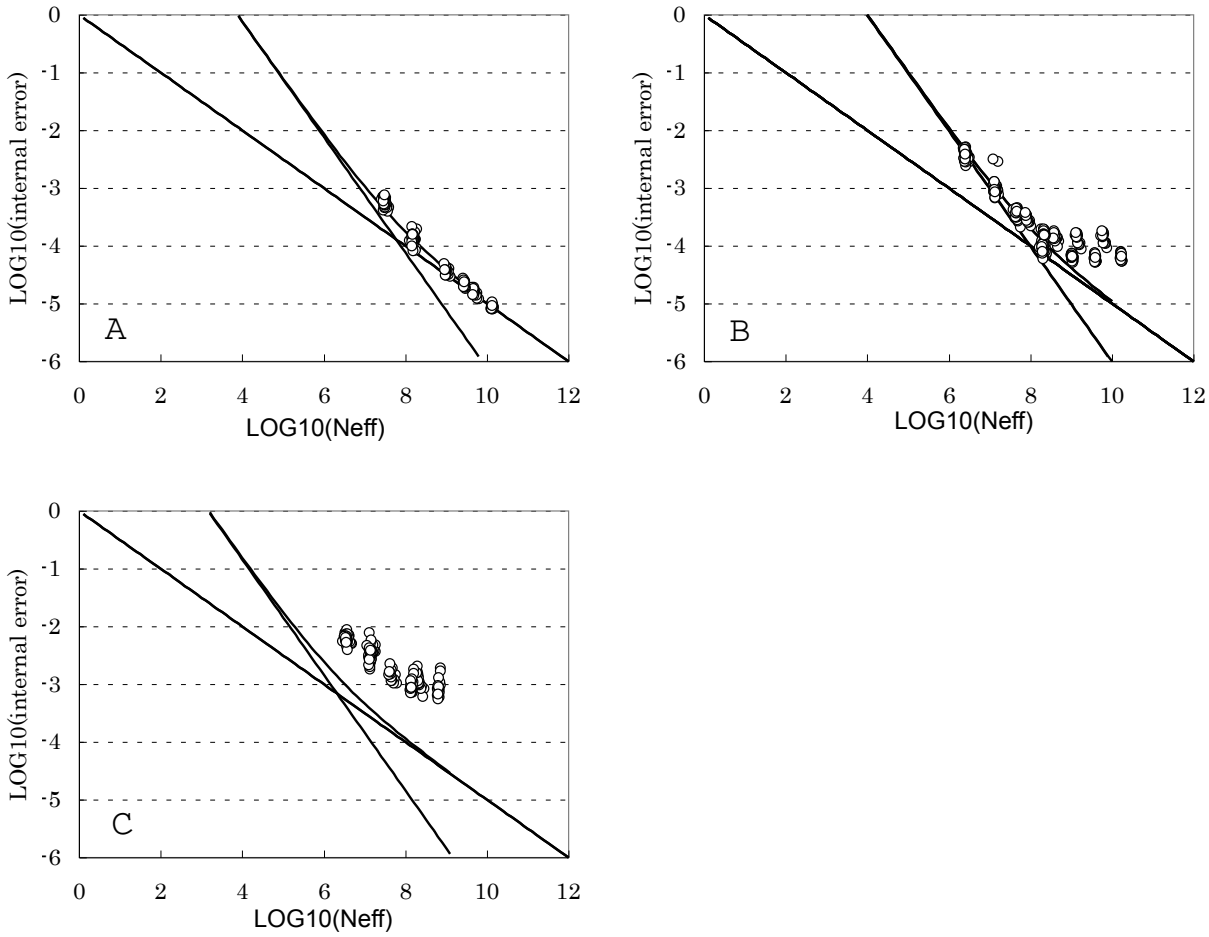

Figure 2.3: The 1σ standard error of the mean for isotope ratios measured during analysis of real samples is compared to theoretical error curves. The effective counts, N_{eff}, is described in the text and is calculated from measured voltages using the appropriate amplifier resistance, Ohm's law, Faraday's constant, and the total integration time. The steep line in each plot (slope=-1) is the predicted relative ratio uncertainty due to j-noise; the shallow line (slope=-1/2) is the error predicted from counting statistics; and the curved envelope is the sum of both effects. (**A**) Ratios where isotopes are multi-collected and both amplifiers have the same resistance follow a theoretical error curve, with amplifier noise dominating at low ion intensities and counting statistics at higher intensities. (**B**) Ratios multi-collected using amplifiers with different resistors exhibit an additional source of error, related to the different response times of each amplifier. This effect limits the estimated internal error to the 0.1 per mil level. Over sufficient cycle times, the different responses are likely integrated and the reported internal error may be an over-estimate. (**C**) Ratios that require a magnet jump between the collecting the different isotopes have lower than theoretical precision due to plasma flicker and drift.

2.5 Blank and Memory Effects

When all the samples and standards in an analytical session have closely matched isotope ratios, repeated measurements of the same dissolved deep-sea coral consistency standard (DSC-CS) are reproducible with a precision that approaches internal error: 0.1 permil. However, real world samples with differnt amounts of spike and less closely matched isotope ratios yield degraded external precision of $\sim$ 1 permil for Sr/Ca. Much of this variability in external error can be explained by a blank effect from a slowly exchanging machine reservoir of calcium, strontium, and magnesium.

To understand this effect better, different amounts of spike were added to samples of the same dissolved deep-sea coral consistency standard. During the first part of an analytical session, consistency standards were spiked to match the same ratio as the isotope ratio standard (SGSk)—all samples and standards were closely ratio matched. The 2σ standard deviation of Sr/Ca in these six deep-sea coral consistency standards is 0.1 permil. For the second half of the same analytical session normally spiked DSC-CS were alternated with over-spiked DSC-CS (twice the amount of spike). Both accuracy and precision are affected when samples are not ratio matched (Figure 2.4 shows Sr/Ca, Mg/Ca was similarly affected). Blank ratios differ between the two parts of the session as well, showing that washout was not complete, despite 8 minute rinse times. Initially the blank ratio is the same as all the samples and standards. Since samples, standards, and the blank all have similar ratios for the first part of the experiment, the memory effect is small or negligible. Starting with the first high ratio over-spiked consistency standard, the blank ratio and sample ratio differ, so a memory effect is expressed as an anomalously low Sr/Ca. As the blank ratio varies dynamically between high and low values throughout the remaining portion of the run, subsequent samples are all affected. Blank relaxation times during this experiment are estimated as $\sim$ 100 minutes.

These results suggests that improved precision while measuring real samples, to the 0.1 per level, are achievable if the blank issue is addressed. Furthermore, under current conditions even large differences in spike amount (x2), still yield $\sim$ 1 permil external precision in Sr/Ca. Machine memory can also affect accuracy if sample and blank ratios differ significantly. For both Me/Ca and uranium analysis in our lab, running three or more isotopic standards at the beginning of each session

typically improves the reproducibility of subsequent measurements. A memory effect may explain the efficacy of this "trick", as the standards exchange with the machine blank pushing it towards standard-like ratios. Higher nebulizer flow rates, a smaller spray chamber, and more concentrated wash acid may help reduce the memory effect in the future.

2.6 Instrumental Mass Fractionation

Isotope ratios measured by ICP-MS are enriched in heavy isotopes with respect to the true sample due to instrumental mass fractionation. This process is thought to occur mostly during the selection of ions from the plasma through the sample and skimmer cones (**?**)Andren:2004p1099); varies in magnitude with cone design or guard electrode potential, and drifts with time. In this study, instrumental mass fractionation is corrected by standard-sample bracketing using the 25Mg, 43Ca, and 87Sr enriched coral matrix standard SGSk described in Fernandez et al. (in press). The magnitude of instrumental fractionation for our tune conditions is typically $\sim 2\%$ per amu for strontium isotopes, $\sim 4\%$ per amu for calcium isotopes, and $\sim 6\%$ per amu for magnesium isotopes, following a mass dependent trend. To correct for drift in instrumental mass fractionation, a time weighted linear model is used to interpolate between bracketing SGSk measurements, where:

$$f_{t=s} = \left(\frac{f_{t=1}}{t_s - t_1} + \frac{f_{t=2}}{t_2 - t_s}\right) / \left(\frac{1}{t_s - t_1} + \frac{1}{t_2 - t_s}\right)$$

and f = (True Ratio)/(Measured Ratio).

Drift correction uncertainty was tested in a typical analytical session by treating every other SGS as a "sample". Bracketing SGS measurements on each side of the "sample"-SGS were used to correct for instrumental mass fractionation. Drift correction error was estimated from residuals between the calculated drift corrected ratio of each SGS and the true value, for a typical error < 0.2 permil. Drift error improves when samples and standards are ratio matched, so blank effect is probably limiting the precision of drift correction as well as sample ratios.

The calcium and strontium isotope composition of SGSk from Fernandez et al. (in press) was

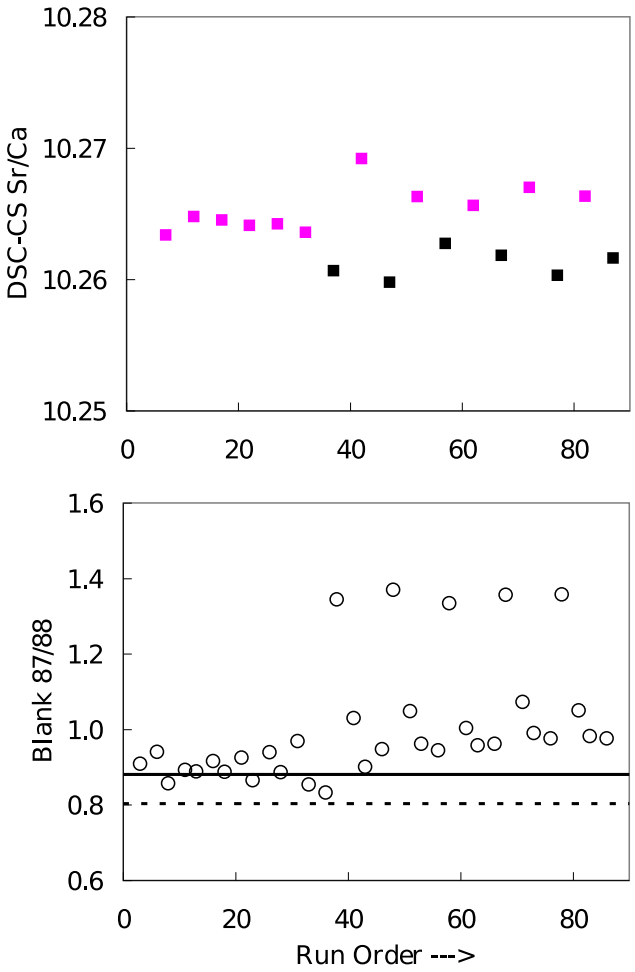

Figure 2.4: Blank memory studied by the repeated analysis of the deep-sea coral consistency standard (DSC-CS) with and without ratio matching. **TOP:** Sr/Ca of DSC-CS during a single analytical session. Samples and standards for the first half of the session all have similar isotope ratios. Half way through the session, samples of DSC-CS with twice the amount of spike (black squares) were alternated with the previous samples, yielding very different isotope ratios. Both accuracy and precision are affected. **BOTTOM:** Blank 87/88 ratio during the same session. At the beginning of the session the blank ratio matches the ratio of the isotopic standard SGSk (dark horizontal line), which is the most frequently analyzed material. The blank ratio is also similar to the ratio of normally spiked DSC-CS (horizontal dashed line), so sample Sr/Ca are unchanged by blank and memory effects. As sample and blank ratios differ from each other, Me/Ca ratios are affected. If this memory issue is addressed, current $\sim$ 1 per mil precision may be improved to the $\sim$ 0.1 per mil precision demonstrated with ratio matched samples.

re-calibrated in this study. Calcium isotopes were standardized using several natural standards: calcium flouride standard from the same batch of material as analyzed by Russell et al. (1978) (Henry Ngo, *personal communication*), deep-sea coral consistency standard, Aldrich CaCO3, and Durango Apatite. The original matrix of the Henry Ngo Calcium Standard is dilute HCl, and I have observed lower precision results when mixing acid matrices during an analytical session. To match the 5% nitric acid matrix of all other samples, the CaF sample was dried, re-dissolved in concentrated HNO_3, dried again, and finally dissolved in 5% HNO_3. In three different standardization sessions, three natural samples were measured between each SGSk analysis. To minimize a systematic memory bias due to the measurement of different ratios, samples were analyzed in random order, with different samples following SGSk throughout the run. The 43/48 and 44/48 value of SGSk was adjusted until the average drift corrected ratio of all natural abundance standards equaled natural ratios 43/48 = 0.7311 ± .0002 and 44/48 = 11.273 ± 0.002 (Russell et al., 1978). The 43/48 ratio of all the natural abundance materials are the same within 1 permil after drift correction (Figure 2.5), this agrees with the small fractionation observed for terrestrial samples (Russell et al., 1978). The resulting re-calibrated SGSk ratios are 43/48 = 9.376 and 44/48 = 11.69. SGSk 43/48 is within 0.7% of the previous calibration for this standard, 9.44 ± 0.03, reported in Fernandez et al. (in press). Strontium isotopes were standardized against NBS SRM 987 and against marine isotope abundances (Table 2.2) using a dissolved sample of deep-sea coral. New isotope values are 88/87 = 1.1116 ± 0.0001 and 86/88 = 0.1282 ± 0.001 for SGSk. Again, these values compare well to the previous calibrations on a single-collector mass spectrometer, differing only 0.1% from the value reported by Fernandez et al. (in press) of 1.113 for 88/87. This re-calibration was necessary to ensure accurate isotope ratio measurements for the experiments described in Chapter 4.

Two related calibrations affect the final Me/Ca ratio of a mixed spike isotope dilution measurement: the isotope ratio reference standard (SGSk) and the isotopic abundances of the mixed spike. Spike abundances are calibrated by isotope dilution measurements on a series of Me/Ca solutions gravimetrically prepared form pure solid standards. Like any other isotope dilution measurement, spike abundances are referenced to a particular SGSk. Since spike abundances were not re-calibrated

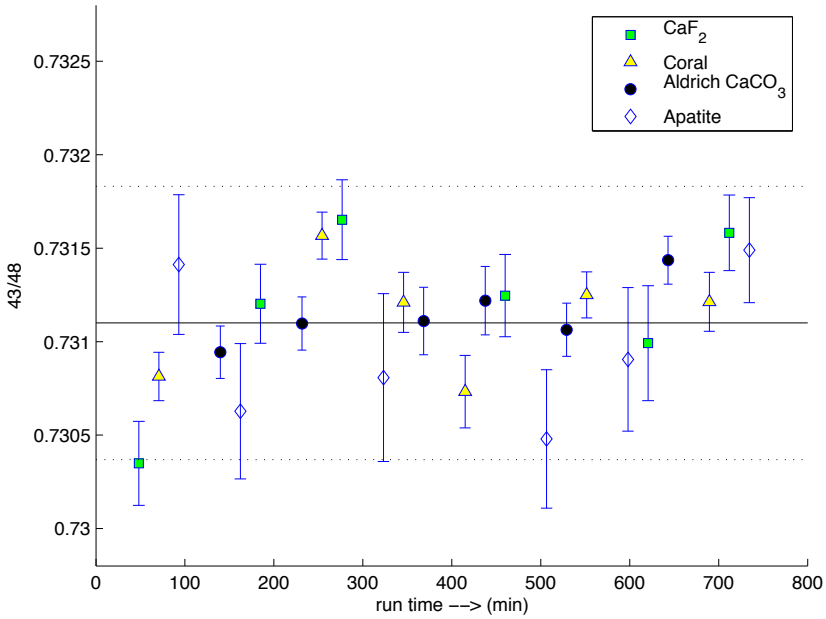

Figure 2.5: The 43/48 of several natural calcium containing materials show limited fractionation. The materials measured in this is experiment differ by less $\pm$ 1 permil, (indicated by the dashed lines). The mean 43/48 of the natural samples measured here is assumed to be 0.7311, the natural abundance 43/48 reported in Russell et al. (1978). This value is then used to calibrate the 48/43 of SGSk.

in this study, the SGSk values of Fernandez et al. (in press) are used with the spike calibrations of Fernandez et al. (in press) to calculate Me/Ca ratios of carbonates. Where just calcium or strontium isotope ratios are measured, in Chapter 4 for example, the new SGSk values are used.

2.7 External Error

Long term external precision of the method, which determines the minimum resolvable Me/Ca signal, is assessed by the regular analysis of a dissolved deep-sea coral consistency standard (Figures 2.6–2.7). The overall long term reproducibility of Sr/Ca, estimated by the 2σ standard deviation of n=62 measurements, is 1 permil, which is small compared to both the 7 permil/degree measured sensitivity of Sr/Ca to temperature in surface coral (Correge, 2006) and the 4 permil/degree inorganic aragonite temperature sensitivity (Gaetani & Cohen, 2006; Dietzel et al., 2004; Kinsman & Holland, 1969). Mg/Ca external error is 8 permil (n=50) which is also small compared to the 7%/degree measured sensitivity of Mg/Ca to temperature in pelagic foraminifera. This performance is a significant improvement over the previous technique in our lab as well as over other published ICP-MS methods.

Accuracy of this method is dependent on spike calibrations. As an external check on Sr/Ca accuracy, seawater collected from the Bermuda Atlantic Time Series (BATS) was measured with this method and found to be within 1% of the reported values for Sr/Ca of other North Atlantic stations reported in DeVilliers (1999).

2.8 Application: Sr/Ca of Bulk Deep-Sea Coral from a Range of Temperatures

Armed with an improved ID-MC-ICP-MS method, Sr/Ca was measured in modern samples of deep-sea coral collected form a range of growth temperatures to test for temperature sensitivity. In all, 69 samples of modern deep-sea coral from five different genera and growth temperatures between 0.5–15 °C were analyzed. The global extent of the coral analyzed in this study are shown on a map in the Appendix (Figure 2.10). Prior to Sr/Ca analysis, samples were removed from the most recent

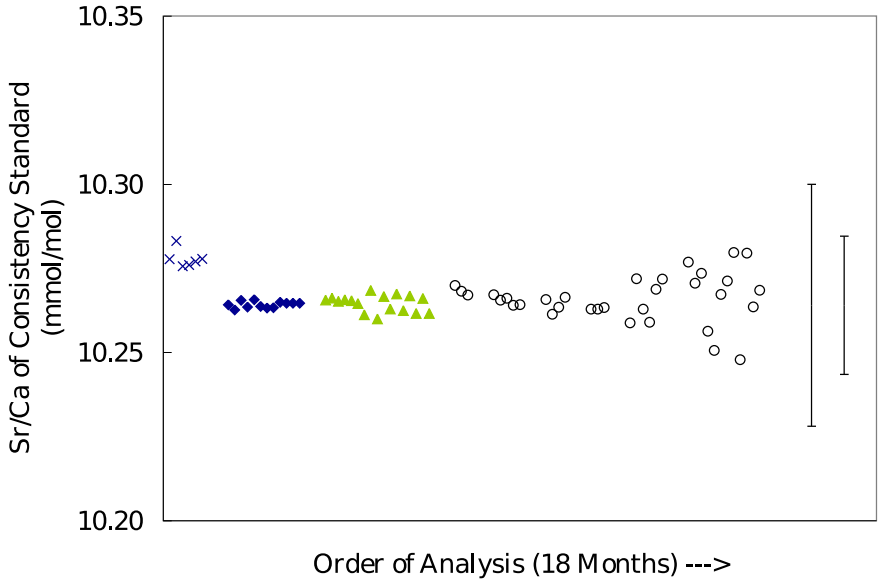

Figure 2.6: Reproducibility of Sr/Ca measurements of a dissolved deep-sea coral consistency standard over 18 months. The overall long term reproducibility, estimated by the 2σ standard deviation of the n=62 measurements, is 1 permil which is small compared to both the 7 permil/degree measured sensitivity of Sr/Ca to temperature in surface coral (large vertical bar) and the 4 permil/degree inorganic aragonite temperature sensitivity (smaller vertical bar). The long term external error estimate includes a 1 permil accuracy offset after the first analytical session (×) as well as standards run during analysis of foraminifera and isotopically enriched seawater—samples with isotope ratios very different than a typical coral sample (high variance data on far right). Standards from several analytical sessions of interest are identified using different markers: (×) session AAI where deep-sea coral were analyzed to test for a Sr/Ca paleothermometer; (♦) session AAM, an additional deep-sea coral temperature calibration session; (▲) memory effect study discussed in Section 2.5.

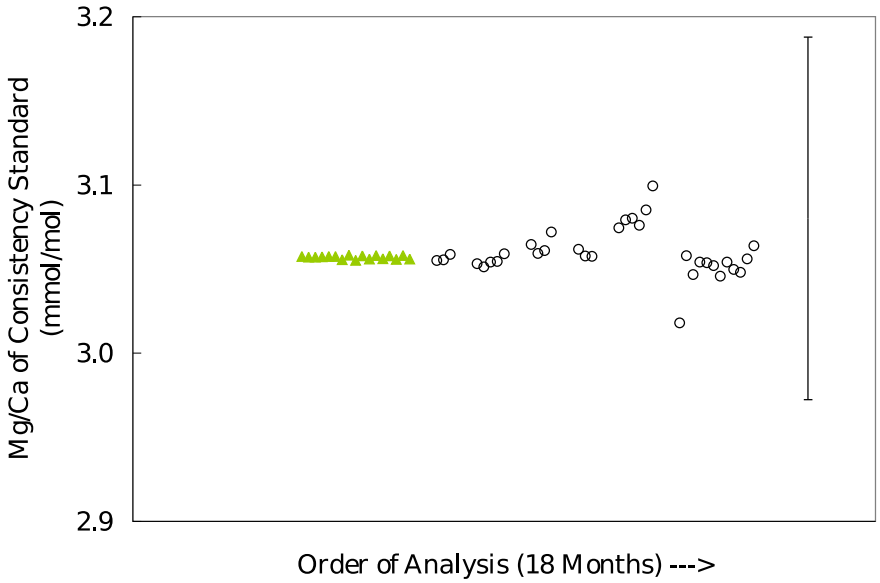

Figure 2.7: Reproducibility of Mg/Ca measurements of a dissolved deep-sea coral consistency standard over 6 months. The overall long term reproducibility, estimated by the 2σ standard deviation of the n=50 measurements, is 8 permil which is small compared to the 7%/degree measured sensitivity of Mg/Ca to temperature in pelagic foraminifera (large vertical bar). The long term external error estimate includes standards run during analysis of seawater, where the Mg/Ca ratio is more than 3 orders of magnitude higher than in the coral standard. Excluding this session, long term external reproducibility is 5 permil. (▲) Standards analyzed during the memory effect study discussed in Section 2.5. There is less data for Mg/Ca than for Sr/Ca since the Mg/Ca method was developed and added to form a combined method later in the study.

portion of each skeleton and subjected to a full trace-metal cleaning protocol (Cheng et al., 2000; Shen & Boyle, 1988).

Results of Sr/Ca measurements in the deep-sea coral *D. dianthus*, the primary target of this study, are compared to the Sr/Ca temperature relationship for inorganically precipitated aragonite (Figure 2.8). These data show Sr/Ca of bulk samples are not usefully correlated with temperature, and Sr/Ca varies by up to 20% between between different bulk samples from the same coral and by similar amounts between different individuals of coral from the same collection location. In *D. dianthus*, Sr/Ca typically falls below the inorganic line. If inorganic aragonite precipitation is a valid reference frame for understanding biomineralization in deep-sea coral, then these data imply that some mechanism acts to lower Sr/Ca during skeletal growth. Other common deep-sea coral were also investigated (Figure 2.10). The genera *Caryophyllia sp.* and *Lophelia sp.* exhibit even less of a temperature relationship than *D. dianthus*. Cohen et al. (2006) calibrated a Sr/Ca paleothermometer in *Lophelia sp.* by tuning SIMS measured Sr/Ca along a growth axis to an instrumental temperature record. This calibration does not appear to apply to bulk samples of coral taken from near constant growth environments, possibly suggesting that Me/Ca results differ depending upon the scale of analysis. The genera *Solenosmilia variabilis* and *Enallopsammia sp.* may show some apparent temperature sensitivity, although, with only eight and five data points, respectively, this relationship may be spurious.

2.9 Conclusion

The results of this study do not support a useful deep-sea bulk skeletal Sr/Ca paleothermometer. This is in contrast to bulk analysis of surface coral cultured at constant temperatures (Reynaud et al., 2007). Since much of the deep-ocean is characterized by near constant environmental conditions over the $\sim$ 100 year life-time of a typical deep-sea coral, high Sr/Ca variability between different coral samples from the same location cannot be attributed to environmental effects. Therefore, this variability is likely a biological effect due to the mechanism of biomineraliztion. Research presented in the next chapter attempts to quantify and map Me/Ca variability in deep-sea coral

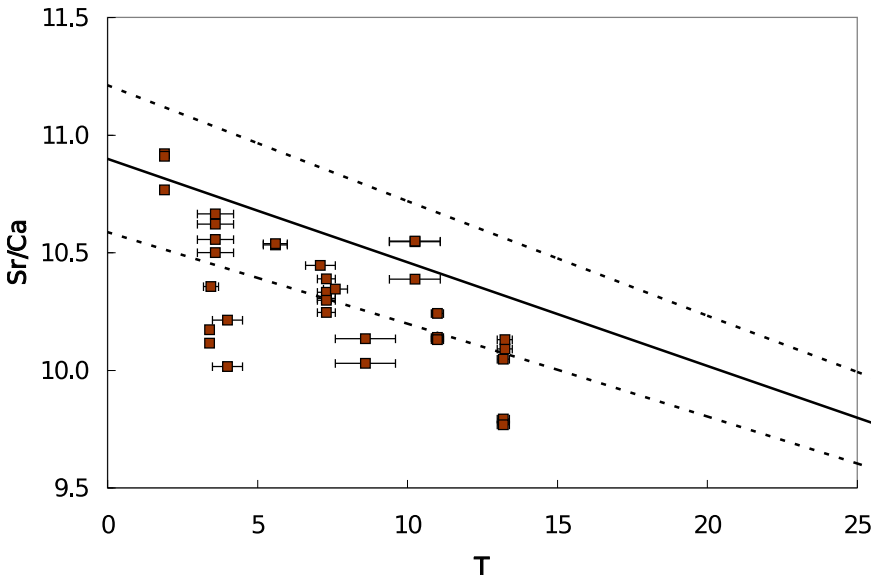

Figure 2.8: Skeletal Sr/Ca of the deep-sea coral *D. dianthus* from a range of growth temperatures do not follow a useful relationship with temperature. Coral analytical error is far smaller than the symbols. Coral data are compared to the Sr/Ca vs. T relationship of inorganically precipitated aragonite (gray line and error envelope). The inorganic line is an error weighted fit of data from three independent studies (Gaetani & Cohen, 2006; Dietzel et al., 2004; Kinsman & Holland, 1969). In some cases variability of up to 20% occurs between different bulk samples from the same coral and between different individuals of coral from the same collection location.

to better understand how biomineralization affects composition towards a better interpretation of paleoproxies.

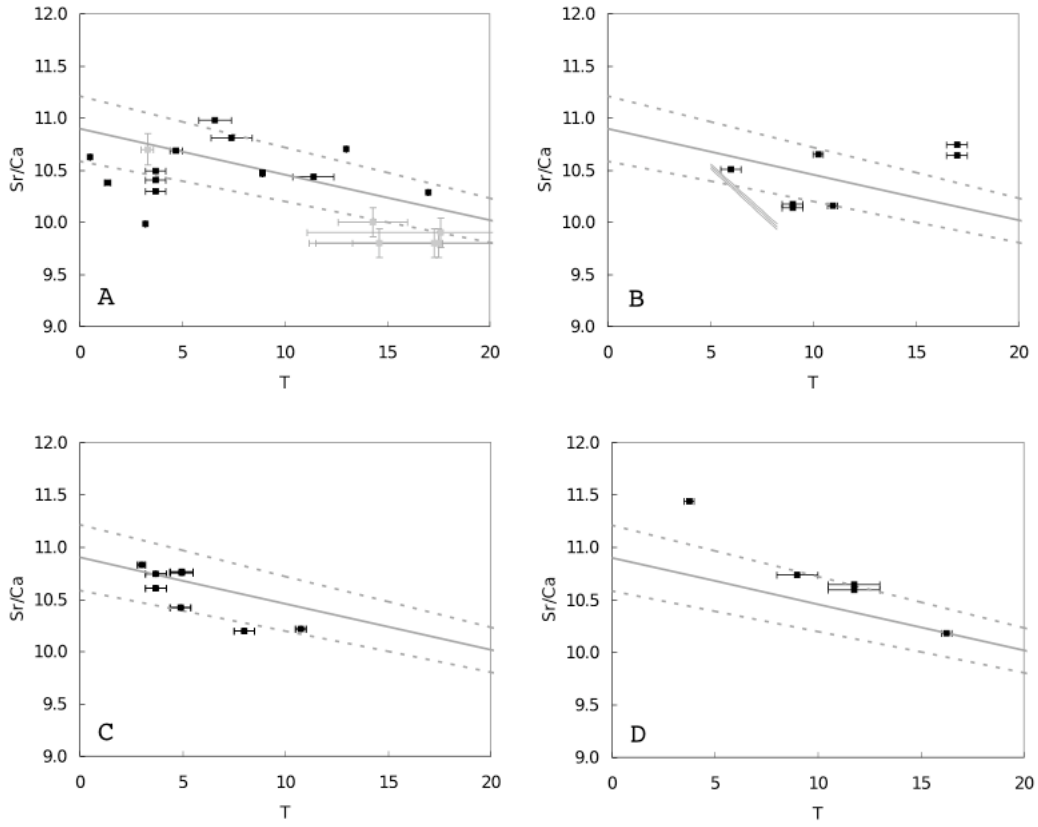

Figure 2.9: Skeletal Sr/Ca of four genus of deep-sea coral compared to the inorganic relationship (gray line and error envelope). **(A)** *Caryophyllia sp.* without significant temperature sensitivity. Previous data from this genus plotted as gray squares and error bars (Shirai et al., 2005). **(B)** *Lophelia sp.* with a flat relationship to T. An empirical calibration of Sr/Ca vs. T using SIMS analysis of a fjord individual that experienced temperature variability is plotted as a steep short gray line and accompanying error envelope (Cohen et al., 2006). Both **(C)** *Solenosmilia variabilis* and **(D)** *Enallopsammia sp.* may show some apparent temperature sensitivity. With only eight and five data points, respectively, this relationship may be spurious.

2.10 Appendix

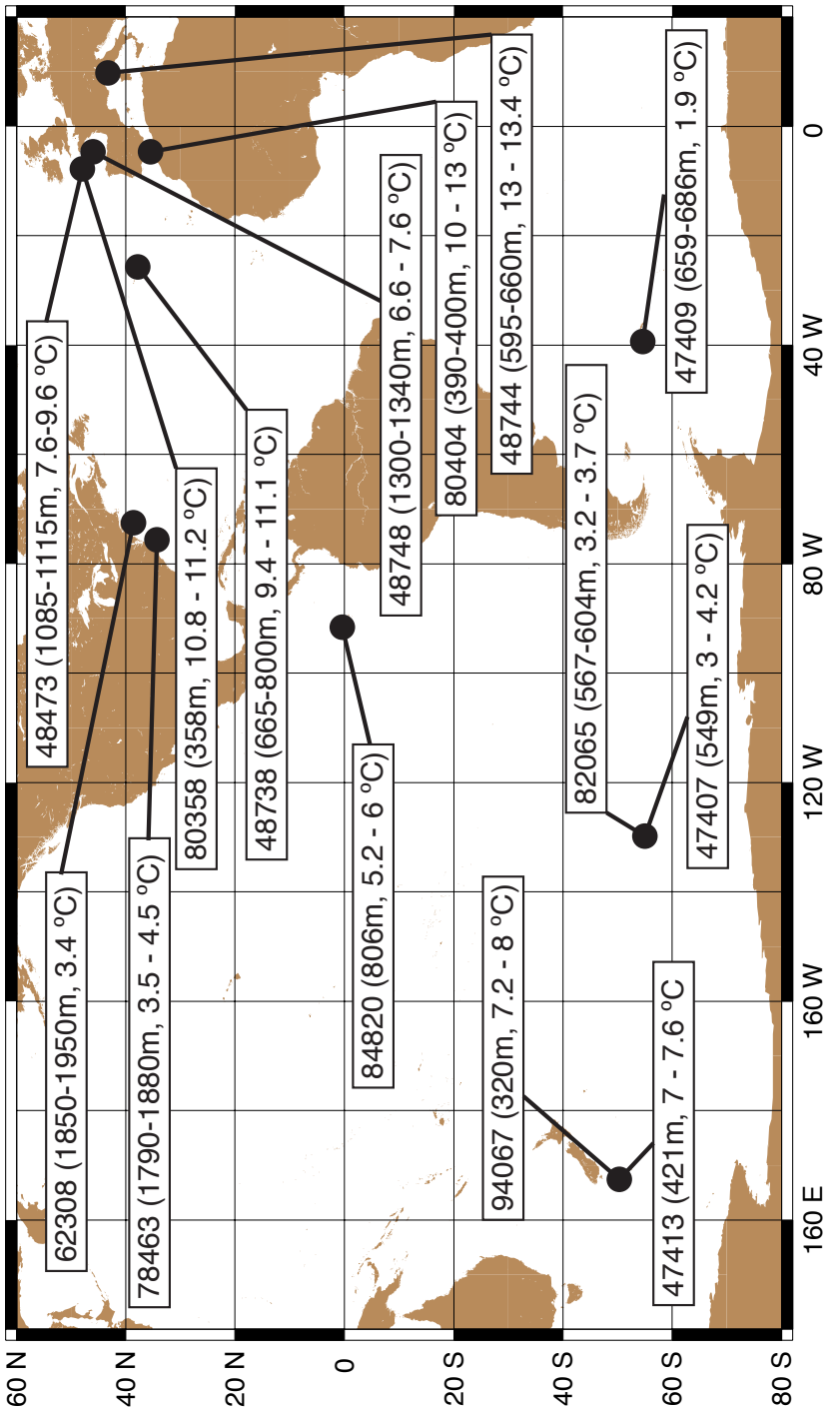

Figure 2.10: Detailed map of the deep-sea coral *D. dianthus* analyzed in this study. Locations are dentified by Smithsonian sample number with associated collection depths and growth temperature as estimated from Levitus & Boyer (1994).

Chapter 3

Sr/Ca and Mg/Ca Vital Effects Correlated with Skeletal Architecture in a Deep-Sea Coral and Closed System Biomineralization

3.1 Introduction

As demonstrated in Chapter 2, a direct temperature relationship in corals from both surface and deep environments is complicated by the overprint of physiological processes during biomineralization or "vital effects" (Weber & Woodhead, 1972). Most thoroughly investigated in surface corals, Me/Ca vital effects are evidenced by: (1) large differences between temperature calibrations for different species and even between individuals within the same species (Correge, 2006); (2) differences in temperature sensitivity between corals and inorganically precipitated aragonite (Correge, 2006; Kinsman & Holland, 1969; Mucci et al., 1989; Dietzel et al., 2004; Gaetani & Cohen, 2006; Zhong & Mucci, 1989); (3) the apparent growth dependence of Me/Ca temperature calibrations (DeVilliers et al., 1994) including similar sensitivity to both light and temperature induced changes to growth rate (Reynaud et al., 2007); (4) spatial variability of Me/Ca and stable isotope proxies across coral skeletal features (Shirai et al., 2005; Cohen et al., 2006, 2001; Allison, 2004; Adkins et al., 2003; Robinson et al., 2006; Meibom et al., 2006, 2004; Allison et al., 2001); and (5) dif-

ferences in Me/Ca-temperature calibrations in the presence or absence of photosymbionts (Cohen et al., 2002). While Me/Ca temperature proxies continue to provide important information on past climate, quantifying and understanding the processes that cause non-temperature related variability in Me/Ca paleothermometers is a major goal of paleoceanography.

The growth environment of the deep-sea is a virtually constant culture medium during a corals lifetime, outside specific regions that experience rapid ventilation. In properly chosen modern deep-sea coral samples, the observed variability of a proxy, isolated from a known and constant environmental background, is attributable entirely to vital-effects. Thus, deep-sea corals are an ideal model system for the study of vital effects. As an additional advantage, deep-sea corals grow far from sunlight and lack the photosymbionts typical of surface corals, enabling calcification to be investigated uncoupled from photosynthesis. Similar patterns of Me/Ca heterogeneity in both surface and deep-sea coral imply some commonality in vital effect mechanism and suggest results from deep-sea corals may be applicable to corals in general (Sinclair et al., 2006). In this study we investigate the magnitude, pattern, and mechanism of Sr/Ca and Mg/Ca vital effects in the scleractinian deep-sea coral *Desmophyllum dianthus* (Esper, 1794, formerly *D. cristagalli*) a globally distributed species with a large available fossil coral collection.

Vital effects often correlate with skeletal structural features, relating spatially resolved geochemical measurements to the biologically controlled process of skeleton formation. The skeletons of both surface and deep-sea corals are composed of the same basic architectural units. In transverse petrographic microsections of a deep-sea coral, two different crystal morphologies are clearly evident by visible light microscopy (Figure 3.1). Acicular, or needle-like, bundles of crystals radiate from regions of small-disorganized granular crystals or Centers of Calcification, COCs. In this study, the term COC refers to interior regions of the coral skeleton typified by small irregular or fusiform crystals, following the terminology of Gladfelter (1983). In *D. dianthus* COCs combine into a 30–100 μm wide optically dense central band. Crystal morphology is related to the process of skeletal growth with the initial precipitation of small fusiform crystals followed by the extension of needle-like crystals, as hypothesized by Gladfelter (1983) and recently documented in living surface corals (Raz-Bahat

et al., 2006), although the relative growth rate of these two crystal forms is still a topic of research.

There is growing evidence that Mg/Ca variability is strongly correlated with skeletal architecture. A study in surface coral shows Mg/Ca doubles in COCs when measured by SIMS with a 30 μm spot (Meibom et al., 2006). Smaller scale sampling, at $\sim$ 400 nm using a NanoSIMS instrument, reveals small regions where Mg increases by an order of magnitude (Meibom et al., 2004). Sr/Ca heterogeneity also correlates with skeletal structure in surface corals, with higher Sr/Ca ratios reported in COCs (Cohen et al., 2001; Allison, 2004; Meibom et al., 2006; Allison et al., 2001). In deep-sea corals, Cohen et al. (2006) used SIMS to measure Sr/Ca and Mg/Ca across the thecal wall of the species *Lophelia pertusa*, observing increased Mg/Ca coincident with, and extending beyond, most opaque bands, with Sr/Ca depleted by a smaller relative amount in the same regions. For the deep-sea coral genus *Caryophillia*, maps of elemental distribution by electronprobe X-ray microanalysis suggest Mg and Sr heterogeneity may correlate with COCs (Shirai et al., 2005). In *D. dianthus*, the target of this study, previous work with other proxies show very depleted δ^{13}C and δ^{18}O within the central band (Adkins et al., 2003) and a region of low uranium content that follows but extends beyond the central band (Robinson et al., 2006). The pattern of tracer heterogeneity suggests skeletal architecture is a key factor in understanding vital effect.

I examine Mg/Ca and Sr/Ca across skeletal features in *D. dianthus* using micromilling to sample with lateral spatial resolution of 10s of micrometers. Micromilled samples allow the use of a rapid isotope-dilution-ICP-MS method to determine precise and accurate metal ratios. We also use electronprobe X-ray microanalysis to analyze Mg/Ca heterogeneity at fine scale. We compare our measurements to inorganic experiments, to previous measurements in deep-sea and surface corals, and interpret our results within the context of models for vital effect mechanism.

Geochemical modeling of biogenic carbonates attempts to explain tracer abundance, tracer heterogeneity, and correlations between tracers using chemical and physical principles within a biological framework. McConnaughey (1989a,b) explained correlated δ^{13}C and δ^{18}O results in corals with an elegant model for isotope behavior paving the way for the systematic study of vital effects. More recently, an equilibrium model of stable isotope vital effects was proposed to explain observed depar-

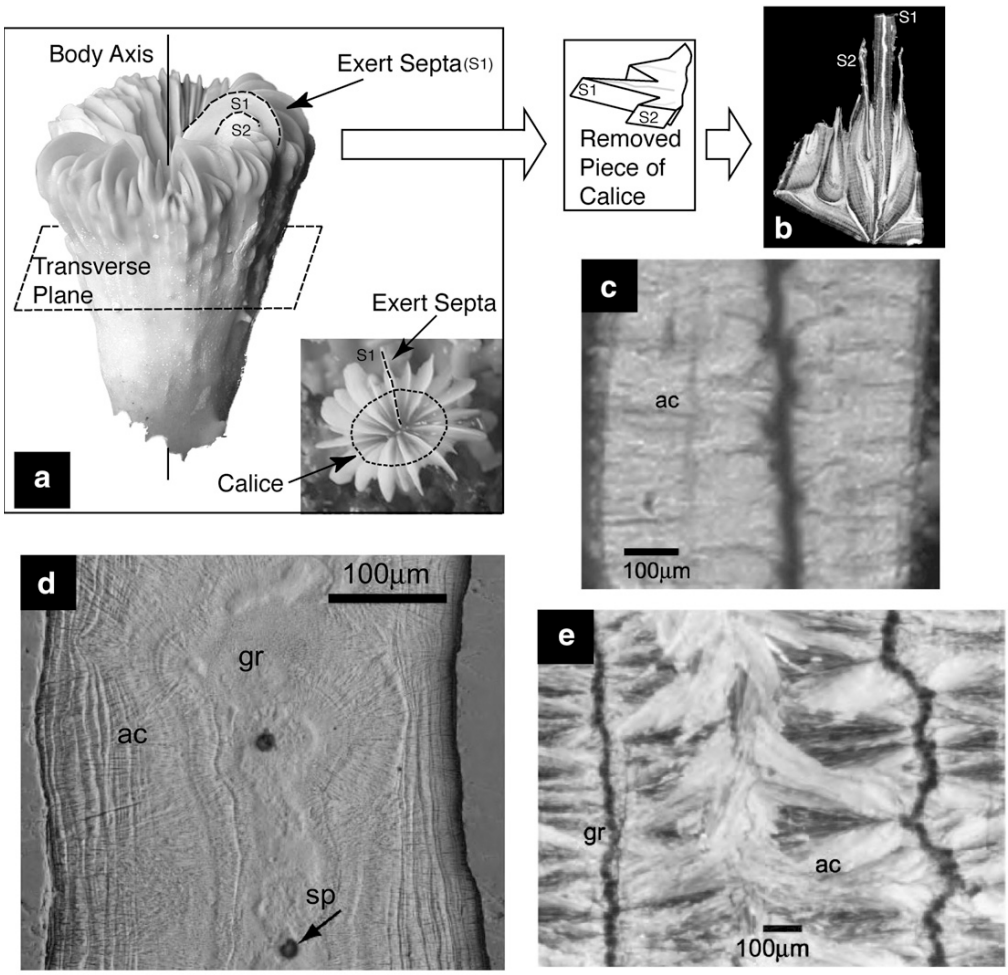

Figure 3.1: Coral skeletal architecture. (**a**) Sampling for petrographic thin sections begins with removal of pie-shaped wedges containing at least one exert septa (S1) from the calice in the transverse plane, and subsequent polishing to $\sim$ 100 μm thickness. The transverse plane is perpendicular to the body axis, roughly cutting the calice into an ellipse. Analysis in this plane gives the view of looking down the body axis toward the oral surface—as seen in figure inset. (**b**) Transmitted light photomicrograph, in negative, of thin section 47407A. White regions are optically dense with an obvious central band in the middle of septa S1. (**c**) Positive transmitted light view of a single septa, the dark, optically dense central band is surrounded by acicular (ac), or needle like, crystals in the outer septa. (**d**) Crystal morphology, granular (gr) irregular crystals making up the centers of calcification (COCs), and surrounding acicular crystals, are evident in this etched SEM image of a septum. (**e**) A 10s of micrometer thick section viewed in positive cross polarized light. In addition to granular crystals, the central band appears to be composed of many sphere like bodies (sp) stacked together. Acicular crystals (ac) show c-axis alignment.

tures from a linear correlation between δ^{13}C and δ^{18}O in corals (Adkins et al., 2003). Several groups have expanded the geochemical approach of combined measurements and models to study Me/Ca vital effects in biogenic carbonates (Cohen et al., 2001, 2002; Elderfield et al., 1996; Russell et al., 2004; Sinclair, 2005; Bentov & Erez, 2006; Sinclair & Risk, 2006). Rather than develop a complete numerical model of biomineralization to complement our measurements, we attempt to test for the presence of an important parameter in most vital effect models, the openness or closedness of the calcifying system to metal ions, and the implied mechanism of Rayleigh fractionation.

Most models of biomineralization involve a privileged space closed to the external environment to some extent, sometimes termed the calcifying fluid or extra-cellular fluid, where a coral isolates seawater and chemically drives precipitation. Anytime there is a closed system and a tracer is discriminated against or preferentially incorporated during coprecipitation, Rayleigh fractionation will occur. Even without a complete understanding of the underlying processes that determine this partitioning, a Rayleigh process is predicted and should be considered. Rayleigh fractionation has been applied previously to explain single element Me/Ca behavior in foraminifera (Elderfield et al., 1996), and has been recently incorporated as a key mechanism along with calcifying solution manipulation and temperature effects to explain Me/Ca variability in a surface (Gaetani & Cohen, 2006) and deep-sea coral (Cohen et al., 2006).

Rayleigh fractionation predicts a quantitative relationship between different Me/Ca ratios in an expression previously developed to understand the evolution of magma melt-systems (Pearce, 1978; Albarède, 1995). Correlated Mg/Ca and Sr/Ca data from micromilled samples are used to test the role of Rayleigh fractionation in Me/Ca vital effects across skeletal structural features and place this mechanism in the context of other tracer vital effects. By examining a key component of many biomineralization models, our work aims to improve the understanding of vital-effect mechanisms during calcification to help better interpret Me/Ca temperature proxies.

3.2 Materials and Methods

Coral Samples: Five individuals of recent *D. dianthus* were loaned from The Smithsonian Institution National Museum of Natural History (Figure 3.2). Two individuals from the same South Pacific location, Smithsonian Collection number 47407, are the focus of most of this study. In situ temperature at the location and depth of 47407 is estimated to be 3.6±0.6°C from Levitus & Boyer (1994).

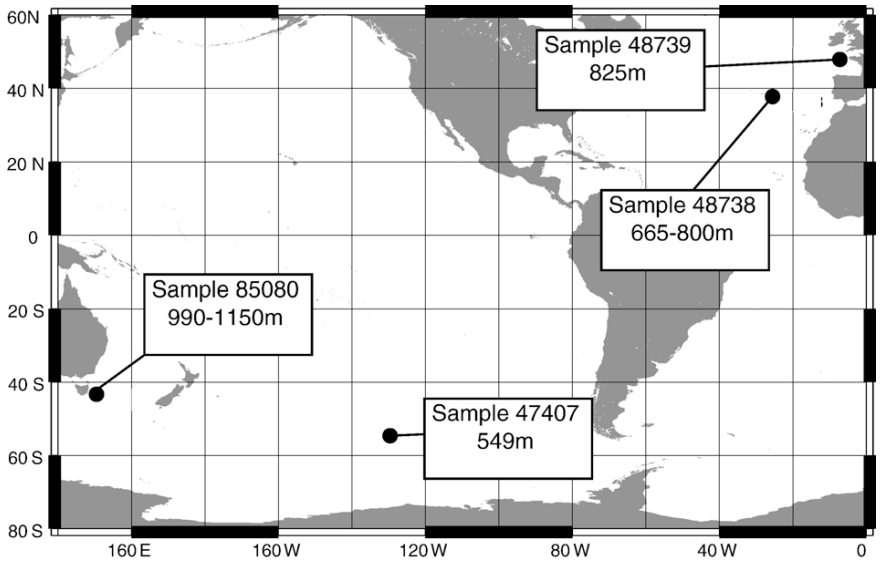

Figure 3.2: Collection locations of the recent deep-sea coral *D. dianthus* samples used in this study. Most of the analyses presented in this paper focus on two individuals from South Pacific location 47407.

Micromilling: Exert septa of two individuals from the same South Pacific location were selected for obvious and wide central bands (samples 47407A and 47407B). Wedges of coral are removed to allow analysis in the transverse plane—equivalent to a top view down the body axis. The coral are then mounted on glass slides with epoxy, ground to a thickness of 200–400 μm on a grinding wheel impregnated with 30 μm diamonds, sonicated without further polishing, and imaged (background grey-scale images in Figure 3.3). A computer controlled micromill (Merchantek) is used to subsample parallel with banding to a depth of $\sim$ 200 μm, starting from one side of the septa and moving across. We believe growth in the transverse plane outward from the central band represents a growth axis, with the oldest material deposited as COCs in the center of the septa. However, the

coral grew in near constant conditions with largely time-invariant environmental parameters, and the sampling method is designed to clearly separate different skeletal regions rather than to follow a particular growth axis. Dashed vertical lines in Figure 3.3 mark successively milled regions and correspond to individual Me/Ca data points. For each data point $\sim$ 100 μg of milled powder is dissolved in 5% trace metal clean HNO3 (Seastar).

Most micro-milled samples in this study were analyzed using the isotope dilution ICP-MS method described in Fernandez et al. (in press), and exhibit lower precision than the improved method described in Chapter 2. The reproducibility (external error) of the sessions where micromilled samples were analyzed was assessed by the repeated measurement of a dissolved deep-sea coral consistency standard. Over three months, 11 measurements of the consistency standard resulted in Mg/Ca and Sr/Ca ratios that varied by 1.3% and 2.1%, respectively (2σ standard deviation). As part of preliminary work, three other individuals of coral were analyzed using an identical method, except with an uncalibrated spike, yielding less precise relative Mg/Ca ratios.

3.3 Results

Mg/Ca is over twice as high in the optically dense central band, as compared to the surrounding septa (Figure 3.3a–b). The outer septal region is characterized by a Mg/Ca of $\sim$ 1.5 mmol/mol while the central band is greater than 3 mmol/mol. The relative Mg/Ca ratios of three other *D. dianthus* individuals collected from separate locations are also enriched up to two fold within the central band (Figure 3.4). Different amounts of smoothing, the incorporation of both central band and outer septal material in the same milling line, may explain differences in the relative enrichment between each coral. Outside the central band, Mg/Ca variability is 18% (2σ standard deviation). Also in this region, Mg/Ca ratios increase with decreasing Sr/Ca ratios.

Unlike Mg/Ca, Sr/Ca ratios show less structure and vary by a smaller relative amount across the coral septa, with a standard deviation of less than 5% (2σ , Figure 3.3c–d). The average Sr/Ca of the two corals 47407A and 47407B, 10.56 and 10.62 mmol/mol, respectively, are statistically identical, given our analytical uncertainty. Comparing all data by skeletal region rather than between indi-

vidual corals, Sr/Ca within the central band varies significantly less than the surrounding skeleton (F-Test, $>$ 98% loc, n=23 and 8) with a mean value in the central band of 10.60.2 (2σ standard deviation). The standard deviation of Sr/Ca in the central band is similar to methodological external error and may represent instrumental variability rather than the lower limit of coral Sr/Ca variability.

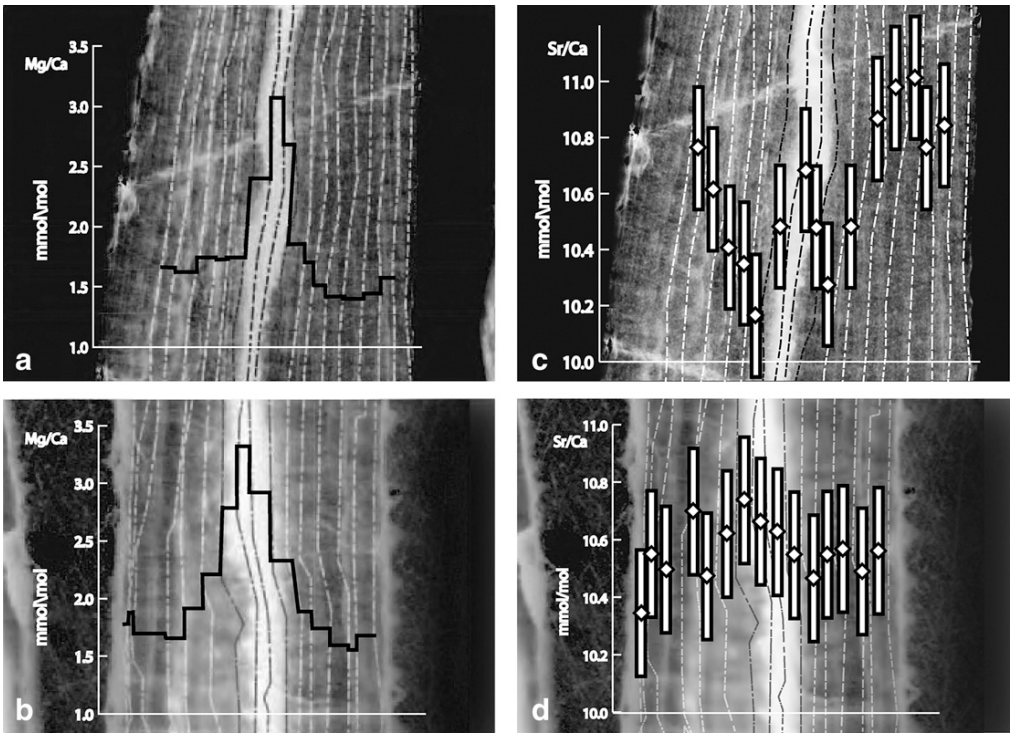

Figure 3.3: Isotope-dilution ICP-MS measurements of Mg/Ca and Sr/Ca across skeletal features in two *D. dianthus* septa. (**a&b**) Mg/Ca of microsamples from septa 47407B and 47407A, respectively, overlaid on negative transmitted light photomicrograph to show sampling locations in relation to skeletal structural features. Mg/Ca ratios double coincident with the optically dense central band. On this scale, $\pm 2\sigma$ error bars are smaller than the line thickness. (**c&d**) Sr/Ca of microsamples across 47407B and 47407A, respectively, with smaller and less structured variability than Mg/Ca. Notice that the range of Sr/Ca is much smaller relative to variations in Mg/Ca. Error bars represent $\pm 2\sigma$ external error. Septa are approximately 1.5 mm across. Central optically dense white band, corresponding to COCs, is 110μm across.

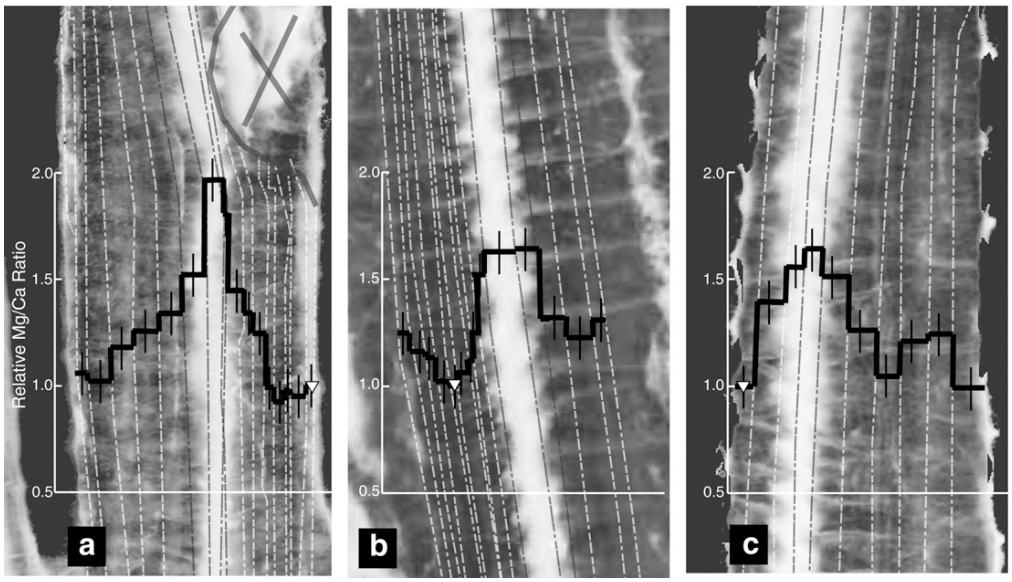

Figure 3.4: Relative Mg/Ca ratios in several coral in relation to structural features. (**a**) Coral 48739, again showing a nearly 2 fold increase in Mg/Ca coincident with the central band. A region of optically dense material removed prior to milling is marked with a large X. (**b&c**) Relative Mg/Ca in coral 48738 and 85080 also increase in the central band. Although the relative increase in Mg/Ca is less than two fold in these two coral, the consistent observation of increased Mg/Ca in the central band was observed in all coral examined in this study. Relative Mg/Ca ratios were determined in reference to a particular microsample within the septa identified as a upside-down triangle in each plot. Error bars are noted by black vertical lines.

3.4 Magnitude and Pattern of Me/Ca Vital Effects and the Inorganic Reference Frame

To quantify the absolute magnitude of vital effects, the partitioning of elements between seawater and coral should ideally be compared to the thermodynamic partitioning of elements between seawater and abiotic aragonite, and then to kinetic effects. Unfortunately, reaching thermodynamic equilibrium in precipitation experiments has proven difficult; see, for example, the discussion in Gaetani & Cohen (2006). Therefore, coral data are typically compared to inorganic experiments with kinetic or other effects which may or may not be present during coral precipitation. Determining a valid inorganic reference frame to compare with coral is a topic of ongoing research.

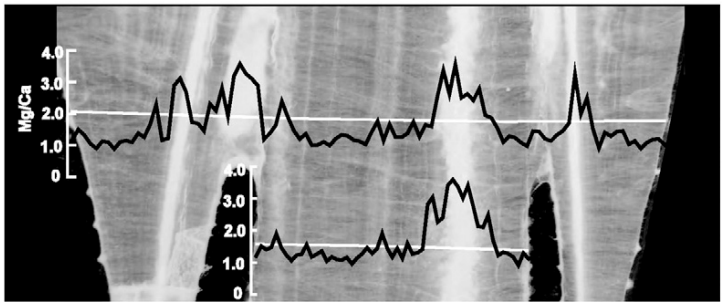

Figure 3.5: Mg/Ca increases in optically dense bands as determined by electron probe X-Ray microanalysis in a thin section of *D. dianthus* from Smithsonian location 47407. White horizontal lines mark path of analysis.

Fortunately, there is general agreement, over a range of experimental conditions and methodologies, between most studies on the partition coefficient of Sr in inorganic aragonite as a function of temperature (Gaetani & Cohen, 2006; Dietzel et al., 2004; Kinsman & Holland, 1969), where the partition coefficient from solution of constant composition is defined as:

$$D_{\mathrm{Sr}}^{arag} = \left(\frac{\mathrm{Sr}}{\mathrm{Ca}}\right)_{aragonite} / \left(\frac{\mathrm{Sr}}{\mathrm{Ca}}\right)_{seawater}.$$

As thoroughly discussed by Gaetani & Cohen (2006), the low partition coefficient of Mucci et al. (1989), by 16% in comparison to the consensus from other studies, may be the result of kinetic effects.

A major control of precipitation rate in inorganic systems is the saturation state of the solution: $\Omega = [Ca2+][CO32-]/k_{sp}$. Mucci et al. (1989) precipitated aragonite from constant composition solutions with saturations states ranging between 2.3 and 5. This is significantly lower than the Ω of > 20 in Kinsman & Holland (1969), Ω between 10–31 for Dietzel et al. (2004), and Ω between 40 and 90 in Gaetani & Cohen (2006). It is unlikely that coral reach the high saturation states found in most of the above mentioned inorganic experiments; possibly making the data of Mucci et al. (1989) more applicable to understanding coral vital effects. However, it is also possible that effects other than kinetics may cause the difference between Mucci et al. and the other studies. In fact, Mucci et al. and Zhong & Mucci (1989) report the partition coefficient for strontium is independent of precipitation rate over the factor of 14 range in precipitation rates explored by their study. Gaetani & Cohen recognize the results of Mucci et al. and Zhong & Mucci, but conclude that the range of low precipitation rates explored in that study is too small to see the differences obvious between Mucci et al and the high Ω studies. Here, we choose to use the larger and more complete dataset of high Ω partition coefficients for Sr to compare with the deep-sea coral, although future work to determine the D_{Sr}^{arag} at slow precipitation rates over a range of temperatures is certainly necessary. Using the combined empirical data of Gaetani & Cohen (2006); Dietzel et al. (2004) and Kinsman & Holland (1969) and assuming a $\mathrm{Sr/Ca}_{seawater}$ of 8.6 mmol/mol (DeVilliers, 1999), the Sr/Ca of inorganic aragonite can be predicted as a function of temperature (solid line and 2σ error envelope in Figure 3.6).

The range of Sr/Ca measured from coral microsamples both within and outside the central band agree with the expected Sr/Ca of inorganic aragonite precipitated at the temperature of coral growth, qualified by the error envelope of the inorganic relationship. Sr/Ca variability in the central band is smaller and statistically different from that of the outer septa. Inorganic behavior and low variability in the central band are consistent with minimal vital effects for Sr/Ca in this region, while the variability in the outer septa suggests the influence of vital effects. Similar mean Sr/Ca values in both the central band and outer septa of *D. dianthus* are in contrast to the results of Cohen et al. (2006) for another species of deep-sea coral, *Lophelia pertusa*, where opaque bands in the theca are

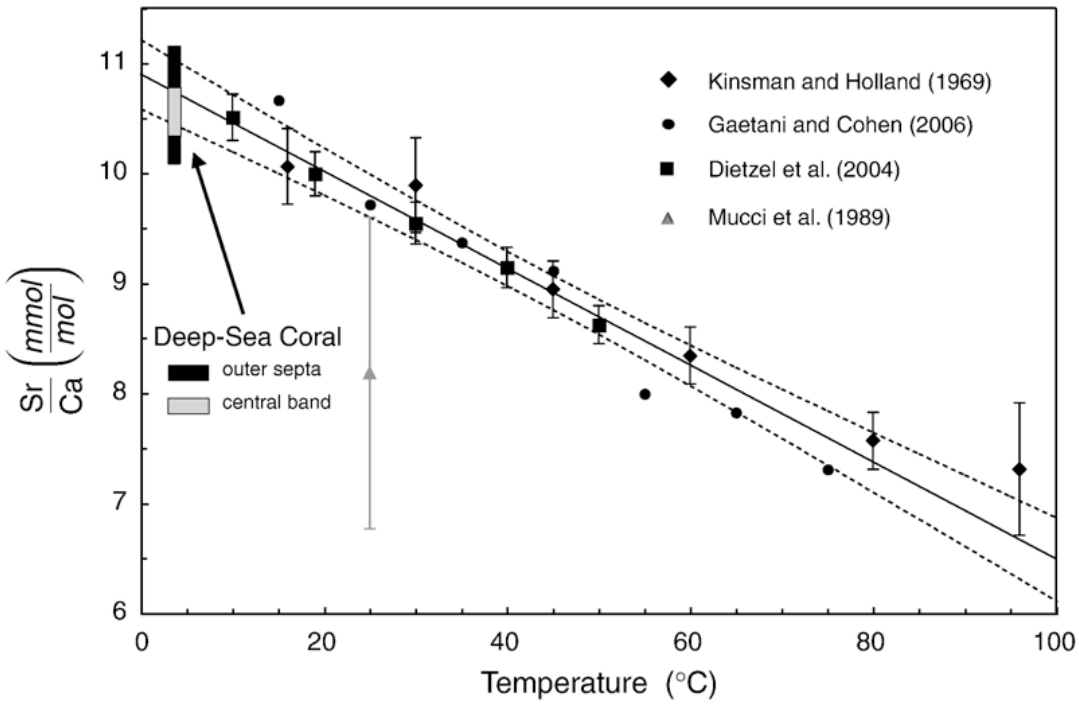

Figure 3.6: Sr/Ca of *D. dianthus* compares well with inorganic aragonite, although the results of Chapter 2 show that Sr/Ca does not follow the inorganic relationship. Black box marks total range of all *D. dianthus* samples where width represents estimated uncertainty in growth temperature. Gray box is smaller range of the central band. Solid line is an error weighted regression of the combined data from Kinsman & Holland (1969) (diamonds), Dietzel et al. (2004) (squares), and Gaetani & Cohen (2006) (circles) assuming a Sr/Ca of seawater of 8.6 mmol/mol. Dashed lines mark the 2σ error envelope of the regression. The slope of this inorganic relationship is 44 ± 6 (μmol Sr) (mol Ca)$^{-1}$ °C^{-1}. The data of Mucci et al. (1989) is also plotted. For the experiments of Kinsman & Holland and Dietzel et al., the largest source of error is the variability between replicate precipitation experiments conducted at the same temperature, represented by 2σ error bars. In Gaetani & Cohen each temperature represents a single precipitation experiment. Since Gaetani & Cohen and Kinsman & Holland used similar methods, the average error of Kinsman and Holland was used to estimate the replicate error of Gaetani & Cohen for the purpose of the weighted linear regression.

associated with decreased Sr/Ca relative to the surrounding skeleton. In surface coral, Cohen et al. (2001) explain both differences in Sr/Ca variability between the COCs and the surrounding skeleton as well as different mean Sr/Ca ratios for these skeletal regions by the influence of photosynthesis. In an elegant test of this hypothesis, Cohen et al. (2002) observed higher Sr/Ca variability outside of COCs in a symbiont containing coral as compared to an aposymbiont individual of the same species. We also observe higher Sr/Ca variability outside COCs, but unlike the surface coral data we see similar means. Our data suggests that some of the difference in Sr/Ca variability between the COCs and the surrounding skeleton is ubiquitous in coral both with and without photosymbionts.

Unlike Sr/Ca, there is a two fold difference in Mg/Ca between the central band and outer septa of *D. dianthus*, following a similar pattern to skeletal features found in surface corals (Meibom et al., 2006, 2004), a commonality noted by Sinclair et al. (2006). As the deep-sea corals in this study grew in near constant environmental conditions, the spatially structured 1.5 mmol/mol variation in Mg/Ca is a clear indication of vital effects and places a lower limit on the magnitude of these effects. The average Mg/Ca of *D. dianthus* compares well to the range of Mg/Ca found by Shirai et al. (2005) from bulk sampling of two different genus of deep-sea coral; but the results of Cohen et al. (2006) in *Lopehelia pertusa* are significantly higher, ranging from 2.6 to 4.3 mmol/mol. Cohen et al. (2006), measure smaller spot sizes than our method, and the larger range in Mg/Ca they observe may represent skeletal variability with less spatial averaging than our method; however, the higher mean Mg/Ca measured by Cohen et al. (2006) as compared to Shirai et al. (2005) and this study cannot be explained by averaging and may represent differences across species of deep-sea coral or differences in growth environments between the studies.

It is difficult to determine the correct inorganic reference frame for magnesium in aragonite. Gaetani & Cohen (2006) were able to establish a clear temperature relationship for Mg/Ca in aragonite, an important and significant achievement. However, assuming a seawater Mg/Ca of 5.1 mol/mol, the data of Gaetani & Cohen predict aragonite should have a Mg/Ca ratio of $\sim$ 10 mmol/mol compared to the range of 1.5 to 3 mmol/mol found in *D. dianthus* and the 4 to 5 mmol/mol Mg/Ca ratios typical of surface corals. To explain the Mg/Ca ratios observed in a surface coral

Diploria and in the deep-sea coral *Lophelia pertusa* consistent with these high inorganic Mg/Ca results, Gaetani & Cohen (2006) and Cohen et al. (2006) invoke a 3-fold to 8-fold reduction of Mg/Ca in the calcifying fluid with respect to seawater. Although there are no direct measurements of Mg/Ca in the calcifying fluid, the energetic cost of manipulating Mg/Ca by such a large amount seems prohibitive without a clear biological purpose (Zeebe & Sanyal, 2002). If Mg/Ca is not manipulated by a large amount, the inorganic results of Gaetani & Cohen (2006) suggest either that there is a large vital effect of an absolute offset in Mg/Ca between corals and inorganic aragonite or that the conditions of the inorganic experiment are not a valid reference frame for coral growth. The only other systematic study on magnesium partitioning in aragonite, the inorganic experiments of Zhong & Mucci (1989), find a Mg/Ca of 3.5 mmol/mol at the one temperature investigated, 25 °C, roughly half the result of Gaetani & Cohen (2006). Unlike the inorganic behavior of Sr/Ca, a consensus of supporting studies over a range of experimental conditions does not exist for Mg/Ca. The large difference between Zhong & Mucci and Gaetani & Cohen suggest further research on the coprecipitation of Mg in aragonite over a range of experimental conditions is a high priority towards understanding inorganic behavior, and by extension, vital effects.

3.5 Correlated Me/Ca Ratios and Rayleigh Fractionation

The correlated variability of multiple tracers can be a strong constraint on vital effect mechanism, as recognized and exploited by Sinclair (2005) in surface corals and more recently by Sinclair et al. (2006) for Mg/Ca and U/Ca in deep-sea corals. A tracer-tracer plot of Sr/Ca vs. Mg/Ca in D. dianthus using the combined data sets of coral 47407A and 47407B (Figure 3.7) shows two trends: (1) outside the central band, Sr/Ca decreases with increasing Mg/Ca in a relationship that is roughly linear but may show some curvature, and (2) inside the central band, corresponding to the centers of calcification (COCs), variable and enriched Mg/Ca is associated with constant Sr/Ca. We test for the presence of a Rayleigh process in these skeletal regions.

Rayleigh fractionation as applied to individual trace metal behavior has been discussed thoroughly elsewhere (Elderfield et al., 1996; McIntire, 1963). Models of coral trace element variability

incorporating Rayleigh fractionation as a key mechanism have also been recently proposed (Gaetani & Cohen, 2006; Cohen et al., 2006). Here we develop a simple and general relationship for multiple Me/Ca ratio behavior during Rayleigh fractionation, similar to the approach of Albarède (1995), and compare this to our data set. Following Elderfield et al. (1996), the Sr/Ca of aragonite precipitated at any point during a Rayleigh process from a closed solution can be calculated from the initial solution composition assuming a constant effective partition coefficient:

$$\left(\frac{\mathrm{Sr}}{\mathrm{Ca}}\right)_{aragonite} = D_{\mathrm{Sr}}^{arag}\left(\frac{\mathrm{Sr}}{\mathrm{Ca}}\right)_{Solution_o} F^{D_{\mathrm{Sr}}^{arag}-1} \tag{3.1}$$

where the extent of precipitation is defined as:

$$F = \left(\frac{[\mathrm{Ca}^{2+}]}{[\mathrm{Ca}^{2+}]_{\mathrm{o}}}\right)_{Solution}.$$

The effective partition coefficient, D_{Sr}^{Coral} relates the Sr/Ca of the coral skeleton to the surrounding seawater and is an empirical measure that integrates the thermodynamics of coprecipitation, kinetics, binding by organic molecules, and all other process acting on strontium under the specific growth conditions of the coral (Morse & Bender, 1990).

Mg/Ca can be described similarly to Equation (3.1), where Sr/Ca is replaced by Mg/Ca and D_{Sr}^{Coral} by D_{Mg}^{Coral}. Since Mg/Ca and Sr/Ca are linked by the extent of precipitation, F, the expressions can be combined, eliminating F, yielding a linear log-log relationship:

$$ln\left(\frac{\mathrm{Sr}}{\mathrm{Ca}}\right)_{Coral} = \frac{[D_{\mathrm{Sr}}^{arag}-1]}{\left[D_{\mathrm{Mg}}^{arag}-1\right]} ln\left(\frac{\mathrm{Mg}}{\mathrm{Ca}}\right)_{Coral} + \left[\left(\frac{\mathrm{Sr}}{\mathrm{Ca}}\right)_{Coral_o} - \frac{[D_{\mathrm{Sr}}^{arag}-1]}{\left[D_{\mathrm{Mg}}^{arag}-1\right]}\left(\frac{\mathrm{Mg}}{\mathrm{Ca}}\right)_{Coral_o}\right] \tag{3.2}$$

where $(\mathrm{Sr/Ca})_{Coral_o}$ and $(\mathrm{Mg/Ca})_{Coral_o}$ refer to the composition of solid skeleton precipitated at the very beginning of the Rayleigh process,

$$\left(\frac{\mathrm{Sr}}{\mathrm{Ca}}\right)_{Coral_o} = D_{\mathrm{Sr}}^{arag}\left(\frac{\mathrm{Sr}}{\mathrm{Ca}}\right)_{Solution_o}.$$

Under the conditions of closed system precipitation with constant partition coefficients and any initial fluid composition, tracer-tracer behavior is predicted to follow Equation (3.2). Testing if correlated tracer behavior follows the functional form of Equation (3.2) is a general test for Rayleigh behavior that does not require knowledge of initial solution conditions or partition coefficients. In the outer septal region of *D. dianthus*, the log-log tracer plot is linear, with an R^2 of ~ 0.6, (solid line, inset Figure 3.7), consistent with a Rayleigh mechanism. (Re-analysis of micromillied samples by the method outlined in Chapter 2, led to an even more significant linear relationship, R^2=0.9, supporting the closed system conclusion.) Equally important, the behavior of Mg/Ca and Sr/Ca in the central band cannot be explained by Rayleigh fractionation. In the deep-sea coral *Lophelia pertusa*, Cohen et al. (2006) also observe decreasing Sr/Ca with Mg/Ca which they explain by a model emphasizing Rayleigh fractionation. Indeed, while the plot of tracer-tracer behavior in (Cohen et al., 2006) is roughly linear it may show some curvature toward low Sr/Ca and high Mg/Ca, as predicted by Equation (3.2). Recently, Sinclair et al. (2006) showed that relative U/Ca and Mg/Ca ratios from both surface and deep-sea corals follow a power law relationship and explained this behavior with end member mixing. As an alternative explanation to end member mixing, a Rayleigh process also predicts a power law relationship between U/Ca and Mg/Ca, and may explain some of the correlated observations.

In Equation (3.2) the slope of the log-log relationship is determined by the partition coefficients of each metal and the intercept is influenced by both the initial solution composition and the partition coefficients. The slope in Equation (3.2) is predicted to be relatively less sensitive to variations in D_{Mg}^{Coral} than D_{Sr}^{Coral}, since D_{Mg}^{Coral} is $<< 1$, driving the denominator of the slope very close to 1 even over a large relative range of D_{Mg}^{Coral}. The low relative sensitivity of a Rayleigh process to variations in D_{Mg}^{Coral} has two implications, (1) the tracer-tracer behavior predicted by a Rayleigh process is robust to even large variations in D_{Mg}^{Coral} and (2) it is difficult to determine a precise D_{Mg}^{Coral} by inverting the fitted slope and using an estimate of D_{Sr}^{Coral}. If D_{Sr}^{Coral} is sensitive to temperature like inorganic aragonite, then the slope of the log-log Rayleigh plot will also be sensitive to temperature—possibly undoing the variability seen in this study and Chapter 2 to yield a useful paleothermometer.

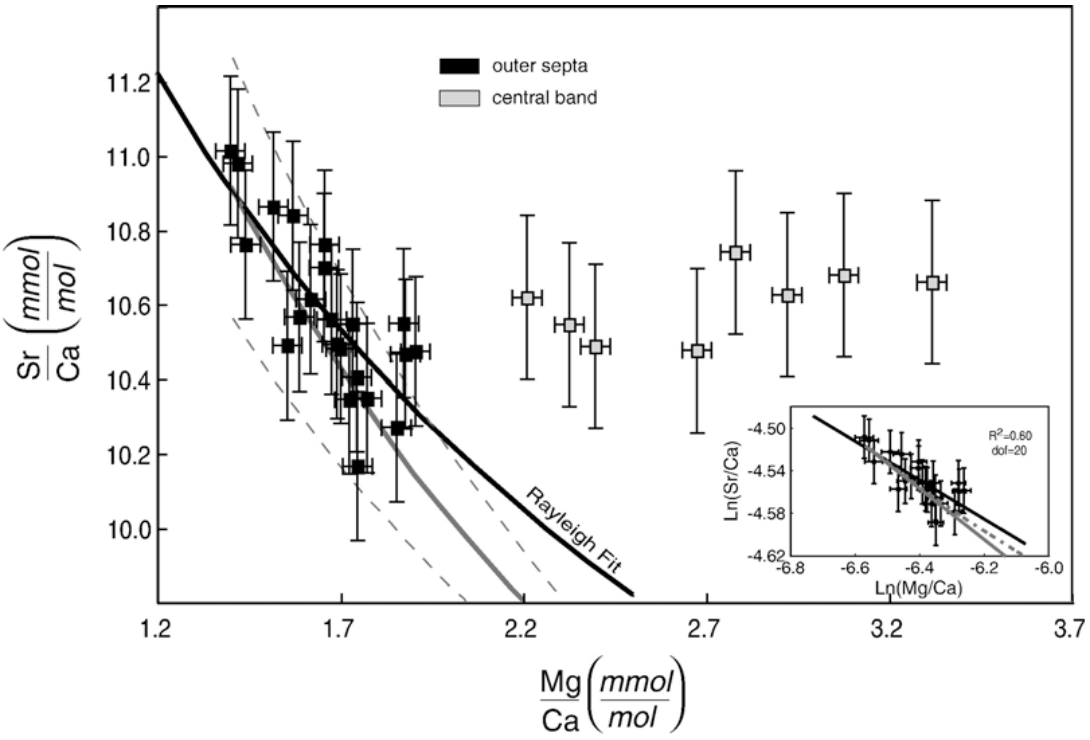

Figure 3.7: Correlated Sr/Ca-Mg/Ca vital effects are consistent with Rayleigh fractionation in the outer septa, but not in the central band. Data points with 2σ error bars are combined measurements from coral 47407A and 47407B, identified by skeletal location. Inset is a log-log plot of outer septa results with a linear model (bold black line) fit to the data ($R^2 = 0.6$). The fit parameters of the linear model in the inset were used to plot the Rayleigh Model in the larger plot (bold black line labeled Rayleigh Fit). As an alternative to fitting the data, Rayleigh behavior can be forward modeled with prescribed parameters. In one scenario, initial Mg/Ca is set to a seawater value; initial Sr/Ca is enriched by 3% compared to seawater; D_{Mg}^{Coral} is set to 2.75×10^{-4}, consistent with the lowest Mg/Ca measurements; and D_{Sr}^{Coral} is set to equal the partition coefficient of inorganic aragonite, 1.24±0.4. The results of this calculation are shown as the grey solid line in the main plot with the dashed error envelope representing a propagation of uncertainty in the inorganic strontium partition coefficient. While most of the discussion in this paper assumes that we sample instantaneous Rayleigh precipitate, the grey solid and dashed lines in the inset are the predicted composition of both instantaneous and accumulated solid, respectively, for the above forward Rayleigh model scenario, with relatively tight agreement.

Instead of inverting partition coefficients from a fit of the log-log relationship, a predicted Rayleigh relationship for tracer-tracer behavior can also be generated from prescribed effective partition coefficients and initial solution composition. For this forward modeling, we use an initial Mg/Ca ratio matching the seawater value of 5.1 mol/mol. We also make the functional assumption that the lowest Mg/Ca ratios measured in our corals correspond to precipitation from the initial unfractionated solution (F =1), implying a D_{Mg}^{Coral} of 2.75x10^{-4}. We choose this partition coefficient because it describes our coral measurements well and does not imply a dramatic modification of the Mg/Ca of the calcifying fluid; however, it is significantly lower than the partition coefficient for Mg in inorganic aragonite as determined by Gaetani & Cohen (2006). As described above, uncertainty in D_{Mg}^{Coral} has a small effect on the slope of the tracer-tracer relationship, making our forward model conclusions relatively insensitive to this functional assumption.

Given the above assumptions, two Rayleigh fractionation scenarios can explain the observed Mg/Ca vs. Sr/Ca relationship of the outer septa. If the abiotic aragonite partition coefficient, D_{Sr}^{arag} , which matches the partition coefficient of the central band, is also taken as an estimate for D_{Sr}^{Coral} in the outer septa, then the correlated data are consistent with a Rayleigh process and a non-seawater initial Sr/Ca ratio of 8.8 mmol/mol, an enrichment of less than 3% (solid grey line and dashed error bounds Figure 3.7). Evidence of active Sr pumping exists from cultured surface corals in a study with chemical inhibitors, (Ferrier-Pages et al., 2002), although, as noted by Sinclair & Risk (2006), the results of this study are also consistent with general inhibition of calcification and may simply evidence Sr coprecipitation rather than active Sr pumping. If Sr pumping is present, this first Rayleigh scenario is consistent with an initial manipulation of the calcifying fluid followed by closed system behavior during precipitation. Changes to solution composition prior to precipitation only affect the intercept of the log-log relationship, shifting the whole plot vertically in log-log space, but otherwise leaving the slope and sign of the tracer-tracer correlation unchanged. In a second scenario, initial Sr/Ca is assumed to match seawater. In this case, our data are consistent with a D_{Sr}^{Coral} in the outer septa of 1.28, within 2σ of the inorganic relationship but different from the D_{Sr}^{Coral} of the central band. Our data support the presence of Rayleigh fractionation in the outer septa but are

unable to distinguish between these two scenarios.

The above expressions describe the composition of instantaneous precipitate, or the most recently formed precipitate at a given F. As it is unclear whether our analytical method samples instantaneous or accumulated solid, both must be considered. The individual Me/Ca ratio of accumulated precipitate, integrated from the start until a given extent of precipitation (from 1 to F), can be derived (Elderfield et al., 1996; Doerner & Hoskins, 1925). Even though the combined tracer-tracer relationship for accumulated solid is non-linear in a log-log plot, Me/Ca correlations are nearly identical between accumulated and instantaneous solids using the same partition coefficients and initial solution composition (solid and dashed lines in inset of Figure 3.7). The most significant difference in tracer-tracer behavior between instantaneous and accumulated solids is the sensitivity to F, with the same paired Sr/Ca and Mg/Ca ratios corresponding to larger extents of precipitation in the accumulated solid than for instantaneous solid. F values are sensitive to the choice of partition coefficients and initial solution composition, which, combined with the difference in F between accumulated and instantaneous precipitant, means that F is underconstrained by our data set. Qualified by this large uncertainty, the largest extent of precipitation in our data, corresponding to the most depleted Sr/Ca ratios and the most enriched Mg/Ca ratios in the outer septa, are consistent with an F value of roughly 0.8 for instantaneous precipitation and an F value of 0.6 for accumulated precipitation.

Rayleigh fractionation acts to lower Sr/Ca from an upper limit of determined by $(\mathrm{Sr/Ca})_{Coral_o} = D_{\mathrm{Sr}}^{arag}\,(\mathrm{Sr/Ca})_{Solution_o}$. If D_{Sr}^{arag} is similar to the inorganic partition coefficient at the coral growth temperature and $(\mathrm{Sr/Ca})_{Solution_o}$ is approximately equal to or slightly higher than seawater, then different extents of Rayleigh fractionation at different temperatures will result in Sr/Ca values that are lower or just over the inorganic Sr/Ca vs. T line. Bulk Sr/Ca of *D. dianthus* over a range of temperatures (data from Chapter 2) behaves exactly this way—the bulk Sr/Ca *D. dianthus* data is consistent with mixtures of closed-system precipitated aragonite where the extent of precipitation (F) does not vary systematically with temperature. Some of the other genera cross the inorganic line which, within the closed-system framework, may signify different extents of initial seawater

modification.

In the above discussion of the Rayleigh mechanism we assume a system closed to all metal cations during precipitation. However, active Ca2+ pumping in surface corals has been demonstrated in culture experiments (Tambutte et al., 1996) and is supported by the discovery of a plasma membrane Ca-ATPase localized to the calcifying region (Zoccola et al., 2004). Provided that the rate of pumping is less than the rate of precipitation, and assuming a constant rates of pumping and precipitation, this process should still produce a linear relationship between Sr/Ca and Mg/Ca in a log-log plot with a negative slope, similar to a completely closed Rayleigh process. On the other hand, if pumping and precipitation occur at the same rate or if pumping outpaces precipitation, the log-log Mg/Ca to Sr/Ca relationship should have a positive slope, unlike our data. Calcium transport prior to precipitation has the potential to modify Me/Ca ratios in the initial calcifying fluid; however, Ca-ATPase driven calcium-proton exchange is effectively alkalinity pumping and perturbs [Ca2+] relatively little while still increasing the saturation state of aragonite dramatically through the speciation of the carbonate system. Together, small changes in initial [Ca+2] and a rate of calcium pumping less than the rate of precipitation may result in initial Me/Ca ratios close to seawater that then progress along a Rayleigh curve, consistent with both the presence of active calcium transport and our data. The constraint of a closed system with regard to non-calcium metal cations does not apply to dissolved inorganic carbon (DIC), which can diffuse through bio-membranes as CO2(aq). A Me/Ca Rayleigh process is therefore consistent with the equilibrium stable isotope vital effect model of Adkins et al. (2003) where δ^{13}C is set by net transmembrane CO2(aq) flux, and δ^{18}O is set by the pH of the calcifying fluid.

3.6 Me/Ca Vital Effect Mechanism in the Central Band

Large variations in Mg/Ca are uncoupled from Sr/Ca in the central band, suggesting that Rayleigh fractionation is not the dominant process influencing Mg and Sr correlation in this region. Understanding this vital effect has implications beyond deep-sea coral, as increased Mg/Ca in COCs appears to be a common feature in both surface and deep-sea coral (Meibom et al., 2006, 2004;

Sinclair et al., 2006). Possible mechanisms for high Mg/Ca in the central band can be evaluated with our data set.

A surface entrapment model predicts precipitation rate dependent behavior of a tracer when growth rate and near-surface solid diffusion are closely matched (Watson, 2004). This model assumes chemical potentials at the surface and in the bulk-solid differ for a tracer, resulting in a difference of chemical composition as the solid traps more or fewer of these end members. For surface entrapment to explain the enriched Mg of the central band, assuming rapid precipitation occurs in this region and traps more of a surface-like composition, the aragonite surface must be enriched in Mg compared to the bulk crystal. Sr/Ca, however, is not observed to systematically vary with Mg/Ca in the central band. Within the surface entrapment framework, this implies that either the bulk and surface composition of aragonite have identical strontium activities, or the balance of near-surface diffusion and precipitation rate are different enough between Sr and Mg such that Sr is insensitive to growth rate over the range of rates that occur during coral growth. While our data are not a direct test of the surface entrapment model, they do highlight key model parameters and predictions if this process is at work in *D. dianthus*. Furthermore, if surface entrapment explains the uncoupled variability of Mg/Ca and Sr/Ca in the central band, the dominance of Rayleigh fractionation in the outer septa may suggest crystal growth rates and consequently surface entrapment effects do not vary significantly in the outer septa.

There is evidence for organic material in coral skeletons that may help regulate biomineralization (Cuif et al., 2003; Puverel et al., 2005). It is possible that the organic matrix or another biomolecule is responsible for enriched Mg in the central band. A biological component that selectively binds Mg but not Sr seems possible given the difference in polarizability between these two cations. This putative biomolecule would have to be localized within the COCs, however, the existence and magnitude of Sr vs. Mg trace element selectivity by organic components within the coral skeleton has yet to be demonstrated.

Differences in Me/Ca behavior between the outer septa and central band raise the possibility of fundamentally different biomineralization mechanisms in these regions. However, previous measure-

ments of U/Ca argue against this. In fission track experiments on *D. dianthus* coral sections similar to ones used in this study, there is a greater than threefold range in [U] across the coral skeleton (Robinson et al., 2006). The pattern of this variation is crucial: the region of low uranium follows but extends well beyond the central band, with [U] largely unchanged across the interface between the central band and the outer septa. If the central band were under the control of a fundamentally different mechanism than the outer septa, it seems unlikely that [U] behavior would remain unchanged across the interface of these two mechanisms. The pattern of [U] suggests a continuous general mechanism describing vital effects and biomineralization. Conclusions about uranium can be generalized to other tracers to the extent that they are influenced by the same processes. Unfortunately the mechanism of U/Ca vital effects is still an open question. Experiments suggest D_{U}^{arag} varies by threefold due to pH and precipitation rate (Russell et al., 2004; Meece & Benninger, 1993), although the relative contributions of these factors and the mechanism of influence are a topic of current research.

While far from a comprehensive list of all processes affecting magnesium, certain conclusions can be made. High Mg/Ca in the central band is not dominated by Rayleigh fractionation; it may be the result of surface entrapment, given key constraints; biomolecules may be at work, although it is impossible to quantitatively assess their role without further characterization; and, finally, there appears to be some mechanistic continuity across all skeletal features.

3.7 Prospect for a Me/Ca Paleothermometer in the Context of Closed System Biomineralization

Data presented in Chapter 2 show that Sr/Ca of bulk sampled deep-sea coral exhibit high variance without a useful temperature relationship. The micro-milling work in this chapter both describe and explain this intra-coral Me/Ca variability. Furthermore this understanding provides a possible way forward that may still produce a useful Me/Ca based paleothermometer. As described in Section 3.5, the slope of Sr/Ca vs. Mg/Ca on a log-log plot is predicted to be dominated by the term $[D_{\mathrm{Sr}}^{Coral} - 1]$.

If this partition coefficient is sensitive to temperature, like the inorganic partition coefficient, then the slope on a log-log plot should vary with T, effectively undoing Rayleigh-induced variability. By making multiple measurements of non-central band material in coral from a range of temperature, by micro-milling or other techniques, it should be possible to test this hypothesis.

The impact of vital effects on the Mg/Ca paleothermometer can be estimated, in the absence of clear inorganic data, by comparing *D. dianthus* with surface corals (Figure 3.8). From Mg/Ca-temperature relationships calibrated in surface corals (Mitsuguchi et al., 1996; Reynaud et al., 2007; Sinclair et al., 1998; Fallon et al., 1999) the total $\sim$ 2 mmol/mol range of Mg/Ca in *D. dianthus* corresponds to $\sim 10^{\circ}$C. Surface coral temperature calibrations correspond best with the outer septa of our deep-sea corals. While the slope of the Mg/Ca temperature relationship, as determined in surface corals, is steeper than that of Sr/Ca, the presence of large vital effects can introduce a false and difficult-to-separate temperature-like signal if different proportions of skeletal regions are sampled during analysis.

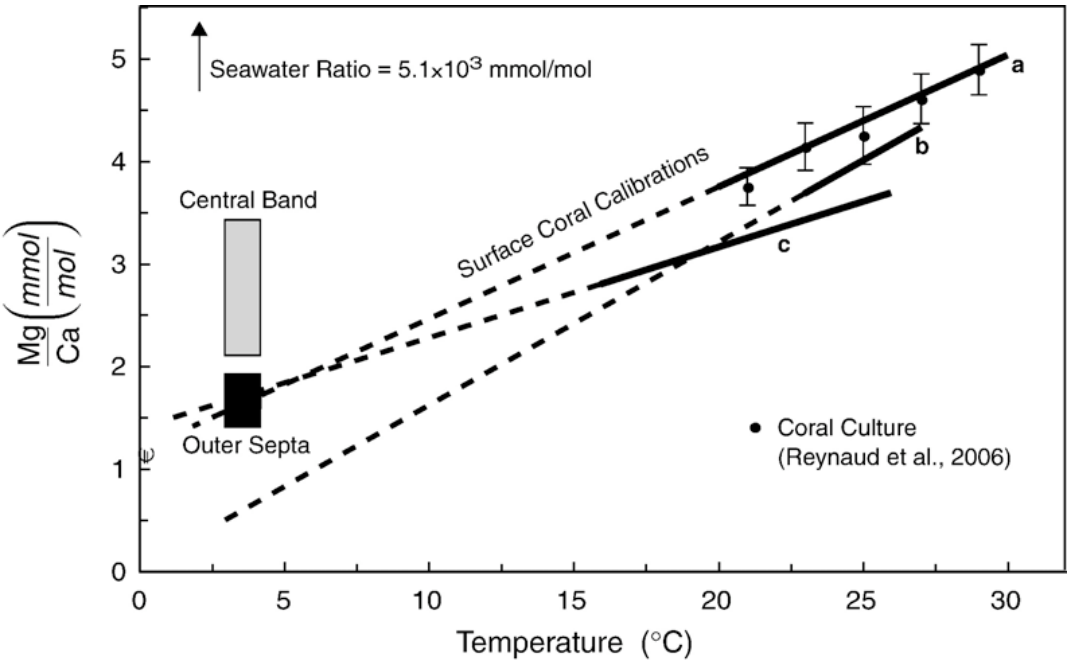

Figure 3.8: Large Mg/Ca vital effects in *D. dianthus* compared to extrapolated surface coral data. Surface coral calibrations: (**line a**) Mitsuguchi et al. (1996), which compares well with recent coral culture experiments of Reynaud et al. (2007), circles. (**line b**) Fallon et al. (1999), (**line c**) Sinclair et al. (1998). Calibrations are marked as solid lines within the temperature range of the respective experiments, and dashed lines over the extrapolated temperature range.

3.8 Conclusion

I determined accurate and detailed co-located Sr/Ca and Mg/Ca ratios across different skeletal regions in two individuals of the deep-sea coral *D. dianthus* through a combination of micromilling and isotope dilution- ICP-MS. Overall, Sr/Ca variability was several %, with Sr/Ca in the optically dense central band varying significantly less than in the surrounding skeleton. Unlike Sr/Ca, mean Mg/Ca varies dramatically between different skeletal regions. Coincident with the optically dense central band, Mg/Ca was at least 3 mmol/mol, more than twice that of the surrounding skeleton. This result appears to be general, as relative Mg/Ca ratios of three other D. dianthus individuals collected from separate oceanographic locations also nearly double within the central band. The difference in the mean Mg/Ca of the central band and surrounding skeleton implies a $\sim 10°C$ temperature signal, when calibrated via Mg/Ca-temperature relationships developed in surface coral. A large non-environmental effect, or vital effect, can obscure and complicate application of a Mg/Ca paleothermometer.

While complicating interpretation of a paleothermometer, vital effects are useful to help understand the mechanism of biomineralization. Outside the central band, Mg/Ca increases with decreasing Sr/Ca. This relationship can be explained by Rayleigh fractionation as shown by a linear tracer-tracer relationship in a logarithmic plot. To be consistent with our accurate measurements of Mg/Ca and Sr/Ca, Rayleigh fractionation can occur from an initial solution where Me/Ca ratios match seawater, provided that the effective strontium partition coefficient (D_{Sr}^{Coral}) differs between the outer septa and central band. Alternatively, if D_{Sr}^{Coral} is the same throughout *D. dianthus* and matches the abiotic partition coefficient, our data is consistent with an initial solution enriched in Sr/Ca by 3% compared to seawater. Rayleigh fractionation implies a closed system during precipitation, at least with respect to trace or minor metal cations. In the central band, Me/Ca ratios are dominated by a non-Rayleigh process with our data constraining a number of possible explanations for vital effects in this region. That Rayleigh fractionation cannot explain the large variability in Mg/Ca within the central band is equally important as our evidence for the presence of Rayleigh fractionation in the outer septa. Given the widespread feature of enriched Mg/Ca in COCs, the

mechanism of this process is an important target of future research. In addition to explaining Me/Ca variability in deep-sea coral, closed-system biomineralization has important implications on the response of skeletal composition to changes in seawater carbonate chemistry. This may provide a helpful tool to better understand the response of coral calcification to anthropogenic ocean acidification, as explored and tested in the next chapter.

Chapter 4

High Spatial Resolution NanoSIMS Analysis to Calibrate Environmental Proxies in Coral Grown During a Short Culture Experiment: Test of Me/Ca Ratio Sensitivity to Carbonate Ion Concentration

4.1 Introduction

Combining geochemical analysis with coral culture has the potential to isolate separate environmental conditions on skeletal composition and growth with applications in paleoclimatology, biomineralization, and ecology. For example, proxy calibrations of organisms cultured under controlled conditions, can be used to (1) ensure accurate reconstructions of past climate; (2) separate environmental signals from biological variability; and (3) resolve the influence of environmental parameters which co-vary in much of the modern ocean, (i.e., T and $[CO_3^{2-}]$), but likely diverged in the past. A version of this approach has been used to test Mg/Ca and Sr/Ca and δ^{18}O sensitivity to temperature and light in coral (Reynaud-Vaganay et al., 1999; Reynaud et al., 2007). Unfortunately, widespread application of coral culture to answer geochemical questions is limited by the large investment of time and energy required to maintain coral culture facilities. Additionally, coral are typically col-

lected from the wild and it is technically challenging to separate the small amount of material grown during experimental culture from the the wild grown initial skeleton. In an attempt to address this second issue, Reynaud-Vaganay et al. (1999) and Reynaud et al. (2007) induced small nubbins of coral to grow laterally on glass slides, clearly distinguishing new growth from the original skeleton over a month long culture period. Very recently, Cohen et al. (2009) grew juvenile coral polyps from larva entirely under controlled conditions for several days to test the response of coral Mg/Ca and Sr/Ca to different carbonate ion concentrations. While both these techniques are useful, the first still requires longer than a month of culture time, limiting the types and pace of experiments, while the second approach limits work to juvenile coral unless long times are again used as the coral reach maturity.

I use the nanoSIMS, a relatively new instrument capable of accurate compositional and isotopic analysis with sub-micron spatial resolution, as a tool to identify and analyze the several-to-10s of micron region of skeletal growth resulting from a short (6-day) culture experiment in adult reef-building coral. The nanoSIMS has been previously applied to answer biomineralization questions in coral (Meibom et al., 2008, 2004). The novel goals of this research are to (1) demonstrate the feasibility of measuring compositional response to short coral culture experiments in adult coral; (2) map the extent and pattern of new skeletal growth to identify processes which control ion transport to the calcifying fluid; and (3) use this technique to quantify the sensitivity of Me/Ca ratios to $[CO_3^{2-}]$ and aragonite saturation in cultured coral. The results of the coral culture experiment will be interpreted within a closed system (Rayleigh) model for biomineralization to constrain explanations for the sensitivity of coral calcification rates to ocean acidification, improving our understanding of how anthropogenic CO2 will impact coral reefs.

In this study seawater culture media is enriched in the naturally low abundance stable isotopes 43Ca, 87Sr, and 136Ba to uniquely label material grown during the experiment. At the start of the experiment a short incubation with Calcein, a CaCO3 binding fluorescent probe, marks the margin of new growth guiding subsequent microanalysis. After the culturing period, NanoSIMS images and spot analysis are used to characterize the newly grown material.

Very recently, Houlbreque et al. (2009) incubated coral for 72 hours in 86Sr followed by nanoSIMS image mapping to resolve discrete 5–10 μm regions of labeled skeleton along a growth front. These results suggest that growth is discontinuous, but coherent, and identifies the size of coral growth units. In the current work, isotopes of several elements are added to the culture solution simultaneously. The dynamics of ion uptake by the skeleton are probed by quantitatively following the location and extent of incorporation compared to solution isotope measurements.

As an initial application we quantify the sensitivity of Sr/Ca, a proxy for temperature, to another important environmental parameter, [CO32-]. Carbonate ion concentration, [CO32-], has varied in the past, possibly biasing Me/Ca-based paelo-records in coral. Carbonate ion concentration also continues to decrease in the modern surface ocean in response to anthropogenic CO_2 emissions. Decreasing carbonate ion concentration reduces the thermodynamic driving force for calcification, or aragonite saturation $\Omega = [\mathrm{Ca2+}][\mathrm{CO32-}]/k_{sp}$. Indeed, experiments generally show coral reduce calcification rate as a response to CO2 enrichment and coincidently lower [CO32-]. (This effect is not followed by some biomineralizing organisms, for example, aragonitic fish otoliths increase in size as a response to higher pCO2 (Checkley et al., 2009).) The mechanism of reduced calcification to acidification is still unclear and somewhat puzzling, as most models of biomineralization invoke a calcifying region controlled more by the organism than the surrounding seawater. This question is relevant as we attempt to anticipate the impact of increasing atmospheric CO_2 and resulting ocean acidification on coral, a major reef-forming organism.

Conceptual Model of Biomineralization Response to Ocean Acidification: I assume that the first step in calcification is the transport of seawater to the calcifying region consistent with the Rayleigh results in Chapter 3 and as supported by recent experiments with fluorescent probes (unpublished work by Jonathan Erez). The calcifying fluid is then closed off from the surrounding seawater consistent with a Rayleigh process, as described in Chapter 3. Alkalinity pumping is used to increase local $[CO_3^{2-}]$, driving precipitation. A plot of alkalinity vs. dissolved inorganic carbon (DIC) completely describes the carbonate system of the calcifying fluid (Figure 4.1). On this plot alkalinity pumping appears as a vertical line. After a nucleating event, precipitation occurs and the calcifying fluid

relaxes to reach a $[CO_3^{2-}]$ in equilibrium with the solid skeleton. While very simple, even this framework provides basic and useful predictions on growth rate and composition. The coral's response to ocean acidification, however, depends on how coral regulate alkalinity pumping—an important undetermined parameter. As a thought experiment, let's consider several scenarios for the regulation of alkalinity pumping.

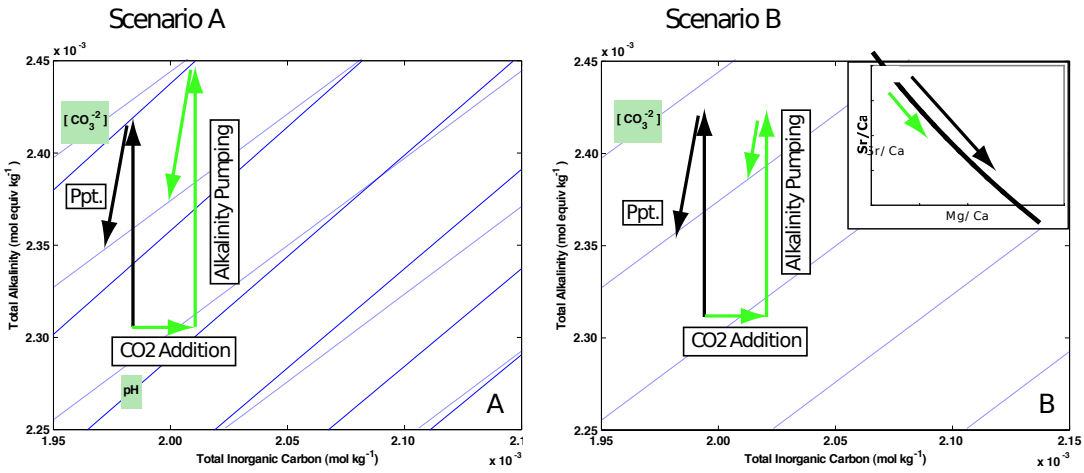

Figure 4.1: Plots of the biomineralizing carbonate system for different scenarios of alkalinity pumping exhibit different predictions of growth and compositional response to ocean acidification as discussed in the text. Dark contours are lines of constant pH and lighter contours are nearly parallel lines of constant carbonate ion concentration. Chemical processes during biomineralization are shown as arrows. Green arrows correspond to the case where carbon dioxide enrichment has occurred. Precipitation (Ppt.) is an arrow that relaxes the system at a slope of 2 back to a contour of carbonate ion concentration in equilibrium with the solid. This vector has a slope of 2 because precipitation of calcium carbonate removes 2 mole equivalents of alkalinity for each mole of dissolved inorganic carbon (DIC). Inset plot is the predicted relationship between Sr/Ca and Mg/Ca for a closed system (Rayleigh) process. The black and green arrows on this plot, corresponding to the normal and acidified case in scenario B, show how different extents of precipitation result in different bulk Me/Ca ratios. While the contour plots were generated using a quantitative treatment of the carbonate system, the exact concentrations are less important in this conceptual model than the trends.

Scenario A:"pH Control". Alkalinity pumping proceeds until a specific-pH is reached. This is biologically appealing in that some control mechanism would be expected to regulate the extent of alkalinity pumping. However, at least in the simple form presented here, this rule for alkalinity pumping is inconsistent with observations of slower coral growth rates in response to CO_2 enrichment (Figure 4.1 A). After CO2 enrichment, this scenario demands that the alkalinity pumping vector increase in vertical length to reach the pH threshold. The size of precipitation vector, however, is

nearly the same length as in the unacidified case since this vector relaxes between two nearly parallel contours, the threshold pH and the equilibrium $[CO_3^{2-}]$. In fact, to the limited extent that contours of pH and [CO32-] are not parallel, the amount of precipitation is predicted to actually increase with ocean acidification. If the number of precipitating events is the major control of calcification rate instead of the extent of precipitation for each event, then the "pH Control" is still consistent with CO_2 enrichment experiments.

Scenario B: Invariant Alkalinity Pumping or "Energy Limited Calcification". This scenario assumes the amount of alkalinity pumping per precipitating event is constant. The same alkalinity pumping vector yields a lower [CO32-] and a smaller precipitation vector for CO2 enrichment consistent with coral culture experiments (Figure 4.1 B). Within the Rayleigh framework, the CO2 enriched case would proceed a shorter distance along the Rayleigh curve resulting in higher bulk Sr/Ca and lower bulk Mg/Ca, a measurable prediction (Figure 4.1 inset plot). The response of other Me/Ca ratios can be predicted for a Rayleigh process based on their partition coefficients, with Ba/Ca behaving like Sr/Ca.

Scenario C: Total Consumption of Dissolved Inorganic Carbon. Me/Ca measurements in a modern deep-sea coral suggest that closed system precipitation proceeds roughly until the complete consumption of DIC (Chapter 3). Since CO2 enrichment increases DIC, complete utilization of the enriched DIC would result in relatively more extensive precipitation and longer travel down the Rayleigh curve. This scenario predicts lower bulk Sr/Ca and higher bulk Mg/Ca, the opposite signal from Scenario B.

These scenarios are hardly an exhaustive list and the qualitative predictions rely on a simple step-by-step model. The utility of the approach is to show the strong potential for bulk metal/calcium ratios to be sensitive to CO_2 enrichment experiments and to demonstrate how this signal can be related to the underlying biomineralization mechanism.

4.2 Experimental Approach

Coral are grown in separate flow-thorough culture chambers. This approach allows uninterupted growth, and eliminates gas exchange with the atmosphere, which would lead to re-equilibration of the carbonate system. In this experiment, carbonate ion concentration and associated aragonite saturation (Ω) are manipulated by changing alkalinity. Schneider et al. showed that coral calcification rates respond similarly to $[CO_3^{2-}]$ irrespective of the method used to manipulate the carbonate system in the surface coral *Acropora*. Continuously replacing the culture solution limits drift in the carbonate system and ensures healthy specimens, as corals require adequate water movement and regular water replacement to happily calcify (Calfo (2007) describes several different approaches to large scale coral propagation). By analyzing the outflow from the culture chamber, the solution chemistry of each chamber is regularly monitored. Furthermore, calcification removes alkalinity, and the drop in alkalinity between the reservoir and outflow water is be used to monitor calcification rate.

Newly grown material is characterized using complementary techniques that collectively span from macro to sub-micron scales. Figure 4.2 provides an overview of skeletal morphology at different spatial scales. Calcein is a CaCO3 binding fluorescent probe that has been used previously to mark growth in foraminifera at the chamber level (Bernhard et al., 2004), its application to coral has also been thoroughly investigated by Erez (unpublished research). In this work a short incubation with Calcein at the beginning of the experiment is used to mark the margin of new growth. Rare Earth Elements (REEs) were also added at different time points during the experiment as time markers to aid in translating linear growth into time, following the approach of Gabitov et al. (2008) in inorganic precipitation experiments, although measuring REEs in the coral skeleton was only partially successful.

To uniquely label the newly grown skeleton, the seawater culture media is enriched in the naturally low abundance stable isotopes 43Ca, 87Sr, and 136Ba. Figure 4.3 describes the labeling schedule for this experiment. After coral culture, bulk micro-samples of different parts of each coral skeleton are separately dissolved and analyzed by MC-ICP-MS to identify regions of signifi-

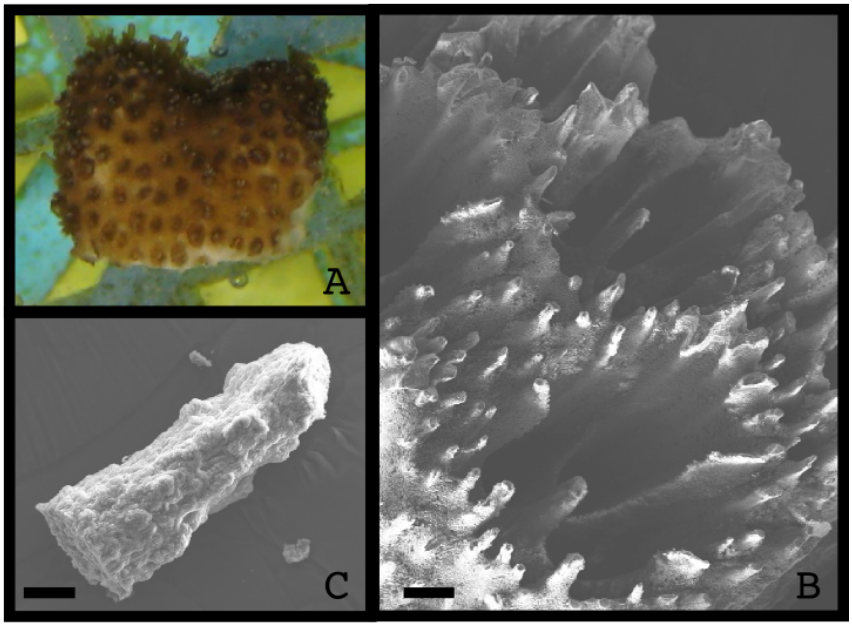

Figure 4.2: *Stylophora sp.* Skeletal Morphology. **(A)** Small living tip broken from an coral used in a separate experiment ($\sim$ 1 cm across). Polyps are the basic individual living units of a colonial coral. Each polyp, seen as dark spots in this image, sits in a cup like skeletal feature, the calyx. While most polyps in this image are retracted, some in the top left corner are open and extended. Much of coral color comes for the photopigments of symbiotic algae that live within the coral host. **(B)** SEM image of the surface of a *Stylophora sp.* skeleton, after the tissue has been completely removed. Cup like depressions are the calyx of each polyp, with vertical plates, or septa, anchoring and protecting the polyp. In the spaces between polyps are many spine like projections. Scale bar is 200μm. **(C)** SEM image of an individual spine removed from the skeletal surface. Scale bar is 20μm.

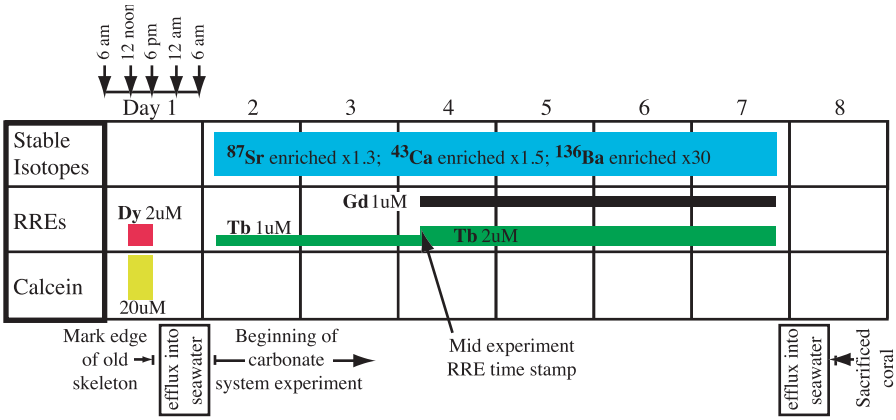

Figure 4.3: Schedule of isotope, rare-earth element (REE) and Calcein labels during coral growth experiment.

cant growth, testing, for example whether septa or spines incorporate more of the enriched isotopes. Once candidate fractions are identified, these parts of the skeleton are removed and mounted on slides for Calcein visualization by confocal fluorescent microscopy. Guided by the Calcein marker, subsequent nanoSIMS analysis is used for final isotopic and compositional characterization of the newly grown material and the junction between previous and new growth.

The nanoSIMs is a relatively new instrument capable of sensitive compositional and isotopic analysis of polished samples with sub-micron spatial resolution. In addition to spot analysis, the nanoSIMS primary beam can be rastered to make isotope images of order 20x20 μm. Guided by fluorescent maps of newly grown material, the nanoSIMS in spot mode is used to characterize the composition of pure newly grown skeletal material for each culture condition. Images are also made of the junction between initial material and the newly grown skeleton to test if all elements are incorporated in the skeleton simultaneously or if there are differences in internal pools and transport for each element. To accurately conduct nanoSIMS spot and image analysis in coral, several methodological and technical challenges are addressed complementing recent work on nanoSIMS methods in carbonates (Sano et al., 2005, 2008).

4.3 Coral Culture Method

Coral Samples: Several nubins of the reef-forming (hermatypic) and symbiont-containing surface coral *Stylophora pistillata* were freshly broken from two larger colonies originally collected in the Gulf of Eilat, Red Sea, Israel. The finger-like nubbins are small pieces of coral (approximately 1–2 cm in length with 1–3 branches each) covered by living tissue on all surfaces except the freshly broken bottom of the coral. These nubbins were acclimated in the seawater aquarium at Hebrew University, Jerusalem for 10 days prior to the growth experiment. Since all nubbins were taken from the same original colony, they should be genetically identical. Of the cut and recovered nubbins, 5 were chosen of similar size and surface area for culture under controlled carbonate ion conditions (Table 4.1). Surface area was estimated assuming a cylindrical geometry ignoring the top and bottom of the cylinder, a common approach in growth studies on branching and pencil shaped coral (Falkowski & Dubinsky, 1981; Schneider & Erez, 2006). The length and width of each branch were either measured directly using the cleaned and dried skeleton or estimated from photographs taken at the end of the experiment. Two additional similarly sized nubbins, corals number 10 and 4, were sacrificed at the beginning of culture experiment right when the other coral were placed in their respective growth chambers but after all the nubbins were incubated with Calcein. These $t = 0$ controls are used to estimate the average initial chemical and isotopic composition of coral nubbins just prior to the growth experiment. They are also used in fluorescent label imaging as a control expected to show the Calcien label without any subsequent growth.

Table 4.1: Surface area and mass of cultured *Stylophora pistillata* nubbins used in this study. Determination of aragonite saturation (Ω) for each culture chamber is discussed below. ‡Coral number 5, cultured in reservoir # 2, was sampled prior to taking a dry mass. A regression between the remaining wet and dry masses show a rough linear correlation ($R^2 = 0.7$). This correlation was used to estimate the unsampled dry mass of coral number 5.

Ω	Reservoir #	Coral #	Surface Area (cm^{-2})	Dry Mass (g)	Wet Mass (g)
4.9	1	9	7.0	1.6	2.8
4.0	4	3	6.0	1.7	3.3
3.4	2	5	6.9	$(2.0)^{\ddagger}$	3.7
2.9	10(3)	7	7.4	2.3	4.3
2.7	9(5)	6	7.3	2.0	3.2

Calcein and Dysprosium Label at Start of Experiment: Immediately prior to culture under controlled carbonate ion conditions, all coral nubbins were labeled with the rare-earth element (REE) dysprosium and the $CaCO_3$ binding fluorescent probe Calcein to mark the begining of the experiment. To a large crystallizing dish containing 750 ml aquarium seawater, 250 uL of stock 1000 μg/ml Dy in 2% HCl was added. Then the solution pH was adjusted to 8.25, similar to typical Red Sea surface pH, by adding 6 mL of saturated $Ca(OH)_2$ solution. Finally 1.5 ml of 10 mM Calcein was added, yielding final concentrations of [Dy] $\sim$ 2 uM and [Calcein] $\sim$ 20 uM. After about 6 hrs of daytime incubation (noon to 6 PM) in the stirred solution at T= 25 ± 1°C, the corals were rinsed in 3 large volumes of aquarium seawater and allowed to efflux into an $\sim$ 2 L volume of stirred seawater overnight with one mid-efflux water change at 2 AM with aquarium water. By allowing Calcein and Dy to efflux from any internal reservoirs overnight, we limit the possibility of contaminating subsequent culture solutions with the pre-experiment marker.

Flow Through Culture Apparatus: After the Calcein/Dy incubation and subsequent efflux, each piece of coral was placed in a different plastic 215 ml flow-through culture chamber. A peristaltic pump was used to separately feed isotopically enriched seawater of controlled chemistry from airtight and dispensable gas sampling bags through 0.19 mm ID tygon tubes (Cole-Parmer) into each magnetically stirred culture chamber. There was no headspace in the o-ring sealed and presumably airtight culture chambers. Flow rates ranged from 4 to 9 g/hr, for about one full exchange of seawater per day. Outflow for each chamber was separately collected for regular analysis of the carbonate system, metal/calcium ratios, and isotope ratios. The chambers were immersed in a temperature controlled bath maintained at 25 ± 0.3°C. The coral, inside clear chambers, were exposed to a regular 12-hr diurnal cycle with the light cycle starting at 6:30 AM and ending at 6:30 PM, except on the last day, when the start of the day was delayed until 8:50am and "nightfall" then extended until 9pm to ensure the full 12hrs of growth under light conditions. No food was added to the culture water during the experiment. The total duration of coral culture in spiked solution was 133 hours, or about 5.5 days.

Culture Solution Preparation and Composition: Culture solutions were prepared in general as

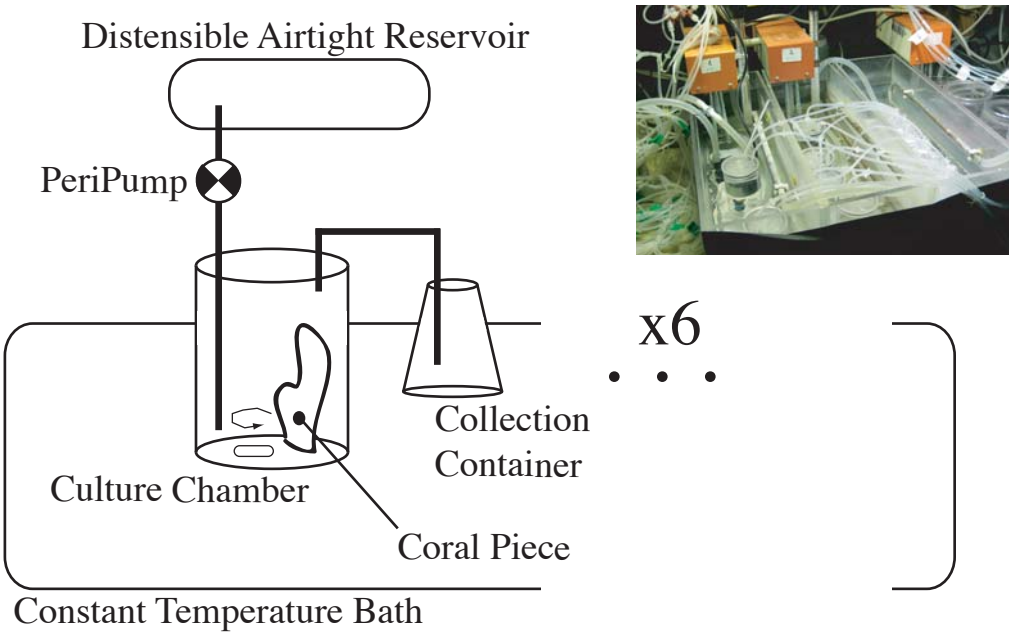

Figure 4.4: Flow through culture apparatus. Five coral were grown in separate airtight and headspace free culture chambers in well mixed, isotopically enriched, and rare-earth element (REE) labeled seawater over a range of carbonate ion concentrations. One additional coral was grown without isotope or REE enrichment under ambient carbonate ion conditions as a control.

follows: a single batch of Gulf of Eilat seawater was spiked with enriched isotopes and terbium. Portions of this well-mixed master solution were then adjusted to different pHs by manipulating alkalinity before being loaded into the airtight reservoir bags. In greater detail, several mg each of $CaCO_3$, $SrCO_3$, and $BaCO_3$ from enriched in ^{43}Ca, ^{87}Sr, and ^{136}Ba , respectively, were separately and gently dissolved in excess HCl. Table 4.2 lists isotope abundances of the individual carbonate solids as reported by Oak Ridge. These dissolved isotope spikes were added to a large carboy containing 10.50 kg of Gulf of Eialt seawater (salinity = 42 ppt). An additional 1.6 mL of stock 1000 ug/ml Tb solution in 2% HCl was also added, making the carboy pH $\sim$ 7.8 and [Tb] $\sim$ 0.96 μM. All stock REE solutions used in this study were purchased from High Purity Standards. Portions of the well-mixed spiked seawater were used to nearly fill small-mouthed 2 L bottles. The pH of each bottle was quickly adjusted with 0.1 M NaOH and gently mixed. The solution was then immediately placed in a collapsed plastic 3 L gas sampling bag by peripump without introducing air bubbles. This process was repeated with each culture solution, minimizing the time between

pH adjustment and loading the reservoir to limit atmospheric exchange. The reservoir bags are especially well adapted for this particular experiment and featured a stopcock to allow removal of solution as well as an airtight septa for introducing solutions, all the while maintaining an air free environment. Sub-samples of each reservoir bag were taken for alkalinity. Culture chambers were then attached to each bag by Tygon tubing and the chambers were half-filled by peri-pump, coral were placed inside, and then the chambers were sealed and filled completely. During the culture

Table 4.2: Oak Ridge spike abundances

$CaCO_3$ Spike Batch: 219501	%	$SrCO_3$ Spike Batch: 136990	%	$BaCO_3$ Spike Batch: 116491	%
^{40}Ca	12.46	^{84}Sr	0.01	^{130}Ba	0
^{42}Ca	0.55	^{86}Sr	0.82	^{132}Ba	0
^{43}Ca	83.58	^{87}Sr	91.26	^{134}Ba	0.08
^{44}Ca	3.35	^{88}Sr	7.91	^{135}Ba	1.03
^{46}Ca	0			^{136}Ba	92.83
^{48}Ca	0.06			^{137}Ba	1.77
				^{138}Ba	4.28

experiment, seawater output from each flow-through culture chamber was allowed to accumulate in separate parafilm covered small mouth plastic jars. To limit atmospheric exchange, the contents of these jars were typically emptied twice daily, with one sample integrating daytime conditions, while the other integrated the entire dark cycle. After weighing, the outflow was separated into subsamples for analysis of the carbonate system, isotope ratios, and metal/calcium ratios. Samples for chemical and isotopic analysis were stored in plastic 1.2 ml screw-top plastic micro-centrifuge vials that were acid leached, rinsed with Q-water several times, and dried in a trace-metal clean flow bench prior to the experiment. While attempts were made to limit atmospheric exchange during outflow collection, it is important to note that any such exchange does not affect alkalinity and alkalinity-based calcification rates.

Nearly half-way through the experiment (at 49 hours), the culture flow was stopped and the REEs Tb and Gd were injected into each reservoir and each culture chamber. This addition roughly doubles the Tb concentration and introduced Gd for the first time, such that [Tb] $\sim$ 2 μM and [Gd] $\sim$ 2 μM in the growth solution. Since the REEs are dissolved in dilute HCl, the alkalinity

of each reservoir and culture chamber were approximately back-titrated with NaOH. Samples for dissolved inorganic carbon (DIC), alkalinity, and pH were taken of each bag after gentle mixing. The reservoirs were then reattached to each sample chamber and flow re-started, with a 30 min period of high flow to help wash out any minor differences in reservoir and chamber composition. At the end of the experiment, a final set of sub-samples were taken from each reservoir.

Carbonate System Measurements: The pH of carbonate system sub-samples was measured immediately in a stirred, closed, and temperature-controlled chamber held at 25°C, the same temperature as the culture experiment. Analysis was conducted with a Radiometer PHM84 pH meter connected to a combination glass electrode. The electrode was standardized daily using NBS buffers and then equilibrated with seawater for at least 30 minutes prior to each round of analysis.

Samples for total dissolved inorganic carbon (DIC) were placed in dark glass bottles with negligible headspace (each bottle contains 66 ml when filled to the top), poisoned with $\sim$ 660 μl of saturated $HgCl_2$, and stored for 18 months. DIC was measured using a CO_2 coulometer (UIC, Inc.) following the method outlined in DOE (1994), standardized to the average value of regularly spaced measurements on Andrew Dickson's (Scripps Institute of Oceanography) seawater reference material, batch #79. The samples were analyzed in in random order during two sessions that were separated by one day. Samples were not opened until just before analysis. Replicate measurements were conducted within a few hours of the first analysis, except for a subset of samples which were saved for cross calibration between the two analytical sessions, these were gently sampled and re-capped with headspace between measurements. The reproducibility of Dickson's standard in the second session was $\pm$9 μmol/Kg or 0.4% relative error (2σ std. dev of 15 standards). This is an improvement over the 3% relative error of the first session (n=17), a result of cleaning and reassembling the gas stripper. Cross calibration samples measured during both sessions also agree within 3%. To assess accuracy, a number of additional factors must also be considered. Salinity differs between the sample and standard, this minor correction to the calibration curve accuracy is not explicitly made, as multiple mass measurements of both sample solutions and the Dickson standard dispensed using the same gas tight syringe are within 0.7% (2σ std dev., average = 1.773 g). A correction for mer-

curic chloride dilution is also ignored. In the limiting case of completely CO_2-free mercuric chloride, this correction would result in a $\sim 1\%$ upward adjustment to the DIC reported here. Given these uncertainties, measurements from the second, higher precision, session are reported as 1% accuracy, while the lower precision measurements are reported as 3% accuracy.

Alkalinity values represent the average of duplicates or triplicates by Gran titration (DOE, 1994). Alkalinity samples were stored in plastic syringes closed with a piece of tubing over the tip for typically hours and at times several days before alkalinity analysis.

Calculation of Carbonate System Speciation: From any two of the carbonate system parameters pH, ALK, DIC, CO_2 fugacity (fCO_2), or $\left[CO_3^{2-}\right]$, the rest can be calculated. The two parameters measured in this experiment are either ALK and DIC or ALK and pH. There are several pH scales for seawater, with different effective equilibrium constants for each scale. It is important to be clear and consistent in choosing a pH scale, as measurements made on one scale and interpreted in another can yield very different results, on the order of 0.1 pHs units (Zeebe & Wolf-Gladrow, 2001). In order to understand the choice of pH scale and accurately calculate carbonate system parameters it is helpful to consider what is physically measured during a pH experiment and the framework used to interpret these results.

The pH of an unknown solution X is is operationally defined by reference to a buffer using a modification of the Nernst equation:

$$pH(X) = pH(B) + \frac{(E_B - E_X + \Delta E_J)\, F}{RT\ ln10}\ ,$$

where E_X and E_B are the electrode potentials developed by the sample and buffer, receptively, ΔE_J is the difference in junction potential for the electrode in the sample compared to the electrode in the buffer ($E_{JX} - E_{JB}$), F is the Faraday constant, R the gas constant, and T the temperature (Bates, 1973). Interpreting pH depends on associating a measurable pH to a chemically relevant quantity. On the NBS scale this means assigning a particular hydrogen ion activity (a_H) to a pH value. NBS buffers are assigned pH values corresponding to theoretical values of a_H based on two

key assumptions: (1) at the limit of dilute HCl solutions, [H] = amount of added HCL; (2) the hydrogen ion activity coefficient (γ_{Cl}) can be accurately estimated from the Debye-Hückel equation to calculate a_H from combined activity coefficients. These assumptions are used to calibrate the potential of a junctionless electrochemical cell which is then itself used to make measurements in primary NBS buffers—associating pH and a_H (Bates, 1973).

High ionic strength solutions like seawater defy both assumptions: (1) activity coefficients diverge from Debye-Hückel; (2) the "free" hydrogen ion concentration in solution is not directly equal to the amount of added strong acid because of competing acid base equilibria present in natural waters. The equilibrium constants of most these other acid-base reactions are well known and can be incorporated into a definition of alkalinity, allowing a calculation of "free" hydrogen ion. (Free hydrogen ion or free proton refer to all rapidly equilibrating species of water solvated protons—the species that interact with a pH electrode and participate in chemical reactions; but free proton does not include weak acids containing non-water components, like HF). Unfortunately, not every relevant acid-base reaction can be incorporated into an alkalinity expression because the equilibrium constants of the following weak bases, written here as dissociation reactions ($\beta = 1/K_a$), are hard to measure in seawater:

$$\mathrm{H^+ + SO_4^{2-} \overset{\beta_{SO4}}{\rightleftarrows} HSO_4^-}$$

$$\mathrm{H^+ + F^- \overset{\beta_F}{\rightleftarrows} HF}\ .$$

High ionic strength pH scales are defined to accommodate these complications (Dickson, 1984). By including $\mathrm{HSO_4^-}$ and HF in the proton definition, these problematic species and the associated dissociation constants are eliminated from both routine carbonate system calculations and the titrations used to establish equilibrium constants. Furthermore, by putting concentrations in moles (kg solution)$^{-1}$ rather than proton activity, it is no longer necessary to attempt to calculate activity coefficients at high ionic strength. Equilibrium constants determined within this framework are therefore effective constants, dependent on bulk composition, salinity, and, of course,

temperature and pressure. Seawater carbonate calculations rely on fitted and interpolated effective equilibrium constants from measurements in synthetic and natural seawater solutions over a wide range of salinities, temperatures, and pressures. We use the seawater scale advocated by Millero:

$$\left[\mathrm{H^+}\right]_{\mathrm{SWS}} = \left[\mathrm{H^+}\right]_{\mathrm{Free}} + \left[\mathrm{HSO_4^-}\right] + [\mathrm{HF}] \; .$$

Equilibrium constants on this scale are complied in Millero (1995) with concentrations in mol (kg solution)$^{-1}$. There are several choices of carbonic acid dissociation constants; we use the results of Mehrbach et al. (1973) as reformulated by Dickson & Millero (1987). This choice of K_1 and K_2 show the best internal consistency between over-determined carbonate system measurements in seawater from global field studies (Lee et al., 2000; Lamb et al., 2002). We include hydroxide ion and boron in the alkalinity definition. Total boron concentration is assumed to vary linearly as a function of salinity, with $B_T = 499$ μmol kg^{-1} at 42 ppt.

To calculate $\left[\mathrm{CO_3^{2-}}\right]$ from pH and ALK, $\mathrm{pH_{NBS}}$ measurements are first converted to a "free" proton concentration $[\mathrm{H^+}]_{Free}$ in mol kg^{-1}:

$$10^{-\mathrm{pH}_{NBS}} = f_H \left[\mathrm{H^+}\right]_{Free} \; .$$

The term f_H is an effective ion activity coefficient, dependent on temperature, ionic strength, and solution composition. We use a value of $f_H = 0.7$ for natural seawater at 25°C and 42 ppt salinity (Mehrbach et al., 1973). Then the total hydrogen ion concentration is calculated from the free hydrogen ion concentration using values of β_{SO4} and β_F from Dickson (1990) and Dickson & Riley (1979), respectively—both are, of course, on the free pH scale. Total sulfate and total fluorine are also assumed to vary linearly with salinity, with $\left[\mathrm{SO_4^{2-}}\right]_T = 33.89$ *mmol kg*$^{-1}$ and $[\mathrm{F}]_T = 84$ μ*mol kg*$^{-1}$ at 42 psu.

For high ionic strength seawater measurements referenced to low ionic strength NBS buffer, differences in the junction potential can also affect the accuracy of the pH measurement. By equilibrating the electrode with seawater for $>$ 30 minutes before each analysis, we reduce drift in ΔE_J during

measurements, but must acknowledge an unknown constant accuracy offset in measured pH. The junction potential only affects $\left[CO_3^{2-}\right]$ calculated from pH and ALK. For the 26 culture time points where ALK, DIC, and pH were all measured, resulting in an overdetermined carbonate system, the two methods are compared (Figure 4.5). By assuming a junction potential of +0.03 pH units most of the $\left[CO_3^{2-}\right]$ calculated from pH and ALK are forced onto the 1:1 line in agreement with values from ALK and DIC. The 0.03 pH unit "correction" is equivalent to 1.8 mV and is similar in magnitude to differences in junction potential, although this correction combines uncertainty in the accuracy of both f_H and ΔE_J, parameters which are indistinguishable in this experiment. This 0.03 pH unit correction is applied to all carbonate ion calculations based on pH and ALK. One way to minimize junction potentials is to use seawater buffers such that there is little difference in ionic strength between the buffer and the sample. pHs can also be directly calibrated to a high ionic strength pH scale using seawater buffers, eliminating uncertainty in the conversion from NBS pH. Despite clear advantages of using high ionic strength buffers, in this and other studies NBS buffers are regularly used due to availability. In assigning a carbonate ion concentration to a particular experimental condition, the average value of the junction potential corrected $\left[CO_3^{2-}\right]$ (pH, ALK) is used, using the full range of values to estimate uncertainty. Effectively we take advantage of the higher precision and more complete set of (pH, ALK) measurements and correct them for accuracy using the lower precision ALK, DIC measurements. All but 2 of the outliers in the figure that fall far from the 1:1 line correspond to the first set of subsamples made during the experiment. Although $HgCl_2$ was added to the first set of DIC bottles after a period of 3–4 hours, possibly contributing to the variability in DIC depending upon the balance of photosynthesis and respiration in the "unkilled" jars, another set of DIC samples where this late addition also occurred does not show the same variability. Since inclusion or exclusion of the points that fall off the 1:1 line in Figure 4.5 has no impact on the average Ω of each culture chamber, and little impact on the range, we retain all data for completeness.

Aragonite saturation (Ω) is the thermodynamic driving force for precipitation or dissolution in

a solution,

$$\Omega = \frac{\left[\mathrm{Ca}^{2+}\right]\left[\mathrm{CO_3}^{2-}\right]}{K_{sp}} \ .$$

We calculate Ω from the carbonate ion concentration, as described above, the aragonite solubility product of Mucci (1983), and make the assumption that calcium varies with salinity such that $\left[\mathrm{Ca}^{2+}\right] = 12.34$ mmol kg^{-1} at 42 psu. While Mucci (1983) determined K_{sp} from carbonate system calculations using pH_{NBS}, these calculations also used the NBS scale equilibrium constants of Mehrbach et al. (1973) and are therefore internally consistent. This K_{sp} value has been used for decades, but it is interesting to consider if a re-calculation to a modern pH scale based on the raw data in Mucci's thesis, much like Dickson & Millero (1987) undertook with Mehrbach et al. (1973), would result in any relevant difference to how the ocean carbon system is modeled?

Dickson's "Total pH Scale",

$$\left[\mathrm{H}^{+}\right]_{\mathrm{T}} = \left[\mathrm{H}^{+}\right]_{\mathrm{Free}} + \left[\mathrm{HSO_4}^{-}\right] \ ,$$

is equally suitable for carbonate system calculations, as long as the associated equilibrium constants are also used. To test if the choice of pH scale and equilibrium constants significantly bias the carbonate system calculations in this study, all results were re-calculated on the total pH scale using the carbonic acid dissociation constants of Lueker et al. (2000), an updated re-formulation of Mehrbach et al. (1973) for the total pH scale; the ancillary constants in DOE (1994); and including a $-[\mathrm{HF}]$ term in the alkalinity expression. Carbonate ion concentrations and aragonite saturations differed by less than 0.6% between the two methods, well below the analytical accuracy, so choice of pH scale and equilibrium constants does not significantly bias our carbonate system calculations.

Re-calculation of data from other ocean acidification experiments led to somewhat different carbonate system parameters. Following the approach of Lee et al. (2000) and Lamb et al. (2002), real seawater carbonate system data complied in the literature were used to test the accuracy of the chosen equilibrium constants and the validity of the custom Matlab equilibrium solving numerics I wrote for this study. The test was conducted using seawater bottle data from GLODAP cruise 18S,

where ALK, DIC, pH, and fCO_2 were all measured (see Sabine et al. (2005) for an overview of the GLODAP project and how to access data). Either (DIC,ALK) or (Alk,pH) were used to calculate the remaining parameters, then calculated fCO_2, pH, or DIC were compared to measured values. The calculated results differed from measured parameters by less than 0.02 pH units, and by less than 2% for fCO_2 and DIC at 20 randomly picked stations and depths spanning a wide range of DIC and ALK, suggesting carbonate system calculations in this study are accurate for real seawater samples like bottle data and the culture media.

Coral Skeletal Sampling: At the end of the growth experiment the coral nubbins and growth chamber were rinsed with 5 volumes of unspiked Gulf of Eilat Seawater. Then the chambers were filled with unspiked Gulf of Eilat seawater and the coral were allowed to effflux for about 14 hrs with two subsamples of the solution for isotope analysis taken at approximately 3 hours and at 12 hours of elapsed effluxing. The coral were then cleaned using an airbrush to remove tissue. After rinsing in distilled water, the samples were dried in an oven at 50°C and stored for several months, with a portion of each coral left at Hebrew University, Jerusalem. Later at Caltech, at least one branch of each coral was cleaned in dilute sodium hypochlorite to remove any traces of tissue, proceeded and followed by several rinses in trace-metal clean water. The cleaned skeletons were then sampled for two different types of experiments: (1) Bulk micro-sampling, followed by dissolution and MC-ICP-MS analysis; and (2) Spine removal, mounting, and nanoSIMS analysis.

During micro-sampling a scalpel was used to remove different types of skeletal material. The different samples were: Spines, Gentle Scrape, Septa, Deep Scrape. First spines and other small fragile features on the exterior surface of the coral skeleton were gently removed by running the sharp blade of a steel scalpel across a small region of coral. This process was monitored using a 10-to-100x binocular microscope until between 90 μg to 1 mg of material was collected. A new sample was then collected by gentle scraping with the scalpel in the same location. Next the sharp point of the scalpel was used to remove septa from within several calyx. The final step was a vigorous scraping with the scalpel to remove a layer from the exterior surface and the interior base of the calyx. The samples were weighed, dissolved in an excess of dilute trace metal clean nitric acid, and analyzed by

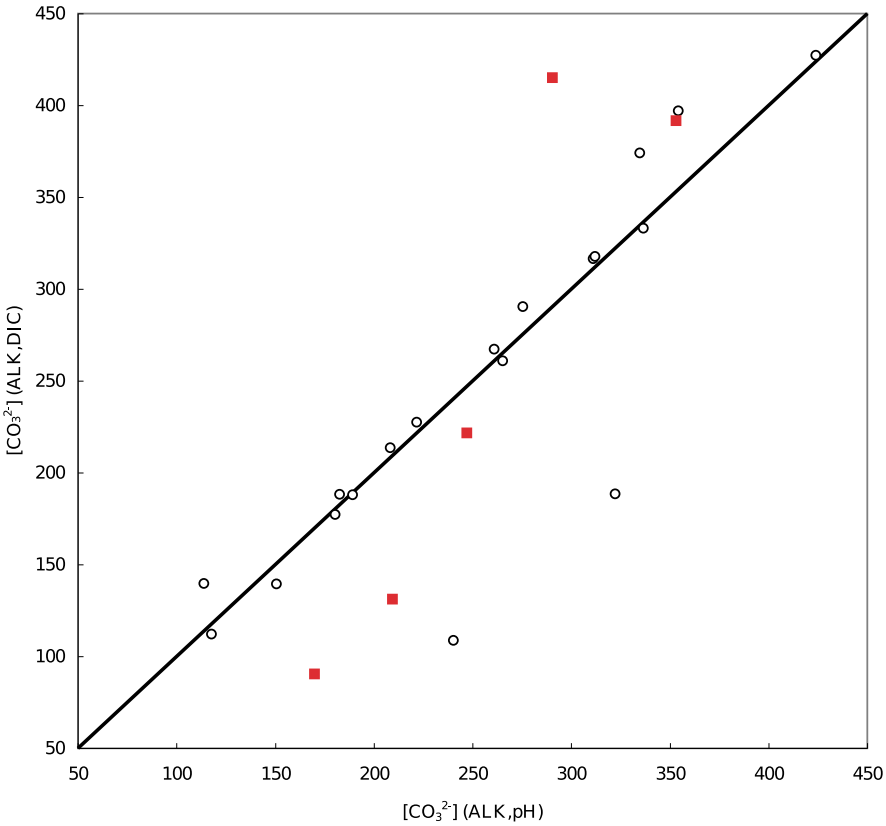

Figure 4.5: Carbonate ion concentration of culture solutions determined using pH and alkalinity compared to using DIC and alkalinity. (○) Each data point represents a different coral culture solution sub-sample where pH, ALK, and DIC were all measured, overdetermining the carbonate system. If the measurements are accurate and the equilibrium constants are internally consistent, then data should fall on the 1:1 line (marked in black). All equilibrium calculations are on the seawater scale at T=25C and 42 ppt Sal, as described in the text. An effective activity coefficient f_H of 0.7 is used to covert from a_H measured on the $\mathrm{pH_{NBS}}$ scale to "free" H ion concentration (Mehrbach et al., 1973). Dissociation constants for bisulfate ion and HF are used to calculate hydrogen ion concentration on the seawater scale from free H ion concentration. Using these assumptions most the data are correlated, but with a non-zero intercept. A hypothetical junction potential of 0.03 pH units makes the pH,Alk data correspond to the Alk,DIC, with most data falling on the 1:1 reference line drawn through 0. (■) Data from the first set of solution measurements which depart from the 1:1 line more than other data, containing most but not all outliers. $HgCl_2$ was added late to the first set of DIC bottles, after a period of 3–4 hours, possibly contributing to the variability in DIC depending upon the balance of photosynthesis and respiration in the "unkilled", but darkened jars, however, another set of DIC samples where this occured does not show the same variability. All data is included in culture chamber analysis, as these outliers have no effect on the average $[CO_3^{2-}]$ or Ω of each culture chamber.

MC-ICP-MS.

After micro-sampling identified the "Spines" fraction as containing a high portion of new growth, a fresh region of each coral was re-sampled for this fraction. The region sampled included a portion of the the top, or apical tip, of the coral. Following removal, the spines were then mounted in a "grain mount" for subsequent fluorescent microscopy and nanoSIMS analysis. To make the grain mount, several spines, each approximately 100 μm long, were picked up from an otherwise clean glass slide on a thin wire coated by warm Araldite resin. These spines were then placed in an $\sim$ 1 mm diameter drop of resin on a 1" glass slide, repeating the process until more than 20 spines were in the drop on the 1" round. Spines from each coral were placed in different well separated drops on the same 1" round. Cross contamination is extremely unlikely as the entire process was monitored using a microscope and spines stuck to the transfer-wire to the point of being difficult to place in the desired location. The mount was cured at 70°C overnight before a fresh layer of resin was used to fill in the spaces between each resin drop, yielding an easy to polish continuous coat of Araldite. The cured grain mount was carefully hand polished in a plane parallel to the slide surface using a range of diamond pastes in organic binder until longitudinal sections of many of the spines had been exposed. Two 1" round grain mounts were made on different days, AA and AB. The first grain mount, AA, underwent a final short vibration polish using 30 nm colloidal silica between fluorescent microscopy and nanoSIMS analysis, which may have resulted in a slight loss of surface material and a minor shift in spatial registration between the two techniques. The second mount, AB, was only polished by hand with no alteration between microscopy and nanoSIMS.

Fluorescence Microscopy: Calcein fluorescence (single photon excitation λ_{max}=494 nm; emission λ_{max}=517) was imaged using a Zeiss 510 Confocal Laser Scanning Microscope housed and maintained by the Biological Imaging Center, Beckman Institute, Caltech. Excitation was with an Ar laser at 488 nm. Fluorescent emission was collected between 500–550 nm. Fluorescent and transmitted light images were taken simultaneously of each sample at a variety of magnifications using air objectives.

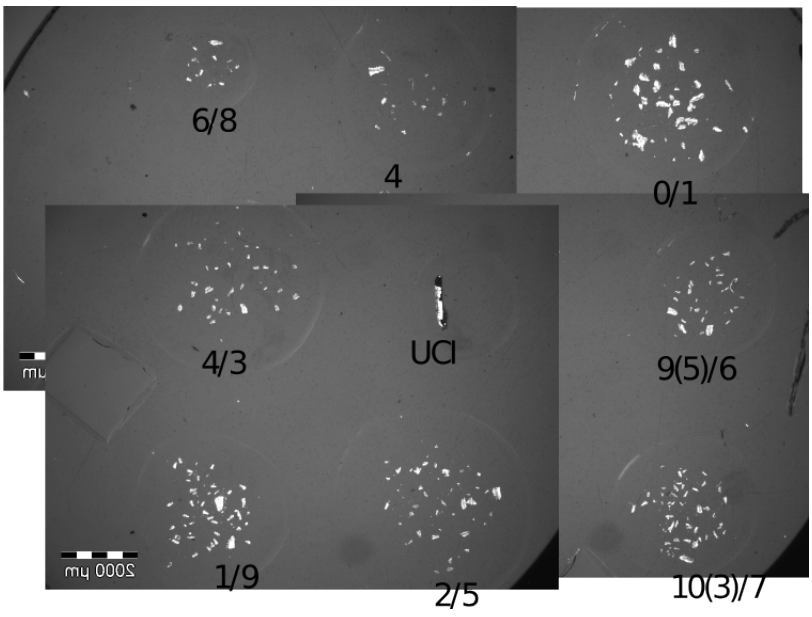

Figure 4.6: Spine grain mount AA with spines from different coral mounted in different locations labeled by chamber/coral number in this montage of microscope images. Chamber 6/8 is a non-isotope spiked control that grew for the same amount of time as other samples. Coral 4 was marked with calcein but then sacrificed at the beginning of the experiment. Coral 0/1 was a piece of natural coral with natural abundance isotope composition that was never calcein labeled. Image reflected left-to-right, to match orientation of nanoSIMS CCD mounted microscope. Black curved areas in lower right are from the edge of the iris on the CCD rather than a part of the sample mount.

4.4 Method of Isotope and Me/Ca analysis Using MC-ICP-MS

Coral Micro-Samples—Me/Ca, Calcium Isotope, and Strontium Isotope Ratios: Coral samples were weighed, dissolved in clean 5% nitric acid, and diluted to approximately $[Ca^{+2}] = 0.2$ mM. Solutions corresponding to initial ($t = 0$) unenriched controls were then analyzed for Sr/Ca and Mg/Ca as described in Chapter 2 using the older but self-consistent SGSk and spike calibrations reported in Fernandez et al. (in press), and assuming natural marine isotope abundances in the coral. Coral micro-samples from all stages of the experiment were measured for calcium and strontium isotopes using the same instrumental technique as the Me/Ca method, but without adding any isotope-dilution mixed spike. Isotope ratios were corrected for instrumental mass fractionation through regular measurement of SGSk. The external analytical uncertainty, measured as the average difference in isotope ratio when the same dissolved coral sample was measured during different analytical sessions and in different run order, was 1.1 permil for 43/48, 0.3 permil for 87/88, 0.6 permil for 44/48, and 0.4 permil for 86/88.

Seawater Calcium Isotope, Strontium Isotope, and Sr/Ca Ratios: Seawater solutions were diluted and run without column chromatography. For seawater solutions, where the sulfur/calcium ratio is almost 3:1, a $^{32}S^{16}O$ interference on ^{48}Ca was resolved optically using the high resolution mode. A filtered seawater sample was used to test the reproducibility and accuracy of isotope and Me/Ca measurements. The natural seawater standard is GEOTRACES Deep Homogenized Isotope Sample - 35 and was collected from 1200 m at the Bermuda Atlantic Time Series (BATS) station as part of the Geotraces Intercalibration Cruise. To test seawater calcium isotope ratio measurements and to ensure interferences had been optically resolved, seawater from BATS (n=18) was compared to unspiked deep-sea coral consistency standard (n=23) measured during the same session. The deep-sea coral consistency standard (DSC-CS) isotope ratios match natural marine values within 0.9 per mil. Furthermore, The 43/48 of BATS and DSC-CS agree to within 3 per mil, about twice the analytical uncertainty, but still a small uncertainty compared to the large spike enrichment > 10

percent. The 86/88 ratios of both dilute BATS seawater and DSC-CS are also the same within 0.4 per mill, which is just over the 0.3 per mil std. error of the measurements. These measurements, standardized to an SGS value of 0.1282, agree with the global 86/88 (Table 2.2).

Unlike the other ratios, 87/88 differs between BATS and DSC-CS by 6.4%. The 87/88 of DSC-CS is within error of the 87/88 value of other modern marine carbonates, suggesting the difference is specific to seawater. An unresolved and uncorrected 87Rb interference in the seawater samples could explain this difference, as seawater Rb/Sr is about 0.018. This interference is not an issue in the coral consistency standard since rubidium is incompatible in carbonates. Indeed the major isotope 85Rb has not been detected in DSC or other coral samples during other analytical sessions.

$$\frac{\langle 87\rangle}{\langle 88\rangle}_{BATS} = \frac{\langle {}^{87}\mathrm{Sr}\rangle + \langle {}^{87}\mathrm{Rb}\rangle}{\langle {}^{88}\mathrm{Sr}\rangle}_{BATS} = \frac{\langle {}^{87}\mathrm{Sr}\rangle}{\langle {}^{88}\mathrm{Sr}\rangle}_{BATS} + \frac{\langle {}^{87}\mathrm{Rb}\rangle}{\langle {}^{88}\mathrm{Sr}\rangle}_{BATS}.$$

To correct for this interference in seawater samples, we make a simplifying assumption that the intensity ratio $\langle {}^{87}\mathrm{Rb}\rangle/\langle {}^{88}\mathrm{Sr}\rangle$ is constant during analysis, based on the stable 87/88 ratio of BATS measurements throughout the analytical session. We make an additional safe assumption that the true 87Sr/88Sr isotope ratio of both DSC-CS and BATS are equal to each other, as strontium isotope fractionation between seawater and biogenic carbonates in cold-water coral is typically less than 0.2 per mil (Rüeggeberg et al., 2008),

$$\frac{\langle {}^{87}\mathrm{Rb}\rangle}{\langle {}^{88}\mathrm{Sr}\rangle}_{SeawaterSamples} \approx \frac{\langle 87\rangle}{\langle 88\rangle}_{BATS} - \frac{\langle 87\rangle}{\langle 88\rangle}_{DSC-CS}.$$

Then the difference between the measured 87/88 intensity ratios of BATS and DSC-CS can be used as a correction factor for unknown culture solutions,

$$\frac{\langle {}^{87}\mathrm{Sr}\rangle}{\langle {}^{88}\mathrm{Sr}\rangle}_{unknown} = \frac{\langle 87\rangle}{\langle 88\rangle}_{unknown} - \frac{\langle {}^{87}\mathrm{Rb}\rangle}{\langle {}^{88}\mathrm{Sr}\rangle}_{SeawaterSamples}.$$

The measured difference in $\langle {}^{87}\mathrm{Rb}\rangle/\langle {}^{88}\mathrm{Sr}\rangle$ between BATS and DSC-CS is 0.0054, very close to the rough estimate of 0.006 based on modern seawater 87Rb/88Sr and similar ionization efficiencies

between the two alkali-earths.

Calcium and strontium isotope ratios of each culture solution were assessed at 4 time points during the growth experiment for a total of 20 culture solution measurements. The average isotope ratios for the culture solution are listed in Table 4.3 and were similar between different growth chambers over the course of the experiment. The largest isotopic variability is for 43/48, where the 2σ std. dev. of the 20 samples is 5 per mil. This variability is correlated with 44/48 rather than 87/88, suggesting an instrumental mass fractionation based (analytical) mechanism rather than true culture solution variability. Isotope ratios are used to calculate culture solution isotope abundances assuming a 2-component mixture between the enriched spikes added to the culture media, as reported by Oak Ridge, and natural abundance seawater (Table 4.2; Tables 2.2 and 2.3). The calcium spike is assumed to be free of strontium, and vice-versa. The culture solution abundances are summarized in Table 4.4.

Table 4.3: Calcium and strontium isotope ratios of the spiked coral culture solution and natural seawater, taking into account the ^{87}Rb correction on 87/88. The accuracy of these measurements are limited by the ~ 1 per mil or better uncertainty in correcting for instrumental mass fractionation, which is larger than the standard error of culture measurements.

	Culture Solution	Natural Seawater
43/48	1.080 ± .006	0.7311
44/48	11.29 ± .04	11.27
87/88	0.1086 ± .0001	0.0848
86/88	0.1195 ± .0001	0.1194

Table 4.4: Culture solution calcium and strontium abundances calculated from measured 43/48 and 87/88 ratios assuming a 2-component mixture between natural abundance seawater and the Oak Ridge produced enriched spikes.

Calcium Isotopes	%	Strontium Isotopes	%
^{40}Ca	96.92	^{84}Sr	0.5452
^{42}Ca	0.6421	^{86}Sr	9.668
^{43}Ca	0.1970	^{87}Sr	8.797
^{44}Ca	2.058	^{88}Sr	80.99
^{46}Ca	.00312		
^{48}Ca	0.1824		

To determine the Sr/Ca of isotopically enriched seawater, the same samples measured for calcium

and strontium isotope ratios were re-measured after addition of the isotope-dilution mixed spike. The Sr/Ca of each sample was then calculated using the culture solution isotope abundances (Table 4.4), rather than natural abundances. The Sr/Ca of the culture solution is 8.736 $\pm$0.007 mmol/mol (2σ std. err. of the mean, n=20). Typical seawater Mg/Ca is $\sim$ 5:1, many orders of magnitude larger than the $\sim$ 2 mmol/mol found in typical coral, making Mg/Ca measurements in seawater using an ID-spike designed for coral unreasonable. Mg/Ca in the culture solution was therefore assumed to match global average seawater, 5.14 mol/mol.

Coral Barium Isotopes: Subsamples of the same dissolved coral solutions analyzed for calcium and strontium isotopes were diluted to $\sim$ 0.4 mM Ca ([Ba]$\sim$ 2 nM, (Shen & Boyle, 1988)). Barium isotopes were measured on Faraday cups using a dedicated method on the Neptune MC-ICP-MS. The ratio ^{136}Ba/^{138}Ba is used to trace new coral growth, since the culture media is enriched in ^{136}Ba and ^{138}Ba is the major natural abundance barium isotope (Table 4.5). ^{136}Ba was enriched to allow nanoSIMS analysis—at high masses the magnet on the nanoSIMS can only disperse ions differing by 2 or more mass units into separate detectors. In retrospect, the interference clean ^{135}Ba would have been a better choice to enrich in the culture media as isotopes of xenon, a trace contaminant in the argon plasma, interfere with ^{136}Ba and several other barium isotopes. Since xenon is in the plasma gas, subtracting blank intensities measured before every sample should remove most of the xenon contribution. However, xenon concentration and isotope composition in the plasma likely evolves over time as the argon dewar warms, changes pressure, and different fractions of the liquid argon vaporize. To explicitly correct for changes in minor xenon interferences, the isotopes ^{129}Xe and ^{131}Xe were monitored in a addition to the clean barium isotopes ^{135}Ba, ^{137}Ba, ^{138}Ba and the mixed-iostope masses: ^{134}Ba and ^{136}Ba.

After blanks are subtracted from all masses, ^{134}Ba and ^{136}Ba are further corrected for residual xenon isotope interferences using the residual ^{131}Xe intensity and assuming natural xenon isotope

Table 4.5: Natural barium isotope abundances are similar across terrestrial and even extraterrestrial samples, as measured in several studies (Eugster et al., 1969; Bacon & Edmond, 1972; Cahn et al., 1977) that all generally agree each other and with the original work by Nier (1938). The barium abundances listed here are directly from Eugster et al. (1969). Also included in this table is a list of xenon isotopes and abundances. Xenon is a trace contaminant in the Ar based plasma, resulting in isobaric interferences on barium peaks. **Bold** lines are masses measured in the barium isotope method.

Ba Isotopes	% Abundance	Xe isotopes	% Abundance
		^{124}Xe	0.10
		^{126}Xe	0.09
		^{128}Xe	1.9
		^{129}Xe	**26.4**
^{130}Ba	0.1058	^{130}Xe	3.9
		^{131}Xe	**21.2**
^{132}Ba	0.1012	^{132}Xe	27.0
^{134}Ba	**2.417**	**^{134}Xe**	**10.5**
^{135}Ba	**6.592**		
^{136}Ba	**7.853**	**^{136}Xe**	**8.9**
^{137}Ba	**11.232**		
^{138}Ba	**71.699**		

abundances,

$$\langle^{136}\mathrm{Ba}\rangle_{corr} = \langle^{136}\mathrm{Ba}\rangle_{mes} - \langle^{131}\mathrm{Xe}\rangle \left(\frac{^{136}\mathrm{Xe}}{^{131}\mathrm{Xe}}\right)_{nat}$$
$$\langle^{134}\mathrm{Ba}\rangle_{corr} = \langle^{1344}\mathrm{Ba}\rangle_{mes} - \langle^{131}\mathrm{Xe}\rangle \left(\frac{^{134}\mathrm{Xe}}{^{131}\mathrm{Xe}}\right)_{nat} .$$

To test the barium method, including corrections, and to standardize the barium isotope composition of SGSk, two natural barium-containing samples, deep-sea coral consistency standard and a witherite sample ($BaCO_3$, Caltech Mineral Collection ID# W20985) were repeatedly analyzed, bracketed by SGSk. Natural barium isotope abundances are similar across terrestrial and even extraterrestrial samples (Eugster et al., 1969; Bacon & Edmond, 1972; Cahn et al., 1977; Nier, 1938), so if the method and corrections are precise, barium isotope ratios of both natural samples should agree with little variability during the session. Figure 4.7 shows the effect of different corrections on barium isotope ratios measured in natural samples, and demonstrates that ^{136}Ba/^{138}Ba can be measured within 1%. The calibrated barium isotope ratios for SGSk are: $137/138 = 0.153 \pm 0.003$, $136/138 = 0.107 \pm .002$, $135/138 = 0.089 \pm 0.003$, $134/138 = 0.032 \pm 0.002$, with about a 3%

instrumental mass fractionation.

4.5 Method of NanoSIMS Analysis

General methodology common to all nanoSIMS analysis is described first, followed by details on spot and image analysis. Where data were collected under significantly different conditions, these differences are noted appropriately. For a description of the nanoSIMS50 instrument see Hillion et al. (1993).

Primary Beam Characteristics and Machine Tuning: When using an $^{16}O^{-}$ primary beam to measure positive metal ions on the nanoSIMS50, intensity and spot size are largely controlled by two apertures. The first, D0, masks the output of the Duoplasmatron oxygen source. This mask forms the image that is then focused on the sample. The second aperture, D1, corrects primary beam aberration, but also attenuates both the primary and secondary ion beams. For the same source brightness, smaller aperture settings correspond to smaller spot sizes and lower primary beam intensity. Beam characteristics typically change between separate analytical session (days to several days) as the source ages between regular cleaning, and are also a function of aperture size and ion optics settings. A Faraday cup, FCo, can be positioned in place of the sample and is used to regularly assess primary beam current. In this study primary beam intensity ranged from 15–3 pA between different analytical sessions and typically remained near constant within most analytical sessions. Beam energy is 8 KeV.

Although the nanoSIMS50 is capable of oxygen primary beam spot sizes < 100 nm, these probe sizes correspond to very low beam currents ($<<$ 2 pA). More intense spots, and therefore larger spots, are typically necessary to yield usable secondary ion currents for minor and trace elements like magnesium and barium in natural carbonates. Actual spot size for a particular analytical session, which can be very different than nominal specifications, is determined by making an ion image of a sharp compositional boundary in a calcium carbonate sample. A small beam will reproduce the abrupt compositional boundary, while larger beams tend to smooth this transition. Spot size, or the minimum resolvable feature using a particular primary beam, is operationally defined as

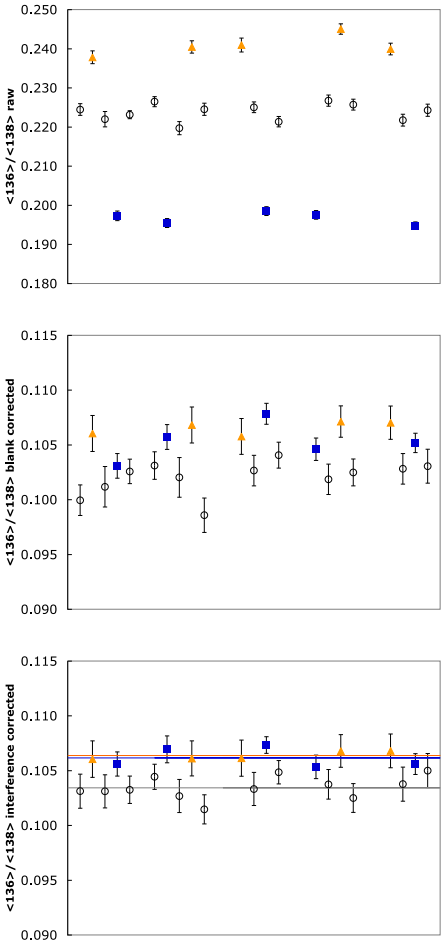

Figure 4.7: Barium isotope intensity ratios after successive corrections. Samples are (■) deep-sea coral consistency standard, (▲) witherite ($BaCO_3$) mineral from England, and (○) SGSk. Vertical error bars are 2σ internal error. Since there is very little natural barium isotope fractionation, both natural samples should have identical $^{136}Ba/^{138}Ba$ ratios when measured using a precise method that properly corrects for the isobaric interference of ^{136}Xe on ^{136}Ba. **TOP:** Raw intensity ratios of samples plotted by run order. Systematic differences in raw ratios likely result because the [Ba] of each standard is somewhat different while the the ^{136}Xe interfernce intensity is near constant. The 136/138 ratio of low [Ba] samples will be more impacted by the same $\langle^{136}Xe\rangle$, resulting in higher ratios. Presumably the order of barium concentrations in the analyzed solutions was DSC-CS > SGSk > witherite. **MIDDLE:** Blank corrected ratios with significant improvement to precision (notice smaller relative range of y-axis compared to top plot.) Since xenon is a trace constituent of the plasma it is present in both samples and acid blanks, thus background subtraction corrects for much of the interference. **BOTTOM:** Explicit interference corrected and background corrected 136/138 ratios show identical mean 136/138 for the natural samples within 2 permil (horizontal lines are the mean values of each type of sample). When this intensity ratio is set to the true natural ratio, correcting an $\sim 3\%$ instrumental mass fractionation, the true 136/138 of SGSk is $0.107 \pm .002$. Variability of the natural standards about their combined mean is used to estimate the precision of the method as $\sim 1\%$ (2σ rel. std. dev., n=10), much smaller than the several-fold enrichment of ^{136}Ba in the culture media. No correction was made for drift in instrumental mass fractionation which could improve precision.

the distance corresponding to 16%-to-84% of the total intensity change in the direction normal to the compositional boundary. The carbonatite standard OKA is known to be heterogeneous at a small scale (Gabitov et al., in preparation), which makes it useful to test primary beam size even if it complicates calibrations using this standard. Figure 4.8 shows a nanoSIMS ion image of a strontium and barium rich inclusion in OKA used to estimated probe size. In this study the smallest demonstrated beam size was $\sim$ 500 nm at 0.5 pA, while the smallest beam size with a *useful* beam current was $\sim$ 800 nm at 5 pA. Since D0 ablates with use, spot size increases over time. Recently a nominally 100 μm aperture widened to $\sim$ 280 μm over a two month period of use. Probe size as determined by compositional boundaries in ion images is typically much smaller than burn marks measured post analysis by SEM, optical microscopy, or using a profilometer (typically by a factor of at least 1.5). As an undamaged gold coat ensures charge dissipation and similar pre-sputter conditions, burn mark size ultimately limits the spacing between nearby spots. In this study new spot locations were typically located at least 1.5 *burn* diameters apart when measured center to center.

Detector Configuration: Secondary ions are collected simultaneously in seven individual secondary electron multiplier (SEM) or "ion counting" detectors, six of which are mounted on movable trolleys. Depending upon the experiment, different ions are collected in each SEM. Trolley configurations for the four spot analysis sessions in this study Ns1–Ns4 are diagramed in Figures 4.9–4.11. Occasionally it is necessary to collect more than seven ions or measure high mass ions separated by only one mass unit, under these circumstances the magnet field is cycled through two or more states in a "combined analysis". Through strategic trolley positioning many isotopes can be collected, although there is currently a software limitation that allows a maximum of eight isotopes to be collected during image analysis. Usually, if the magnet field is set so that $^{88}Sr^{+}$ or higher masses fall into the high mass SEM, then adjacent masses cannot be simultaneously measured because it would require the trolleys to collide, for example $^{42}Ca^{+}$ and $^{43}Ca^{+}$ or $^{87}Sr^{+}$ and $^{88}Sr^{+}$. (This is different than mass-resolving power discussed below, which refers to the ability to measure only one of several nearby or overlapping peaks with a single SEM). To measure nearby calcium and strontium

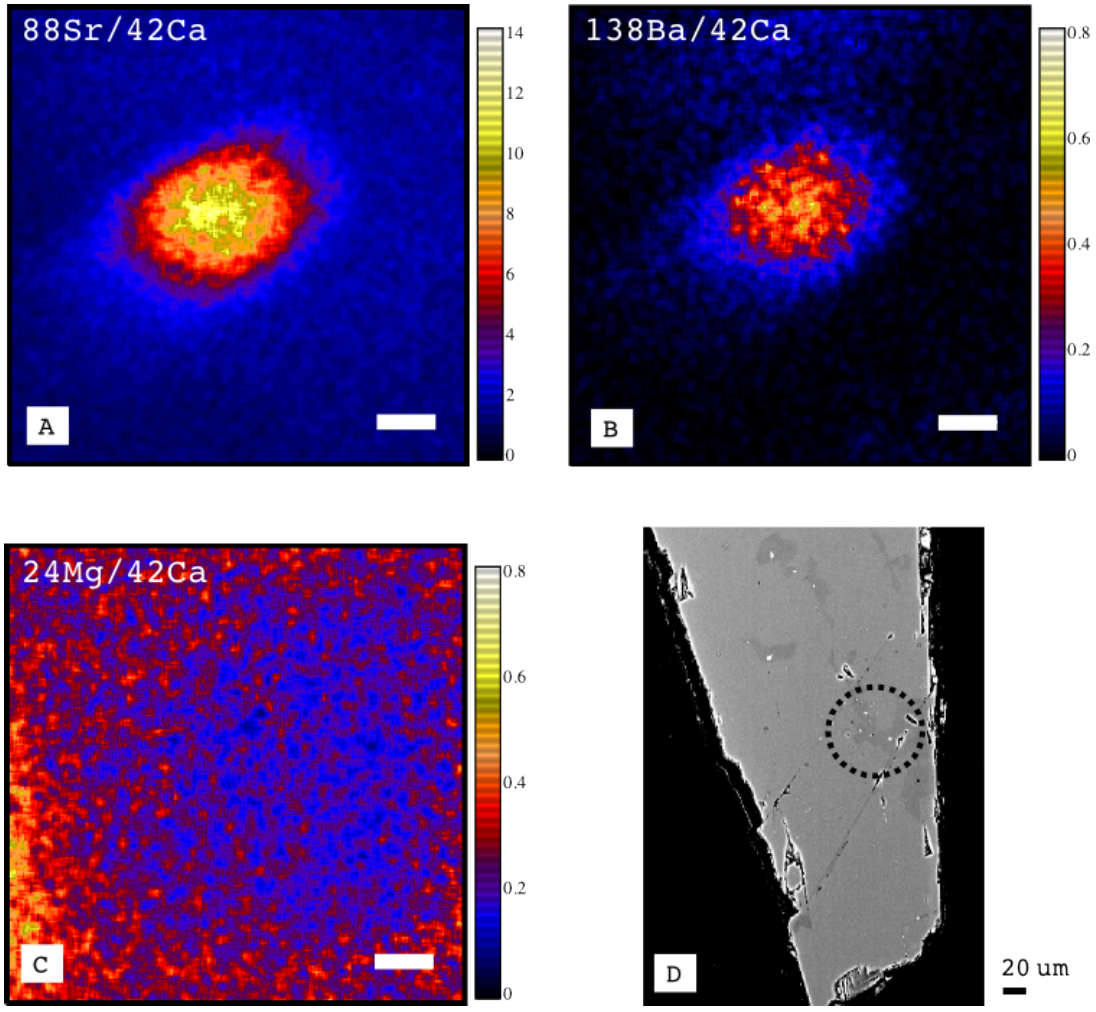

Figure 4.8: NanoSIMS ion ratio images of a heterogeneous region in the calcium carbonate mineral OKA carbonatite (white scale bar is 1 μm). (**A** and **B**) The roughly 3μm diameter inclusion is characterized by high strontium and barium. (**C**) The Mg/Ca ratio in inclusion does not differ from the surrounding matrix . Topography can sometimes produce artifacts in nanoSIMS images, the fact that there is no signal in the magnesium image supports that these are images of a true compositional feature. Assuming the edge of the inclusion is perfectly abrupt, profiles across the grain edge in ion image **A** yield a maximum estimate for primary beam size of $\sim$ 500 nm at $\sim$ 0.5 pA. Analysis of the same feature with a more useful beam current of 5 pA resulted in a probe size of 800 nm. (**D**) Backscattered secondary electron image of OKA carbonatite identifying the general region of nanoSIMS image analysis. OKA carbonatite heterogeneity is discussed in more detail by Gabitov et al. (in preparation).

isotopes in some experiments, appropriate trolleys are positioned as close as physically possible to each other. Then, to capture the off-center ion beam, the high mass resolving deflectors of adjacent SEMs were set to larger than normal deflection voltages. The ESA of each SEM was then re-tuned for sensitivity and peak shape. Detector gain varies between SEMs by more than 50%, but gain drift during a single session is negligible for anything but very intense ion beams.

Figure 4.9: NanoSIMS trolley configuration identifying the ionic species focused into each trolley for sessions Ns1 and Ns2. Bold trolleys were positioned directly against each other and larger than typical deflection voltages used to collect closely spaced ions.

T1	T2	**T3**	**T4**	T5	**T6**	**T7**
$^{24}Mg^+$	$^{40}Ca^+$	$^{42}Ca^+$	$^{43}Ca^+$	$^{40}Ca_2^+$	$^{87}Sr^+$	$^{88}Sr^+$

T1	**T2**	**T3**	T4	T5	T6	T7
$^{24}Mg^+$	$^{42}Ca^+$	$^{43}Ca^+$	$^{86}Sr^+$	$^{88}Sr^+$		$^{138}Ba^+$
			$^{87}Sr^+$	$^{88}SrH^+$	$^{136}Ba^+$	

Figure 4.10: NanoSIMS trolley configuration: Session Ns3. Multiple lines signify a change in magnetic field as part of a "combined method". Bold trolleys were positioned directly against each other and larger than typical deflection voltages used to collect closely spaced ions.

T1	T2	T3	T4	T5	T6	T7
	$^{24}Mg^+$	$^{40}Ca^+$	$^{42}Ca^+$	$^{43}Ca^+$	$^{87}Sr^+$	$^{88}Sr^+$

Figure 4.11: NanoSIMS trolley configurations: Session Ns4.

Molecular Interferences: Unlike ICP-MS, doubly-charged species (for example $^{87}Sr^{2+}$) are not detected on the nanoSIMS reflecting the different energies and physics for ion formation between in these methods. However, molecular ions are common in the secondary ion beam, which can interfere with $^{88}Sr^+$, $^{24}Mg^+$, and other species of interest. Energy filtering was investigated as a tool to reduce molecular isobaric interferences. As sample energy offset is made more negative, dimer formation does decrease but incurs a disproportionate penalty in sensitivity (Figure 4.12). Therefore, energy filtering is not an effective tool to eliminate molecular interferences under the analytical conditions used for this set of experiments. However, an energy offset of about -20 V to -30 V, corresponding to a wide and stable maximum in secondary beam atomic ion current, is still necessary to ensure sensitivity and stability. This offset is probably necessary to accommodate

steady-state charge build-up in $CaCO_3$, which is an insulator. Since molecular species cannot be eliminated, interferences from these species must either be optically resolved using the high mass resolving power of the nanoSIMS50 or corrected offline by monitoring molecular formation.

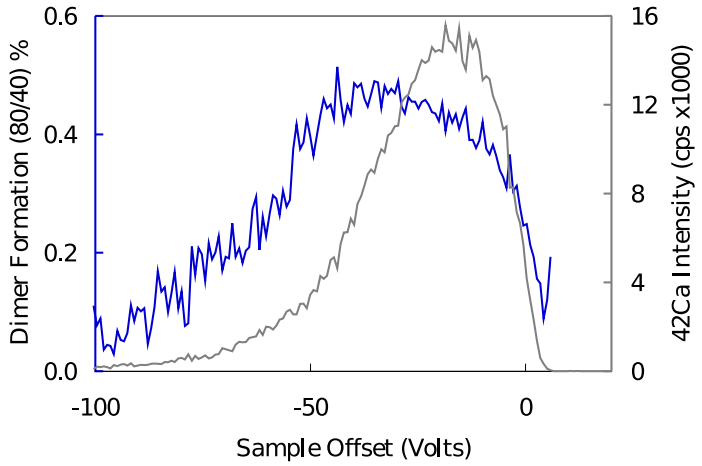

Figure 4.12: Dimer formation rate (blue line, left axis) decreases at negative energy offsets, but these energy offsets reduce sensitivity (gray line, right axis) too much to be a useful technique on the nanoSIMS. To generate this figure ion beams of $^{48}Ca^{+}$ and $^{40}Ca^{2+}$ were monitored in a carbonate sample as energy offset was adjusted. $^{48}Ca^{+}$ was converted to $^{42}Ca^{+}$ and $^{40}Ca^{+}$ intensities assuming natural calcium isotope abundances Russell et al. (1978). Maximum sensitivity in this study typically corresponds to an offset between 15 and 35 volts. This negative offset probably reflects steady-state charge accumulation in the insulating carbonate sample, despite gold coating. The best sample offset to maximize sensitivity varied little between different analytical sessions.

Hydride Molecular Interferences: During instrument tuning, calcium hydride ($^{40}CaH^{+}$) formation was detected at mass 41 in the carbonatite standard OKA, with a yield of $\sim$ 0.5 % ($^{40}CaH^{+}/^{40}Ca^{+}$). (The major abundance potassium peak is not present at mass 39 so a contribution from $^{41}K^{+}$ at mass 41 can be safely ruled out). Strontium hydride formation was also estimated from $^{88}SrH^{+}/^{88}Sr^{+}$ in a strontionite sample, with a similar formation rate of 0.5–1%. Hydrides are therefore present with a yield of up to 1%. Hydrides of one element interfering with atoms from another element are capable of causing large systematic errors, with $^{23}NaH^{+}$ on $^{24}Mg^{+}$ a potentially significant interference in many natural carbonates. Luckily this interference is optically resolved using a mass resolving power (MRP) of only 1900. Typical MRP for this study was 2000 to 3000 ($M/\Delta M$) using Cameca's 10%-to-90% peak width definition. It should be noted that this definition of MRP includes the flat top part of a peak, corresponding to the exit slit width, and therefore

underestimates the ability to optically resolve different masses. The peak edge MRP definition is a more relevant minimum criterion for optical resolution as it represents the ability to separately measure plateaus on the shoulder of composite peaks. The peak edge MRP is typically $\sim$ 10,000 in this study (5%-to-95%). A mass 24 peak shape demonstrates optical resolution of $^{24}Mg^{+}$ from the expected location of $^{23}NaH^{+}$ (Figure 4.13). $^{87}SrH^{+}$ is a non-optically resolvable interference on $^{88}Sr^{+}$. Luckily ^{88}Sr abundance is much larger than ^{87}Sr so this interference has little impact on 88/42 ratios, $\leq$0.1% assuming the measured hydride formation rate of $\leq$1%. In session Ns3, an attempt was made to explicitly correct for strontium hydride formation by measuring both $^{87}SrH^{+}$ and $^{88}Sr^{+}$. It is hard to regularly re-center on the low intensity $^{87}SrH^{+}$ peak and magnet drift unfortunately compromises the usefulness of these data.

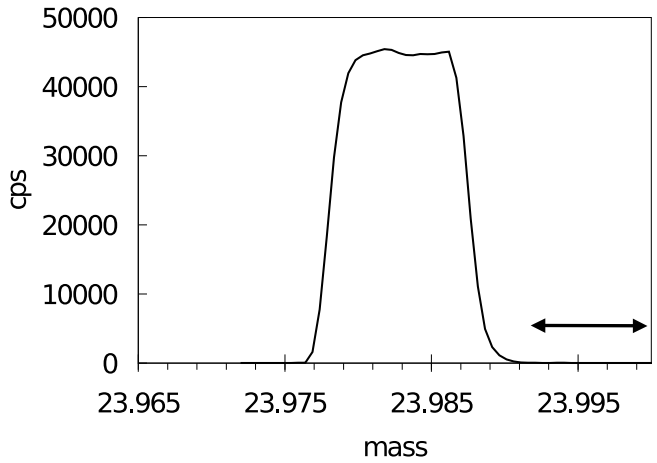

Figure 4.13: $^{24}Mg^{+}$ peak shape with a measured mass resolving power (M/ΔM) of 2100 using Cameca's 10%-to-90% peak width definition (MRP = 9600 using the peak edge definition). An arrow marks the predicted location of $^{23}NaH^{+}$. $^{24}Mg^{+}$ is clearly resolved from this potential interference. Data were collected with a large primary beam to boost intensity of both the $^{24}Mg^{+}$ peak and any $^{23}NaH^{+}$ peak.

Dimer Molecular Interferences: The isobaric interferences from calcium dimers on strontium isotopes, of which ^{88}Sr suffers from the largest interference, are difficult to optically resolve, requiring a MRP $>$ 9000, and have been the topic of previous SIMS method development research (Weber et al., 2005). This interference can potentially bias Sr/Ca ratios, affecting accuracy when standards and samples are not closely matched in Sr/Ca. If dimer formation rate is similar for different carbonate samples then the dimer contribution can be treated as a constant background present in

all standards and samples. This background shifts all measured 88/42 higher by a similar absolute offset. The dimer background contribution is therefore operationally accounted for by the intercept in a linear calibration curve 88/42 to Sr/Ca.

Dimer formation was monitored in session Ns2 from $^{40}Ca^{+}$ and the relatively clean and resolvable $^{40}Ca_2^{+}$ peak at mass 80. While dimer yield is similar for most carbonate standards, both OKA carbonatite and a high magnesium speleothem sample (LAS) exhibit 15% lower $^{40}Ca_2^{+}/^{40}Ca^{+}$ ratios. For strontium-rich OKA the dimer is already only a very minor correction (15% of 1 per mil is insignificant). For LAS the error in the dimer correction is an expected negative offset of < 2 per mil. These effects are small and the constant background assumption is used as an operational dimer correction for all data in this study.

From measured dimer formation rates it is possible to roughly estimate the intercept of an ideal Sr/Ca vs 88/42 calibration curve, assuming no other interferences and perfect Sr/Ca accuracy. For session Ns2, $^{40}Ca_2^{+}/^{40}Ca^{+}$ is roughly 1.7×10^{-3} and 42/40 is consistently 6.5×10^{-3}. Following the approach outlined in Weber et al. (2005), assuming natural abundances, and assuming similar gains in all the detectors, the estimated y-intercept of the calibration curve should be 1.1×10^{-3}, which compares very well with the measured y-intercept of $1.0 \pm 0.2 \times 10^{-3}$ from the calibration regression for that session. This analysis shows that dimers are present and need to be accounted for, but can be corrected during routine multi-standard calibrations as long as samples and standards are all $CaCO_3$ with only minor impurities that do not exhibit large dimer formation matrix effects.

Spot analysis: Each spot is typically pre-sputtered for several to tens of minutes using a primary beam with approximately twice the probe current used during analysis. Following pre-sputtering the lower current analytical beam is applied and several secondary ion beam settings are automatically tuned for intensity. Counts at each detector are then measured over a number of cycles for a specific integration time of several seconds each. During the "combined analysis" of session Ns3 cycles were collected for 35 seconds each alternating between different magnet field strengths. A magnet settling time of 5 seconds was used between magnet hops. Prior to final peak centering and subsequent analysis, the magnet was cycled between the two field states for approximately one hour

to develop a stable hysteresis at the same rate as eventual data collection.

Generally, 2 μm x 2 μm rastering is used to spread beam power more evenly over the spot area. While the beam is rastered over the whole 2 μm x 2 μm region, counts are only collected for the inner 95% of raster area to limit edge effects. An integer number of counts for each cycle represents the rawest form of data output by the machine during spot measurements. Subsequent data analysis is conducted offline. On the Caltech nanoSIMS50, an electronic delay is used to accurately set deadtime at 44 ns. The highest counting rates for most ions in this study are less than 3 kcps. Even at 10 kcps, a dead-time correction of less than 0.5% is required, therefore dead-time is ignored.

Intensity Ratio Drift, Internal Error, and External Precision: Mixed element intensity ratios (24/42, 88/42, and 138/42) drift during spot analysis on the nanoSIMS50. For example, almost all carbonate standards analyzed during run Ns2 show a consistent drift in 24/42 of near -20% over the 10 minutes of data collection. For 88/42 a smaller and more scattered drift is observed of $\pm$10%. In some cases intensity ratios exhibit steep and exponential-like decay for several 10s of cycles followed by an approximately linear low drift region, while other spots only drift linearly. Drift is thought to result from the sputtering process rather than particular compositional depth profiles, since spots at different locations and in different carbonate materials show similar drifts. Mixed element ratios, like 24/42 and 88/42, behave differently from single element isotope ratios, like 42/40, 43/40 and 87/88. Single element isotope ratios typically and rapidly attain a non-drifting steady-state value.

An initial exponential high drift feature, when present, suggests approach to a new steady-state ion-impregnation/sputtering condition following the pre-sputter. Internal error typically improves by excluding this high drift region, although excluding too many cycles means fewer counts and less internal precision. To investigate the effect of start cycle choice on internal error the average intensity ratio and internal error of each spot were calculated off-line using a range of start cycles.

A linearly drifting s intensity ratio, R, can be fit to a line of the form:

$$R = \overline{R} + m(t - \overline{t}) \ ,$$

where $\bar{t}$ is the mean cycle-start time and the two fitting parameters are the slope, m, and $\overline{R}$. We know the time between each cycle exactly so there is no uncertainty in t. Under these conditions, the parameter $\overline{R}$ resulting from a liner regression of cycle data against time is identical to the simple mean of the ratios. Thus modeling the data as a line does not change the estimate for the mean ratio of a spot. However, modeling a drifting signal as a line does improve the internal error estimate, as this error is no longer biased by drift. This correction may be important when comparing measured and theoretical counting statistic error. The drift-corrected internal error is calculated from the residuals between the linear model and each R_i, e.g., the standard error of the mean, $\sigma_{\overline{R}}$, is calculated using the following adaptation of the simple standard error equation (Bevington, 1969):

$$\sigma^2_{\overline{R}} = \frac{1}{N}\sum_{i=1}^{n} \frac{\left[R_i - \overline{R} + m(t-\bar{t})\right]^2}{N-2} \ .$$

For nanoSIMS data collected during this study, drift-corrected standard error and a simple standard error typically differ by less than a factor of two. The drift-corrected internal error, $2\sigma_{\overline{R}}$, is used to test whether removing early cycles improves the linear fit, thus identifying the portion of spot analysis where sputtering results in a consistent or linear drift. Typically, removal of the first 10%–55% of cycles leads to improved internal and external precision. For each session the same cut-off is applied consistently to all spots. During session Ns3, ratios were collected for nearly an hour at each spot and a change in drift slope was noted near the end of each spot. For this session the final 15% of data were also removed. The coral spot analysis results do not change significantly nor is the interpretation affected as a function of rejecting different cycles, rather, this process solely improves internal error and external reproducibility. Exclusion of any cycles precedes application of a modified Z statistical test to remove outliers farther than 4σ from the median. This step typically removes between one and two cycles out of every 100.

Counting statistics, through the Poisson distribution, imposes a fundamental lower limit on internal error. As discussed in Section 2.4, comparing theoretical and actual internal error is a useful technique to identify sources of error and aid experimental design. Figure 4.14 shows that

internal error follows the counting statistic limit for most nanoSIMS data collected in this study. There is no Johnson noise term since ions are collected using SEMs rather than as an amplified current in a Faraday cup.

External error, or the reproducibility of multiple spot measurements ultimately determines the minimum resolvable signal that can be measured on the nanoSIMS. While precision is fundamentally limited by internal error, differences in instrumental conditions between samples and between different analytical sessions often exceeds this limit. In the absence of perfectly homogenous carbonate materials, I measure multiple spots in several carbonate standards; identify the standard(s) with the best internal spot reproducibility; and use these materials to study how analytical parameters affect precision. The best reproducibility for a particular intensity ratio is then taken as an operational upper-estimate of machine precision. Several natural carbonate samples spanning a wide range of Me/Ca ratios were identified and assembled as potential SIMS standards by Rinat Gabitov: OKA carbonatite (OKA); Blue-Calcite used by Anne Cohen and colleagues at WHOI (BCC); Speleothem carbonate (LAS); Calcite-135 from the UC Berkeley mineral collection (135-CC); and calcite from the mineral collection at Rensselaer Polytechnic Institute (RPI). Two additional standards were later added to this collection: Aragonite mineral from the collection at Hebrew University, Jerusalem (HUJ); and, optical grade calcite used at UC Irvine as a 14-carbon "dead" standard (UCI).

Internal and external error were compared during analytical session Ns2, when 24 total spots were measured across all the standards. During this session, BCC exhibited a 24/42 external error of less than 0.5% (2σ of std dev of 3 points). These BCC measurements, which were measured in a random order with the 21 other spots, demonstrate that external error of better than 1% is achievable for 24/42 on the nanoSIMS. All other materials exhibit external 24/42 variability greater than internal error by a large amount, which we interpret as resulting from heterogeneity in the standards themselves. During this same session the 88/42 ratios of BCC, CAL, RPI, and UCI show external reproducibility that is comparable to internal error of 2.5% at best (BCC) but typically closer to 6%.

These results guided the design of coral analysis nanoSIMS sessions Ns3 and Ns4: low hetero-

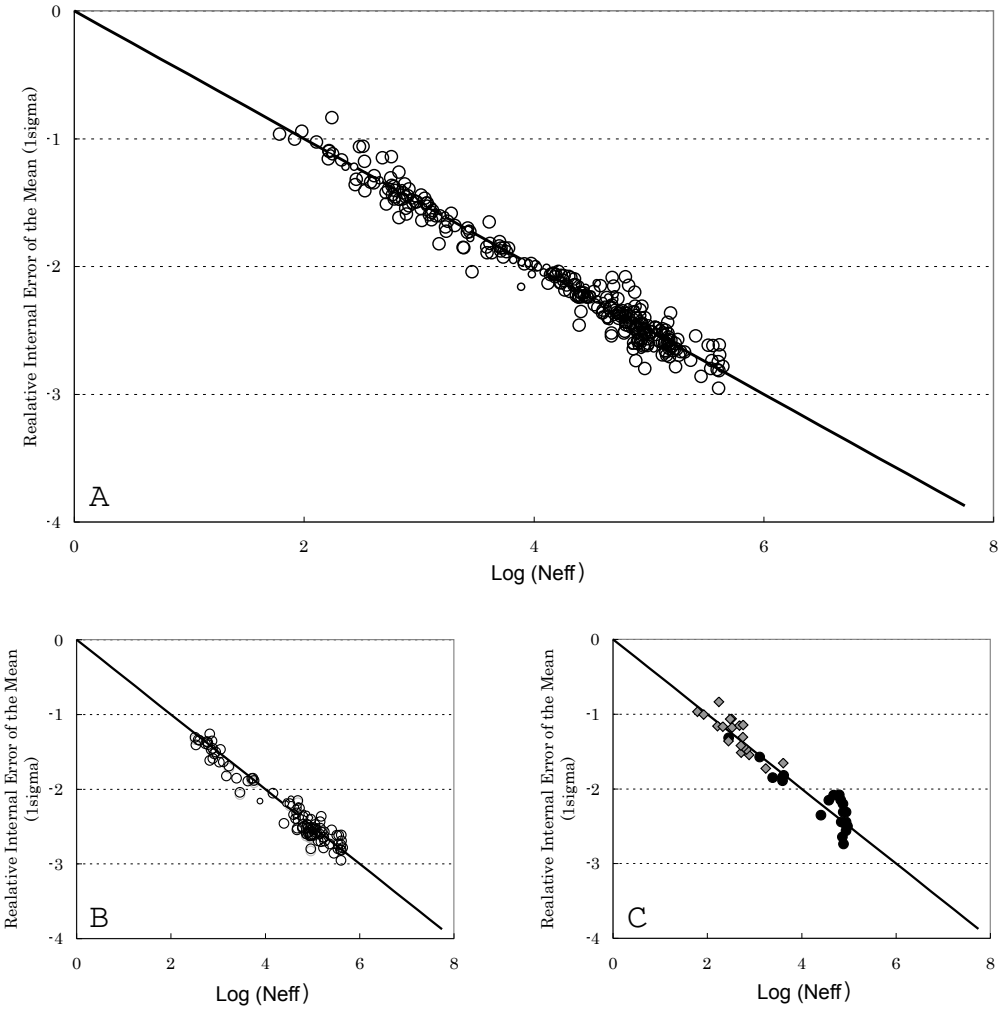

Figure 4.14: NanoSIMS internal error generally follows the theoretical counting statistics line. (**A**) Data for standard errors of all ratios during spot analysis on the nanoSIMS in this study. The largest departure from counting statistics occurs for 87/88 during session Ns3. Session Ns3 was the only "combined analysis" in this study, involving a change in magnet field between the accusation of certain isotopes. (**B**) A plot of the subset of internal errors from only those ratios in session Ns3 where both isotopes were analyzed using true multi-collection at the same magnet position. (**C**) A plot of internal errors for the two ratios (⧫)136/138 and (•)87/88 where isotope counts in the numerator and denominator were collected at different magnet positions and times. If the additional error in 87/88 comes from secondary beam variability captured thorough the "combined analysis" method, then the 136/138 data must be too noisy to exhbit the same effect. During this study typical ion intensity for $^{42}Ca^{+}$ is $\sim$ 3000 cps, although sensitivity differs between and within sessions.

geneity BCC was used as a consistency standard to assess instrumental reproducibility and more cycles were collected to improve internal error. External reproducibility of spot measurements in BCC for sessions Ns2–Ns3 is summarized in Table 4.6, showing substantially worse external error during coral analysis sessions. As discussed later in this chapter, Sr/Ca nanoSIMS measurements of newly grown coral skeleton also vary by 5% and 7% for sessions Ns3 and Ns4, matching the reproducibility of Sr/Ca measurements in BCC. Therefore, external analytical error probably limits Sr/Ca precision for coral data in this study. Mg/Ca varies by 65% in the cultured skeleton, far larger than even the largest Mg/Ca external error of 11% during session Ns4.

Several instrumental conditions differ between analytical sessions and even between different spots, which may or may not explain the observed external error. After poor external reproducibility was identified during session Ns3, several technical approaches were attempted to improve precision. Anecdotally, I noticed that ion peak positions differ as a function of secondary beam tuning, which is in turn affected by sample height (Z). In an attempt to limit error from Z-position drift, the Z-position was kept constant during session Ns4. A major contributor to Z-position variability is switching between the ion analysis mode and the in-machine CCD mode, a process which requires significant stage movement and was done regularly during session Ns3. For the earlier and higher precision session Ns2, limiting Z-position movement was a simple matter of designating target regions and allowing the stage to automatically move between new locations. This sort of automatic positioning is sufficient for large samples. When measuring small coral spines, however, micron-level spatial precision is necessary. This spatial precision requires manual positioning. Prior to any spot analysis in session Ns4, images of each sample location were made with the in-machine CCD. Using these images and calcien fluorescence maps as guides, the stage was manually positioned for each sample by real-time ion imaging. Drift in automatic peak centering may also contribute to decreased precision. In an attempt to avoid this issue, each detector was re-centered manually between every measurement in Ns4. Despite this and other careful work, it appears another uncontrolled factor must be contributing to external error. During sessions Ns3 and Ns4 source stability operated below specification due to a dirty lens in the primary stack, with several precent jumps in current every

10 minutes, it is unknown if this contributed to external error.

Table 4.6: External error of nanoSIMS Me/Ca spot measurements as assessed by the repeated analysis of the Blue Calcite carbonate standard. Coral analysis sessions Ns3 and Ns4 are characterized by worse external error than session Ns2, where only standards were measured. External error is better than internal error for session Ns2, probably teh reuslt of a small number of analyses. Four consistency standard spots were measured in each of sessions Ns3 and Ns4, while only 3 spots were measured in session Ns2.

session	24/42 external error (%)	24/42 internal error (%)	88/42 external error (%)	88/42 internal error (%)
Ns2	0.3	2.2	2.5	3
Ns3	2.6	1.1	5	1
Ns4	11	0.9	7	2

Calibration Using Carbonate Standards: Analyses of standards with known composition are necessary to convert intensity ratios measured on the nanoSIMS into accurate Me/Ca ratios. Several small pieces (0.1–1 mg) of each carbonate standard assembled by Rinat Gabitov were analyzed by ID-ICP-MS to establish accurate Me/Ca ratios. These data show that some materials exhibit significant Me/Ca heterogeneity between different large "chunks" and even between ~ 100 μg pieces of the same $\sim$ mg crystals (Figure 4.15). For example, there is $> 3\%$ variability between samples from the same small crystal of the commonly used carbonate standard OKA. On the other hand, both Sr/Ca and Mg/Ca appear to be homogenous within small crystals of Blue-Calcite (BCC), supporting the homogeneity observed in limited nanoSIMS surveys. Crystals were broken into two or more pieces with one piece mounted for SIMS analysis and the other piece set aside for ID-ICP-MS. Where intra-crystal heterogeneity is small, compositional analysis on one piece should apply to the second mounted sample as well. Since OKA is known to be heterogeneous in Mg/Ca and Sr/Ca, this standard was not included in final calibrations of coral data. All the carbonate standards were mounted in a single holder using this calibration technique to estimate "grain matched" Me/Ca ratios (Figure 4.16).

Measurements in carbonate standards show that intensity ratios of 24/42 and 88/42 vary linearly with Mg/Ca and Sr/Ca, respectively, over a nearly 100-fold range, although slopes are different for each of the four sessions (Figure 4.17). Even though calibration curves are linear over a large range of Me/Ca ratios, single point calibrations are sensitive to any compositional differences between a

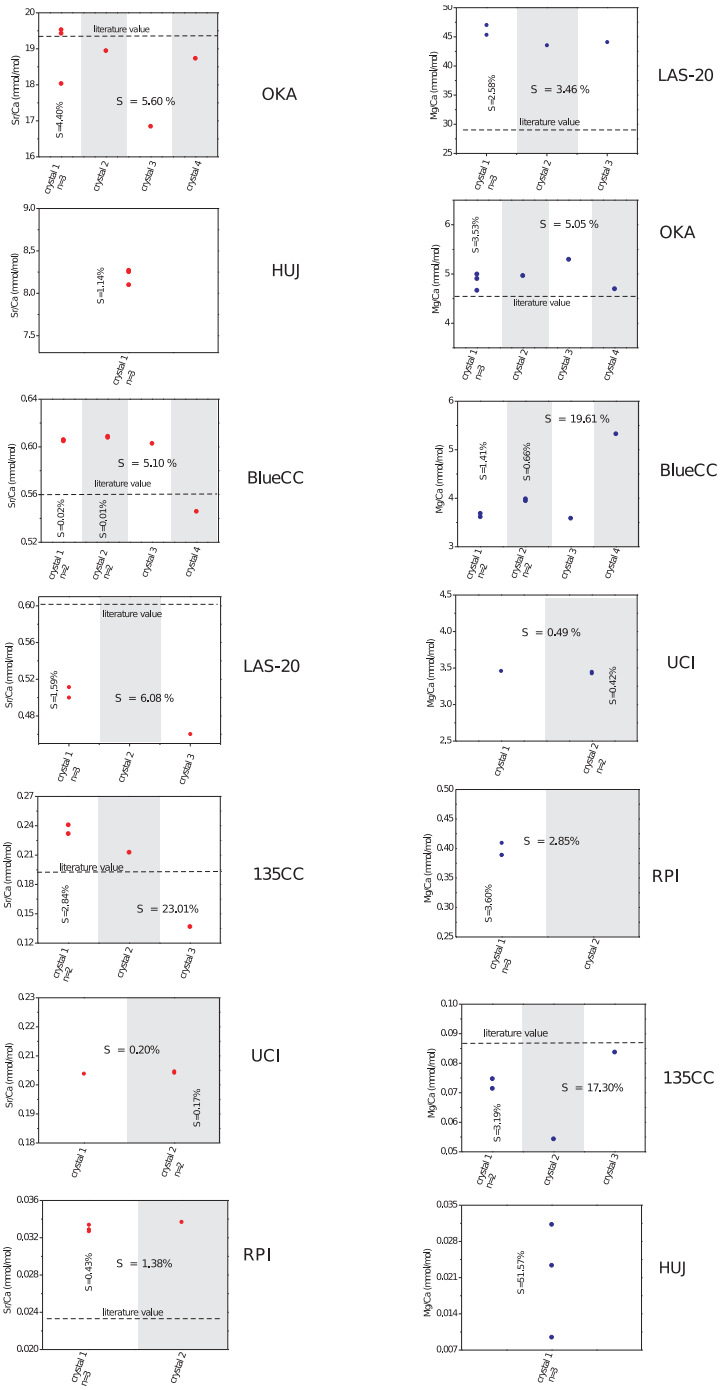

Figure 4.15: ID-ICP-MS Me/Ca ratios of carbonate standards showing a range of values between different large chunks and even within small $\sim$ mg sized crystals. For example, there is $> 3\%$ variability between samples from the same small crystal of the commonly used carbonate standard OKA. Data are presented for Sr/Ca on the left, Mg/Ca on the right, and are organized in order of decreasing Me/Ca ratios from the top. Data from different crystals are separated on the x-axis, with inter-crystal variability(S) written horizontally and intra-crystal heterogeneity written vertically (also S). I collected and initially assembled the data presented here. The figure was significantly improved by Rinat Gabitov and included in Gabitov et al. (in preparation), which also contains a detailed discussion of previous literature values for these standards.

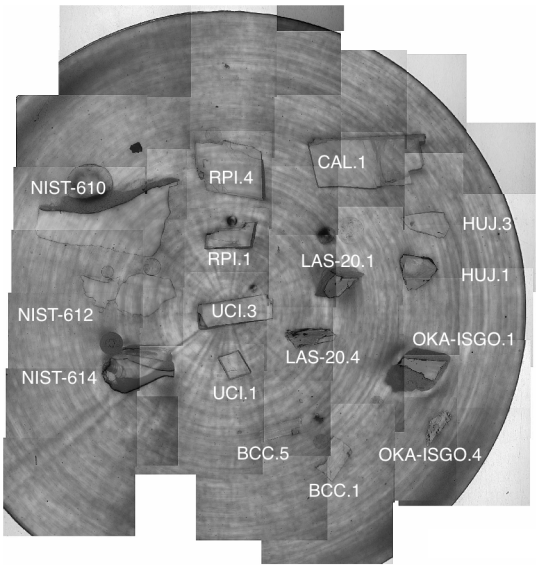

Figure 4.16: Carbonate standards for nanoSIMS analysis were mounted in a 1 cm diameter bullet using araldite resin after each piece was broken for grain-matched Me/Ca ratios by ID-ICP-MS. The bullet was later modified to fit a larger range of sample holders by milling off a portion of one side.

mounted crystal and the grain matched bulk analysis. For this reason, multiple point calibrations will lead to the most accurate measurements. Interestingly the slope of Mg/Ca and Sr/Ca calibrations appear inversely correlated: while session Ns1 is the steepest Sr/Ca calibration line, it is the most shallow Mg/Ca calibration. The intensity ratios 24/42 and 88/42 also drift with opposite slopes during spot analysis.

To better understand what controls Me/Ca accuracy and calibration curve slope, element ratio drift as a function of sputtering time was studied in detail. Starting with a fresh gold covered surface 88/42 first overshoots to low values and then increases with time during spot analysis (Figure 4.18). For the same spots, 24/42 decreases exponentially with time. While 24/42 and 88/42 rarely achieve steady state they do converge towards low relative drift. In general, higher beam currents and smaller areas result in shorter relaxation times: at high current, near-linear drift is achieved more quickly. This result suggests that the integrated current density or "pre-sputter dose", in Coulombs per square micron, may control the time evolution of intensity ratios. However, plots of 24/42 and 88/42 vs. pre-sputter dose for a number of beam conditions show that high intensity beams require more total ions to converge. This may mean that some zeroth-order process (time dependent, current

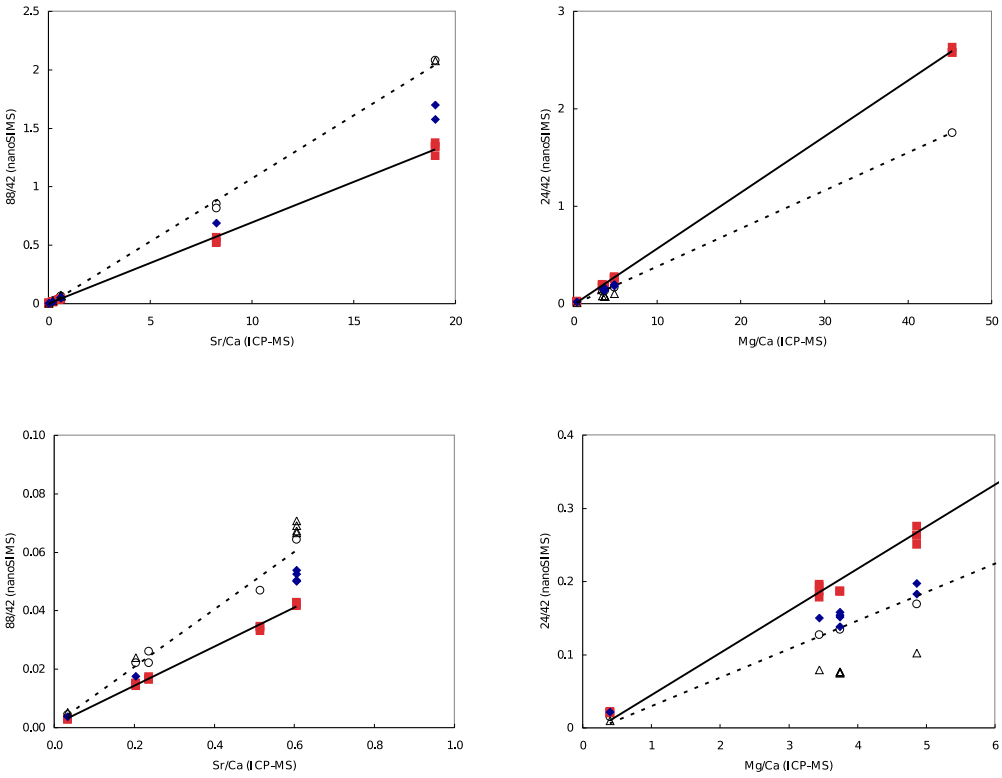

Figure 4.17: NanoSIMS spot analysis intensity ratios of carbonate standards compared to grain matched ICP-MS Me/Ca ratios. ICP-MS metal/calcium ratios are in mmol/mol. **TOP-LEFT:** nanoSIMS 88/42 compared to ID-ICP-MS measured Sr/Ca. **BOTTOM-LEFT:** The same data, but zoomed in to show low Sr/Ca measurements in greater detail. **RIGHT:** Mg/Ca Calibration curves of all data and zoomed-in to show detail at low Mg/Ca. Each of the four analytical sessions presented in this study is noted with a different symbol: (◯) Ns1; (■) Ns2; (△) Ns3; (⧫) Ns4. Within each analytical session a linear relationship between nanoSIMS intensity ratios and ICP-MS data allows accurate calibration. Different slopes between analytical sessions demonstrates the need to analyze standards during each session. The slope of Mg/Ca and Sr/Ca calibrations appear inversely correlated: while session Ns1 (dashed line) is the steepest Sr/Ca calibration line it is the most shallow Mg/Ca calibration. The opposite is true of session Ns2 (solid line). This result is explained by opposing drift patterns for 24/42 and 88/42 as described in the text. Typical coral Sr/Ca is 8 to 10 mmol/mol and typical Mg/Ca is 1 to 4 mmol/mol.

independent) contributes to pre-sputter effects on mixed element ratios. Moderate beam currents of 10–40 pA over 5–10 minutes efficiently yield low drift behavior.

Both primary beam intensity and pre-sputter time typically differ between analytical sessions. This can result in different extents of intensity ratio drift. More pre-sputter dose will tend to yield higher mean 88/42 and lower mean 24/42 for a particular constant composition. Therefore, higher pre-sputter doses will also result in steeper 88/42 calibration slopes and lower 24/42 slopes. During session Ns1 (dashed line in Figure 4.17) both primary current and pre-sputter time were twice that of session Ns2, explaining why Ns1 has a steeper Sr/Ca calibration and a shallower Mg/Ca calibration than Ns2. Thus differences in pre-sputter explain the relative slopes of different calibration lines.

Since mixed element intensity ratio drift is sensitive to primary current, ion source stability is expected to be a component of external error. Area also controls pre-sputter dose, thus only similarly sized spots and images should be compared and calibrated with each other. Furthermore three different NIST glasses were also measured during sessions Ns1 and Ns2, resulting in very different pre-sputter drift than carbonates. This result underlies the importance of matrix matching samples and standards, and suggests glasses are poor standards for carbonate materials in SIMS analysis.

To generate calibration curves for each session, nanoSIMS intensity ratios from carbonate standards and Me/Ca ratios from ICP-MS measurements were fit to a linear regression weighted by errors in both x and y (Press et al., 1992). The full range of Me/Ca values for all measurements in the same "grain matched" crystal are used to estimate uncertainty in ICP-MS Me/Ca ratios. Uncertainty for each nanoSIMS spot is the 2σ internal standard error of the mean using a linear drift model with the appropriate start and end cycles. The magnesium poor-standards HUJ and CAL, with Mg/Ca < 0.08 mmol/mol, were excluded from Mg/Ca calibration lines because of low $^{24}Mg^{+}$ counts and high relative error. For run Ns2, where all standards were measured, uncertainty in the Sr/Ca calibration fitting parameters propagate into an accuracy error estimate of $\sim 2\%$ (95% LOC) for a coral-like sample (Sr/Ca: 8 to 10 mmol/mol). Accuracy error of calibration curve Ns2 at a coral-like Mg/Ca of 2–4 mmol/mol is $< 6\%$.

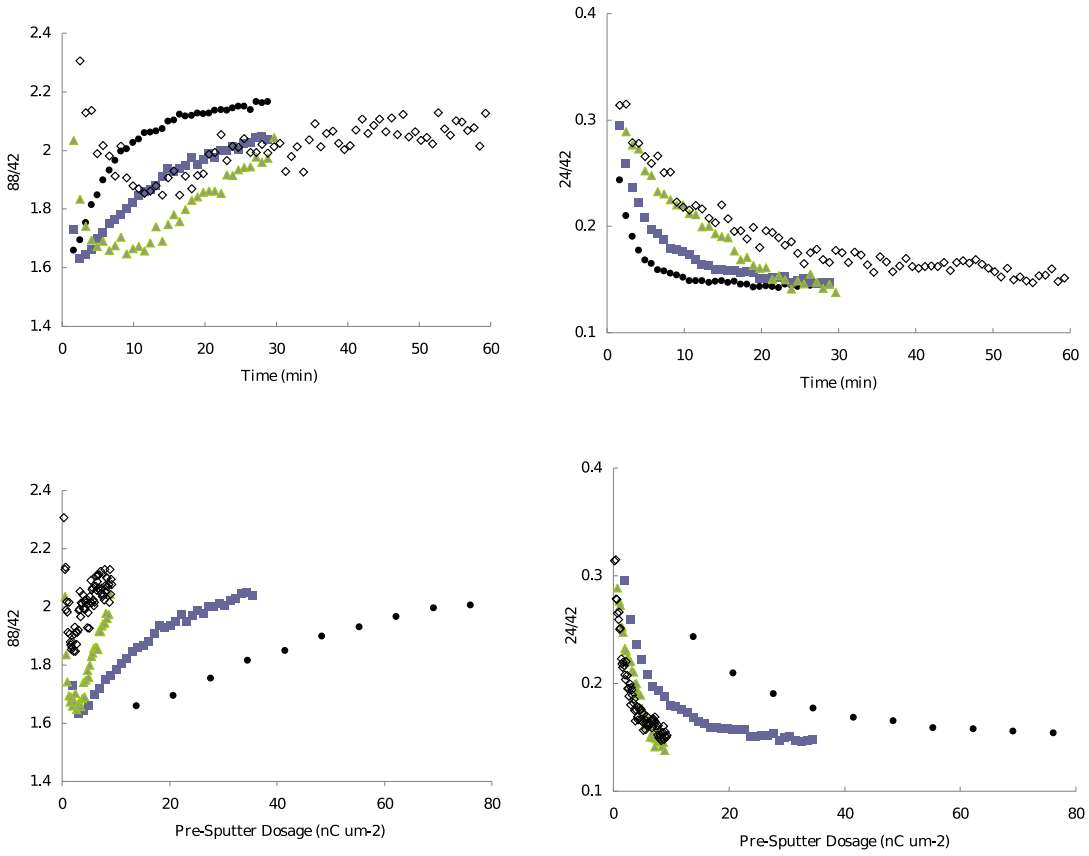

Figure 4.18: Plots of 24/42 and 88/42 for each cycle in 2μmx2μm "spot" measurements of the high magnesium and high strontium carbonate standard OKA carbonatite. Each spot was measured using a different primary beam intensity. The cycle data are labeled from dark to light in order of decreasing primary beam intensity : (●) 280pA; (■) 40pA; (▲) 10 pA; (◇) 4pA. **TOP-LEFT:** Starting with a fresh gold covered surface 88/42 first overshoots to low values and then increases with time. **TOP-RIGHT:** 24/42 decreases exponentially with time. In general, higher beam currents and smaller areas result in shorter relaxation times: at high current low/near-linear drift is achieved more quickly. In other experiments, larger raster area increases relaxation time. **BOTTOM:** The same intensity ratio data are plotted against a measure of "pre-sputter dose", the integrated current density, in Coulomb μm^{-2}. As high intensity beams require more total ions to converge, intensity ratio convergence is not just determined by dose. This may mean that some zeroth-order process (time dependent, current independent) contributes to pre-sputter effects on mixed element ratios.

The 43/42 ratio of OKA carbonate determined by nanoSIMS spot analysis is systematically lower than other carbonates for an unknown reason. While this standard was not used to calibrate any of the coral results presented below it may be an important result in future research. An un-resolved 26Mg16O interference may be capable of causing this effect.

Correction for Non-Natural Isotope Abundances: Calibration curves calculated by comparison to carbonate standards assume natural isotope abundances. For spiked coral, both 88Sr and 42Ca abundances are slightly lower than natural. The correction is:

$$\left(\frac{\mathrm{Sr}}{\mathrm{Ca}}\right)_{Coral} = \frac{^{88}A_{natural}}{^{88}A_{enriched}} \frac{^{42}A_{enriched}}{^{42}A_{natural}} \left(\frac{\mathrm{Sr}}{\mathrm{Ca}}\right)_{Measured/Calibrated},$$

or a factor of about 1.02 increase of the true Sr/Ca over the the Sr/Ca resulting from the calibration line regression assuming natural abundance. Correcting before or after applying the standard curve has negligible impact on the final Sr/Ca result (< 0.02 per mil).

The abundance correction for Mg/Ca is:

$$\left(\frac{\mathrm{Mg}}{\mathrm{Ca}}\right)_{Coral} = \frac{^{42}A_{enriched}}{^{42}A_{natural}} \left(\frac{\mathrm{Mg}}{\mathrm{Ca}}\right)_{Measured/Calibrated},$$

since Mg isotopes are not enriched in this experiment, but this is only a 0.1 per mil correction, and therefore negligible.

Ion Image Analysis: Images were collected during two sessions, Ni1 and Ni2, separated by four months. The same spine samples used in spot analysis were analyzed for images, in some cases the burn marks from other sessions were used to guide analysis, although fresh gold covered locations were used for all final data reported in this study. All images are 20x20 μm with 128x128 pixels, unless otherwise noted. Several sequential image planes are collected in each location. During a combined analysis method, a complete image plane is collected at one magnet position, the magnet field is changed allowing for settling time, and the region rastered again to measure ions associated with the second magnet position. This process is repeated for each ion image plane. While six or more planes are collected for each image, early planes are are usually un-even in 42Ca due to

incomplete pre-sputtering, while latter planes become un-even due to charge build-up. Only the subset of planes that yield even and homogenous $^{42}Ca^{+}$ ion images were analyzed.

The integer number of counts collected at each pixel is the rawest form of data output by the nanoSIMS50 in this study. Data were processed offline using custom scripts in Matlab. Counts from all planes with homogenous 42Ca intensity are summed for each pixel. A moving box average centered on each pixel is applied to each intensity image (5x5 pixel boxes for every ratio except 87/88, where a 9x9 pixel box is used). Ratio images are made using the averaged data. The ratio at each pixel is simply the ratio of the numerator counts at that location divided by the denominator counts at that same pixel. Instrumental mass fractionation is corrected by referencing to the average ratio of non-spiked (natural abundance) regions of the coral within each image. Fractionation corrections are not used between different images due to differences in pre-sputter conditions.

During Session Ni1 a 50 pA pre-sputter beam was first applied over a 22x22 μm region. This pre-sputter was run like a typical analysis, collecting and displaying image data, and continued until two planes had been collected or until the first homogenous 42Ca image. True image analysis was then started with a 5 pA primary beam in a 20x20 μm square. Too long of data collection or pre-sputter results in progressively uneven images, so there is a relatively small number of planes that can be collected. Dwell time at each of the 128x128 pixels was between 0.015–0.1 seconds. Detectors were set-up with the same trolley configuration as Session Ns3 (See Figure 4.10).

For Session Ni2 image data was collected as a 20x20 μm square starting from a fresh gold surface. A separate pre-sputter was not used, instead image data was continuously collected and un-even images eliminated in post-processing. Primary beam current throughout the analysis was 8.6 pA. Images were rastered as 128x128 pixels with 0.03 second dwell time. Detectors were set-up as shown in Figure 4.19 to monitor Rare Earth Elements (REEs) as well as strontium and calcium isotopes. REE masses were chosen to avoid oxides and dimers. A standard rich in the single isotope REE terbium was used to fingerprint the often confusing mass spectrum near Tb, Gd, and Dy. A large background at mass 155 in coral swamps any structured gadolinium signal. This may result from the relatively high [Gd] in seawater compared to most other REEs. Very few counts of dysprosium were

detected in any image. In Session Ni1 and Ni2, the ion in Trolley 7, 138Ba and 162Dy, respectively, seemed to drift towards zero counts early in each analysis. This loss of counts may be a result of magnet drift during combined analysis that is somehow more acute at Trolley 7; some other unexplained analytical issue; or reflect a real and unexpectedly low number of counts for these ions in coral samples. Between each image, REEs were re-peak centered using a mixed REE standard. Typical sensitivity with a 8.6 pA primary beam was 1000 cps for 42Ca, 100 cps for 87Sr, 400 cps for 43Ca, 1200 cps for 88Sr.

T1	T2	T3	T4	T5	T6	T7
	$^{42}Ca^{+}$	$^{87}Sr^{+}$		$^{155}Gd^{+}$	$^{159}Tb^{+}$	$^{162}Dy^{+}$
	$^{43}Ca^{+}$	$^{88}Sr^{+}$				

Figure 4.19: NanoSIMS trolley configuration: Session Ni2.

Image Profiles: Isotope ratio profiles across compositional boundaries are generated from raw image data using a custom Matlab script. First the compositional boundary is identified by drawing a line in a 43/42 image. The boundary is then converted into the "single-step mask", a bit-map approximation of the junction, using Bresenhams line algorithm. The bit-map mask is composed of an integer number of pixels, which means that each step along the profile results in an integer number of counts, eliminating interpolation and simplifying error estimation. This mask is moved along a path perpendicular to the boundary from one edge of the image to the next in pixel length steps. Isotope intensity at each step is the sum of all counts from each pixel in the mask across the subset of planes with homogeneous 42Ca intensity. The counts for each pixel in a profile step are the un-averaged raw count data to avoid any artificial smoothing.

4.6 Coral Growth Conditions and Growth Rates

Regular collection and analysis of culture solution chemistry provides a detailed record of the carbonate system during coral growth. Flow rates and the alkalinity of each chamber are summarized in Figures 4.20–4.21. Where there is missing flow or alkalinity data, values were interpolated from bracketing measurements. All the alkalinity, pH, DIC and flow measurements collected during this

study as well as calculated carbonate chemistry are summarized in the Appendix (Table 4.12). Average aragonite saturation (Ω) of each culture chamber was calculated from these data, and this Ω is used to identify each culture condition in subsequent figures. The Gulf of Eilat seawater used in this study is more saline than the mean ocean and therefore has a higher [Ca^{2+}]. For the same [CO_3^{2-}], *in situ* Ω will be higher in Gulf of Eilat water as compared to the mean ocean.

Carbonate ion and associated Ω were primarily manipulated by adjusting reservoir alkalinity. In Figure 4.21 the alkalinity of each chamber starts with near reservoir values, but decreases due to calcification. This result has two important implications: (1) [CO_3^{2-}] drifts during the experiment, but this drift is generally small compared to differences between each chamber, except for the two lowest Ω chambers at the end of the experiment (Figure 4.22), and (2) the difference between culture chamber and reservoir alkalinity through time can be used to estimate whole coral calcification rates.

Calcification Rate From Flow-Through Alkalinity Measurements: To calculate the calcification rate we balance fluxes of alkalinity into and out of each culture chamber,

$$\frac{dALK}{dt} = \frac{ALK_{RES} \times Flow}{Chamber\ Size} - \frac{ALK \times Flow}{Chamber\ Size} - \frac{1}{2}\frac{Ppt}{Chamber\ Size}\ , \tag{4.1}$$

where ALK and ALK_{RES} refer to the culture chamber and reservoir, respectively, in units of μequiv kg^{-1}; $Flow$ is the peri-pump driven flow rate through the chamber in kg hr^{-1}; $Chamber\ Size$ is in kg; and Ppt is the calcification flux in moles of $CaCO_3$ hr^{-1}. One mole of calcium carbonate removes two mole equivalents of alkalinity, resulting in the factor of 1/2 in the precipitation term. The data actually collected during the culture experiment, the accumulated output flow from each culture chamber between t_o and t_f, represent time integrated fluxes. Integrating Equation (4.1) over the collection period and using the fact that reservoir alkalinity (ALK_{RES}) is constant over this time yields:

$$\frac{[ALK(t_f) - ALK(t_o)]}{Chamber\ Size} = ALK_{RES}\int_{t_o}^{t_f} Flow\ dt - \int_{t_o}^{t_f} (ALK)(Flow)\ dt - \frac{1}{2}\int_{t_o}^{t_f} Ppt\ dt\ .$$

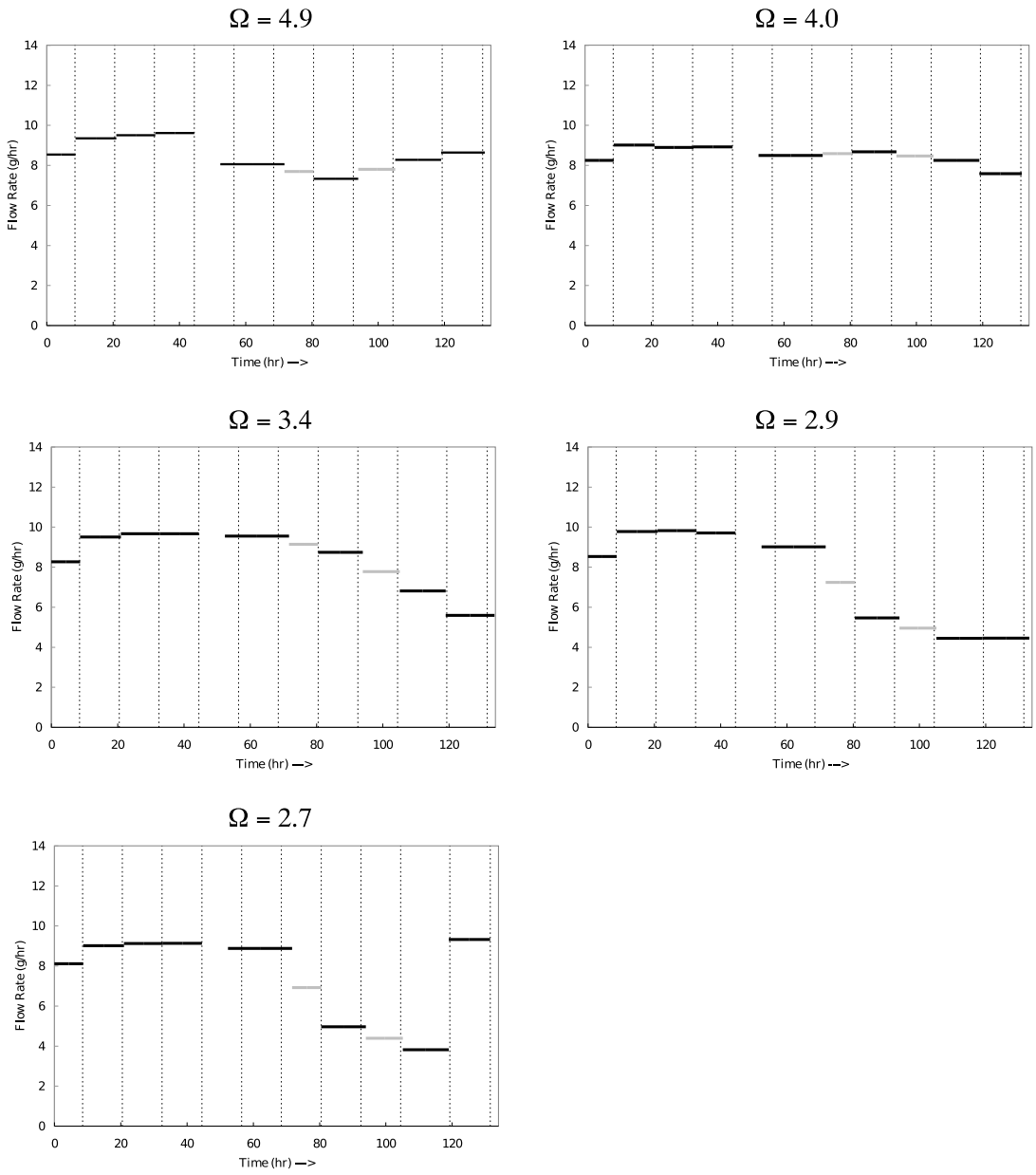

Figure 4.20: Flow rate through culture chambers in g/hr. Short jump in flow rate after the first interval resulted from an adjustment to peri-pump speed. Although measurements were taken during most of the experiment, flows do not exist for all time or alkalinity points, nor do alkalinities exist for all flow and time points, owing to sample size and time constraints. Grey bars represent interpolated flows to fill missing data.

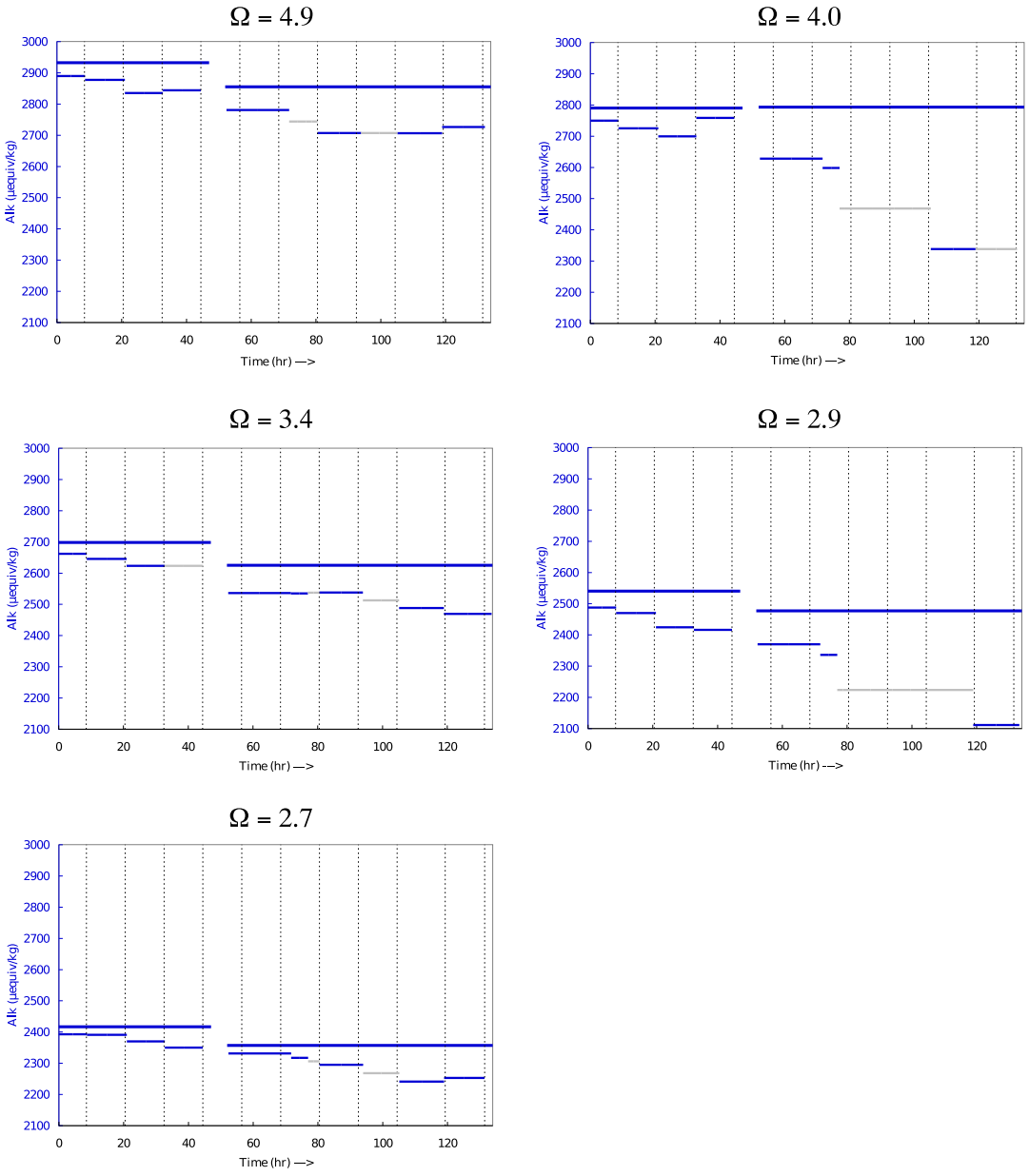

Figure 4.21: Alkalinity of accumulated culture chambers outflow during growth experiment. Flat and bold horizontal lines mark the reservoir alkalinity; the alkalinity flowing into the culture chamber through the peri-pumps. A mid-experiment shift in reservoir alkalinity is a result of adding an REE time-mark dissolved in HCL to each bag, and approximate re-titration of the alkalinity to the original condition. The alkalinity of culture chamber output is plotted as horizontal bars, where the start and end of the bar signify the beginning and end of the collection period. Grey horizontal bars mark interpolated values as alkalinity was not measured for all time points due to sample size and/or time limitations. Vertical dashed lines mark the transition between subsequent light and dark photo-periods, starting with light at the far left.

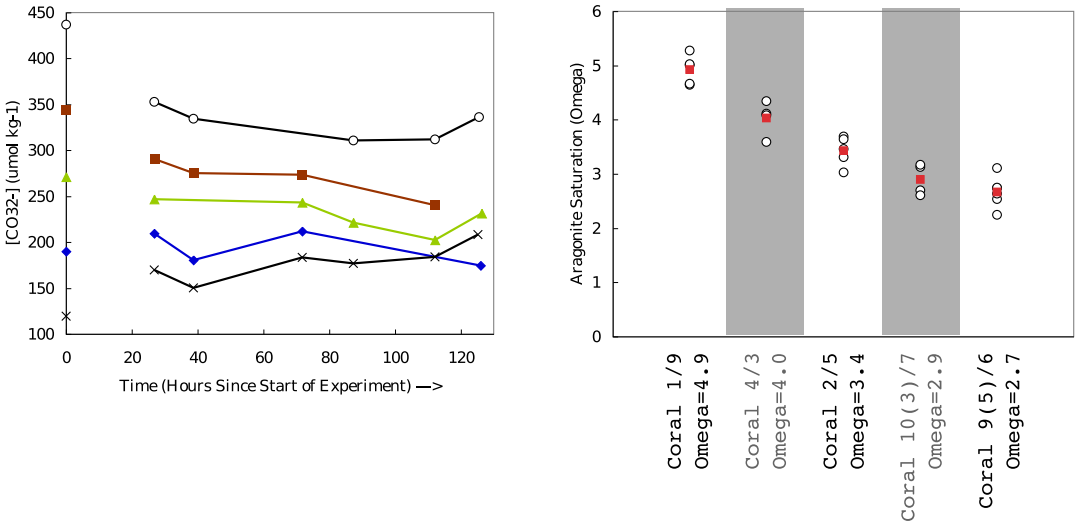

Figure 4.22: **LEFT:** $\left[CO_3^{2-}\right]$ in culture solutions during culture experiment. Time in hours from start of experiment. Value at time 0, on left axis. corresponds to initial reservoir $\left[CO_3^{2-}\right]$. (◯) Ω=4.9; (■) Ω=4.2; (▲) Ω=3.4; (♦) Ω=2.9; (×) Ω=2.7. **RIGHT:** (◯) Calculated aragonite saturation in each chamber during coral culture. (■) Average aragonite saturation of chamber.

Integrated flow is measured directly by taking the total mass of the culture chamber outflow, the term,

$$\int_{t_o}^{t_f} (ALK)(Flow)\, dt\ ,$$

is simply the mole equivalent of alkalinity in the outflow container. The alkalinity drop across each time-step is used to estimate the change in reservoir alkalinity and then the above equations are solved for precipitation during the collection period. For the first time-step, the reservoir value is used as the initial alkalinity, as each chamber was initially filled with unaltered reservoir water. In mostly chambers the last alkalinity time point before the REE spike fortuitously has a similar alkalinity as the post-REE spike reservoir values, so the average between these alkalinities are used to estimate the chamber alkalinity just post REE spike addition.

Precipitation rates normalized to coral surface area during each collection period are plotted in Figure 4.23. For the early part of the culture period, when separate day and night samples were collected regularly, many of the chambers appear to exhibit a diurnal cycle with light enhanced calcification during the day. Total precipitation during the experiment is plotted vs. carbonate ion in Figure 4.24. While the lowest Ω chamber calcified the least, the most obvious result is the

significantly higher calcification rate for coral grown at Ω=4.0. Most of this growth occurred after the mid-experiemt REE spike (Figure 4.24). Before this time, alkalinity derived calcification rates agree better between the different conditions, with the lowest daytime calcification at the lowest Ω, and a clear difference between day and night calcification.

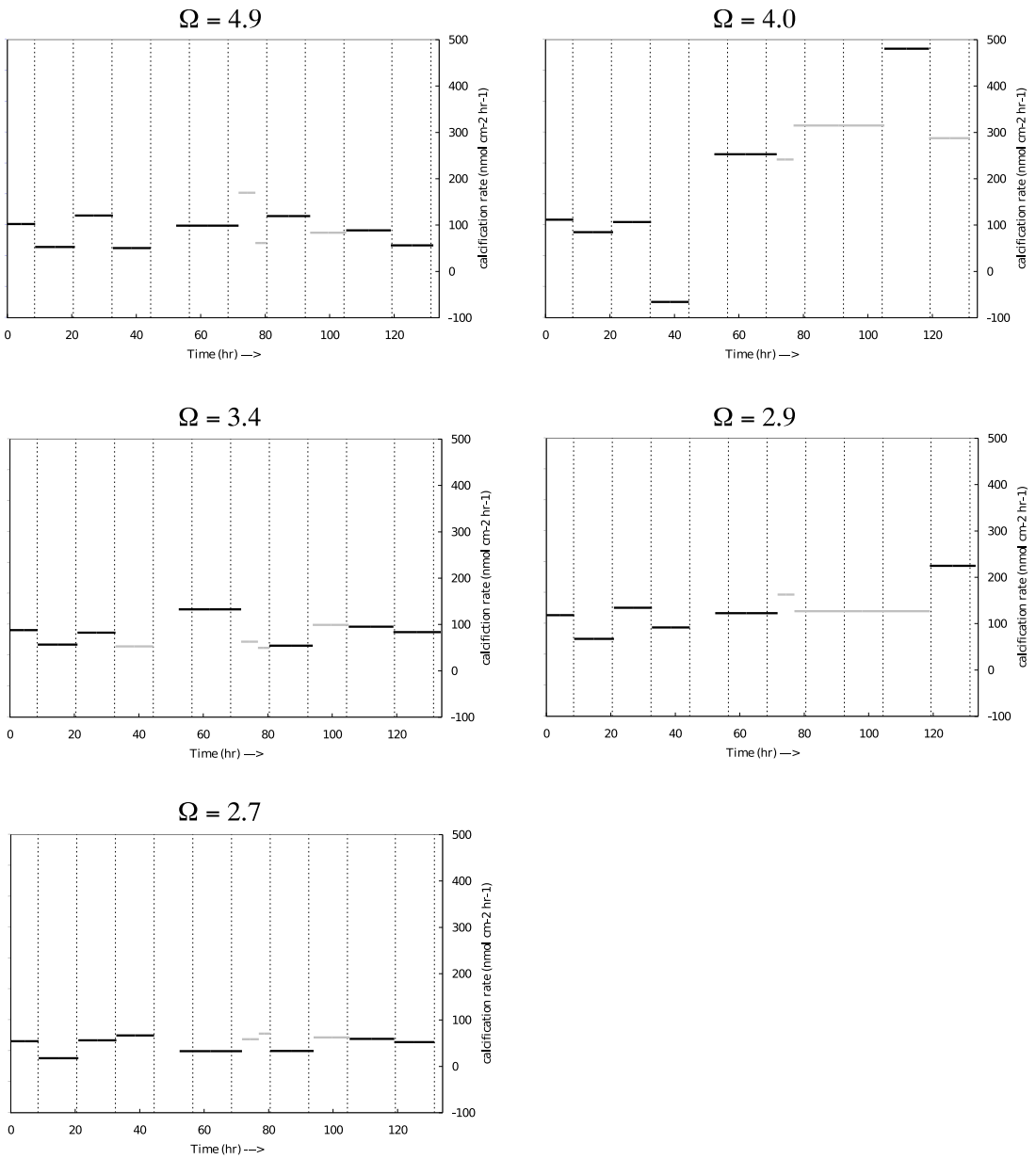

Figure 4.23: Calcification rate by alkalinity method in chambers over time. For the early part of the culture period, when separate day and night samples were collected regularly, many of the chambers appear to exhibit a diurnal cycle with light enhanced calcification during the day.

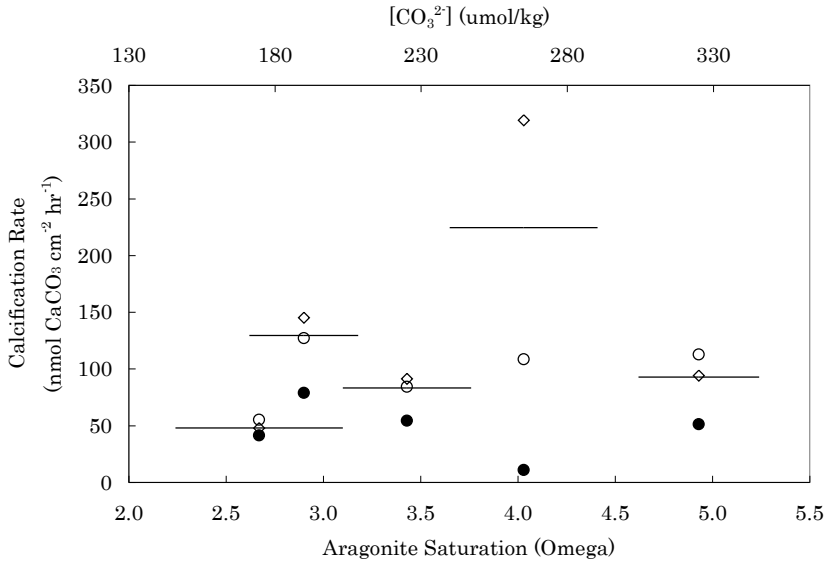

Figure 4.24: Carbonate ion effect on calcication rate by differences in the alkalinity flux. Horizontal bars represent the full range, over all time points, of calculated $\left[CO_3^{2-}\right]$ for each treatment rather than the smaller uncertainty in the typical $\left[CO_3^{2-}\right]$. The alkalinity data is divideed into different time periods: average (○) day and (●) night calcification rates in each chamber prior to the mid-experiment REE addition, as well as (◇) post-REE-spike combined day and night calcification rate. While the lowest Ω coral calcified the least, a high calcification rate for the $\Omega = 4.0$ coral is again one of the most obvious results. It is clear that most of the Ω=4.0 growth occurred late in the experiment, after REE addition. Overall, day calcification is somewhat sensitive to Ω, while dark calcification is uncorrelated with Ω. The coral grown at Ω=2.9 calcifies at a somewhat higher rate than other coral, even compared to the pre-REE growth of rapidly calcifying coral Ω=4

4.7 Bulk Isotope Ratios of Microsampled Coral to Localize Experimental Growth

Micro-samples are collected by scraping or breaking parts of a coral skeleton. These samples presumably represent a mixture of unknown proportions between any material grown during the experiment and initial skeletal material. Since the culture media is enriched in both ^{87}Sr and ^{43}Ca, we use these isotopes as tracers for new growth. Consistent with skeletal growth during the culture experiment, analysis of micro-sampled coral by MC-ICP-MS shows the incorporation of both ^{87}Sr and ^{43}Ca above natural abundances with negligible enrichment of the un-spiked isotopes ^{86}Sr and ^{48}Ca (Figure 4.25). To test if micro-samples are indeed a mixture of new and initial skeleton, the isotope data are compared to the calculated mixing relationship between exactly two end-members: (1) natural abundance coral skeleton from before the culture experiment; and (2) skeleton grown during the growth experiment with isotope abundances matching the spiked culture solution.

For a sample composed of unknown proportions of initial unspiked and newly grown spiked material (Figure 4.26), the strontium isotope ratio is simply the ratio of the number of moles (n) of each isotope from both regions,

$$\left(\frac{87}{88}\right)_{measured} = \frac{^{87}n_o + ^{87}n_x}{^{88}n_o + ^{88}n_x}. \tag{4.2}$$

With some algebra we can put (4.2) in terms of natural and spike isotope ratios:

$$\begin{aligned}
\left(\frac{87}{88}\right)_m {}^{88}n_o + \left(\frac{87}{88}\right)_m {}^{88}n_x &= {}^{87}n_o + {}^{87}n_x \\
\left(\frac{87}{88}\right)_m {}^{88}n_x - {}^{87}n_x &= {}^{87}n_o - \left(\frac{87}{88}\right)_m {}^{88}n_o \\
{}^{88}n_x \left[\left(\frac{87}{88}\right)_m - \left(\frac{87}{88}\right)_x\right] &= {}^{88}n_o \left[\left(\frac{87}{88}\right)_o - \left(\frac{87}{88}\right)_m\right] \\
\frac{^{88}n_x}{^{88}n_o} &= \left[\frac{\left(\frac{87}{88}\right)_o - \left(\frac{87}{88}\right)_m}{\left(\frac{87}{88}\right)_m - \left(\frac{87}{88}\right)_x}\right].
\end{aligned} \tag{4.3}$$

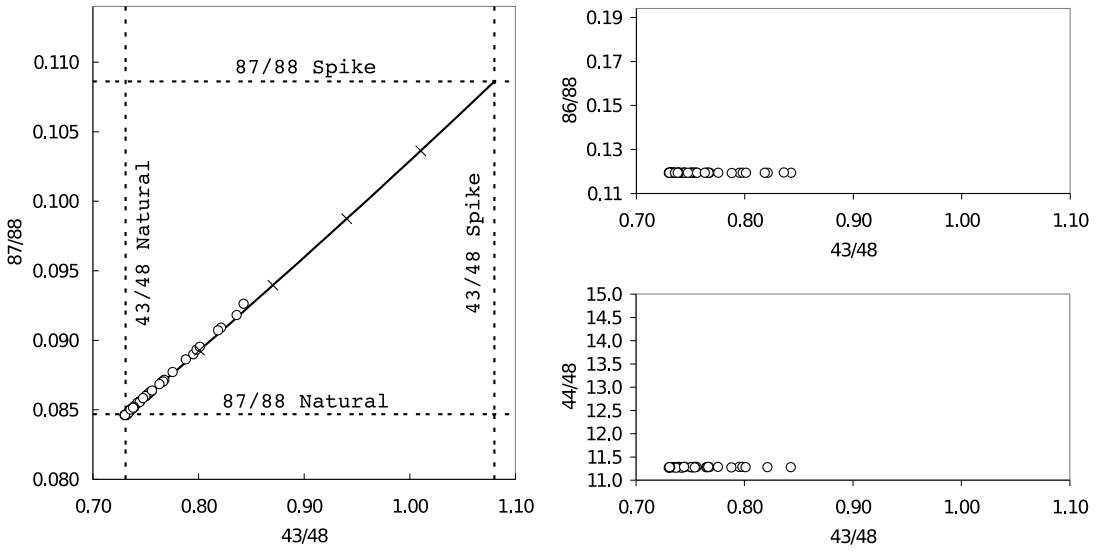

Figure 4.25: Stable isotope analysis of micro-sampled coral by MC-ICP-MS demonstrates spike incorporation. **LEFT:** (◯) Calcium and strontium isotope ratios of all micro-sampled coral spanning every growth condition (n=60). Internal error is smaller than the symbol size. Incorporation of both ^{87}Sr and ^{43}Ca, which were enriched in the culture media, shows that growth occurred during the experiment. The isotope ratios of natural abundance seawater and the enriched culture solution are marked by dashed lines. Coral micro-samples plot close to the predicted mixing relationship between natural abundance seawater and the enriched culture media (solid line). Hash marks on the mixing line indicate new growth mole fractions of 0.2, 0.4, 0.6, and 0.8. The most enriched samples obtained by micro-sampling are still more than 60 mole percent initial skeleton. Departure of isotope ratios from the line or curvature would suggest either significantly different Me/Ca in the two end-members or substantially preferential incorporation of one element, as described in the text. For this figure, the mixing line was plotted using a q from the ID-ICP-MS measured initial coral Sr/Ca and the new growth end-member Sr/Ca measured by nanoSIMS spot analysis. Near $q = 1$, differnt choices of q all yield similar figures. **RIGHT:** Neither 86/88 nor 44/48 vary significantly with 43/48, as expected for these non-enriched isotopes. Therefore, the 43/48 vs. 87/88 relationship is unlikely to be a fractionation effect, instrumental or otherwise, and instead represents real incorporation of spike in the newly grown material. The y-axis of the right-hand plots are set to same relative range as the graph on the left for easy comparison.

Figure 4.26: Schematic of a coral micro-sample composed of unknown proportions of both initial skeletal material and spiked growth during experimental conditions. By measuring the stable isotope ratios of a micro-sample, combined with knowledge of several other parameters, it is possible to determine the mole fraction of new growth and estimate the Me/Ca ratio of the newly grown material.

Similarly, for the calcium isotopes ^{43}Ca and ^{48}Ca,

$$\frac{^{48}n_x}{^{48}n_o} = \left[\frac{\left(\frac{43}{48}\right)_o - \left(\frac{43}{48}\right)_m}{\left(\frac{43}{48}\right)_m - \left(\frac{43}{48}\right)_x}\right]. \tag{4.4}$$

In an important aside, Equation (4.4) can be multiplied by ^{48}Ca abundances to yield the relative proportions of new and initial growth:

$$f = \frac{\mathrm{Ca}_x}{\mathrm{Ca}_o} = \frac{^{48}n_x}{^{48}n_o}\frac{^{48}A_o}{^{48}A_x},$$

which can be also expressed as the mole fraction of new skeleton,

$$\chi_x = \frac{f}{f+1}.$$

Dividing Equations (4.3) and (4.4) above, we obtain an expression for mixing between a spiked and unspiked end member for the four isotope system,

$$\left[\frac{\left(\frac{43}{48}\right)_o - \left(\frac{43}{48}\right)_m}{\left(\frac{43}{48}\right)_m - \left(\frac{43}{48}\right)_x}\right] = \frac{\left(\frac{88}{48}\right)_o}{\left(\frac{88}{48}\right)_x}\left[\frac{\left(\frac{87}{88}\right)_o - \left(\frac{87}{88}\right)_m}{\left(\frac{87}{88}\right)_m - \left(\frac{87}{88}\right)_x}\right]. \tag{4.5}$$

Following the notation and derivation described in Albarède (1995, p. 19) from this point on, Equation (4.5) becomes

$$\frac{x_o - x_m}{x_m - x_x} = q\frac{y_o - y_m}{y_m - y_x} \tag{4.6}$$

where

$$x = \left(\frac{43}{48}\right), \quad y = \left(\frac{87}{88}\right), \text{and} \quad q = \frac{\left(\frac{88}{48}\right)_o}{\left(\frac{88}{48}\right)_x}.$$

The mixing equation is sensitive to the Me/Ca ratio of the newly grown material through the term q,

$$q = \frac{\left(\frac{88}{48}\right)_o}{\left(\frac{88}{48}\right)_x} = \frac{\left(\frac{\mathrm{Sr}}{\mathrm{Ca}}\right)_o \frac{^{88}A_o}{^{48}A_o}}{\left(\frac{\mathrm{Sr}}{\mathrm{Ca}}\right)_x \frac{^{88}A_x}{^{48}A_x}}.$$

To compare the micro-sampled data to a mixing line, we need to expand Equation ((4.6)) and solve

for y_m as a function of x_m:

$$(x_o - x_m)(y_m - y_x) = q(x_m - x_x)(y_o - y_m) \ ,$$

$$x_o y_m - x_o y_x - x_m y_m + x_m y_x = q(x_m y_o - x_m y_m - x_x y_o + x_x y_m) \ ,$$

$$y_m(x_o - q x_x) + x_m(y_x - q y_o) = x_m y_m(1-q) + x_o y_x - q x_x y_o \ ,$$

$$y_m\left(\frac{x_o - q x_x}{1-q}\right) + x_m\left(\frac{y_x - q y_o}{1-q}\right) = x_m y_m + \left(\frac{x_o y_x - q x_x y_o}{1-q}\right). \tag{4.7}$$

With the following substitutions,

$$\alpha = \left(\frac{x_o - q x_x}{1-q}\right), \quad \beta = \left(\frac{y_x - q y_o}{1-q}\right), \text{and} \quad \gamma = \left(\frac{x_o y_x - q x_x y_o}{1-q}\right),$$

Equation (4.7) can be further simplified

$$\alpha y_m + \beta x_m = x_m y_m + \gamma \tag{4.8}$$

$$x_m y_m - \alpha y_m = \beta x_m - \gamma$$

$$y_m(x_m - \alpha) = \beta x_m - \gamma$$

$$\boxed{y_m = \frac{\beta x_m - \gamma}{(x_m - \alpha)}}. \tag{4.9}$$

Equation (4.9) describes a hyperbola; this is more obvious when it is placed in an alternate form. Equation (4.8) is subtracted from a cross term on both sides of the equation,

$$\begin{array}{cccccc} & & & +\alpha\beta & = & +\alpha\beta \\ -x_m y_m & -\alpha y_m & -\beta x_m & & = & -\gamma \\ \hline \\ x_m y_m & -\alpha y_m & -\beta x_m & +\alpha\beta & = & \alpha\beta \quad -\gamma \end{array}$$

and then factored

$$\boxed{(x_m - \alpha)(y_m - \beta) = \alpha\beta - \gamma}.$$

Here α and β are vertical and horizontal asymptotes, respectively, which constrain end member isotope ratios, but typically over-estimate the difference between the end memebers.

The above equations predict 43/48 vs. 87/88 ratios of a mixture should trace out a curve from natural to fully spiked with curvature depending on the relative Sr/Ca of the two portions. The position of a sample on this curve is a function of the proportion of new growth (f or χ_x). Figure 4.25 shows that 43/48 vs. 87/88 of coral micro-samples in this study compare well with a mixing line calculated assuming a q near 1 (similar initial and final Sr/Ca).

Isotope ratio measurements are plotted separately for each coral in Figure 4.27. Sub-samples of coral grown at higher aragonite saturations show greater mole fractions of new growth. The type of sub-sample, whether it came from a gentle scrape on the coral surface or is composed of broken septa, also affects the observed mole fraction of new growth. Sub-samples with the most new growth generally follow the order: surface scrape > spines > more vigorous scraping > bottom of polyps and septa. This result was used to choose candidate samples for nanoSIMS analysis. Taken together, this data also suggests more growth probably occurred in coral grown at higher Ω, but it is possible that high mole fractions of new growth were not sampled in low Ω coral.

Table 4.7: Nubbin samples for calcification rate by $^{43}Ca/^{48}Ca$ isotope bulk analysis. Polyp number is easy to count on these small and irregularly sized samples. It is also the basic unit of the coral ultrastructure. For this reason polyp number and surface area are used as normalizing factors for calcification rate. On two nubbins of coral, both the total number of polyps and surface area were measured, yielding 70 polyps cm^{-2}, the factor used to convert between polyp and surface area normalized calcification rates in this study.

Ω	Reservoir/Coral	# polyps	mass (mg)
4.9	1/9	7	9.92
4.0	4/3	8	14.98
3.4	2/5	10	34.77
2.9	10(3)/7	4	7.59
2.7	9(5)/6	8	15.84

To more systematically calculate calcification rates from 43/48, similar wedge shaped samples were taken from each coral and analyzed. These samples contain several polyps and are expected to integrate and average the contribution of different skeletal regions to growth. Each small sample (10–30 mg) was cut from the top of a nubbin using a dremel tool, resulting in similarly sized

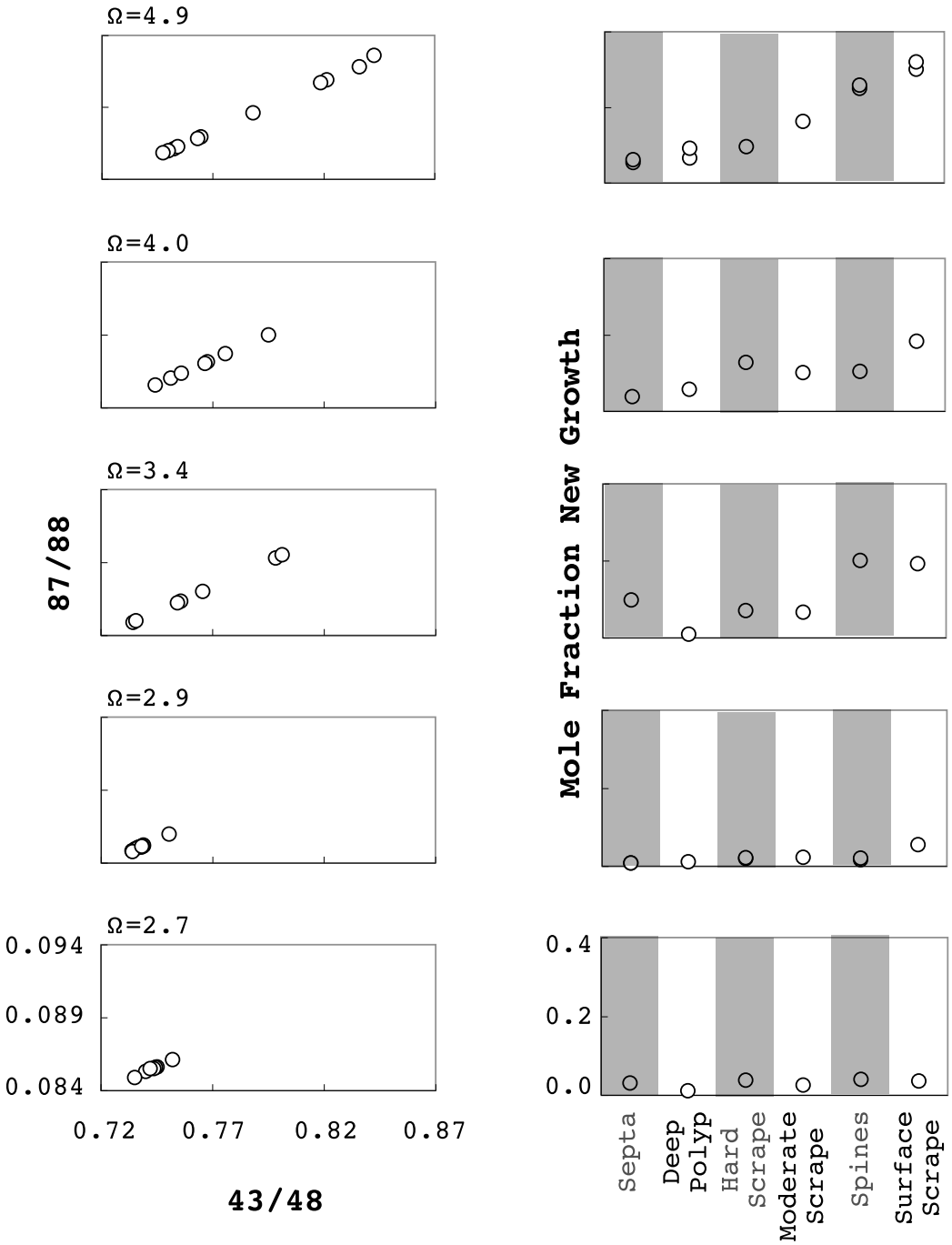

Figure 4.27: **LEFT:** Isotope ratios of coral micro-samples plotted separately by growth condition show the extent of isotope incorporation increases from bottom to top, following aragonite saturation (Ω). **RIGHT:** Mole fraction of new growth for each micro-sample depending upon the skeletal region, calculated from 43/48. New growth is regionally distributed with the highest proportions of new growth found in the spines or by gently scraping the surface. The septa and material deep in the polyps typically exhibit the smallest fraction of new growth. All plots in each column have identical axes.

portions of the nubbin tip (Table 4.7). Samples were weighed on a microbalance, ground in a mortar and pestle, subsampled, dissolved in trace metal clean nitric acid, and analyzed for calcium and strontium isotope ratios as described in the methods section. The amount of new growth was determined from Equation 4.4 and the total mass of the sample, an adaptation of the stable isotope method for relative growth rates in foraminifera described by Lea et al. (1995). Calcification rates were normalized to surface area and number of polyps in the sampled region. Figure 4.28 shows 43/48 derived calcification rates as a function of aragonite saturation. Calcification rate generally increases with aragonite saturation (Ω) and culture solution $\left[CO_3^{2-}\right]$. There is a three-fold difference in calcification rate between the lowest and highest treatments. A very high calcification rate for the second to highest carbonate ion concentration (Ω=4.2) exceeds this trend, but does match a similar results from alkalinity based growth rates (Figure 4.24). The subsamples taken for isotopic analysis were removed from the top part of the coral, a region associated with higher than average growth rates in other studies. Sampling from a high growth region may contribute to the approximately two-fold higher rate of calcification by ^{43}Ca compared to the alkalinity method.

Bulk isotope analysis can also be used to determine the Sr/Ca of skeletal material grown during the culture experiment. First, Equation (4.5) is used to determine q for each micro-sample. At higher mole fractions of new growth, the there is a larger isotope ratio signal compared to natural abundance and q is less scattered (Figure 4.29). For this reason, micro-sample data are not used for compositional calculations where the mole fraction of new growth is less than 0.035. To determine the Sr/Ca of the experimentally grown material from q the initial Sr/Ca of each micro-sample must be known. An average initial Sr/Ca is estimated from measurements on the two $t = 0$ corals sacrificed at the beginning of the culture experiment. The average Sr/Ca and Mg/Ca of several skeletal measurements in these initial coral is 9.5 $\pm$ 0.2 mmol/mol and 4.8 $\pm$ 0.7 mmol/mol, respectively (Figure 4.30). The 2.3% and 14% variability in initial Sr/Ca and Mg/Ca is a major limit on using bulk micro-sampling and spike ratios to calculate the the composition of new growth. The mean Me/Ca ratios do seem to vary systematically, with high Sr/Ca in the septa, for example. Given the already large varibailty in q of $\sim$ 4%, this bias is ignored, but would have to be considered in higher

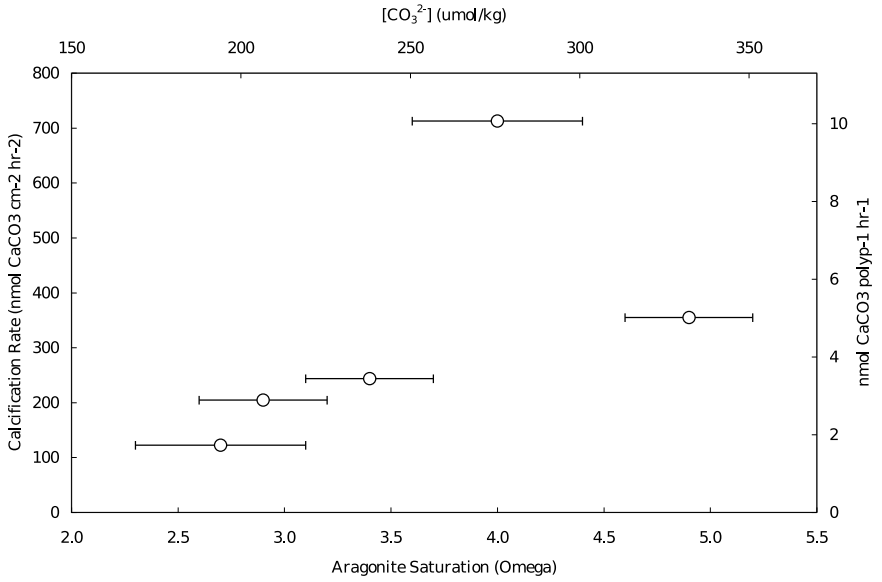

Figure 4.28: Carbonate ion effect on calcication rate by bulk $^{43}Ca/^{48}Ca$ isotope ratios of coral nubbin samples. Calcification rate generally increases with aragonite saturation (Ω) and culture solution $\left[CO_3^{2-}\right]$. There is a three fold difference in calcification rate between the lowest and highest treatments. A very large calcification rate for the second-to-highest carbonate ion concentration (Ω=4.0) does not fit this trend, but does match a similar results from alkalinity based growth rates (Figure 4.24). Horizontal bars represent the full range, over all time points, of calculated $\left[CO_3^{2-}\right]$ for each treatment rather than the smaller uncertainty in the mean $\left[CO_3^{2-}\right]$. Uncertainty in calcification rate is not plotted. Multiple samples from each coral could ideally be used to assess uncertainty in coral calcification rate. The subsamples taken for isotopic analysis were removed from the top part of the coral, a region associated with higher than average growth rates in other studies. Sampling from a high growth region may contribute to the approximately two fold higher rate of calcification by ^{43}Ca compared to the alkalinity method.

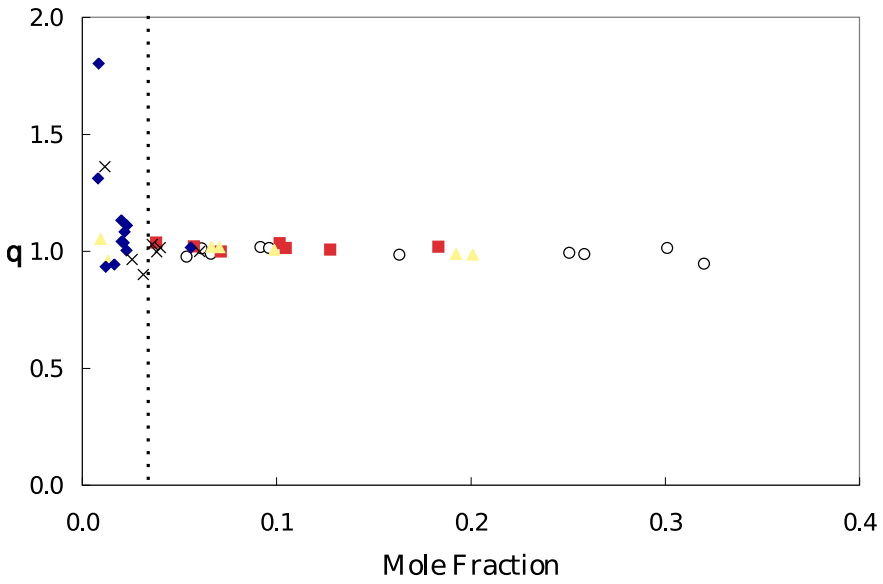

Figure 4.29: q, the relative Sr/Ca ratio of initial and new growth, exhibits higher scatter at low mole fractions due to the small enriched isotope signal. Calculations of new growth region Sr/Ca only use data from micro-samples with mole fractions greater than 0.035 (points to the right of the vertical dashed line). Coral micro-samples labeled by here by growth condition: (◯) Ω=4.9; (■) Ω=4.0; (▲) Ω=3.4; (♦) Ω=2.9; (×) Ω=2.7.

precision work. The average Sr/Ca of newly grown material does not differ significantly between the different growth conditions when qualified by the sizable uncertainty. From the combined data of all coral micro-samples with mole fractions of new growth greater than 0.035, the Sr/Ca of the newly grown material is calculated as 9.6 ±0.4 (2σ std. dev., n= 27). This method could be improved by increasing spike enrichment for higher precision and by applying a technique to exactly determine the initial composition of each sample; details of these improvements will be described elsewhere.

Barium isotope data was also collected for coral micro-samples, however, culture solution barium isotope data was not measured. An attempt was made to estimate the end member isotope ratio of the culture solution by fitting all measured pairs of 136/138 and 43/48 to the mixing equation with two tunable parameters, q and $(136/38)_x$. The Matlab-based fitting method minimizes the sum of the squares of the difference between model and data using the multi-dimensonal optimization function *fminsearch*. High 136/138 data points were weighted to be more significant in the fit to minimize the problems seen at low q in the 87/88 vs. 43/48 analysis. The resulting q and $(136/38)_x$ were sensitive to the initial seed value, or guess, but values that fit the data and where the mixing line

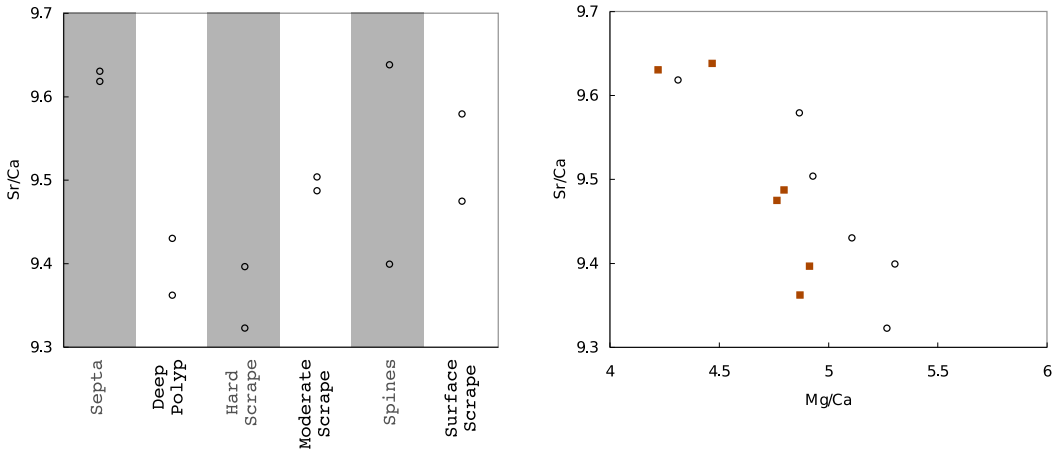

Figure 4.30: Me/Ca ratios of initial coral skeleton from ID-ICP-MS measurements on two individuals sacrificed at $t = 0$. To test if initial Me/Ca ratios in this experiment vary with gross skeletal region, the same types of micro-samples were collected in these coral as was done for the spiked samples. The average Sr/Ca and Mg/Ca of several skeletal measurements in these initial coral ($t = 0$) are 9.5 $\pm$ 0.2 mmol/mol and 4.8 $\pm$ 0.7 mmol/mol, respectively. **LEFT:** In the context of large variability, septa exhibit the highest Sr/Ca while material deep in the polyps or skeletons show the lowest Sr/Ca. **RIGHT:** Sr/Ca decreases with increasing Mg/Ca reminiscent of micro-milling data from deep-sea coral. Different symbols distinguish samples from two separate nubbins sacrificed at $t = 0$. The patterns of Me/Ca in this coral may be atypical of natural samples as the sample resided in an aquarium with non-seawater minor metal composition for many days prior to being sacrificed. Regardless, all coral in the experiment experienced a similar set of conditions prior to the culture experiment and the average composition of initial coral can be estimated from the data in these plots.

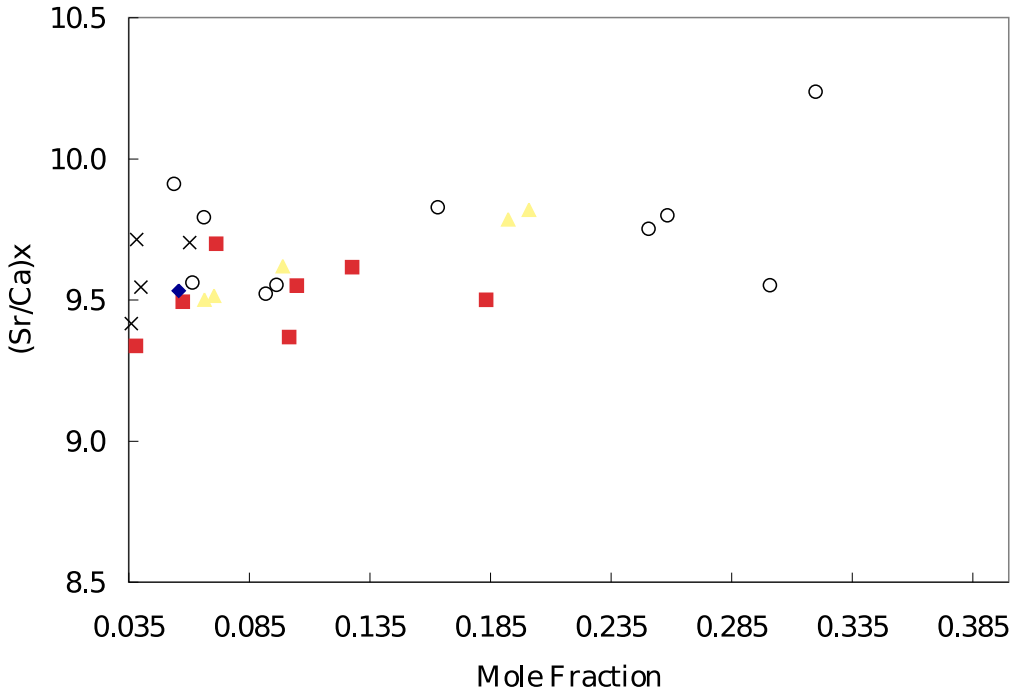

Figure 4.31: Calculated Sr/Ca of new growth from bulk isotope measurements on coral micro-samples. Coral micro-samples labeled by growth condition: (◯) Ω=4.9; (■) Ω=4.2; (▲) Ω=3.5; (♦) Ω=2.9; (×) Ω=2.5. The results are characterized by large variability, which is expected given the moderate spike enrichments and uncertainty in initial coral composition for each micro-sample. The mean of coral grown at Ω=4.9 is slightly higher than the combined mean, while the next lowest Ω, 4.2, averages slightly lower than the combined mean. That these samples represent the two highest enrichments suggests there is no systematic trend in the bulk isotope derived Sr/Ca vs. Ω. Combining data from all growth conditions, the mean Sr/Ca of newly grown material is calculated as 9.6 ±0.4 mmol/mol (2σ std. dev., n= 27). The Sr/Ca of micro-samples from coral grown at Ω=3.5 appears to slightly increase with mole fraction.

appears to pass through most of the data are $q \sim 0.35$, $(136/138)_x \sim 3.2$. This approach assumes that the q of all corals are identical, which is an untested assumption. Clearly an independent measure of the culture water barium isotopes is preferred. The measured data, mixing model and estimated solution 136/138 are shown in Figure 4.32. The barium isotope ratio 136/138 for each coral and by skeletal region is summarized in Figure 4.33, showing similar patterns as the 43/48 data: the maximum extent of enrichment increases with Ω and the immediate surface and spines are also most enriched in ^{136}Ba.

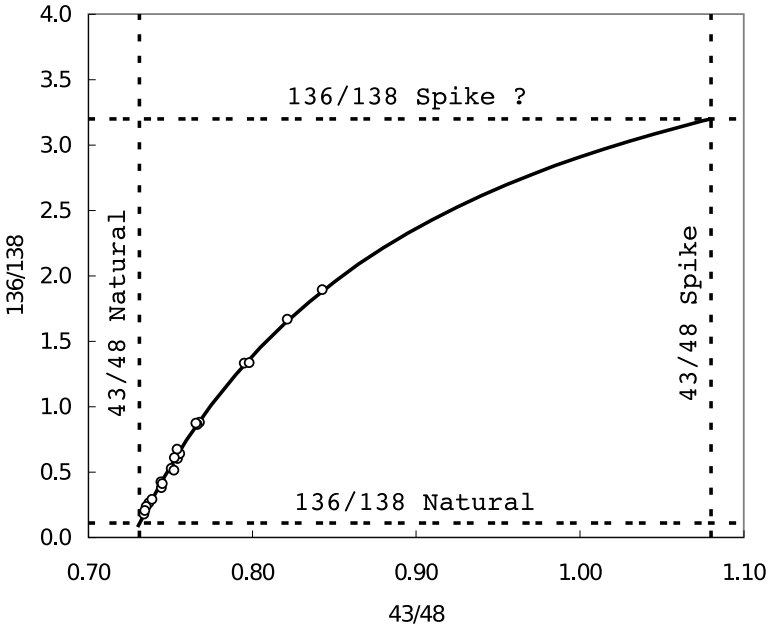

Figure 4.32: (◯) Barium isotope ratios of coral micro-samples shows incorporation of ^{136}Ba, demonstrating skeletal growth during the experiment and co-precipitation of barium. (Solid line) Data were fit to a 2-end memeber mixing line by adjusting the unknown parameters q and the 136/138 of the spike end-member as described in the text. The estimated values from the fit are $q \sim 0.35$, $(136/138)_x \sim 3.2$.

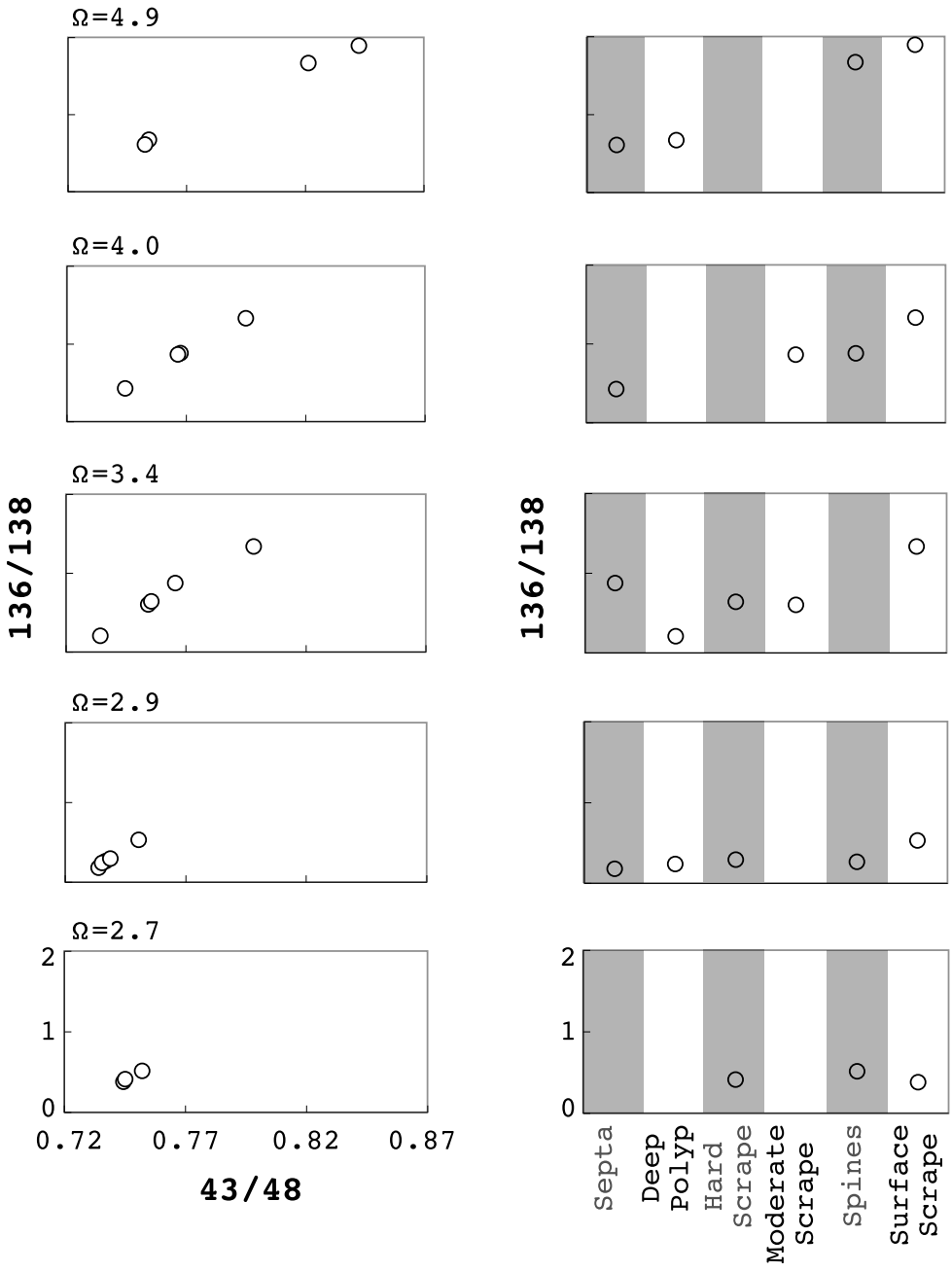

Figure 4.33: **LEFT:** Barium isotope ratios of coral micro-samples plotted separately by growth condition show the extent of isotope incorporation increases from bottom to top, following aragonite saturation (Ω) like 43/48 and 87/88. **RIGHT:** The 136/138 ratio is still plotted on the y-axis, but the data are seprated depending upon the skeletal region. New growth is regionally distributed following a similar pattern as 43/48, but with a larger relative signal reflecting the higher culture solution enrichment in ^{136}Ba. All plots have identical y-axes.

4.8 Calcein Fluorescence Maps Experimentally Grown Skeleton at the Micron Scale

In total $\sim$ 960 coral "spines" were mounted, polished, and surveyed for calcein fluorescence. Most mounted coral pieces did not fluoresce. Out of each hundred spines surveyed between 1 to 3 were promising candidates with measurable new growth beyond a clear calcein label (Figure 4.34 and Table 4.8). The relative scarcity of candidate spines suggests episodic growth, either during the 6-hour calcein labeling period or during the entirety of the 6-day experiment. Two controls support the conclusion that calcein marks the beginning of the coral culture experiment: (1) spines prepared from a coral skeleton that was never exposed to calcein do not fluoresce; (2) several spines from a $t = 0$ coral sacrificed just after the calcein labeling experiment fluoresce on the outer surface but show no evidence of additional growth. Additional calcein images of each spine with the location of nanoSIMS spots or images are included below in the nanoSIMS image section.

Table 4.8: Frequency and distribution of candidates spines with measurable new growth beyond a clear calcein label.

Ω	Reservoir/Coral	Total Pieces Surveyed	Candidate Spines
4.9	1/9	222	2
4.0	4/3	173	5
3.4	2/5	183	3
2.9	10(3)/7	195	5
2.7	9(5)/6	190	2

Coral spine growth is anisotropic. The aspect ratio of most candidate spines is about 2:1 (length:width), although it ranges from 0.5 to 3. Of course, the length of spines prepared during this experiment is controlled by the break-point and likely depend as much on the sampling technique as geometry. It is clear, however, that spines do grow more along the major axis than on the sides, both from the basic spine morphology and calcien images. Linear growth was measured perpendicular to the calcein label towards the outer surface along the major geometrical dimension. Linear growth measured for all 15 candidate spines range from 90 to 5 μm (Figure 4.35). The coral grown at Ω=2.9 exhibited high and more variable linear growth, while the lowest [CO_3^{2-}] treatment

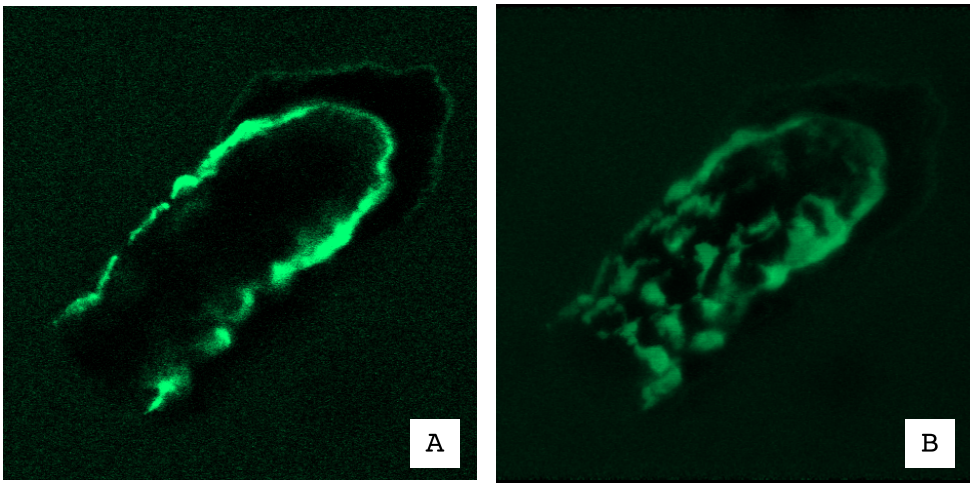

Figure 4.34: Bright green calcein fluorescence marks the junction between initial skeletal material and new growth in these confocal microscopy images. **(A)** Image of a mounted and sectioned spine in the plane of the polished surface. A faint green line reflected from the edge of the coral marks the outside edge of the spine. Faint edge effects are probably seen because excitation and emission wavelengths are similar resulting in some leakage of reflected light through the filters into the detector. This reflected background signal is clearly distinguishable from the more intense calcein fluorescence. This ~ 90 μm long spine is A2 from Coral 1/9 grown at Ω=4.9. **(B)** A series of fluorescent images taken successively deeper into the coral spine were used to construct a 3-D projection of the labeled calcein surface. In this image the plane of the sample is at the bottom as if one is looking up into a the sample, so deeper is up. The convex down surface marks what this spine looked like at the beginning of the coral culture experiment. Bright regions on the surface match the external texture of spines from SEM images (Figure 4.2) and suggest that over short periods of time growth may occur in spatially discrete units.

spines (Ω=2.7) also show the lowest linear growth at 9 and 5 μm. Only 6 of the labeled "spines" exhibit prototypical long and skinny geometry. If the linear growth of only these similarly shaped samples coral are compared the same general trends remain: Ω=2.9 shows exceptional growth and the low Ω coral grew the least. By assuming continuous growth over the 6-day experiment the lower bound for linear coral growth rate is estimated as 0.8–15 μm/day. Houlbreque et al. (2009) made NanoSIMS images of 86Sr incubations in the massive coral *Porites porites* observing variable growth rates between 1.6–3 μm/day, near the typical value of my experiment .

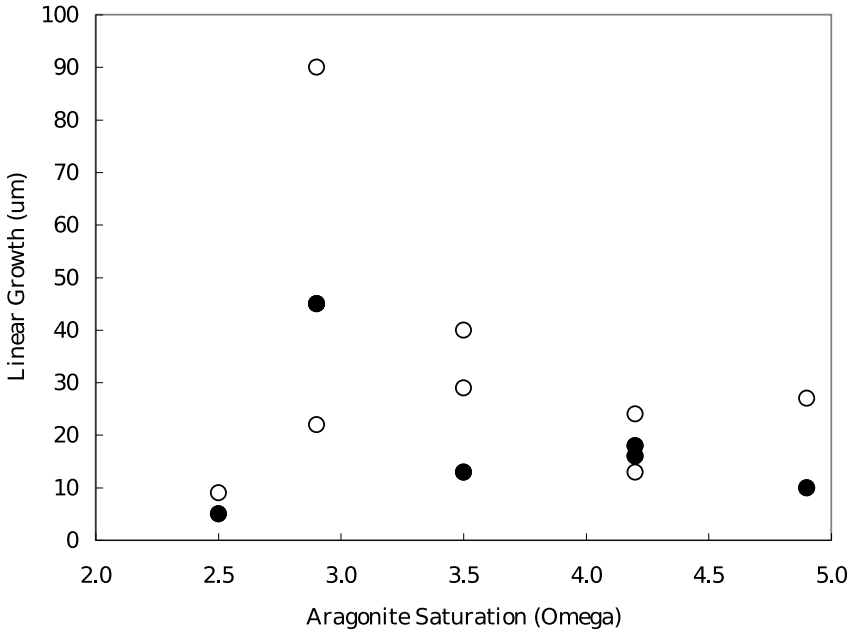

Figure 4.35: (◯) Length of new growth in 15 calcein labeled spines spanning all culture conditions. (•) Growth data for spines with prototypical long and skinny geometry. Both the complete data and the smaller subset of similarly shaped spines follow the same patterns: (1) the coral grown at Ω=2.9 grew longer and with more variability than other treatments, (2) the lowest [CO_3^{2-}] coral grew the least.

Polishing does not produce a prefect longitudinal plane through the center of each spine, potentially biasing the the apparent linear extension. The effect is not as significant in spines where geometry can help distinguish if the sample is cut in a roughly longitudinal section or if the section is more transverse. In inorganic precipitation experiments, where spherical samples are common, chord planes could substantially bias estimates of linear growth. In future work something that identified a center line, either from skeletal morphology or induced by artificial labeling may be

useful to guide polishing. About 100 spines need to be prepared for each candidate so it may not be practical to perfectly section every sample.

4.9 NanoSIMS Image Analysis of the Experimentally Grown Coral Skeleton

Ion Image Maps: The bulk isotope measurements presented above prove that isotopes enriched in the culture media are incorporated in the coral skeleton, demonstrating both new growth and exchange between ions in seawater and the calcifying fluid. However, these bulk measurements only reveal the pattern of spike incorporation at a gross scale. Guided by fluorescence maps, 20x20 μm isotope images were collected using the nanoSIMS at the calcein margin in an attempt to isotopically, compositionally, and geometrically characterize new growth. At least one spine from each culture condition was analyzed. Images of both 43/42 and 87/88 show a clear continuous boundary between the pre-experiment un-spiked initial skeleton and new growth incorporating enriched isotopes. These data are summarized in Figures 4.36–4.48. Intensity maps of the trace ions 136Ba and Tb also show a similar pattern as the other enriched isotopes. Intensity maps are used for 136Ba, because very few counts of the normalizing ion 138Ba were collected. During "combined analysis" the top trolley where 138Ba was collected often seemed to drift off peak. Images of the unenriched isotope ratio 86/88 are homogenous with no evidence of a growth boundary. Taken together with the even 42Ca intensity images, the 86/88 data argue against the boundary resulting from analytical artifacts or topography. Using post-analysis burn marks, the images were placed on maps of calcien fluorescence. The new growth boundary identified in isotope images agrees surprisingly well with the calcein label. Coral 2/5, spine 1, image 2 is the only example where there may be a gap between the calcien label and the spike boundary. Terbium intensity follows the spike region in all but spine 10(3)/70C, image 6, where very low counts make any pattern hard to discern. The mid-experiment REE spike, which doubled [Tb] seems to have been captured in the lowest Ω spine image 9(5)/6, at about the location predicted by a linear growth age model. As discussed in the methods section, analytical issues likely

confuse the interpretation of gadolinium and dysprosium.

In the new growth region, isotope ratios are homogeneous, with histograms of pixel ratios clearly distributed between a natural abundance population and an isotopically enriched population. Images collected entirely within the new growth region are also isotopically homogeneous (not shown here). Image isotope ratios are corrected for instrumental mass fractionation and differential collector gain by normalizing a region of un-spiked growth to natural abundance. The 43/42 ratio of new growth matches the ICP-MS determined 43/42 of the enriched culture solution suggesting we have mapped the pure new growth end member inferred from bulk analysis of micro-samples (profile data in Figures 4.36–4.48). The 87/88 ratio of each newly grown region is typically somewhat lower than the culture ratio, qualified by precision of low counts from each pixel. One exception is coral spine 9(5)/60A, where 87/88 is higher than the culture value. While it is easy to imagine processes that result in 87/88 lower than the culture solution (like a constant mixing rate with a very slow turn-over internal pool), going higher than the culture media is harder to explain. Therefore an analytical issue may be influencing the accuracy of 87/88 in these images. Spot analysis is used to probe 87/88 and other isotopes with high precision in the experimentally grown skeleton as discussed below.

Much like the pre-sputter study results explored during nanoSIMS spot method development, 88Sr/42Ca and 24Mg/42Ca drift inversely across different planes during image acquisition. The images in this study were collected with varying amounts of pre-sputtering making accurate comparison of Me/Ca ratios between different images difficult. With careful analysis, a stable source, consistent application of the same analytical parameters, and regular images of standards, it seems likely that accurate Me/Ca ratios could be derived from images using a similar approach as spot analysis. In this study accurate Me/Ca ratios of the new growth end member are measured using the proven method of spot analysis, as discussed below. It is still possible, however, to interpret within image 24/42 and 88/42 variability to detect and describe compositional patterns of Mg/Ca and Sr/Ca.

Maps of the elemental ratio 88Sr/42Ca typically show lower Sr/Ca in the natural grown skeleton compared to the experimental growth, although 88/42 is similar across the boundary in two coral

spines. Skeletal material before the culture experiment is likely to be hetergeneous in Me/Ca ratios as a result the dynamic pre-culture aquarium and open ocean environment. The difference in 88/42 between the two regions means that the ratio $q = (88/42)_o/(88/42)_x \neq 1$ in the area near the boundary. From the relative values of 88/42 within each image, q ranges from 0.8 to 1 close to the boundary. Bulk analysis of micro-samples described in Section 4.7 samples much more of the heterogenous initial skeleton, including natural grown material from when the coral was still in the Gulf of Eilat, therefore, it is reasonable to expect differences between the $q \sim 1$ form bulk analysis and the q at a much smaller scale. The ratio q is only important in that it affects the curvature of predicted isotope mixing lines, but it does not impact compositional spot analysis completely within either end-member.

A more interesting observation is a consistent low 24Mg/42Ca band just inside the initial material from the spike boundary. This pattern is observed in all three images where 24/42 was collected. The pattern may reflect the solution chemistry of the calcien labeling solution where $Ca(OH)_2$ was added to increase alkalinity and encourage growth, effectively reducing the Mg/Ca of the solution. To adjust flow-through chamber culture solution alkalinity, NaOH and HCl were used rather than $Ca(OH)_2$, so low 24Mg/42Ca is not expected in the experimentally grown region. If this interpretation is correct, it is further evidence that skeleton grown during the calcein labeling period directly contacts the new growth boundary.

Dynamics at the New Growth Boundary: Compared to the 10s of microns of linear growth in most spines, there is a sharp boundary between unlabeled and the experimentally grown stable isotope enriched skeleton. Profiles of $^{43}Ca/^{42}Ca$ across the new growth boundary in several spines show an abrupt transition between natural abundance ratios and a spike ratio matching culture solution (Figures 4.36–4.48). The 43/42 response lengths of seven profiles from six spines range from 1.2–2.0 μm, where response length is defined as the distance it takes for the the 43/42 signal to rise from 16% to 84% of the enriched value. This is the same definition used to define nanoSIMS spot size from profile across compositional boundaries, allowing easy comparison between the two values. For a simple one-box reservoir exchanging directly with seawater the 16% to 84% response

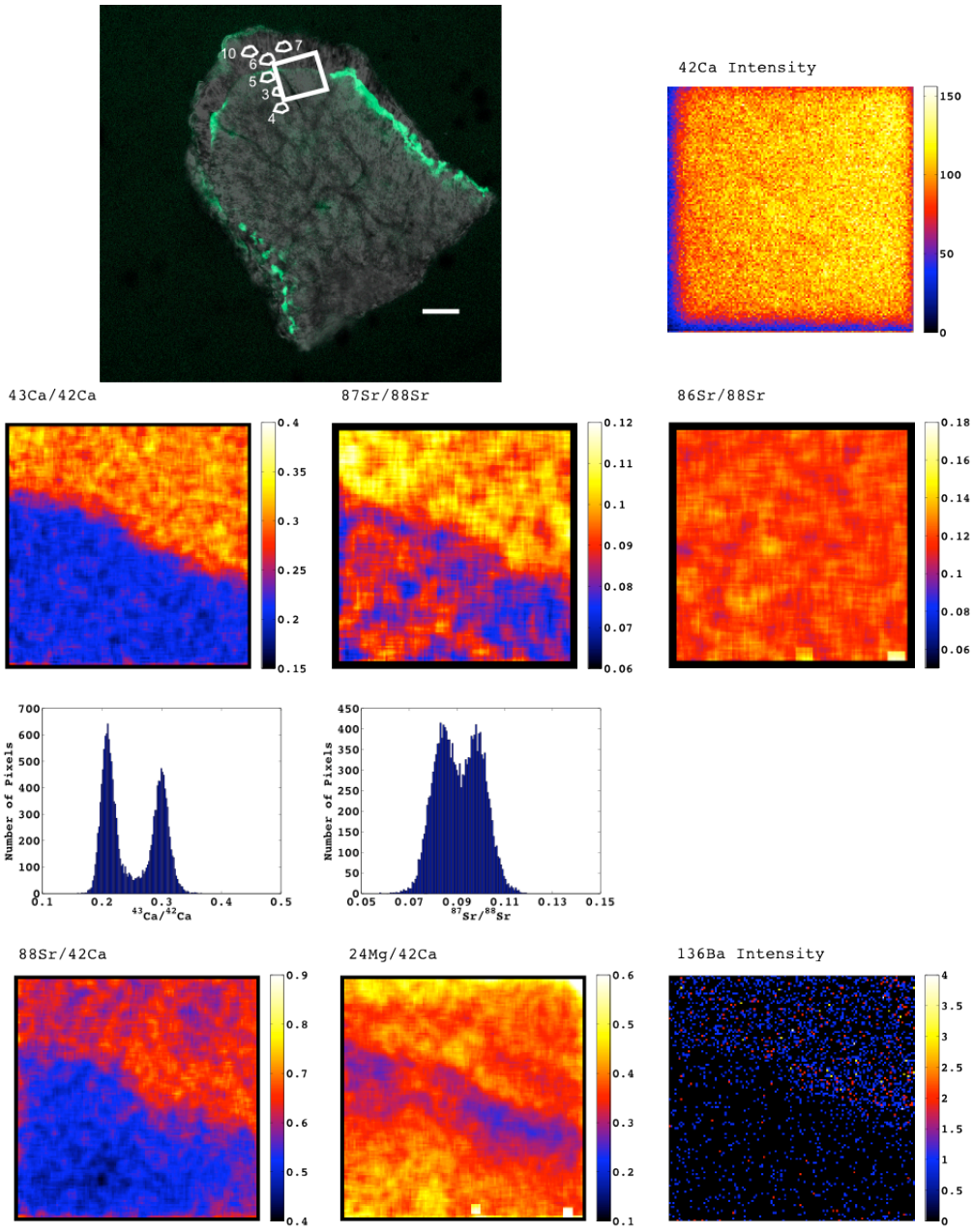

Figure 4.36: A 20x20 μm nanoSIMS ion image shows clear a continuos boundary in 43/42, 87/88 and 136Ba intensity at the junction between initial skeleton and new growth in Coral 4/3, Mount AA, Spine A2, Image 1 grown at Ω=4.2. This boundary corresponds to the calcein margin as demonstrated when the post-analysis image burn mark is placed on a map of coral fluorescence (scale bar 20 μm). Histograms of pixel ratios clearly distributed between a natural abundance population and an isotopically enriched population. Images of the unenriched isotope ratio 86/88 are homogenous with no evidence of a growth boundary. Taken together with the even 42Ca intensity images, these data argue against the boundary resulting from analytical artifacts or topography. 88Sr/42Ca show a typical pattern of lower Sr/Ca in the natural grown skeleton compared to the experimental growth. A consistent pattern of low 24Mg/42Ca just inside the initial material from the spike boundary is seen in this and other spines. Counts from all planes with even 42Ca images were summed to make these images. The 43/42, 88/42, and 24/42 images were further processed using a 5x5 pixel moving box average; while a 9x9 pixel box was applied to the 87/88 ion image. Black edges mask edge effects from the moving box average.

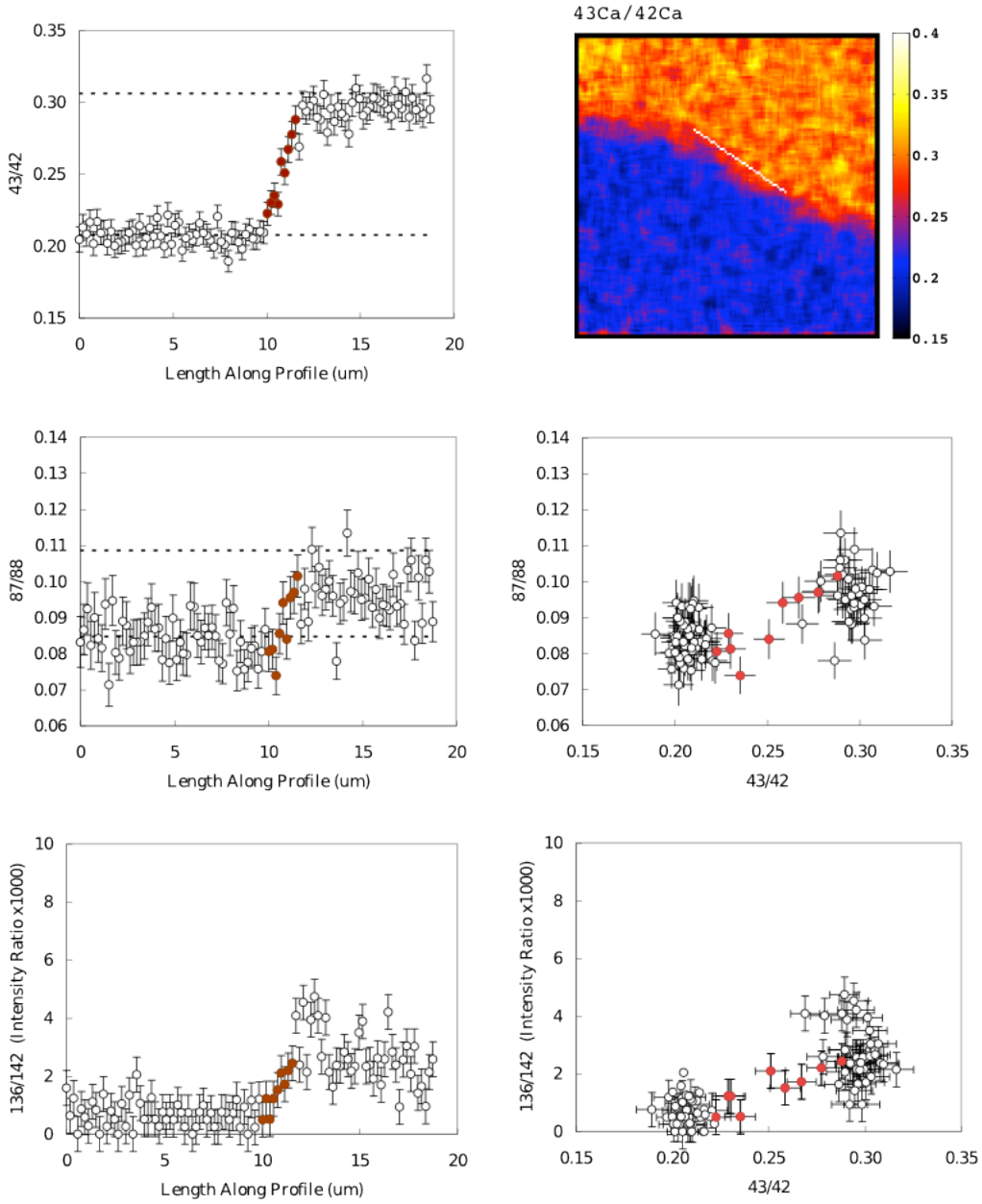

Figure 4.37: Isotope ratio profile taken perpendicular to marked boundary line. Each profile step comes from the sum of counts in the 39 pixels of the profile line marked on the figure. Profile step size is 190 nm. Dashed limes mark natural and spike isotope ratios from ICP-MS measurements. The 16%–84% width of the boundary in the 42/43 image is 1.5 μm. The points in this boundary are marked in red. The same red points are marked in each plot of this figure to help compare 43/42 to 87/88 and 136/42. Error bars are 1σ from counting statistics. For 136Ba, where counts are sometimes zero, the error is estimated from the average counts of similar ratios. In this profile 87/88 and 136/42 may lag 42/43 slightly, although it is hard to tell. As discussed in the text, 87/88 is lower than spike end-member. Profile 1, Coral 4/3, Mount AA, Spine A2, Image 1, Session Ni1.

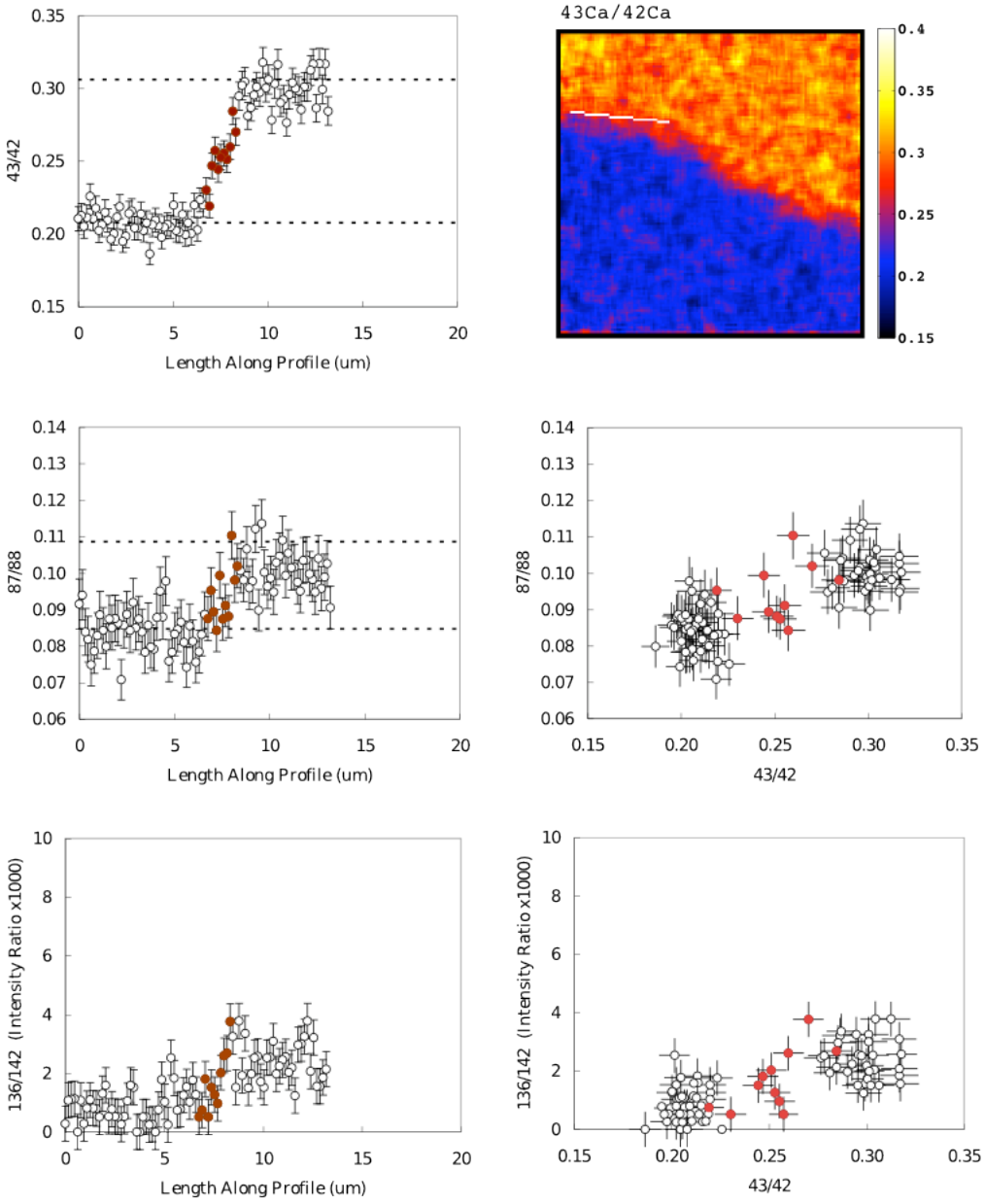

Figure 4.38: In this profile 87/88 may lead, but only by a few points. The two profiles from different locations on this same image give 1.5 and 1.6 microns for the rise time, building some confidence in the analytical procedure. Profile 2, Coral 4/3, Mount AA, Spine A2, Image 1, Session Ni1.

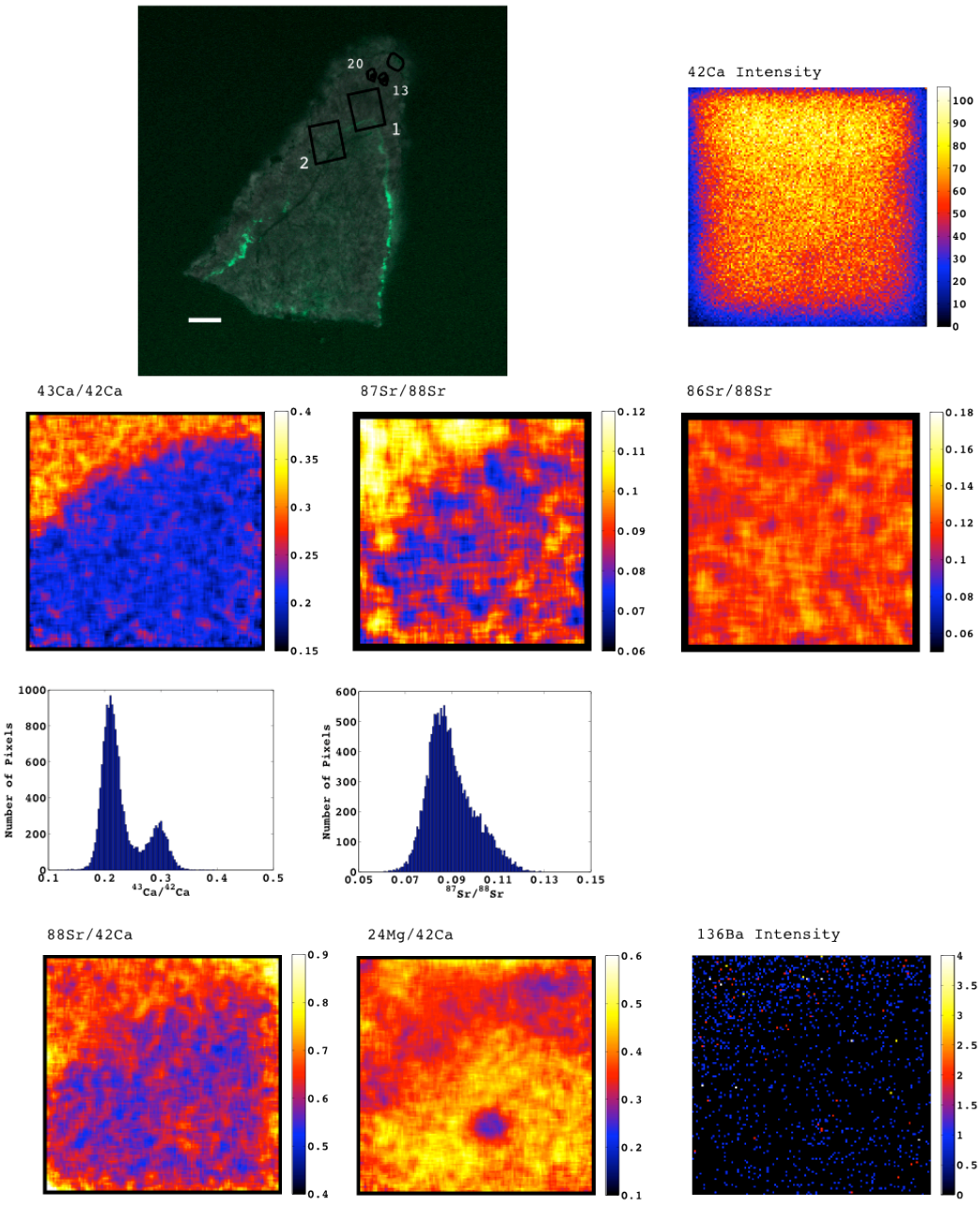

Figure 4.39: NanoSIMS ion image of boundary between initial skeleton and new growth. The low 24/42 spot is not present in other isotope ratios. Coral 2/5, Mount AA, Spine 1, Image 2.

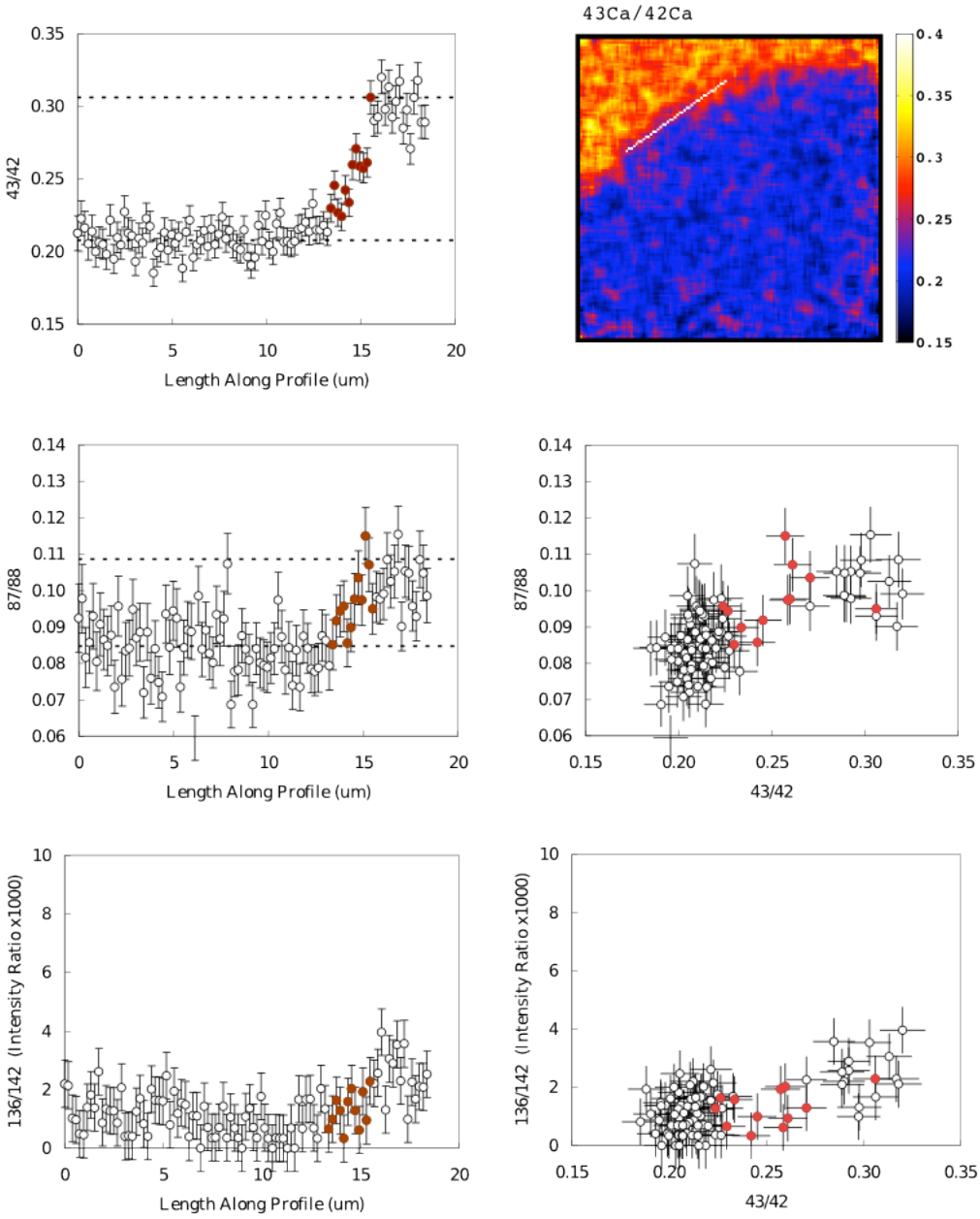

Figure 4.40: This image has roughly twice the counts as the profile for image 1 of the same coral (below). The 43/42 profile may start upwards in a slow rise. While this could mixing into a reservoir, it is also similar to the effect of a profile line hitting the edge of a feature slightly off angle. 87/88 looks synchronous with 43/42. Coral 2/5, Mount AA, Spine 1, Image 2.

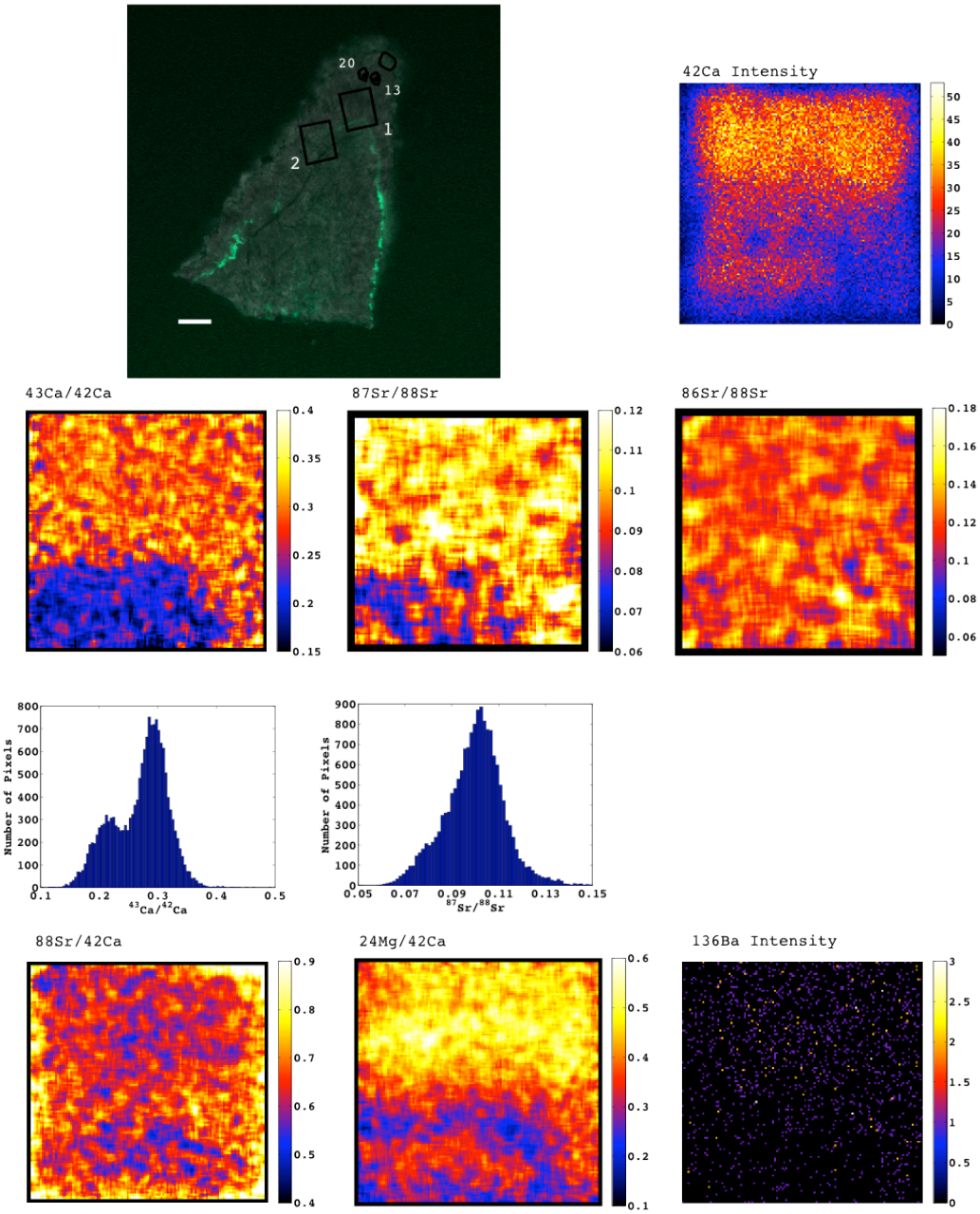

Figure 4.41: NanoSIMS ion image of boundary between initial skeleton and new growth. The 42Ca intensity image for this region is less homogenous than most images, a result of the duo source cutting out during pre-sputtering. Pre-sputtering was re-started after fixing the source but the top of image recived more pre-sputter ions than rest of image. Coral 2/5, Mount AA, Spine 1, Image 1.

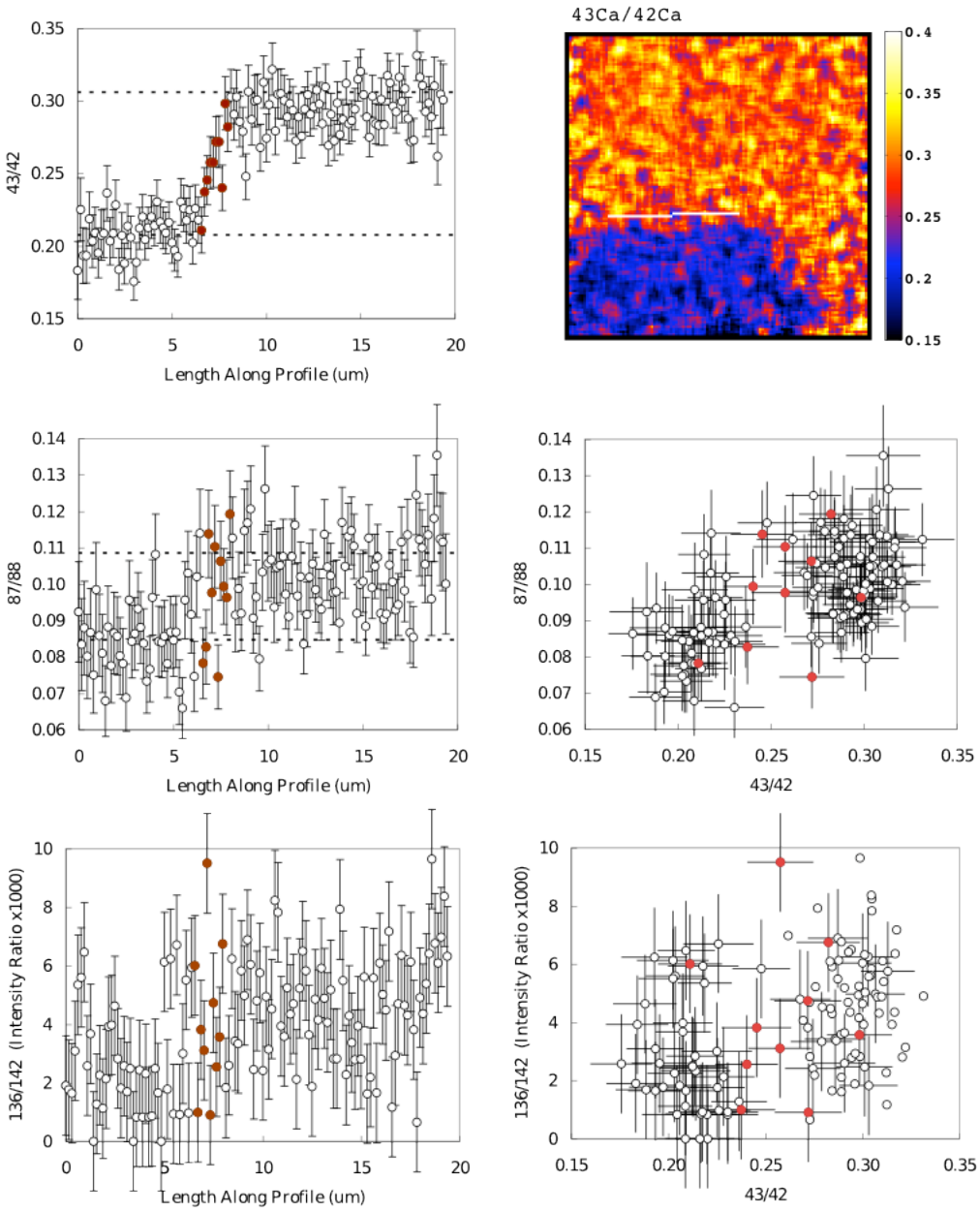

Figure 4.42: This image and profile have fewer counts than the previous two images, a result of few planes with even 42Ca images. High uncertainty makes it hard to compare different isotopes and reject either synchronous or asynchronous timing. This profile rise time is shorter than the other image on this spine but it is the higher growth rate axis, if response time were same the for all profiles then this profile would have been expected to show a longer rise time not a shorter one. Coral 2/5, Mount AA, Spine 1, Image 1.

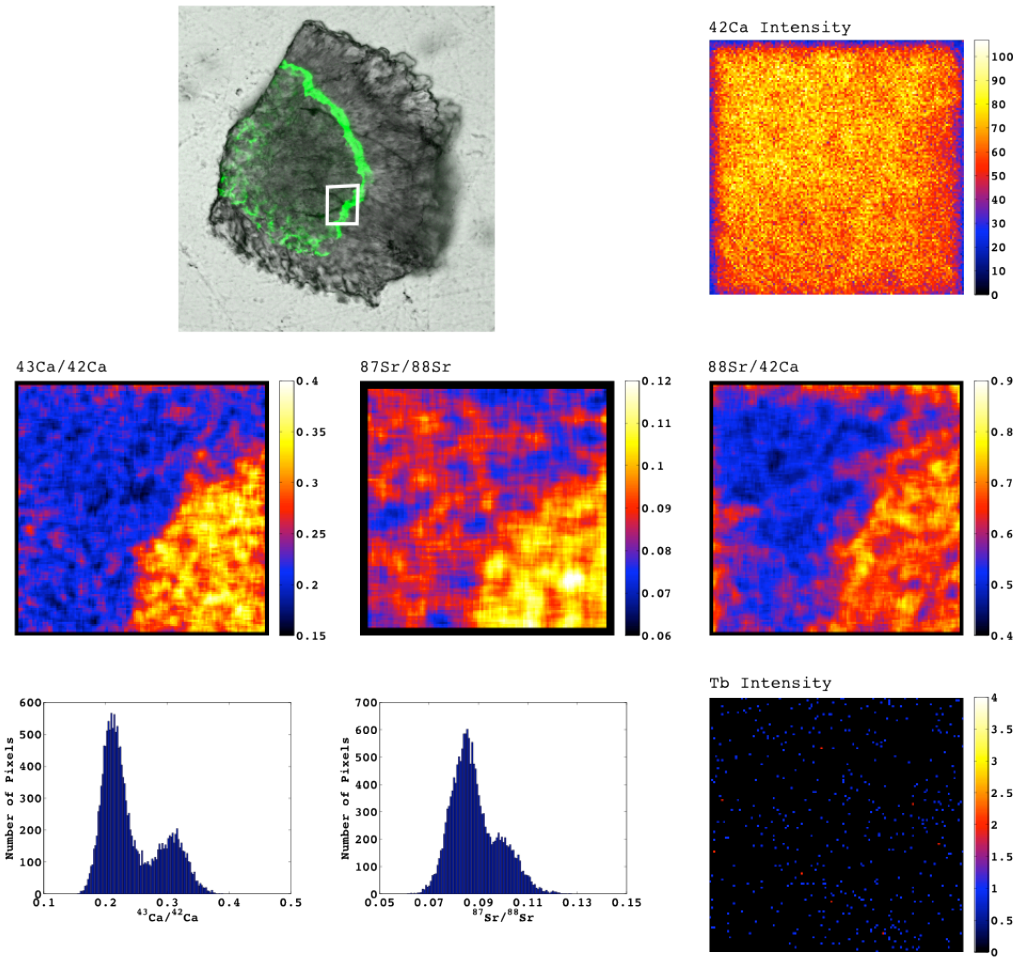

Figure 4.43: NanoSIMS ion image of boundary between initial skeleton and new growth in Coral 10(3)/7, Mount AB, Spine 0C, Image 6. Spine is roughly 130 μm long by 150 μm wide.

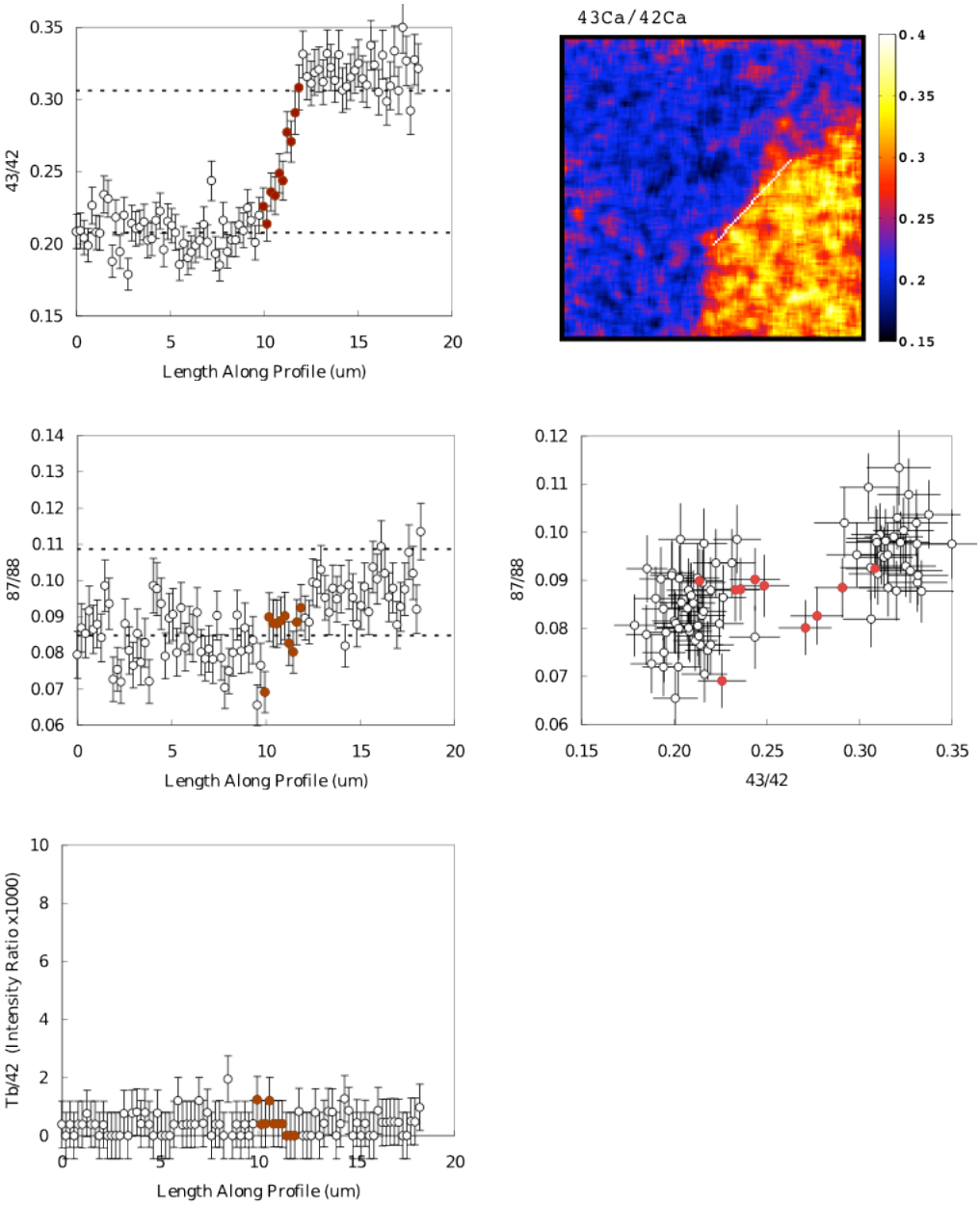

Figure 4.44: This profile is of the boundary along a very high growth rate axis and should best resolve any asynchronicity between different elements. The ratio 87/88 may lag 43/48 by a few points, but it is not very clear. Although differences in dynamics between 43/42, 87/88, and other species cannot be completely ruled out, taking all the profile data together there is no consistent observable difference. Terbium counts for this image are really low which may mean no Tb signal, in contridiction to other images, or that this peak was lost during analysis. Coral 10(3)/7, Mount AB, Spine 0C, Image 6.

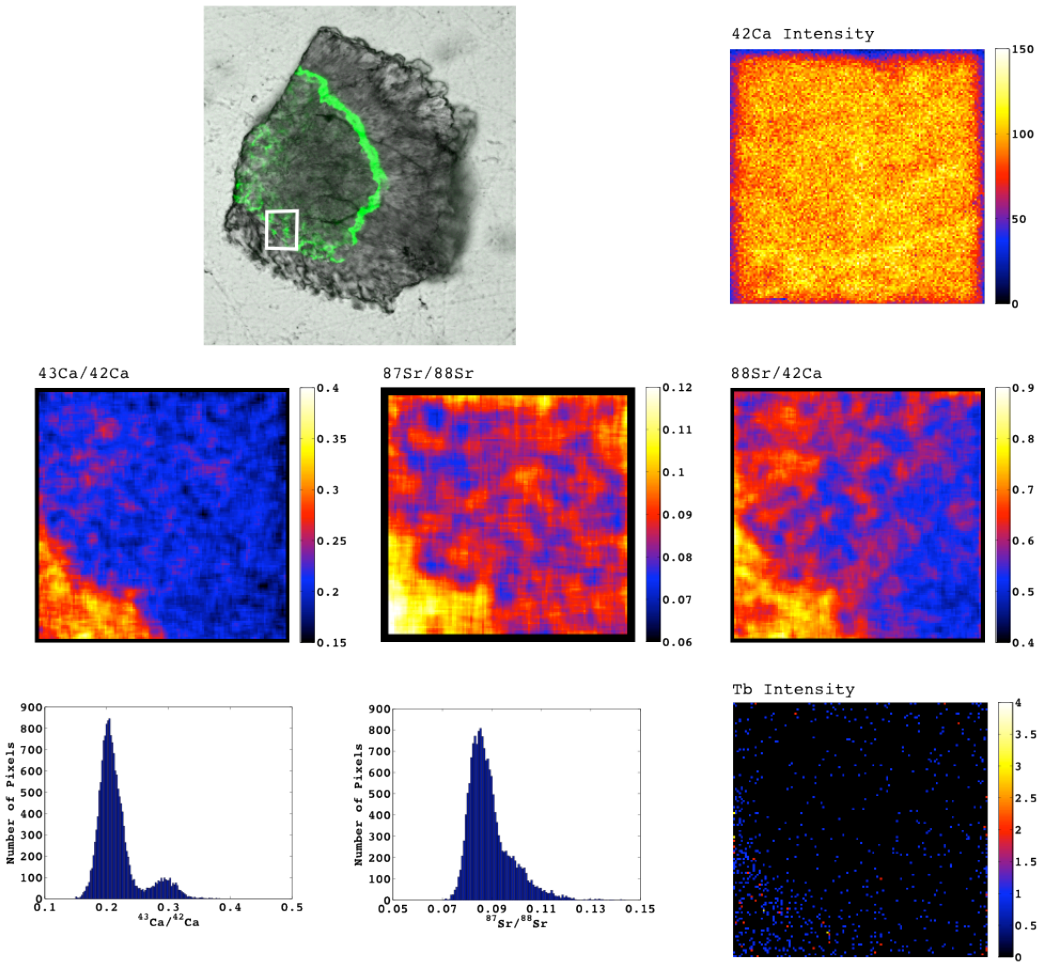

Figure 4.45: NanoSIMS ion image of boundary between initial skeleton and new growth in Coral 10(3)/7, Mount AB, Spine 0C, Image 4. Spine is roughly 130 μm long by 150 μm wide.

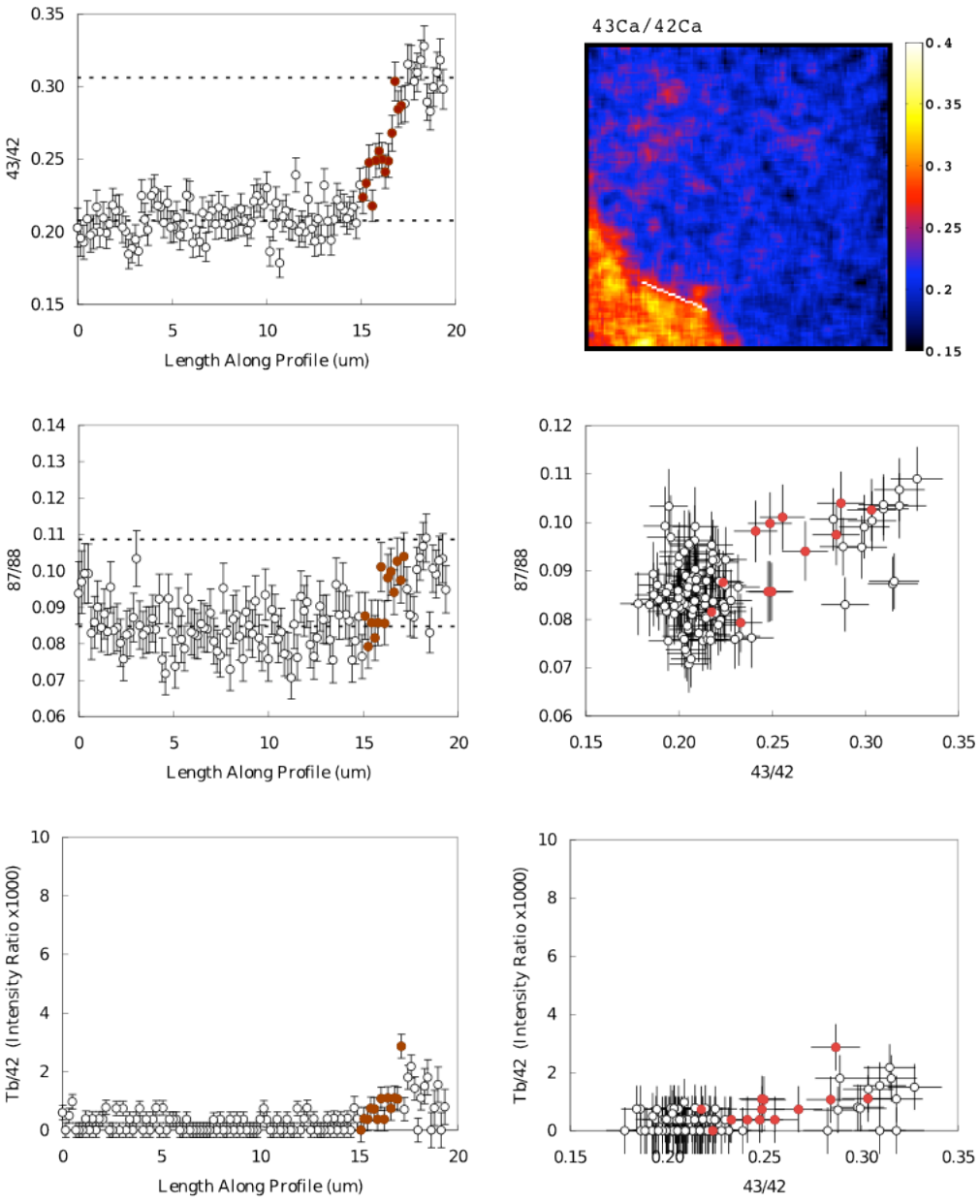

Figure 4.46: The 43/42 response length is similar to the other image on this spine, but these images are from very different growth rate axes. The 87/88 rise is centered on the same place as the 43/48 rise, but looks like a step function as low 87/88 transitions directly to high 87/88. Coral 10(3)/7, Mount AB, Spine 0C, Image 4.

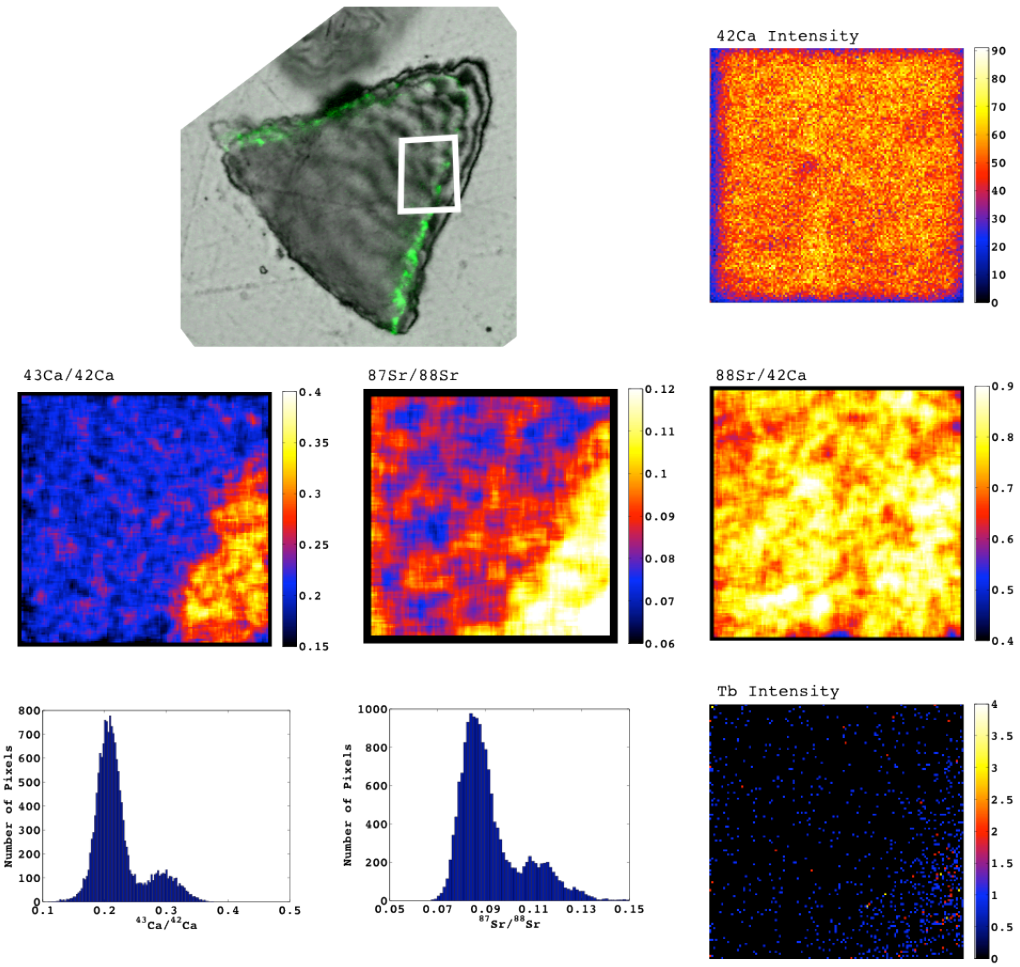

Figure 4.47: NanoSIMS ion image of boundary between initial skeleton and new growth in Coral 9(5)/6, Mount AB, Spine 0A.

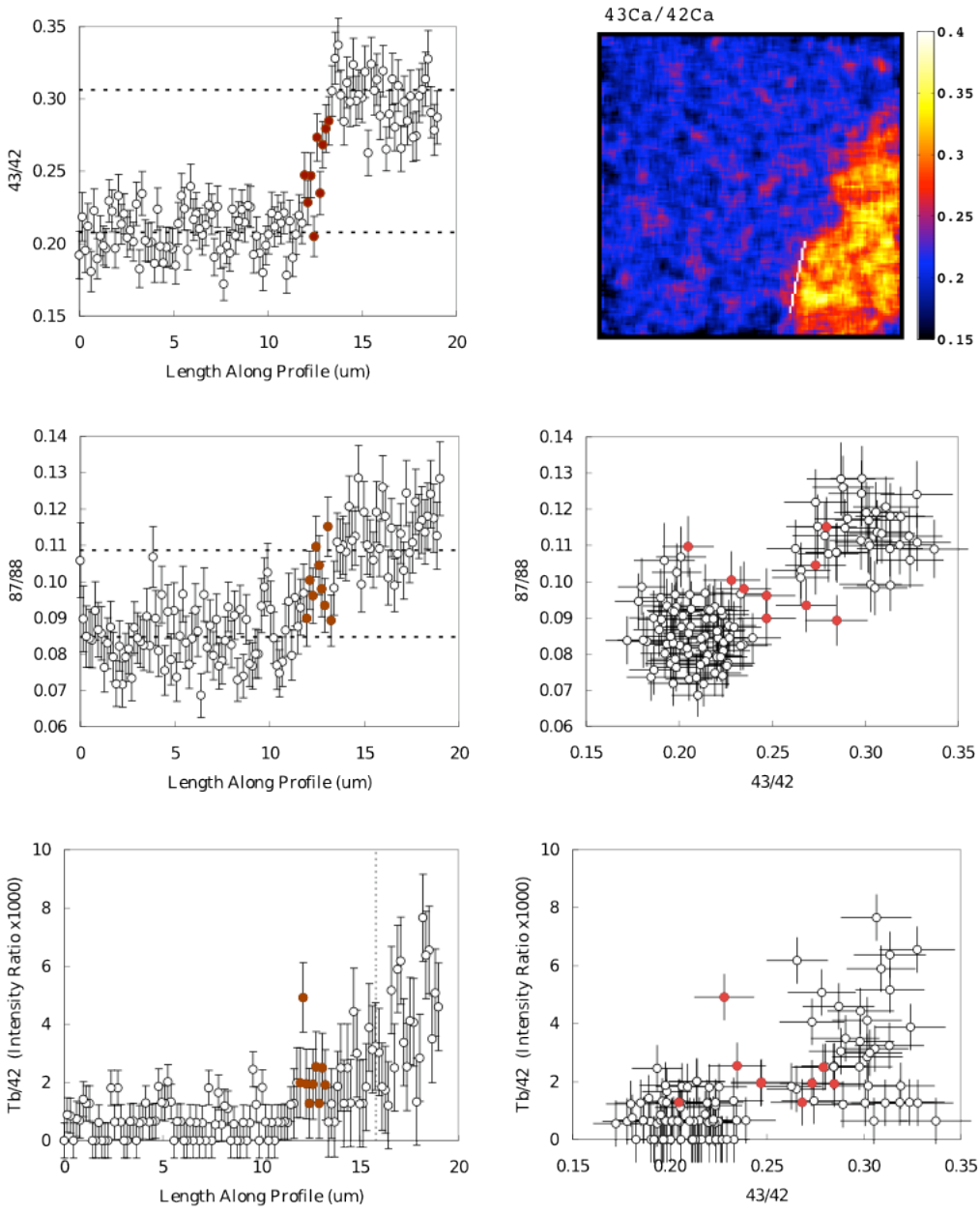

Figure 4.48: Tb/42Ca appears to pass through three values: low Tb, high Tb and higher Tb (closer to edge). Vertical dashed line in Tb/42Ca plot marks the predicted REE spike addition (where Tb was doubled at $\sim$ 50 hours into the experiment). This predicted location was calculated assuming linear growth between the calcein mark and the outer edge of the skeleton over the 133 hour experiment. The transition between high Tb and higher Tb is near the expected location of the mid-experiment REE spike. Unlike most other profiles, 87/88 in this profile is higher than the culture solution ratio. It is easy to imagine processes that result in 87/88 lower than the culture solution (like a constant mixing rate with a very slow turn-over internal pool), but going higher than the culture media is hard. Therefore an analytical issue may be influencing the accuracy of 87/88 in these images. Coral 9(5)/6, Mount AB, Spine 0A.

time is the same as $1.7\tau_e$, where τ_e is the e-folding time.

Distances can be converted into time assuming a linear growth rate between the calcein mark and the outer part of the skeleton drawn from the imaged junction. As described in Section 4.8 above, linear growth rates vary by more than a factor of five between different corals and spines. This means that the small range of 43/42 response lengths result in a range of response time scales from 4 to 20 hours. This variability does not vary systematically with culture conditions. Several processes can affect the 43/42 rise time, possibly explaining the range of observed results.

Both nanoSIMS spatial resolution and processes within the coral during biomineralization affect the response length scale. Two pieces of evidence argue that spot size is not the primary control on measured response lenghts: (1) during session Ni1 the response length is larger than the $\sim$ 800 nm measured spot size (spot size was not determined during session Ni2); (2) response length scale does not differ significantly between the two analytical sessions that were separated by four months—it is unlikely that machine changes combined with differences in tuning resulted in similar primary beam probe sizes. While probe size is finite and acts to somewhat broaden the response length, this effect probably does not dominate the 43/42 profile slope. Even though most profiles were taken across sharp boundaries, no boundary is perfectly straight and irregular edges can act to increase the apparent 43/42 response time. Qualified by limited analytical broadening, the 43/42 profiles can be interpreted as a real signal in the coral.

Converting length to time using initial and final time control points assumes linear growth. In spine 956 the linear growth rate assumption appears to agree with a rise in Tb corresponding to the mid-experiment REE spike. The REE spike is neither predicted nor observed in any of the other profiles. If growth does occur linearly with time in all spines, then the calcifying environment at different parts of the same coral and even within the same spine experience different rates of calcium exchange with the surrounding seawater. This explanation implies that calcification occurs from different ion pools separated by space and/or time and that the e-folding turnover times of calcium and other analyzed elements in these pools range from 2 to 11 hours.

Alternatively, similar response lengths between different spines can be interpreted as evidence for

Table 4.9: Measured response lengths and calculated e-folding time of isotope uptake from image profiles across new-growth boundaries. The e-folding time is calculated from response length assuming linear growth along a growth axis originating from the boundary and drawn perpendicular to the external surface of the spine.

Ω	Response Length (μm)	e-Folding Time (hours)	Reservoir/Coral	Image	Profile	Session
4.0	1.5	5.2	4/3	1	1	Ni1
4.0	1.6	5.6	4/3	1	2	Ni1
3.4	1.2	2.2	2/5	1	1	Ni1
3.4	2	11	2/5	2	1	Ni1
2.9	2	8.5	10(3)/7	4	1	Ni2
2.9	1.8	2.8	10(3)/7	6	1	Ni2
2.7	1.2	11	9(5)/6	1	1	Ni2

a similar rate of calcium exchange. If this is the case then spine growth cannot be linear with time over the entire growth experiment. Speculatively, this may occur if discrete units of growth like those imaged in calcein surface maps (Figure 4.34) and described by Houlbreque et al. (2009) precipitate from a single reservoir or reservoirs with similar turnover times. Over several days, precipitating different numbers of these units would then yield different apparent linear growth rates at spatial scales > 10 μm even if the growth kinetics of each unit are similar.

For each cross boundary profile, the other isotope ratios typically behave similarly to 43/42. In Figures 4.36–4.48, the profile points between 16%–84% of the 43/42 response are marked in red. These same points are marked in all the other isotope ratios. There is no strong evidence of asynchronous behavior, although the width of the 43/42 rise means that small differences in strontium, barium, and terbium behavior may not be evident, so the possibility of different dynamics cannot be excluded at less than hour time scales.

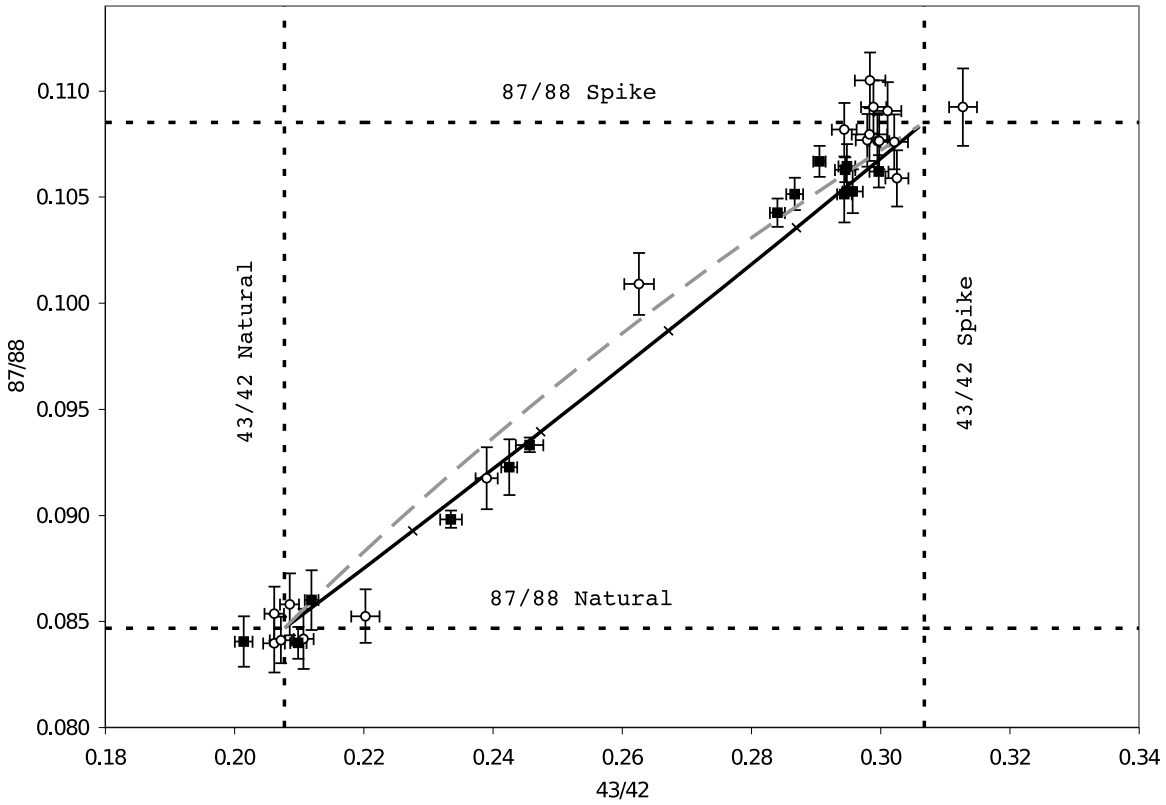

Figure 4.49: Calcium and strontium isotope ratios from nanoSIMS spot analysis of cultured coral spines. Spot data cluster at the spiked and un-spiked end members with a few intermediate points. Most of the intermediate spots fall close to a mixing line between these end members. Combined with image data showing a homogeneously labeled new growth region, these data suggest it is possible to make spot measurements of the new growth end-member. (■) are data from spot analysis session Ns3, while (○) were collected during session Ns4, error bars are 2σ internal standard error of the mean. Isotope ratios are corrected from instrumental mass fractionation by normalizing spots data from regions well inside the calcein marks to natural abundance ratios. Therefore, the points in the lower left corner are not independent of the dashed lines marking calcium and strontium isotope ratios of natural marine abundances and spike culture ratios. The solid line is a 4-isotope mixing relationship between a natural marine isotope abundances end-member and a spiked culture end-member, assuming a $q = (88/42)_o/(88/42)_x \sim 1$. Hash marks on the model line signify 0.2 unit changes in the mole fraction of an end member. The gray dashed mixing model was generated assuming a $q = 0.8$, the lowest value estimated from near-boundary images. The highest isotope points cluster at a slightly lower calcium and strontium isotope ratio than spike end member, which may represent a small accuracy error in either the nanoSIMS measurements, the culture seawater MC-ICP-MS data or both. Black squares cluster at a different location than the open circles, suggesting that uncertainty in the accuracy of the nanoSIMS instrumental mass fractionation correction, which is different for each analytical session may be the major source of this accuracy difference. Alternatively, but presumably less likely, skeletal material could precipitate from a pool that is slightly diluted by natural calcium for those spines analyzed in session Ns4 and by both natural calcium and natural strontium during session Ns3.

4.10 Isotopic and Chemical Composition of the Experimentally Grown Coral Skeleton by NanoSIMS Spot Analysis

Spot measurements in coral spines using the nanoSIMS capture both the natural abundance and the spiked culture media end member, as well as a few intermediate values, as shown in a plot of calcium and strontium isotope ratios (Figure 4.49). As detailed in Section 4.7, we can compare these results to the mixing relationship. From comparison of calcein maps and post-analysis SEM images of burn marks, spots with intermediate isotope values were all from locations very near the calcein boundary. The intermediate values could result from measurements that span the boundary, including both both unspiked and spiked material, or measurements that sample the $\sim$ 1–2 micron response region detailed in the image and profile analysis of Section 4.9.

The 87/88 ratios from spiked material in nanoSIMS images and image profiles spanned the culture value, but were typically lower, while 43/42 is consistently at the culture end member value. The higher precision spot analysis data presented here show that the highest isotope points cluster at a slightly lower calcium isotope ratio than the culture value. Strontium isotope ratios are lower than the spike end member for session Ns3 but match the spike ratio for session Ns4. Image and spot data do not show a consistent offset between coral isotopes by micro-analsyis and the culture solution ratios. Differences between these values may represent a small accuracy error in either the nanoSIMS measurements, the culture seawater MC-ICP-MS data, or both. Black squares cluster at a different location than the open circles, suggesting that uncertainty in the accuracy of the nanoSIMS instrumental mass fractionation correction, which is different for each analytical session, may be the major source of this accuracy difference. Alternatively, but presumably less likely, skeletal material could precipitate from a pool that is slightly diluted by natural calcium for those spines analyzed in session Ns4 and by both natural calcium and natural strontium for spines taken from the same corals that were analyzed during session Ns3.

Combined with images showing the homogeneously labeled region of new growth, spot data

demonstrate that it is possible to analyze the composition of newly grown skeletal material corresponding to a short (6-day) coral culture experiment. Sr/Ca and Mg/Ca of spines from each culture condition are reported using only spots totally within the new growth region, e.g. those with isotope ratios similar to that of the culture solution.

Despite growth conditions spanning from 180 to 330 $\mu mol\ \left[CO_3^{2-}\right]$, the Sr/Ca of coral measured by spot analysis during session Ns3 vary by 6% ($2\sigma, n = 19$), similar to the external Sr/Ca error estimated from repeated measurement of the blue calcite standard (Figure 4.50). Using independent calibration curves for each analytical session, this represents an average Sr/Ca of 9.2 mmol/mol. The spot data range from 8.8 to 9.8, but do not vary systematically with culture media carbonate ion concentration. If Sr/Ca variability is limited by random analytical error, then the mean Sr/Ca of spots from each culture condition can be used to estimate true spine composition. Mean Sr/Ca ratios for each growth condition agree remarkably well, with a total relative range of 1.4%. Within this small variability, Sr/Ca is not systematically sensitive to carbonate ion concentration from 180 to 330 μmol kg^{-1}. Unlike the Sr/Ca results, Mg/Ca variability is much larger than external error. This large relative signal is uncorrelated with the carbonate ion growth condition (Figure 4.51). The relative 2σ standard deviation of Mg/Ca point measurements is 60% (or 40% if one high Mg/Ca point is excluded). Mean values for each condition also differ by 25% if only spines with more than one point are considered ($> 80\%$ for all "means"). Cross plots of Sr/Ca vs. Mg/Ca are uncorrelated, nor do patterns emerge when groups are separated by carbonate ion or by analytical session.

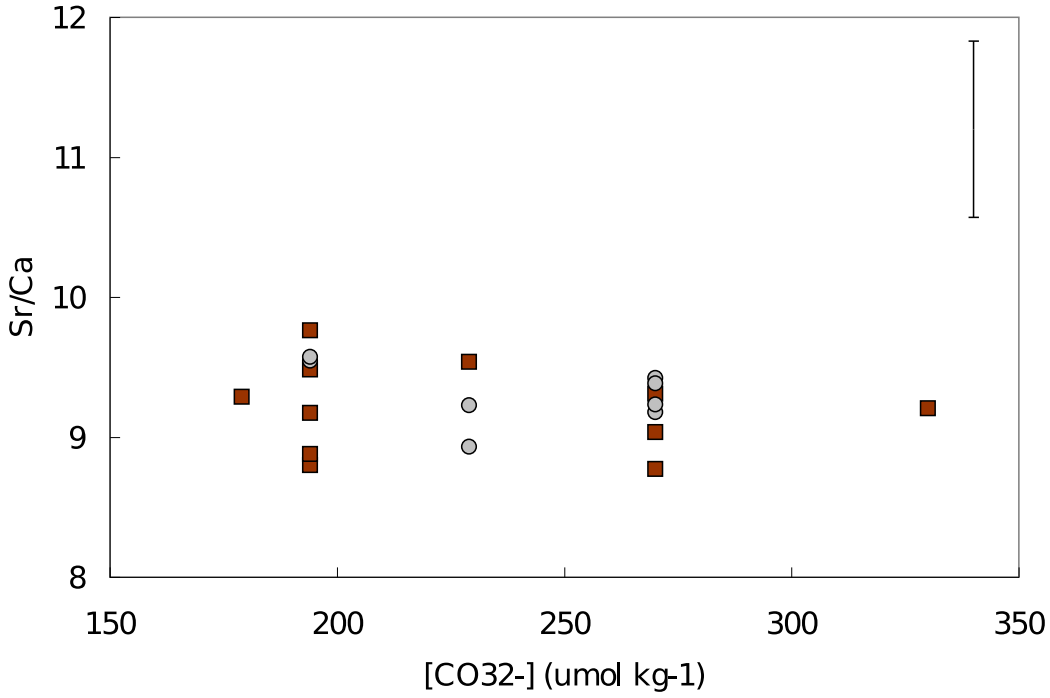

Figure 4.50: Sr/Ca ratio of coral skeleton experimentally grown under different carbonate ion concentrations as measured by nanoSIMS spot analysis. Sr/Ca values are similar between different growth conditions within the range explored in this experiment. Results are similar between different analytical sessions: (◯) Ns3 and (■) Ns4, building confidence in the calibration method. External error for these sessions is plotted in the top right corner (2 standard deviations of the Sr/Ca values from repeated measurements on the carbonate standard Blue Calcite)

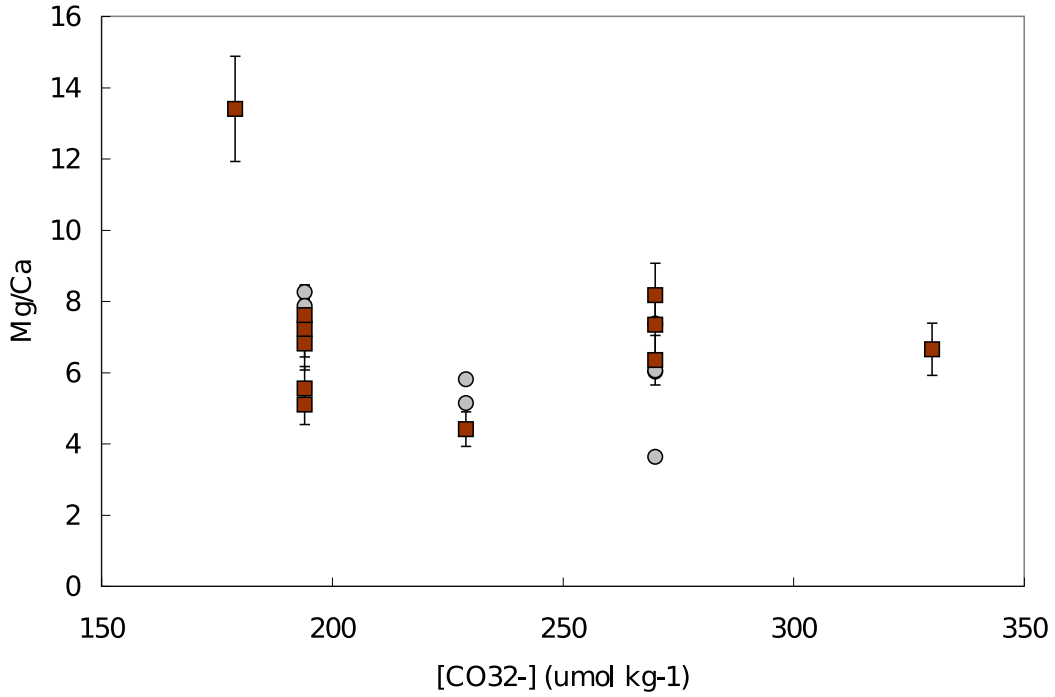

Figure 4.51: Mg/Ca ratio of coral skeleton experimentally grown under different carbonate ion concentrations as measured by nanoSIMS spot analysis. Symbols distinguish different analytical sessions: (◯) Ns3 and (■) Ns4. Error bars are external error, the 2σ standard deviation of repeated measurements on the carbonate standard Blue Calcite. For session Ns3, error bars are smaller than the symbols. Notice much larger relative variability in Mg/Ca measurements compared to Sr/Ca. Unlike the Sr/Ca results, which may be limited by methodological precision, Mg/Ca variability is much larger than external error, showing large variability that is generally uncorrelated with the carbonate ion growth condition.

4.11 Carbonate Ion Effect on Coral Calcification and Growth Rate

Effect of $[CO_3^{2-}]$ *on Coral Growth Rate:* Several techniques are used in this study to determine the relative calcification rates and linear growth rates of cultured coral as a function of $[CO_3^{2-}]$ and aragonite saturation, Ω: bulk $^{43}Ca/^{48}Ca$ of coral nubbin tips (Figure 4.33); alkalinity flux balancing in the culture chambers (Figures 4.23–4.24); linear growth rates from calcein images (Figure 4.35); and maximal extent of new growth in coral micro-samples from cross plots of $^{87}Sr/^{88}Sr$ vs. $^{43}Ca/^{42}Ca$ and $^{136}Ba/^{138}Ba$ vs. $^{43}Ca/^{42}Ca$ (Figures 4.27 and 4.28).

The bulk $^{43}Ca/^{48}Ca$ method shows a general trend of decreasing calcification rate with decreasing Ω, with a two fold difference between the lowest Ω conditions and coral with typical modern values, Ω= 2.9–3 . The exception to this trend is a very high calcification rate at Ω=4. This coral also has anomalously high calcification rates by the alkalinity method. The time resolution of the alkalinity method shows that most of this growth occurred near the end of the experiment. The lowest Ω coral also calcifies the least in the alkalinity data, by a factor of roughly two. The remaining three coral show no significant trend with Ω in the alkalinity data, unlike the bulk $^{43}Ca/^{48}Ca$ results, which may represent a difference in the precision of the two methods. The maximal extent of precipitation from micro-sampled coral also follow a clear trend with the most new growth in high Ω coral, although this method is easily biased by the random selection of different pieces of coral. Linear growth data only agree with the calcification rate data in that the lowest Ω again shows the least growth, by a factor of two to three. Otherwise there is no clear trend in linear growth rates with Ω. Given the small sample size of spines measured for growth rate in this study, intra-coral variability in linear growth rate could easily confuse any trend if it exists.

Absolute growth rates vary dramatically between different coral experiments, highlighting the difficulty of growing these finicky organisms, the lack of a reliable normalizing factor to compare different coral, and the need to cross calibrate calcification measuring methods. Calcification rates can be normalized to a number of different physiological parameters. Since the best choice is un-

clear, calcification rates are published in a range of different units, complicating cross experiment comparisons. The most popular units are nmol $CaCO_3$ (mg coral tissue protein)$^{-1}$ hr^{-1} and nmol $CaCO_3$ cm^{-2} hr^{-1}, although Marshall & Clode (2004) argue μmol $CaCO_3$ (g skeletal dry weight)$^{-1}$ is universally applicable across different genus and coral body plans. Table 4.10 lists a selection of published calcification rates, focusing on culture experiments involving *Stylophora* or where aragonite saturation was manipulated in a controlled fashion. Measurements of tissue protein mass as a function of surface area in *Stylophora* can be used to covert between different calcification rate units. Falkowski & Dubinsky (1981) report 1.9 mg cm^{-2} using Stylophora collected from the same location as used in this study, but two decades previous, while Reynaud et al. (2003) measured 0.72 mg protein cm^{-2} in the aquarium-raised *Stylophora* used by the Monaco group in a number of the tabulated studies (Moya et al., 2006). Our growth rates are somewhat lower than other published results, but well within the large range of published growth rates, especially given the uncertainty in conversion between different normalizing factors. Explaining the range of calcification rates and physiological measurements from different studies is an important goal towards better understanding environmental influences on coral growth. Possible sources of variability include patchiness in coral behavior over space and time; the large number of environmental factors that influence calcification in coral; the engineering challenge of controlling these parameters in a saltwater aquarium; and, different techniques used to measure coral growth: buoyant weight, alkalinity, and radioactive tracers. Variability in calcification rates makes it difficult to directly compare the effect of Ω on growth between different studies. Following a general approach in the field, results are recast as % change in calcification rate relative to a within-study control sample.

Coral acidification experiments, where Ω is decreased to simulate the effect of increased pCO2, typically, but not always, show diminished growth at lower than ambient Ω. In the early work of Gattuso et al. (1998), with the same coral as this study, *Stylophora pistillata*, low [Ca^{2+}] artificial seawater was used to manipulate Ω from 1 to 6. Above Ω=2, calcification rates are near constant, but calcification rates dropped at $\Omega < 2$ to 50% of the higher values by Ω=1. When the carbonate system is manipulated to control Ω, the effect of aragonite saturation is less clear even if the combined

results of all studies genrally support a robust effect. In the most systematic work to date, Schneider & Erez (2006) measured calcification rates in the quickly growing reef coral *Acropora eurystoma* over a large range of aragonite saturations. Ω is roughly linearly related to calcification rates ($R^2 = 0.55$) regardless of the approach used to manipulate Ω, alkalinity, DIC, or pCO2 bubbling. Other culture experiments and mesoscale experiments on reefs tend to support this trend, with calcification decreasing by $\sim$ 10–35% when pCO2 doubles (Ω from about 3.8 to 2.3) (Langdon et al., 2000; Marubini et al., 2003; Silverman et al., 2007). In a departure from these results, Reynaud et al. (2003) only see an acidification effect at elevated temperatures.

The data collected in this thesis support a limited carbonate ion effect on calcification, expressed most significantly as diminished growth for the lowest Ω culture condition by about 50%. Bulk and micro-sampled stable isotope methods support generally increasing calcification rates with Ω across all culture conditions. Given the noisy correlations between Ω and calcification rate in other carefully conducted studies, this weak effect may be typical. To see a stronger effect, much lower Ωs could have been explored. Given the expense and effort of each coral culture condition, this study was designed to span a geologically relevant range of aragonite saturations, from the expected Ω of tropical surface water at the Last Glacial Maximum to the predicted value of the same water in 2100 assuming the IPCC "business as usual" scenario IS92a.

The growth data also demonstrate that different coral in the culture experiment span significant variability in both calcification rate and linear growth rate. Most of the Me/Ca data in this study come from three coral grown between Ω=2.9–4. Both bulk $^{43}Ca/^{48}Ca$ and alkalinity techniques suggest the coral grown at Ω=4 calcified with at least twice the rate of the other coral, and that most of this increase occurred near the end of the experiment. Spot measurements in a spine from this coral were taken from both the near boundary region, corresponding to the beginning of the experiment, and the distal tip, corresponding to the end of the experiment. Additionally, calcein maps show that spines grown at Ω=2.9 exhibit linear growth rates of twice to five times those of other coral. Since average Sr/Ca ratios between all coral spines are similar, no calcification rate or linear growth rate effect on Sr/Ca is detected.

Table 4.10: Coral calcification rates under controlled culture conditions showing a large range of reported values. Results from this culture experiment are lower than but not dramatically different from other studies. Data from this study correspond to the calcification rate of ambient seawater condition by both alkalinity and stable isotope method. The stable isotope calcification rate is presented as an area normalized calcification rate using the factor 70 polyps $cm^{-}2$, the average polyp density in two coral used in this study. Data from other studies are day or "light" calcification rates of select culture experiments that focused on *Stylophora* or where aragonite saturation was manipulated. In studies where the carbonate system was manipulated the data tabulated here corresponds to the ambient modern condition, rather than CO_2 enriched or depleted conditions. **Bold** calcification rates are the published value in the reported units, while non-bold are re-calculated values. Conversion between mg protein and surface area uses the factors (*) 0.72 mg protein cm^{-2} or (†) 1.9 mg protein cm^{-2}, from Reynaud et al. (2003) and Falkowski & Dubinsky (1981), respectively. Where calcification rates are measured under the same conditions for several individuals the variability is tabulated here as the 2σ standard deviation of the sample. Another marine calcifier, foraminifera, have similar absolute calcification rates ($\sim$ 200 nmol $CaCO_3$ cm^{-2} hr^{-1}) as coral, but due to their small mass this is a large relative growth rate of >20% day^{-1}

.

nmol $CaCO_3$ cm^{-2} hr^{-1}	nmol $CaCO_3$ (mg protein)$^{-1}$ hr^{-1}	μmol $CaCO_3$ (g dry mass)$^{-1}$ hr^{-1}	Species	Study (method for calcification rate)
Alkalinity : **80** Stable ^{43}Ca: **250**	110 * 40 †	**0.2**	*Stylophora pistillata*	Present study (Alkalinity) (Stable ^{43}Ca)
115 ± 15 * 300 ± 40 †	**160 ± 20** (n=6)	**3.2**	*Stylophora pistillata*	Moya et al. (2006) (^{45}Ca)
200–300	280–420 * 100–160 †		*Acropora eurystoma*	Schneider & Erez (2006) (Alkalinity)
		0.2–1.2	several	Marshall & Clode (2004) (^{45}Ca)
		40	*Stylophora pistillata*	Reynaud et al. (2003) (Buoyant wt)
150 ± 90 (n=4)	210 ± 130 * 80 ± 50 †		*Stylophora pistillata*	Amat (2000) (Alkalinity)
360 ± 180 * 900 ± 500 † 600 ± 65 * 1600 ± 180 †	artificial seawater: **480 ± 250** (n=5) natural seawater: **830 ± 90** (n=6)		*Stylophora pistillata*	Gattuso et al. (1998) (Alkalinity)

4.12 Ion Dynamics During Biomineralization

Synchronous incorporation of calcium, strontium, barium, and terbium in the coral skeleton suggests that: (1) there is ion exchange between seawater and the calcifying fluid, and (2) these elements are influenced by similar transport mechanisms. It is unlikely that a selective active transport mechanism, like an ion pump, would act on all these ions similarly, considering they span a range of size, polarizability, and charge. One way to explain indiscriminate exchange between seawater and the calcifying fluid is if seawater exchanges directly with the calcifying fluid. Direct seawater exchange is supported by recent research with bulky cell membrane impermeable fluorescent dyes that move from seawater into growing coral skeletons (Jonathan Erez, unpublished results); is consistent with the initial starting fluid of a Rayleigh model for Me/Ca vital effects in deep-sea coral (Gagnon et al., 2007); and is invoked to help explain 18O and 13C vital effects in the same species of deep-sea coral (Adkins et al., 2003).

Incorporation of 43Ca and other isotopes in this experiment is not not infinitely abrupt. The range of 43/42 observed in ion images at the spike boundary suggests ions from the surrounding seawater mix to some extent with an internal pool during transport to the calcifying fluid. This reservoir has an estimated e-folding turnover time of 2 to 11 hours, much longer than any of the calcium pools identified in 45Ca efflux experiments (Tambutte et al., 1996).

4.13 Me/Ca Sensitivity to $[CO_3^{2-}]$ and Ω in Coral and Other Biominerals

Despite covering a large range of carbonate ion concentrations and calcification rates, the average Sr/Ca of nanoSIMS spot measurements from all culture conditions are within 1.4% of each other. Compared with the reported $\sim 0.7\%$ per degree C response of surface coral to temperature (Correge, 2006), these data suggest that temperature is a more significant control on Sr/Ca than [CO32-] in the studied coral over a large range of culture solution aragonite saturations that nearly span the full range of mean tropical Ωs from the Last Glacial Maximum (LGM) to double modern pCO_2.

The results from this study are complemented by the very recent work of Cohen et al. (2009) where juvenile *Favia fragum*, another symbiont-containing surface coral, were grown from larvae at different aragonite saturations ranging from Ω=3.7 to the very undersaturated value of Ω=0.2. Sr/Ca data from the studies are compared using partition coefficients,

$$D_{\mathrm{Sr/Ca}} = \frac{(\mathrm{Sr/Ca})_{coral}}{(\mathrm{Sr/Ca})_{seawater}} ,$$

to normalize differences in culture solution Sr/Ca. Where growth conditions overlap between the experiments, results are similar with no significant change in $D_{\mathrm{Sr/Ca}}$ above Ω=2.4 (Figure 4.52). There is an offset in $D_{\mathrm{Sr/Ca}}$ between the two studies that may be attributable to different Sr/Ca standardization techniques, or may represent a true species offset in composition. The two undersaturated points show a strong trend towards higher Sr/Ca at low Ω. Other biominerals may show similar patterns, in the calcite precipitating single-celled marine organisms foraminifera, shell Mg/Ca is near constant from ambient to high pH, but at low pH, corresponding to lower calcite saturation values, Mg/Ca becomes progressively higher (Figure 4.54). If this pattern is truly general in marine calcifiers, then the mechanism promises to be a basic component of biomineralization.

Unlike the high Mg/Ca variability seen in coral spines during this study, Mg/Ca varies inversely with Sr/Ca in juvenile *Favia fragum*. Cohen et al. (2009) convincingly demonstrate that Me/Ca ratios across different Ωs follow a Rayleigh curve. Applying the analysis from Chapter 3 to their data and assuming that the magnesium partition coefficient falls within the very wide range $0 < D_{Mg/Ca} < 0.2$, then the strontium partition coefficient can be determined from the slope of the linear log-log relationship yielding a $D_{Sr/Ca} \approx 1.23$. This requires at least a small enrichment in initial calcifying fluid Sr/Ca over seawater be consistent with the observed high Sr/Ca values, but the enrichment is within the apparent accuracy offset between the two studies.

A closed-system (Rayleigh) interpretation of the data implies that that the extent of precipitation, f, increases with Ω. The finite alkalinity pumping or "energy limited" scenario described in Figure 4.1 of the introduction results in exactly this effect: the same total amount of alkalinity pumping for

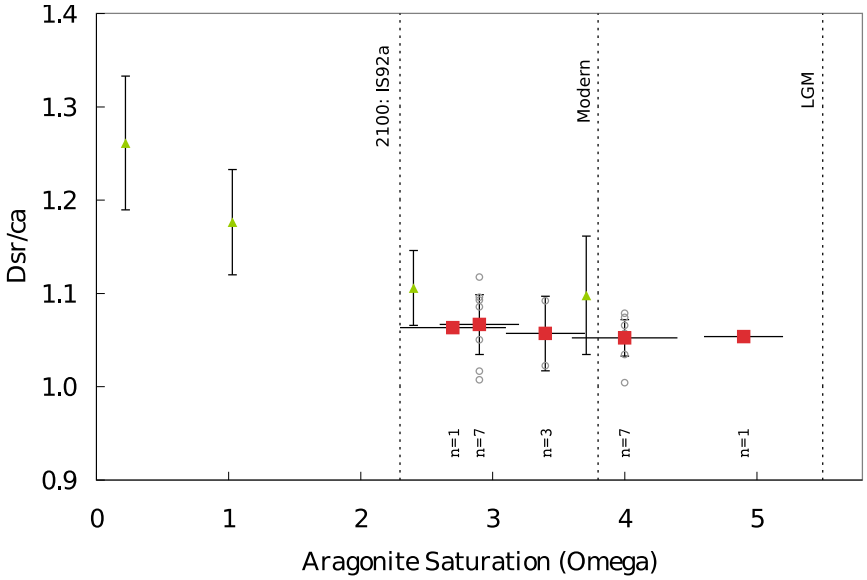

Figure 4.52: Mean Sr/Ca distribution coefficients of cultured coral do not change significantly with aragonite saturation, except at very low saturations. (■) Average distribution coefficient ($D_{\mathrm{Sr/Ca}}$) of spot measurements in experimentally grown coral from this study, where $D_{\mathrm{Sr/Ca}} = (\mathrm{Sr/Ca})_{coral} \,/\, (\mathrm{Sr/Ca})_{seawater}$ and culture media Sr/Ca = 8.7 mmol/mol. Mean Sr/Ca ratios for each growth condition agree remarkably well, with a total relative range of 1.4%. Horizontal bars show the full range of carbonate ion experienced by each coral during the culture experiment and (○) mark the individual nanoSIMS spot measurement used to calculate the mean. (▲) Results from the acidification study of Cohen et al. (2009) in juvenile *Favia fragum*, another symbiont containing surface coral (aquarium water Sr/Ca reported as 8.9 mmol/mol for this experiment). Dashed vertical lines identify approximate mean tropical surface ocean aragonite saturation at the Last Glacial Maximum (LGM) (Tripati et al., 2009), when atmospheric $p\mathrm{CO}_2$ was 180–200 ppm; for the modern ocean (Broecker et al., 1979) interacting with a $p\mathrm{CO}_2$ of $\sim$ 370 ppm; and the predicted value in 2100 assuming "business as usual" anthropogenic CO_2 emissions according to IPCC scenario IS92a leading to a $p\mathrm{CO}_2$ of $\sim$ 790 ppm (Orr et al., 2005). Vertical error bars for all data are the 2σ standard error of the mean.

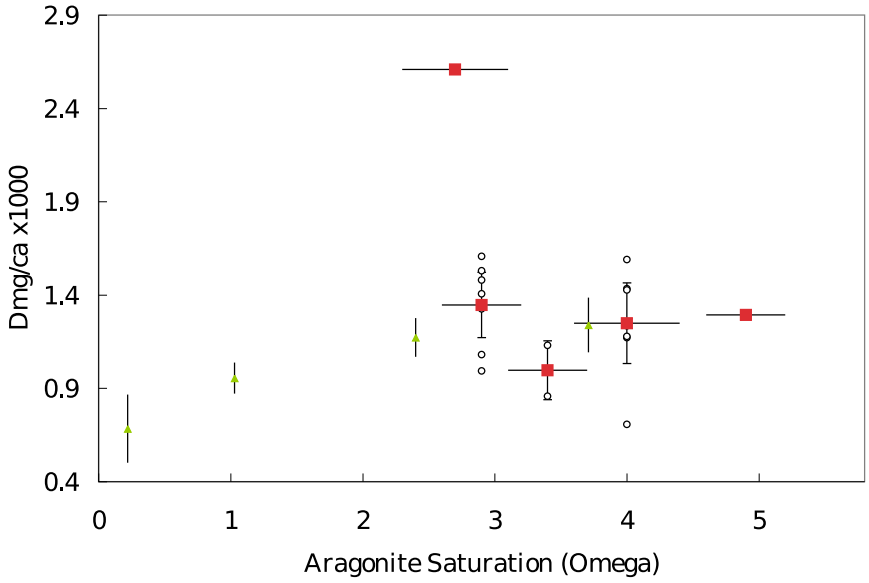

Figure 4.53: Mg/Ca distribution coefficients of cultured coral with high relative variability and low Mg/Ca at low Ω. (■) Average distribution coefficient ($D_{\mathrm{Mg/Ca}}$) of spot measurements in experimentally grown coral from this study, where $D_{\mathrm{Mg/Ca}} = (\mathrm{Mg/Ca})_{coral} / (\mathrm{Mg/Ca})_{seawater}$. Mean values for each condition in this study excluding the low Ω, high Mg/Ca point, differ by 25%. Horizontal bars show the full range of carbonate ion experienced by each coral during the culture experiment and (○) mark the individual nanoSIMS spot measurement used to calculate the mean. (▲) Results from the acidification study of Cohen et al. (2009) in juvenile *Favia fragum*, another symbiont containing surface coral.

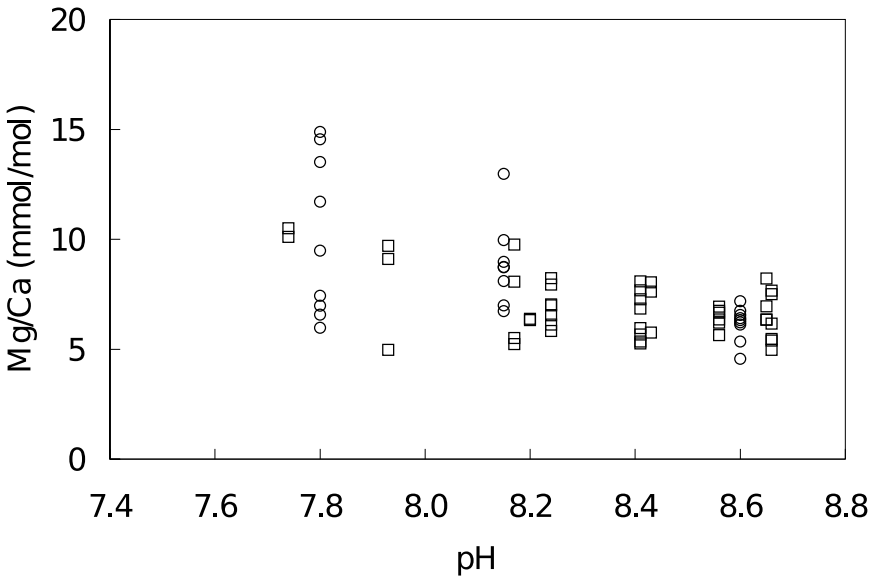

Figure 4.54: Mg/Ca sensitivity to pH in the cultured foraminifera *O. universa* form the studies of (◯) Lea et al. (1999) and (□) Russell et al. (2004). At mid to normal pH, mean foram Mg/Ca exhibits low pH sensitivity, however Mg/Ca increases significantly at low pH.

each precipitation event will yield less skeleton as Ω decreases. However, near-constant Sr/Ca at $\Omega > 2.4$, which is a clear result of both studies, is inconsistent with continuously variable extents of precipitation. Above Ω=2.4, the coral data behave more like the "pH controlled" scenario in Figure 4.1, where different initial seawater carbonate system parameters still result in the same amount of precipitation. Reconciling these differences within the Rayleigh framework requires some threshold Ω. Below this value, coral no longer chooses to pump enough alkalinity to reach the target pH. Conceptually it is not too difficult to imagine that from high to moderately low Ω coral are capable of manipulating the calcifying fluid to reach a target pH, but at very low Ω are incapable of reaching this target. The threshold extent of precipitation f=Ca/Ca$_o$=0.56, assuming a $D_{Sr/Ca} \approx 1.23$ from the log-log fit and that the highest measured coral Sr/Ca represents material precipitated at f=1.

As an alternative to the Rayleigh model, incongruent dissolution of the coral skeleton could explain the apparent Ω sensitivity of Me/Ca ratios at the very low aragonite saturations used in Cohen et al. (2009). In fact Cohen et al. (2009) describe in detail that the coral grown at very low Ω show diminished fine skeletal features in SEM images, which may be evidence of dissolution. Experiments by Fine & Tchernov (2007), demonstrate that exposing coral to pH<7.6 over months leads to complete dissolution of the skeleton, even though coral are covered by tissue. Surprisingly the coral skeleton regenerates when the remaining polyps are subsequently exposed to higher pH seawater. The lowest Ω coral in Cohen et al. (2009) were also grown at pH of 7.6. To reproduce inverse trends in Mg/Ca and Sr/Ca requires preferential dissolution of a magnesium rich and slightly strontium depleted phase. Cleaning studies of coral skeletons show that a Mg-rich phase is preferentially dissolved during weak-acid digestions (Watanabe et al., 2001; Mitsuguchi et al., 2001). A recent study in the massive coral *Porites* compares cores with signs of dissolution to contemporaneous regions of nearby pristine coral, showed preferential dissolution of Mg while Sr and U were enriched in the remaining skeleton (Hendy et al., 2007).

If dissolution explains the Me/Ca variability in coral at low Ω, then calcification may be robust to carbonate ion effects, with the balance between dissolution and precipitation affecting final

skeletal Me/Ca. Environmental conditions that affect this balance could lead to large changes in calcification. Speculatively, high respiration rates, possibly driven by high temperature, may act to amplify the effect of ocean acidification. Even more speculatively, if deep-sea coral metabolism is slower than surface coral, then the reduced respiration driven dissolution may help explain the ability of these coral to thrive at low Ω. Since uranium varies inversely with magnesium in coral (Sinclair et al., 2006), and low uranium is associated with magnesium rich centers of calcification of deep-sea coral (Robinson et al., 2006), U/Ca ratios may be affected by dissolution as well. Any tracer that could distinguish unaltered skeleton from partially dissolved skeleton would then be very useful for interpreting Me/Ca paleo-proxies in coral.

4.14 Conclusion

Skeletal growth during a 6-day coral culture experiment was located, mapped, and compositionally characterized, demonstrating the feasibility of short proxy calibration studies in adult coral for the first time. As an initial application I quantified the sensitivity of Sr/Ca, a proxy for temperature, to another important environmental parameter, [CO32-]. Five branches of *Stylophora sp.* coral were all grown at 25C but at different and near constant carbonate ion concentrations, from 180 to 400M (pH of 7.9 to 8.5), resulting in a two fold range in calcification rate. Despite the range of carbonate ion concentrations and calcification rates, the average Sr/Ca of nanoSIMS spot measurements corresponding to each condition are within 1.2% (2σ std. dev. of the 5 means) compared with the reported $\sim$ 0.7% per degree C response of surface coral to temperature. These data suggest that temperature is a more significant control on Sr/Ca than [CO32-] or calcification rate in the studied coral, supporting the use of Sr/Ca as a paleoproxy. Within the framework of a closed system (Rayleigh) model for biomineralization, these data suggest similar extents of calcification over the range of culture conditions. The results constrain explanations for the sensitivity of coral calcification rates to ocean acidification, improving our understanding of how anthropogenic CO2 will impact coral reefs.

4.15 Appendix

Table 4.11: Summary of carbonate system measurements during coral growth. Gray lines are from time-points prior to the addition of a mid-experiment REE spike. Calculations and measurements explained in the methods section.

date	Container #	diurnal cycle	Start Time	Final Time	duration (hr)	intial mass (g)	final mass (g)	flow (g/hr)
Dec-10-2007	1	Resirviour - initial						
Dec-12-2007	1	Resirviour- post RRE						
Dec-15-2007	1	Resirviour-final						
Dec-10-2007	1	Day	10:00 AM	6:40 PM	8.67	46.6	120.6	8.54
Dec-10-2007	1	Night	6:40 PM	7:00 AM	12.33	46.9	162.2	9.35
Dec-11-2007	1	Day	7:00 AM	6:45 PM	11.75	46.6	158.3	9.51
Dec-11-2007	1	Night	6:45 PM	6:30 AM	11.75	46.9	159.8	9.61
Dec-12-2007	1	Day+Night	2:24 PM	9:45 AM	19.35	46.6	202.4	8.05
Dec-13-2007	1	Day (short)	9:45 AM					
Dec-13-2007	1	Night	6:30 PM	8:00 AM	13.50	46.9	145.8	7.33
Dec-14-2007	1	Night	7:10 PM	9:00 AM	13.83	46.9	161.4	8.28
Dec-15-2007	1	Day	9:00 AM	10:11 PM	13.18	**44.2**	158.1	8.64
Dec-10-2007	2	Resirviour - initial						
Dec-12-2007	2	Resirviour- post RRE						
Dec-15-2007	2	Resirviour-final						
Dec-10-2007	2	Day	10:00 AM	6:40 PM	8.67	46.7	118.3	8.26
Dec-10-2007	2	Night	6:40 PM	7:00 AM	12.33	46	163.2	9.50
Dec-11-2007	2	Day	7:00 AM	6:45 PM	11.75	46.7	160.3	9.67
Dec-11-2007	2	Night	6:45 PM	6:30 AM	11.75	46	159.6	9.67
Dec-12-2007	2	Day+Night	2:24 PM	9:45 AM	19.35	46.7	231.4	9.55
Dec-13-2007	2	Day (short)	9:45 AM					
Dec-13-2007	2	Night	6:30 PM	8:00 AM	13.50	46	164	8.74
Dec-14-2007	2	Night	7:10 PM	9:00 AM	13.83	46	140.2	6.81
Dec-15-2007	2	Day	9:00 AM	11:42 PM	14.70	**44.6**	126.8	5.59
Dec-10-2007	3	Resirviour - initial						
Dec-12-2007	3	Resirviour- post RRE						
Dec-15-2007	3	Resirviour-final						
Dec-10-2007	3	Day	10:00 AM	6:40 PM	8.67	47.1	121	8.53
Dec-10-2007	3	Night	6:40 PM	7:00 AM	12.33	46.2	166.8	9.78
Dec-11-2007	3	Day	7:00 AM	6:45 PM	11.75	47.1	162.5	9.82
Dec-11-2007	3	Night	6:45 PM	6:30 AM	11.75	46.2	160.2	9.70
Dec-12-2007	3	Day+Night	2:24 PM	9:45 AM	19.35	47.1	221.4	9.01
Dec-13-2007	3	Day (short)	9:45 AM					
Dec-13-2007	3	Night	6:30 PM	8:00 AM	13.50	46.2	119.9	5.46
Dec-14-2007	3	Night	7:10 PM	9:00 AM	13.83	46.2	107.6	4.44
Dec-15-2007	3	Day	9:00 AM	11:12 PM	14.20	**44.6**	107.8	4.45
Dec-10-2007	4	Resirviour - initial						
Dec-12-2007	4	Resirviour- post RRE						
Dec-15-2007	4	Resirviour-final						
Dec-10-2007	4	Day	10:00 AM	6:40 PM	8.67	46.5	118	8.25
Dec-10-2007	4	Night	6:40 PM	7:00 AM	12.33	47.1	158.2	9.01
Dec-11-2007	4	Day	7:00 AM	6:45 PM	11.75	46.5	151	8.89
Dec-11-2007	4	Night	6:45 PM	6:30 AM	11.75	47.1	151.9	8.92
Dec-12-2007	4	Day+Night	2:24 PM	9:45 AM	19.35	46.5	210.9	8.50
Dec-13-2007	4	Day (short)	9:45 AM					
Dec-13-2007	4	Night	6:30 PM	8:00 AM	13.50	47.1	164.2	8.67
Dec-14-2007	4	Night	7:10 PM	9:00 AM	13.83	47.1	161.2	8.25
Dec-15-2007	4	Day	9:00 AM	9:47 PM	12.78	**44.1**	141	7.58
Dec-10-2007	5	Resirviour - initial						
Dec-12-2007	5	Resirviour- post RRE						
Dec-15-2007	5	Resirviour-final						
Dec-10-2007	5	Day	10:00 AM	6:40 PM	8.67	46.8	117.1	8.11
Dec-10-2007	5	Night	6:40 PM	7:00 AM	12.33	46.8	158	9.02
Dec-11-2007	5	Day	7:00 AM	6:45 PM	11.75	46.8	154	9.12
Dec-11-2007	5	Night	6:45 PM	6:30 AM	11.75	46.8	154.1	9.13
Dec-12-2007	5	Day+Night	2:24 PM	9:45 AM	19.35	46.8	218.5	8.87
Dec-13-2007	5	Day (short)	9:45 AM					
Dec-13-2007	5	Night	6:30 PM	8:00 AM	13.50	46.8	113.8	4.96
Dec-14-2007	5	Night	7:10 PM	9:00 AM	13.83	46.8	99.5	3.81
Dec-15-2007	5	Day	9:00 AM	9:28 PM	12.47	**44.5**	160.7	9.32
Dec-10-2007	6	Resirviour - initial						
Dec-12-2007	6	Resirviour- post RRE						
Dec-15-2007	6	Resirviour-final						
Dec-10-2007	6	Day	10:00 AM	6:40 PM	8.67	47.3	118	8.16
Dec-10-2007	6	Night	6:40 PM	7:00 AM	12.33	46.8	161.5	9.30
Dec-11-2007	6	Day	7:00 AM	6:45 PM	11.75	47.3	155.6	9.22
Dec-11-2007	6	Night	6:45 PM	6:30 AM	11.75	46.8	157.7	9.44
Dec-12-2007	6	Day+Night	2:24 PM	9:45 AM	19.35	47.3	211.8	8.50
Dec-13-2007	6	Day (short)	9:45 AM					
Dec-13-2007	6	Night	6:30 PM	8:00 AM	13.50	46.8	139.3	6.85
Dec-14-2007	6	Night	7:10 PM	9:00 AM	13.83	**47**	108	4.41
Dec-15-2007	6	Day	9:00 AM	11:58 PM	14.97	**44.8**	111.5	4.46

Table 4.12: Continued summary of carbonate system measurements during coral growth. Gray lines are from time-points prior to the addition of a mid-experiment REE spike. Calculations and measurements explained in the methods section.

date	Container #	diurnal cycle	pH	ALK (μmol eq / kg)	DIC (μmol/kg)	est DIC err	[CO3] (ALK,DIC)	[CO3] (pH,ALK)	Omega (pH,ALK)
Dec-10-2007	1	Resirviour - initial	8.519	2932				450	6.73
Dec-12-2007	1	Resirviour- post RRE	8.500	2844	2242	22	427	424	6.34
Dec-15-2007	1	Resirviour-final	8.516	2866				437	6.54
Dec-10-2007	1	Day		2890					
Dec-10-2007	1	Night		2877					
Dec-11-2007	1	Day	8.383	2835	2285	23	392	353	5.28
Dec-11-2007	1	Night	8.348	2844	2321	70	374	335	5.00
Dec-12-2007	1	Day+Night		2781					
Dec-13-2007	1	Day (short)	8.367						
Dec-13-2007	1	Night	8.335	2707	2261	23	317	311	4.65
Dec-14-2007	1	Night	8.337	2706	2258	23	318	312	4.66
Dec-15-2007	1	Day	8.379	2726	2256	23	333	337	5.03
Dec-10-2007	2	Resirviour - initial	8.289	2698				287	4.29
Dec-12-2007	2	Resirviour- post RRE	8.250	2626	2250	23	267	261	3.90
Dec-15-2007	2	Resirviour-final	8.260	2624	2258	23	261	265	3.96
Dec-10-2007	2	Day		2662					
Dec-10-2007	2	Night		2646					
Dec-11-2007	2	Day	8.220	2623	2318	23	222	247	3.69
Dec-11-2007	2	Night	8.176		2304	69			
Dec-12-2007	2	Day+Night		2536					
Dec-13-2007	2	Day (short)	8.232	2535				244	3.64
Dec-13-2007	2	Night	8.178	2538	2219	22	227	222	3.31
Dec-14-2007	2	Night	8.140	2488				203	3.03
Dec-15-2007	2	Day	8.219	2469				232	3.46
Dec-10-2007	3	Resirviour - initial	8.117	2540				198	2.96
Dec-12-2007	3	Resirviour- post RRE	8.088	2471	2211	22	188	183	2.73
Dec-15-2007	3	Resirviour-final	8.104	2483	2224	22	188	189	2.83
Dec-10-2007	3	Day		2488					
Dec-10-2007	3	Night		2470					
Dec-11-2007	3	Day	8.173	2424	2258	23	131	209	3.13
Dec-11-2007	3	Night	8.094	2416	2171	65	177	180	2.70
Dec-12-2007	3	Day+Night		2370					
Dec-13-2007	3	Day (short)	8.202	2336				212	3.17
Dec-13-2007	3	Night	8.172						
Dec-14-2007	3	Night	8.107						
Dec-15-2007	3	Day	8.152	2111				174	2.61
Dec-10-2007	4	Resirviour - initial	8.397	2790				355	5.31
Dec-12-2007	4	Resirviour- post RRE	8.395	2793	2232	22	397	354	5.30
Dec-15-2007	4	Resirviour-final	8.410	2498	2239	22	189	322	4.82
Dec-10-2007	4	Day		2750					
Dec-10-2007	4	Night		2725					
Dec-11-2007	4	Day	8.296	2699	2103	21	415	290	4.34
Dec-11-2007	4	Night	8.252	2758	2355	71	290	275	4.12
Dec-12-2007	4	Day+Night		2628					
Dec-13-2007	4	Day (short)	8.284	2598				273	4.09
Dec-13-2007	4	Night	8.268		2206	22			
Dec-14-2007	4	Night	8.273	2338	2208	22	109	240	3.59
Dec-15-2007	4	Day	8.353		2140	21			
Dec-10-2007	5	Resirviour - initial	7.915	2417				128	1.91
Dec-12-2007	5	Resirviour- post RRE	7.872	2355	2170	22	140	114	1.70
Dec-15-2007	5	Resirviour-final	7.887	2359	2224	22	112	118	1.76
Dec-10-2007	5	Day		2393					
Dec-10-2007	5	Night		2391					
Dec-11-2007	5	Day	8.073	2370	2278	23	91	170	2.54
Dec-11-2007	5	Night	8.014	2350	2165	65	140	151	2.25
Dec-12-2007	5	Day+Night		2331					
Dec-13-2007	5	Day (short)	8.126	2317				183	2.74
Dec-13-2007	5	Night	8.112	2295				177	2.64
Dec-14-2007	5	Night	8.147	2241				184	2.75
Dec-15-2007	5	Day	8.213	2253	1938	19	214	208	3.11
Dec-10-2007	6	Resirviour - initial	8.118	2616				205	3.06
Dec-12-2007	6	Resirviour- post RRE	8.080	2550	2274	23	201	186	2.78
Dec-15-2007	6	Resirviour-final	8.116	2555				199	2.98
Dec-10-2007	6	Day		2589					
Dec-10-2007	6	Night		2595					
Dec-11-2007	6	Day	8.107	2579	2117	21	321	198	2.96
Dec-11-2007	6	Night	8.092	2571	2306	69	195	192	2.87
Dec-12-2007	6	Day+Night		2551					
Dec-13-2007	6	Day (short)	8.173	2527				219	3.27
Dec-13-2007	6	Night			2199	22			
Dec-14-2007	6	Night	8.220	2481				233	3.49
Dec-15-2007	6	Day	8.250	2459				243	3.64

Bibliography

Adkins, J., Boyle, E., Curry, W., & Lutringer, A. (2003). Stable isotopes in deep-sea corals and a new mechanism for "vital effects". *Geochim. Cosmochim. Acta*, *67*(6), 1129–1143.

Adkins, J., McIntyre, K., & Schrag, D. (2002). The salinity, temperature, and δ^{18}O of the glacial deep ocean. *Science*, *298*(5599), 1769–1773.

Albarède, F. (1995). *Introduction to Geochemical Modeling*. Cambridge University Press.

Alibert, C., & McCulloch, M. (1997). Strontium/calcium ratios in modern *Porites* corals from the Great Barrier Reef as a proxy for sea surface temperature: Calibration of the thermometer and monitoring of ENSO. *Paleoceanography*, *12*(3), 345–363.

Allison, N. (2004). High-resolution Sr/Ca records in modern *Porites lobata* corals: Effects of skeletal extension rate and architecture. *Geochem. Geophys. Geosyst.*, *5*(5), 1–10.

Allison, N., Finch, A., Sutton, S., & Newville, M. (2001). Strontium heterogeneity and speciation in coral aragonite: Implications for the strontium paleothermometer. *Geochim. Cosmochim. Acta*, *65*(16), 2669–2676.

Amat, A. (2000). *Coral Growth and Atmospheric CO_2 Variations: Biological and Climatological Implications*. Ph.D. thesis, Université Pierre et Marie CURIE (PARIS VI).

Bacon, M., & Edmond, J. (1972). Barium at Geosecs-III in southwest pacific. *Earth Planet. Sci. Lett.*, *16*(1), 66.

Bates, R. G. (1973). *Determination of pH, Theory and Practice*. John Wiley & Sons: New York, 2nd ed.

Beck, J., Edwards, R., Ito, E., Taylor, F., Recy, J., Rougerie, F., Joannot, P., & Henin, C. (1992). Sea-surface temperature from coral skeletal strontium calcium ratios. *Science*, *257*(5070), 644–647.

Beck, W., Grossman, E., & Morse, J. (2005). Experimental studies of oxygen isotope fractionation in the carbonic acid system at 15°, 25°, and 40°C. *Geochim. Cosmochim. Acta*, *69*(14), 3493–3503.

Bentov, S., & Erez, J. (2006). Impact of biomineralization processes on the Mg content of foraminiferal shells: A biological perspective. *Geochem. Geophys. Geosyst.*, *7*, Q01P08.

Bernhard, J., Blanks, J., Hintz, C., & Chandler, G. (2004). Use of the fluorescent calcite marker calcein to label foraminiferal tests. *Journal of Foraminiferal Research*, *34*(2), 96–101.

Bevington, P. R. (1969). *Data Reduction and Error Analysis for the Physical Sciences*. McGrawHill Book Company.

Böhm, F., Gussone, N., Eisenhauer, A., Dullo, W.-C., Reynaud, S., & Paytan, A. (2006). Calcium isotope fractionation in modern scleractinian corals. *Geochim. Cosmochim. Acta*, *70*(17), 4452–4462.

Broecker, W. (2002). *The Glacial World According to Wally*. Eldigio Press: Palisades, NY.

Broecker, W., Takahashi, T., Simpson, H., & Peng, T. (1979). Fate of fossil-fuel carbon-dioxide and the global carbon budget. *Science*, *206*(4417), 409–418.

Cahn, L., Drummond, D., Edmond, J., & Grant, B. (1977). Barium data from atlantic GEOSECS expedition. *Deep-Sea Res.*, *24*(7), 613–649.

Calfo, A. (2007). *Book of Coral Propagation: Reef Gardening for Aquarists*, vol. 1. Reading Trees: Monroeville, PA, 2 ed.

Checkley, D. M., Dickson, A. G., Takahashi, M., Radich, J. A., Eisenkolb, N., & Asch, R. (2009). Elevated CO_2 enhances otolith growth in young fish. *Science*, *324*(5935), 1683–1683.

Cheng, H., Adkins, J., Edwards, R., & Boyle, E. (2000). U-Th dating of deep-sea corals. *Geochim. Cosmochim. Acta*, *64*(14), 2401–2416.

Cohen, A., Layne, G., Hart, S., & Lobel, P. (2001). Kinetic control of skeletal Sr/Ca in a symbiotic coral: Implications for the paleotemperature proxy. *Paleoceanography*, *16*(1), 20–26.

Cohen, A., Owens, K., Layne, G., & Shimizu, N. (2002). The effect of algal symbionts on the accuracy of Sr/Ca paleotemperatures from coral. *Science*, *296*(5566), 331–333.

Cohen, A. L., Gaetani, G. A., Lundälv, T., Corliss, B. H., & George, R. Y. (2006). Compositional variability in a cold-water scleractinian, *Lophelia pertusa*: New insights into "vital effects". *Geochem. Geophys. Geosyst.*, *7*(12), 1–10.

Cohen, A. L., Mccorkle, D. C., Putron, S. D., Gaetani, G. A., & Rose, K. A. (2009). Morphological and compositional changes in the skeletons of new coral recruits reared in acidified seawater: Insights into the biomineralization response to ocean acidification. *Geochem. Geophys. Geosyst.*, *10*(7), 1–12.

Correge, T. (2006). Sea surface temperature and salinity reconstruction from coral geochemical tracers. *Palaeogeogr. Palaeocl.*, *232*(2-4), 408–428.

Cuif, J., Dauphin, Y., Doucet, J., Salome, M., & Susini, J. (2003). XANES mapping of organic sulfate in three scleractinian coral skeletons. *Geochim. Cosmochim. Acta*, *67*(1), 75–83.

DePaolo, D. (1986). Detailed record of the Neogene-Sr isotopic evolution of seawater from DSDP site-590B. *Geology*, *14*(2), 103–106.

DePaolo, D., & Ingram, B. (1985). High-resolution stratigraphy with strontium isotopes. *Science*, *227*(4689), 938–941.

DeVilliers, S. (1999). Seawater strontium and Sr/Ca variability in the Atlantic and Pacific oceans. *Earth Planet. Sci. Lett.*, *171*, 623–634.

DeVilliers, S., Nelson, B., & Chivas, A. (1995). Biological-controls on coral Sr/Ca and δ^{18}O reconstructions of sea-surface temperatures. *Science*, *269*(5228), 1247–1249.

DeVilliers, S., Shen, G., & Nelson, B. (1994). The Sr/Ca-temperature relationship in coralline aragonite—influence of variability in (Sr/Ca)seawater and skeletal growth-parameters. *Geochim. Cosmochim. Acta*, *58*(1), 197–208.

Dickson, A. (1984). pH scales and proton-transfer reactions in saline media such as sea-water. *Geochim. Cosmochim. Acta*, *48*(11), 2299–2308.

Dickson, A. (1990). Standard potential of the reaction: AgCl(s)+$\frac{1}{2}$H$_2$(g) = Ag(s) + HCl(aq) and the standard acidity constant of the ion HSO4$^-$ in synthetic sea-water from 273.15 k to 318.15 k. *J Chem. Thermodyn.*, *22*(2), 113–127.

Dickson, A., & Millero, F. (1987). A comparison of the equilibrium-constants for the dissociation of carbonic-acid in seawater media. *Deep-Sea Res.*, *34*(10), 1733–1743.

Dickson, A., & Riley, J. (1979). Estimation of acid dissociation-constants in seawater media from potentiometric titrations with strong base. 1. The ionic product of water—K$_w$. *Marine Chemistry*, *7*(2), 89–99.

Dietzel, M., Gussone, N., & Eisenhauer, A. (2004). Co-precipitation of Sr^{2+} and Ba^{2+} with aragonite by membrane diffusion of CO_2 between 10 and 50 °C. *Chem. Geol.*, *203*, 139–151.

DOE (1994). *Handbook of methods for the analysis of the various parameters of the carbon dioxide system in sea water*, vol. 2. ORNL/CDIAC-74.

Doerner, H., & Hoskins, W. (1925). Co-precipitation of radium and barium sulfates. *J. Am. Chem. Soc.*, *47*, 662–675.

Elderfield, H., Bertram, C., & Erez, J. (1996). A biomineralization model for the incorporation of trace elements into foraminiferal calcium carbonate. *Earth Planet. Sci. Lett.*, *142*, 409–423.

Eugster, O., Tera, F., & Wasserburg, J. (1969). Isotopic analyses of barium in meteorites and in terrestrial samples. *J Geophys. Res.*, *74*(15), 3897–3908.

Falkowski, P., & Dubinsky, Z. (1981). Light-shade adaptation of *Stylophora pistillata*, a hermatypic coral from the Gulf of Eilat. *Nature*, *289*(5794), 172–174.

Fallon, S., McCulloch, M., & van Woesik, R. (1999). Corals at their latitudinal limits: laser ablation trace element systematics in *Porites* from Shirigai Bay, Japan. *Earth Planet. Sci. Lett.*, *172*, 221–238.

Fernandez, D., Gagnon, A., & Adkins, J. (in press). Mg/Ca and Sr/Ca measurements in natural calcium carbonates: assesment of accuracy with an isotope dilution ICP-MS method. *Geostandards and Geoanalytical Research*.

Ferrier-Pages, C., Boisson, F., Allemand, D., & Tambutte, E. (2002). Kinetics of strontium uptake in the scleractinian coral *Stylophora pistillata*. *Mar Ecol-Prog Ser*, *245*, 93–100.

Fietzke, J., & Eisenhauer, A. (2006). Determination of temperature-dependent stable strontium isotope ($^{88}Sr/^{86}Sr$) fractionation via bracketing standard MC-ICP-MS. *Geochem. Geophys. Geosyst.*, *7*, Q08009.

Fine, M., & Tchernov, D. (2007). Scleractinian coral species survive and recover from decalcification. *Science*, *315*(5820), 1811.

Gabitov, R., Gaetani, G., Watson, E., Cohen, A., & Ehrlich, H. (2008). Experimental determination of growth rate effect on U6+ and Mg^{2+} partitioning between aragonite and fluid at elevated U6+ concentration. *Geochim. Cosmochim. Acta*, *72*, 4058–4068.

Gabitov, R., Gagnon, A., Adkins, J., & Eiler, J. (in preparation). Accurate Metal/Calcium ratio measurements in carbonates by SIMS and nanoSIMS and an assesment of heterogenity in common carbonate standards.

Gaetani, G., & Cohen, A. (2006). Element partitioning during precipitation of aragonite from seawater: A framework for understanding paleoproxies. *Geochim. Cosmochim. Acta*, *70*, 4617–4634.

Gagnon, A. C., Adkins, J. F., Fernandez, D. P., & Robinson, L. F. (2007). Sr/Ca and Mg/Ca vital effects correlated with skeletal architecture in a scleractinian deep-sea coral and the role of Rayleigh fractionation. *Earth Planet. Sci. Lett.*, *261*(1-2), 280–295.

Ganachaud, A., & Wunsch, C. (2000). Improved estimates of global ocean circulation, heat transport and mixing from hydrographic data. *Nature*, *408*, 453–457.

Gattuso, J., Frankignoulle, M., Bourge, I., Romaine, S., & Buddemeier, R. (1998). Effect of calcium carbonate saturation of seawater on coral calcification. *Global Planet. Change*, *18*(1–2), 37–46.

Gladfelter, E. (1983). Skeletal development in *Acropora cervicornis*. II: Diel patterns of calcium carbonate accreation. *Coral Reefs*, *2*, 91–100.

Hendy, E. J., Gagan, M. K., Lough, J. M., McCulloch, M., & deMenocal, P. B. (2007). Impact of skeletal dissolution and secondary aragonite on trace element and isotopic climate proxies in *Porites* corals. *Paleoceanography*, *22*(4), PA4101.

Hillion, F., Daigne, B., Girard, F., & Slodzian, G. (1993). A new high performance instrument: the Cameca Nanosims 50. In *Proceedings of the Nith International SIMS Conference*. Wiley.

Houlbreque, F., Meibom, A., Cuif, J.-P., Stolarski, J., Marrocchi, Y., Ferrier-Pages, C., Domart-Coulon, I., & Dunbar, R. B. (2009). Strontium-86 labeling experiments show spatially heterogeneous skeletal formation in the scleractinian coral *Porites porites*. *Geophys. Res. Lett.*, *36*, L04604.

John, S., & Adkins, J. (submitted). Analysis of dissolved iron isotopes in seawater. *Marine Chemistry*.

Kinsman, D., & Holland, H. (1969). Co-precipitation of cations with $CaCO_3$. 4. Co-precipitation of Sr^{2+} with aragonite between 16 and 96 °C. *Geochim. Cosmochim. Acta*, *33*(1), 1–7.

Kleypas, J., Buddemeier, R., Archer, D., Gattuso, J., Langdon, C., & Opdyke, B. (1999). Geochemical consequences of increased atmospheric carbon dioxide on coral reefs. *Science*, *284*(5411), 118–120.

Lamb, M., Sabine, C., Feely, R., Wanninkhof, R., Key, R., Johnson, G., Millero, F., Lee, K., Peng, T., Kozyr, A., Bullister, J., Greeley, D., Byrne, R., Chipman, D., Dickson, A., Goyet, C., Guenther,

P., Ishii, M., Johnson, K., Keeling, C., Ono, T., Shitashima, K., Tilbrook, B., Takahashi, T., Wallace, D., Watanabe, Y., Winn, C., & Wong, C. (2002). Consistency and synthesis of Pacific Ocean CO_2 survey data. *Deep-Sea Res. II*, *49*(1–3), 21–58.

Langdon, C., Takahashi, T., Sweeney, C., Chipman, D., Goddard, J., Marubini, F., Aceves, H., Barnett, H., & Atkinson, M. (2000). Effect of calcium carbonate saturation state on the calcification rate of an experimental coral reef. *Global Biogeochem. Cycles*, *14*(2), 639–654.

Lea, D., & Martin, P. (1996). A rapid mass spectrometric method for the simultaneous analysis of barium, cadmium, and strontium in foraminifera shells. *Geochim. Cosmochim. Acta*, *60*, 3143–3149.

Lea, D., Martin, P., Chan, D., & Spero, H. (1995). Calcium uptake and calcification rate in the planktonic foraminifer *Orbulina universa*. *The Journal of Foraminiferal Research*, *25*, 14–23.

Lea, D., Mashiotta, T., & Spero, H. (1999). Controls on magnesium and strontium uptake in planktonic foraminifera determined by live culturing. *Geochim. Cosmochim. Acta*, *63*(16), 2369–2379.

LeCornec, F., & Correge, T. (1997). Determination of uranium to calcium and strontium to calcium ratios in corals by inductively coupled plasma mass spectrometry. *Journal of Analytical Atomic Spectrometry*, *12*(9), 969–973.

Lee, K., Millero, F., Byrne, R., Feely, R., & Wanninkhof, R. (2000). The recommended dissociation constants for carbonic acid in seawater. *Geophys. Res. Lett.*, *27*(2), 229–232.

Levitus, S., & Boyer, T. (1994). *World Ocean Atlas, 4: Temperature*. U.S. Department of Commerce: Washington, D.C.

Lueker, T., Dickson, A., & Keeling, C. (2000). Ocean pCO_2 calculated from dissolved inorganic carbon, alkalinity, and equations for K_1 and K_2: validation based on laboratory measurements of CO_2 in gas and seawater at equilibrium. *Marine Chemistry*, *70*(1–3), 105–119.

Marshall, A., & Clode, P. (2004). Calcification rate and the effect of temperature in a zooxanthellate and an azooxanthellate scleractinian reef coral. *Coral Reefs*, *23*(2), 218–224.

Marubini, F., Ferrier-Pages, C., & Cuif, J. (2003). Suppression of skeletal growth in scleractinian corals by decreasing ambient carbonate-ion concentration: a cross-family comparison. *P. Roy. Soc. Lond., B Bio.*, *270*(1511), 179–184.

McConnaughey, T. (1989a). ^{13}C and ^{18}O isotopic disequilibrium in biological carbonates .1. Patterns. *Geochim. Cosmochim. Acta*, *53*(1), 151–162.

McConnaughey, T. (1989b). ^{13}C and ^{18}O isotopic disequilibrium in biological carbonates .2. Invitro simulation of kinetic isotope effects. *Geochim. Cosmochim. Acta*, *53*(1), 163–171.

McIntire, W. (1963). Trace element partition coefficients—A review of theory and applications to geology. *Geochim. Cosmochim. Acta*, *27*, 1209–1264.

Meece, D., & Benninger, L. (1993). The coprecipitation of Pu and other radionuclides with $CaCO_3$. *Geochim. Cosmochim. Acta*, *57*(7), 1447–1458.

Mehrbach, C., Culberson, C., & Hawley, J. (1973). Measurement of the apparent dissociation constants of carbonic acid in seawater at atmospheric pressure. *Limnol. Oceanogr.*, *18*, 897–907.

Meibom, A., Cuif, J., Hillion, F., Constantz, B., Juillet-Leclerc, A., Dauphin, Y., Watanabe, T., & Dunbar, R. (2004). Distribution of magnesium in coral skeleton. *Geophys. Res. Lett.*, *31*.

Meibom, A., Cuif, J.-P., Houlbreque, F., Mostefaoui, S., Dauphin, Y., Meibom, K. L., & Dunbar, R. (2008). Compositional variations at ultra-structure length scales in coral skeleton. *Geochim. Cosmochim. Acta*, *72*(6), 1555–1569.

Meibom, A., Yurimoto, H., Cuif, J.-P., Domart-Coulon, I., Houlbreque, F., Constantz, B., Dauphin, Y., Tambutte, E., Tambutte, S., Allemand, D., Wooden, J., & Dunbar, R. (2006). Vital effects in coral skeletal composition display strict three-dimensional control. *Geophys. Res. Lett.*, *33*(11), L11608.

Millero, F. (1995). Thermodynamics of the carbon dioxide system in the oceans. *Geochim. Cosmochim. Acta*, *59*, 661–677.

Mitsuguchi, T., Matsumoto, E., Abe, O., & Uchida, T. (1996). Mg/Ca thermometry in coral skeletons. *Science*, *274*, 961–963.

Mitsuguchi, T., Uchida, T., Matsumoto, E., Isdale, P., & Kawana, T. (2001). Variations in Mg/Ca, Na/Ca, and Sr/Ca ratios of coral skeletons with chemical treatments: Implications for carbonate geochemistry. *Geochim. Cosmochim. Acta*, *65*(17), 2865–2874.

Morse, J., & Bender, M. (1990). Partition-coefficients in calcite—Examination of factors influencing the validity of experimental results and their application to natural systems. *Chem. Geol.*, *82*(3–4), 265–277.

Moya, A., Tambutte, S., Tambutte, E., Zoccola, D., Caminiti, N., & Allemand, D. (2006). Study of calcification during a daily cycle of the coral *Stylophora pistillata*: implications for 'light-enhanced calcification'. *J. Exp. Biol.*, *209*(17), 3413–3419.

Mucci, A. (1983). The solubility of calcite and aragonite in seawater at various salinities, temperatures, and one atmosphere total pressure. *American Journal of Science*, *283*(7), 780–799.

Mucci, A., Canuel, R., & Zhong, S. (1989). The solubility of calcite and aragonite in sulfate-free seawater and the seeded growth-kinetics and composition of the precipitates at 25 °C. *Chem. Geol.*, *74*(3–4), 309–320.

Nier, A. (1938). The isotopic constitution of strontium, barium, bismuth, thallium and mercury. *Phys. Rev.*, *54*(4), 275–278.

Orr, J., Fabry, V., Aumont, O., Bopp, L., Doney, S., Feely, R., Gnanadesikan, A., Gruber, N., Ishida, A., Joos, F., Key, R., Lindsay, K., Maier-Reimer, E., Matear, R., Monfray, P., Mouchet, A., Najjar, R., Plattner, G., Rodgers, K., Sabine, C., Sarmiento, J., Schlitzer, R., Slater, R., Totterdell, I., Weirig, M., Yamanaka, Y., & Yool, A. (2005). Anthropogenic ocean acidification over the twenty-first century and its impact on calcifying organisms. *Nature*, *437*(7059), 681–686.

Pearce, T. (1978). Olivine fractionation equations for basaltic and ultrabasic liquids. *Nature*, *276*, 771–774.

Press, W. H., Teukolsky, S. A., Vetterling, W. T., & Flannery, B. P. (1992). *Numerical Recipes in C: The Art of Scientific Computing, 2nd Ed.*. Cambridge University Press.

Puverel, S., Tambutté, E., & Pereira-Mouries, L. (2005). Soluble organic matrix of two Scleractinian corals: Partial and comparative analysis. *Comparative Biochemistry and Physiology, B*, *141*, 480–487.

Ramos, F., Wolff, J., & Tollstrup, D. (2004). Measuring $^{87}Sr/^{86}Sr$ variations in minerals and groundmass from basalts using LA-MC-ICPMS. *Chem. Geol.*, *211*(1–2), 135–158.

Raz-Bahat, M., Erez, J., & Rinkevich, B. (2006). In vivo light-microscopic documentation for primary calcification processes in the hermatypic coral *Stylophora pistillata*. *Cell. Tissue Res.*, *325*(2), 361–368.

Reynaud, S., Ferrier-Pages, C., Meibom, A., Mostefaoui, S., Mortlock, R., Fairbanks, R., & Allemand, D. (2007). Light and temperature effects on Sr/Ca and Mg/Ca ratios in the scleractinian coral *Acropora sp. Geochim. Cosmochim. Acta*, *71*(2), 354–362.

Reynaud, S., Leclercq, N., Romaine-Lioud, S., Ferrier-Pages, C., Jaubert, J., & Gattuso, J. (2003). Interacting effects of CO_2 partial pressure and temperature on photosynthesis and calcification in a scleractinian coral. *Global Change Biol.*, *9*(11), 1660–1668.

Reynaud-Vaganay, S., Gattuso, J., Cuif, J., Jaubert, J., & Juillet-Leclerc, A. (1999). A novel culture technique for scleractinian corals: application to investigate changes in skeletal $\delta^{18}O$ as a function of temperature. *Mar. Ecol-Prog. Ser.*, *180*, 121–130.

Robinson, L. F., Adkins, J. F., Fernandez, D. P., Burnett, D. S., Wang, S. L., Gagnon, A. C., & Krakauer, N. (2006). Primary U distribution in scleractinian corals and its implications for U series dating. *Geochem. Geophys. Geosyst.*, *7*, Q05022.

Robinson, L. F., Adkins, J. F., Scheirer, D. S., Fernandez, D. P., Gagnon, A., & Waller, R. G. (2007). Deep-sea scleractinian coral age and depth distributions in the northwest Atlantic for the last 225,000 years. *Bull. Mar. Sci.*, *81*(3), 371–391.

Rüeggeberg, A., Fietzke, J., Liebetrau, V., Eisenhauer, A., Dullo, W.-C., & Freiwald, A. (2008). Stable strontium isotopes ($\delta^{88/86}$Sr) in cold-water corals — A new proxy for reconstruction of intermediate ocean water temperatures. *Earth Planet. Sci. Lett.*, *269*(3–4), 569–574.

Russell, A., Hönisch, B., Spero, H., & Lea, D. (2004). Effects of seawater carbonate ion concentration and temperature on shell U, Mg, and Sr in cultured planktonic foraminifera. *Geochim. Cosmochim. Acta*, *68*(21), 4347–4361.

Russell, W., Papanastassiou, D., & Tombrello, T. (1978). Ca isotope fractionation on Earth and other solar-system materials. *Geochim. Cosmochim. Acta*, *42*(8), 1075–1090.

Sabine, C. L., Key, R. M., Kozyr, A., Feely, R. A., Wanninkhof, R., Millero, F. J., Peng, T.-H., Bullister, J. L., & Lee, K. (2005). *Global Ocean Data Analysis Project: Results and Data.* Tech. Rep. ORNL/CDIAC- 145, NDP-083, Carbon Dioxide Information Analysis Center, Oak Ridge National Laboratory, U.S. Department of Energy, Oak Ridge, Tennessee.

Sano, Y., Shirai, K., Takahata, N., Amakawa, H., & Otake, T. (2008). Ion microprobe Sr isotope analysis of carbonates with about 5 μm spatial resolution: An example from an ayu otolith. *Applied Geochemistry*, *23*(8), 2406–2413.

Sano, Y., Shirai, K., Takahata, N., Hirata, T., & Sturchio, N. (2005). Nano-SIMS analysis of Mg, Sr, Ba and U in natural calcium carbonate. *Analytical Sciences*, *21*(9), 1091–1097.

Schneider, K., & Erez, J. (2006). The effect of carbonate chemistry on calcification and photosynthesis in the hermatypic coral acropora eurystoma. *Limnol. Oceanogr.*, *51*(3), 1284–1293.

Schrag, D. (1999). Rapid analysis of high-precision Sr/Ca ratios in corals and other marine carbonates. *Paleoceanography*, *14*(2), 97–102.

Shen, C., Chiu, H., Chiang, H., Chu, M., Wei, K., Steinke, S., Chen, M., Lin, Y., & Lo, L. (2007). High precision measurements of Mg/Ca and Sr/Ca ratios in carbonates by cold plasma inductively coupled plasma quadrupole mass spectrometry. *Chem. Geol.*, *236*(3–4), 339–349.

Shen, G., & Boyle, E. (1988). Determination of lead, cadmium and other trace-metals in annually-banded corals. *Chem. Geol.*, *67*(1–2), 47–62.

Shirai, K., Kusakabe, M., Nakai, S., Ishii, T., Watanabe, T., Hiyagon, H., & Sano, Y. (2005). Deep-sea coral geochemistry: Implication for the vital effect. *Chem. Geol.*, *224*(4), 212–222.

Silverman, J., Lazar, B., & Erez, J. (2007). Effect of aragonite saturation, temperature, and nutrients on the community calcification rate of a coral reef. *J. Geophys. Res.—Oceans*, *112*(C5), C05004.

Sinclair, D. (2005). Correlated trace element "vital effects" in tropical corals: A new geochemical tool for probing biomineralization. *Geochim. Cosmochim. Acta*, *69*(13), 3265–3284.

Sinclair, D., Kinsley, L., & McCulloch, M. (1998). High resolution analysis of trace elements in corals by laser ablation ICP-MS. *Geochim. Cosmochim. Acta*, *62*(11), 1889–1901.

Sinclair, D., & Risk, M. (2006). A numerical model of trace-element coprecipitation in a physicochemical calcification system: Application to coral biomineralization and trace-element 'vital effects'. *Geochim. Cosmochim. Acta*, *70*(15), 3855–3868.

Sinclair, D., Williams, B., & Risk, M. (2006). A biological origin for climate signals in corals—Trace element "vital effects" are ubiquitous in Scleractinian coral skeletons. *Geophys. Res. Lett.*, *33*(17), L17707.

Smith, S., Buddemeier, R., Redalje, R., & Houck, J. (1979). Strontium-calcium thermometry in coral skeletons. *Science*, *204*(4391), 404–407.

Takahashi, T., Sutherland, S., Sweeney, C., Poisson, A., Metzl, N., Tilbrook, B., Bates, N., Wanninkhof, R., Feely, R., Sabine, C., Olafsson, J., & Nojiri, Y. (2002). Global sea-air CO_2 flux based on climatological surface ocean pCO_2, and seasonal biological and temperature effects. *Deep-Sea Res., Part II*, *49*, 1601–1622.

Tambutte, E., Allemand, D., Mueller, E., & Jaubert, J. (1996). A compartmental approach to the mechanism of calcification in hermatypic corals. *J. Exp. Biol.*, *199*, 1029–1041.

Trenberth, K., & Caron, J. (2001). Estimates of meridional atmosphere and ocean heat transports. *J. Climate*, *14*(16), 3433–3443.

Tripati, A., Roberts, C., & Eagle, R. (2009). Coupling of CO_2 and Ice Sheet Stability Over Major Climate Transitions of the Last 20 Million Years. *Science*, *(in press)*.

Watanabe, T., Minagawa, M., Oba, T., & Winter, A. (2001). Pretreatment of coral aragonite for Mg and Sr analysis: Implications for coral thermometers. *Geochemical J.*, *35*(4), 265–269.

Watson, E. (2004). A conceptual model for near-surface kinetic controls on the trace-element and stable isotope composition of abiogenic calcite crystals. *Geochim. Cosmochim. Acta*, *68*, 1473–1488.

Weber, J., & Woodhead, P. (1972). Temperature dependence of oxygen-18 concentration in reef coral carbonates. *J Geophys. Res.*, *77*(3), 463–473.

Weber, P., Bacon, C., Hutcheon, I., Ingram, B., & Wooden, J. (2005). Ion microprobe measurement of strontium isotopes in calcium carbonate with application to salmon otoliths. *Geochim. Cosmochim. Acta*, *69*(5), 1225–1239.

Wieser, M., Buhl, D., Bouman, C., & Schwieters, J. (2004). High precision calcium isotope ratio measurements using a magnetic sector multiple collector inductively coupled plasma mass spectrometer. *Journal of Analytical Atomic Spectrometry*, *19*(7), 844–851.

Wieser, M., & Schwieters, J. (2005). The development of multiple collector mass spectrometry for isotope ratio measurements. *International Journal of Mass Spectrometry*, *242*(2–3), 97–115.

Zeebe, R., & Sanyal, A. (2002). Comparison of two potential strategies of planktonic foraminifera for house building: Mg^{2+} or H^+ removal? *Geochim. Cosmochim. Acta*, *66*(7), 1159–1169.

Zeebe, R., & Wolf-Gladrow, D. (2001). *CO_2 in Seawater: Equilibrium, Kinetics, Isotopes*. (Elsevier Oceanography Series, 65). Elsevier: Amsterdam.

Zhong, S., & Mucci, A. (1989). Calcite and aragonite precipitation from seawater solutions of various salinites—precipitation rates and overgrowth compositions. *Chem. Geol.*, *78*(3–4), 283–299.

Zoccola, D., Tambutté, E., & Kulhanek, E. (2004). Molecular cloning and localization of a PMCA P-type calcium ATPase from the coral *Stylophora pistillata*. *Biochim. Biophys. Acta*, *1663*, 117–126.